Theses and Dissertations

Summer 2015

Flow around porous barriers: fundamental flow physics and applications

Keshav Basnet
University of Iowa

FLOW AROUND POROUS BARRIERS:
FUNDAMENTAL FLOW PHYSICS AND APPLICATIONS

by

Keshav Basnet

A thesis submitted in partial fulfillment
of the requirements for the Doctor of
Philosophy degree in Civil and Environmental Engineering
(Hydraulics)
in the Graduate College of
The University of Iowa

August 2015

Thesis Supervisor: Associate Professor George Constantinescu
Adjunct Professor Marian Muste

Graduate College
The University of Iowa
Iowa City, Iowa

CERTIFICATE OF APPROVAL

_____

PH.D. THESIS

_____

This is to certify that the Ph.D. thesis of

Keshav Basnet

has been approved by the Examining Committee for
the thesis requirement for the Doctor of Philosophy
degree in Civil and Environmental Engineering
(Hydraulics) at the August 2015 graduation.

Thesis Committee: _____
                          George Constantinescu, Thesis Supervisor

                          _____
                          Marian Muste, Thesis Supervisor

                          _____
                          Jacob Odgaard

                          _____
                          William Eichinger

                          _____
                          Albert Ratner

To my previous adviser Professor Robert Ettema, my parents, family and friends

ACKNOWLEDGMENTS

ABSTRACT

Investigating flow and turbulence structure around a barrier mounted on the ground or placed in its vicinity is a fundamental problem in wind engineering because of many practical applications related to protection against adverse effects induced by major wind storms (e.g., hurricanes) and snow events (e.g., snow fences used to reduce adverse effects of snow drifting on the roads). In this work the focus is on the case when the obstacle/barrier is porous and the shape of the obstacle is close to a high-aspect-ratio rectangular cylinder situated in the vicinity of the ground. The study employs a range of numerical and experimental techniques to achieve this goal that include 3D LES and 2D RANS numerical simulations, and RTK survey and 3D photogrammetry techniques to measure ground elevations and snow deposits in the field.

In the first part of the study, high-resolution large eddy simulations are used to understand the fundamental flow physics of flow past 2D solid and porous vertical plates with a special focus on describing the unsteady wind loads on the obstacle, vortical structure of the turbulent wake, spectral content of the wake, the separated shear layers and of the characteristics of the large-scale vortex shedding behind the plate, if present. Results show that LES can accurately predict mean flow and turbulence statistics around solid/porous cylinders. Then, a detailed parametric study of flow past vertical solid and porous plates situated in the vicinity of a horizontal bed is performed for the purpose of understanding changes in the mean flow structure, turbulence statistics and dynamics of large scale coherent structures as a function of the main nondimensional geometrical parameters (bottom gap for solid and porous plates, and porosity and average hole size of porous plates) and flow variables (e.g., bed roughness) that affect the wake flow. In particular, the LES flow fields allowed clarifying how the interactions between the bottom

and the top separated shear layers change with increasing bottom gap and what is the effect of the bleeding flow on the interactions between the separated shear layers that determine the coherence of the large-scale eddies at large distances from the wake.

In the second part of the thesis, a novel methodology based on field monitoring of the snow deposits and RANS numerical simulations is proposed to improve the design of snow fences and in particular the design of lightweight plastic snow fences that are commonly used to protect roads in the US Midwest against the snow drifting. The goal of the design optimization procedure is to propose a snow fence design that can retain a considerable amount of snow within a shorter downwind distance compared to fences of standard design. A major contribution of the present thesis was the development of a novel non-intrusive image-based technique that can be used to quantitatively estimate the temporal evolution of the volume of snow trapped by a fence over long periods of time. This technique is based on 3-D close range photogrammetry. Results showed that this technique can produce estimations of the snow deposits of comparable accuracy to that given by commonly used methods. This is the first application of this type of techniques to measurements of the snow deposits.

PUBLIC ABSTRACT

Investigating flow around an obstacle/barrier is a fundamental problem in wind engineering because of many practical applications related to protection against adverse effects induced by major wind storms (e.g., hurricanes) and snow events (e.g., snow fences used to reduce adverse effects of snow drifting on the roads). In this work the focus is on the case when a rectangular porous vertical plate is situated in the vicinity of the ground. The study employs a range of numerical and experimental techniques to achieve this goal.

In the first part of the study, high-resolution three dimensional large eddy simulations (LES) are used to understand the fundamental flow physics of flow past solid and porous vertical plates with a special focus on describing the unsteady wind loads on the plate, turbulence structures behind the plate and bed friction velocity. Results show that LES can accurately predict mean flow and turbulence statistics around solid/porous cylinders. Then, a detailed parametric study of flow past vertical solid and porous plates situated in the vicinity of a horizontal bed is performed for the purpose of understanding changes in the mean flow structure, turbulence statistics and dynamics of large scale coherent structures as a function of the main geometrical parameters (relative bottom gap for solid and porous plates, and porosity and average hole size of porous plates) and flow variable (bed roughness) that affect the wake flow. In particular, the LES flow fields allowed clarifying how the potential region of particles deposition and sediment entrainment vary with the main geometrical parameters and flow variable.

In the second part of the thesis, a novel joint methodology based on both field monitoring of the snow deposits and two dimensional RANS numerical simulations is proposed to improve the design of snow fences and in particular the design of lightweight plastic snow fences that are commonly used to protect roads in the US Midwest against the

snow drifting. The goal of the design optimization procedure is to propose a snow fence design that can retain a considerable amount of snow within a shorter downwind distance compared to fences of standard design. Results showed that snow fences with new design proposed in this study are a better option to protect roadways against snow drifting in regions with narrow right of ways. Another major contribution of this study is to propose, develop protocols and test a novel image-based technique that can be used to quantify the snow deposits trapped by a snow fence over time. This technique is based on three dimensional close range photogrammetry (CRP) which is a non-intrusive method that eliminates the need to perform man-made measurements during the storms, which are difficult and sometimes dangerous to perform. The protocols developed in this study allowed continuous measurements of snow deposits over time using images remotely that eliminates the need to visit the site for field measurements during the harsh weather. This is the first application of this type of techniques to measurements of the snow deposits trapped by a fence.

TABLE OF CONTENTS

LIST OF TABLES

LIST OF FIGURES

xiv

xv

xvi

CHAPTER 1 INTRODUCTION

Investigating flow and turbulence structure around an obstacle/barrier mounted on the ground or placed in its vicinity is a fundamental problem in wind engineering because of many practical applications related to protection against adverse effects associated with severe winds and particles (e.g., snow, sand and dust) drifting (e.g., see Dong et al., 2010; Cong et al., 2011). Porous barriers installed close to the ground have been widely used in environmental and industrial engineering applications to modify velocity and turbulence distributions in their vicinity (Figure 1.1). Of particular importance for wind engineering applications is the case when the obstacle/barrier is porous and the shape of the obstacle is close to a high-aspect-ratio rectangular cylinder or plate (Figure 1.2). Two common examples are: windbreaks or shelter fences (see Figures 1.3 through 1.5) and wind fences (e.g., sand fence, snow fence, dust fence etc.; see Figures 1.6 through 1.8). Most of these types of porous barriers have their length much larger than their height such that the mean flow field is two-dimensional in a good approximation.

The presence of a solid or porous obstacle in the vicinity of the ground alters the flow characteristics around it and affects transports phenomena in the wake of the obstacle and within the region where the approaching flow is deflected by the adverse pressure gradient introduced by obstacle. At least for obstacles of relatively low porosity, separation and recirculation regions can form upwind and downwind of the obstacle (Figure 1.1). The dimensions of the recirculating regions depend on the ratio between the boundary layer thickness of the approaching flow and the obstacle height and also on the shape of the obstacle and its position relative to the ground (Hwang et al., 1999).

In most of the aforementioned practical applications, the main challenge is to design the porous barrier such that it effectively acts toward alleviating adverse effects induced

1

by snow storms and/or severe winds. A deep understanding of the fluid mechanics of flow past porous two-dimensional high-aspect ratio rectangular obstacles and dynamics of large scale turbulence is a prerequisite for developing effective designs of porous barriers used in various engineering applications.

1.1 Motivation

In many practical applications, it is essential to control the flow structure downwind of the obstacle/barrier to fit a specific need. In wind engineering applications, the obstacle is generally called a fence. Such obstacles can be classified either as structural fences if the fence is made from wood, plastic, metal or other materials (Figures 1.5 through 1.8) or living fences if trees and/or bushes form the fence (Figures 1.3 and 1.4).

Windbreaks and shelterbelts have played and continue to play a significant role in protecting man and his micro-environment. For example, shelter fences and wind barriers in the form of vertical plates are widely used as artificial windbreaks (Dong et al., 2010) to locally reduce the flow velocity within a given region so that one can mitigate the damage caused by wind (e.g., region downwind of a porous barrier can act as a shelter offering protection from hurricanes or can be used to protect soil from erosion; see Figures 1.3 through 1.5).

Besides the sheltering effect, another topic of great practical interest related to flow past porous fences is the amount of particles deposited, the deposition patterns, and the length of region where particles deposit on the downwind side of the fence. Porous fences in the form of plates placed vertically on the ground have long been used as wind fences to control drifting of sand and snow. Wind fences are just a particular type of surface-mounted porous barriers subject to an incoming flow, often containing particulates. The use of such

2

wind fences can result in a dramatic decrease of problems related to blowing and drifting particles (e.g., snow, sand and dust) on roadways and railways by reducing the speed of the particles and promoting deposition of particles downwind of the fence (Figures 1.6 through 1.8). If properly designed, the wind fence can control where sand shifts or snow drifting occurs. Wind fences can also be used as an effective way to control Aeolian sand transport (Saif et al., 2010). This is why wind fences are widely used not only in cold areas but also in coastal and arid regions (Lee and Kim, 1999; Dong et al, 2007).

Among all the aforementioned applications of shelter and wind fences, the use of wind fences to mitigate snow drifting in the vicinity of roads is the most important type of application for the US Midwest states where heavy snow event occur over the winter time. Two of the main causes for reduction in driver visibility and safety, poor driving conditions on the road, degradation of road quality (e.g., due to saline water infiltration under the pavement after the snow melts) and, ultimately, for increased accidents during the winter season are the blowing snow that reaches the road and the accumulation of snow on the roadway (snow drifting). Large drifts of snow can reduce the effective road width. Blowing snow crossing the road can significantly impair drivers' visibility. Removing mechanically snow from the roadways is very costly due to equipment expenses and salaries of the snow removal crews. It additionally results in lower usage of the roads between the time the snow deposits and the time the snow is removed (e.g., see Tabler, 1991 and 2003; Iowa DOT: Iowa's Cooperative Snow Fence Program, 2005; Sañudo-Fontaned et al., 2011). The use of wind fences, if properly designed (e.g., in terms of position, height, orientation, porosity, bottom gap), can result in a dramatic decrease of problems related to snow blowing and

drifting in regions where their development is common. Such wind fences are generally referred to as snow fences.

Figure 1.8 clearly illustrates the difference between a road area not protected by snow fences, where snow particles drift toward the road and snow accumulates in the vicinity and over the road, and a neighboring road area protected by a structural snow fence, where snow drifting is much less and the snow accumulation in the immediate vicinity of the road and over the road is negligible. These differences substantiate the main role of installing wind fences along highways or railways, which is to retain the blowing particles upwind of the roadway area.

Porous plates are also used in environmental engineering applications related to mitigation of wind-blown dust emissions at industrial sites where porous plates are used to reduce the wind-blown particle emissions to the environment and to minimize the loss of raw materials resulting in a needless waste. In the recent years, porous fences are also used as a solution to reduce the fugitive particle emission from aggregate piles in the open storage yards of harbor areas (e.g., see Cong et. al., 2011; Duan et. al., 2011b).

Some other examples of engineering applications where porous barriers are used to modify flow and turbulence characteristics are rows of tubes placed near heat-exchanger walls, porous plates used as vortex generators to improve the cooling in electronic circuits and as turbulence generators in wind tunnels.

To be able to optimize the performance of a porous fence/plate for a given application, one first need to understand how the flow and turbulence structure change with the various relevant design parameters (Figure 1.2). For all these reasons, understanding the physics of flow around vertical porous two-dimensional (2D) obstacles and the wake

structure downwind of such porous obstacle is of considerable interest for many engineering applications.

1.2 Description of the Problem

The flow past 2D porous fences presents both similarities and differences with the widely studied flow past solid cylinders of different shapes situated far from lateral boundaries. In the case of flow past long 2D cylinders and plates, the characteristics of the large-scale vortex shedding can be strongly affected by the presence of a nearby wall oriented parallel to the incoming flow direction. In fact, the large-scale vortex shedding behind the cylinder can be completely suppressed if the gap between the wall and the bottom of the cylinder is sufficiently small (Bosch et al., 1996). Because vortex shedding induces unsteady drag forces on the cylinder and increased mixing in the wake, it is of considerable practical importance and so are the questions of whether shedding occurs or not and what the influence of wall proximity is on the vortex shedding (Bosch et al., 1996). The following discussion focuses on 2D high-aspect-ratio rectangular cylinders which will be referred as plates. This is because most wind fences resemble long 2D porous plates.

The characteristics of the flow around a porous plate situated in the vicinity of a wall surface are a strong function of the porosity of the plate (P), the bottom gap ratio (G/H) and the relative hole-size (d/H) of the plate (Figure 1.2). The bottom gap is the open space between the ground and bottom of the plate. The porosity P is defined as the ratio of open area of the plate to its total frontal area excluding the bottom gap. The wake structure is a strong function of the porosity, the bottom gap and the relative hole-size of the plate. Other parameters that influence the wake structure are the Reynolds number, Re, defined with the mean incoming flow velocity, U_0, and the fence height, H, the roughness of the ground

(bottom wall surface), k, the relative turbulence intensity of the incoming flow and the aspect ratio of the plate (ratio of the obstacle height, H, to the plate thickness, t). Additionally in the case of porous plates, the shape of the openings (strips, circular or elliptical openings) and their arrangement can influence the flow past the plate.

Several studies (e.g., Seginer, 1972; Heisler and Dewalle, 1988; Dong et al., 2007 and 2010) have shown that the porosity is a main parameter influencing the characteristics of the turbulent flow field around the porous plate (e.g., degree of velocity reduction and turbulence amplification induced in the wake). In the particular case of snow and sand fences, the characteristics of the turbulent velocity field behind the fence affect particle deposition patterns and determine over what distance significant particle deposition will occur downwind of the fence. Experimental studies (e.g., Castro, 1971; Perera, 1981; Lee and Kim, 1999) have showed that above a critical value of the porosity, there is no reversed flow behind the plate, similar to the reversed flow observed in the widely studied case of a solid (zero porosity) surface mounted obstacle. This also means that there is no well-defined recirculation region in the wake of a porous fence if the fence porosity is larger than a certain threshold value. Another important observation is that the mean structure and dynamic behavior of the wake flow changes significantly with the height of the bottom gap (Martinuzzi et al, 2003). In the case of snow and sand fences, the bottom gap serves to reduce particles accumulation in the immediate vicinity of the fence and is an important design parameter that controls the total particles trapping capacity of the fence (Tabler, 2003).

1.3 Research Needs and Justification of Research Approach

To optimize the design of a porous plate for one of the applications discussed in the previous sections, it is essential to understand how the main geometrical and flow parameters affect the main features of the mean flow and turbulence structure, the dynamics of the large scale vortex shedding and of other coherent structures present in the mean and instantaneous flow fields, unsteady forces on the plate and the capacity of flow to entrain particles from bottom surface.

Though a lot has been gained in understanding the physics of the flow past 2D vertical solid and porous plates from experimental investigations (e.g., see Dong et al., 2007), information from such investigations does not always provide a sufficient description of the wake structure and role of the large scale turbulence. This is mainly because such investigations provide mainly mean flow and turbulence statistics measurements in a limited number of cross section situated upwind and downwind of the plate. Generally, these experimental investigations do not provide information on the boundary shear stresses, unsteady loads on the fence and the interactions between the large scale coherent structures in the flow. At best, the dynamics of the coherent structures is visualized in a 2D plane in which PIV measurement are performed. No 3D PIV investigations which would allow understanding the role of 3D instabilities and their effects on the quasi-2D large scale coherent structures were yet reported for this type of flows.

On the other hand, sufficiently well resolved eddy-resolving numerical methods can provide three-dimensional visualizations of the entire (time-averaged and instantaneous) flow fields. The 3D mean and instantaneous flow fields available from such numerical simulations can be easily used to visualize and characterize the coherence, shape

and dynamics of the main coherent structures in the flow and their interactions with other coherent structures or with the bed. Moreover, such simulations can provide information on quantities that are very difficult to accurately estimate based on experimental measurements. For example, measurements of the instantaneous bed shear stress distributions are practically impossible to achieve experimentally.

Thus, numerical investigations based on Direct Numerical Simulation (DNS), Large Eddy Simulation (LES) or hybrid RANS-LES techniques (see Rodi et. al, 2013) can provide additional valuable insight into the structure of wake flow behind solid and porous vertical plates. For the Reynolds numbers of interest in practical applications (Re $\geq 10^4$), where the incoming flow is highly turbulent, LES solvers that avoid the use of wall functions and use non-dissipative discretization schemes and sub-grid scale models appear to be the best option given their proven accuracy for massively separated flows. This is why, in the present study the effect of the main geometrical and flow parameters that determine the wake past vertical solid and porous plates will be investigated based on 3D LES simulations performed on fine meshes that resolve the viscous sub-layer and using a non-dissipative code in which the effect of the small scales on the resolved scales is modeled using the dynamic Smagorinsky model.

Besides acquiring a fundamental understanding of the physics of flow past solid and porous vertical plates situated in the vicinity of a horizontal surface, numerical simulations can be used in conjunction with field measurements to improve the design of wind fences. As already mentioned, in the present study one is interested to improve the design of snow fences and in particular the design of lightweight plastic snow fences that are commonly used to protect roads in the US Midwest against the snow drifting. This

solution is adopted in many regions of U.S. because such fences can be easily and rapidly deployed or removed from the field. A main design challenge occurs when the right of way of the road to be protected is too narrow to allow placing standard design snow fences (porosity close to 50%) at the distance from the edge of the roadway recommended by the guidelines. Given this constraint, there is a need to optimize the design of these fences (e.g., by decreasing their porosity while increasing their bottom gap) such that they can retain a considerable amount of snow within a shorter downwind distance compared to fences of standard design. Thus, there is a need to optimize design of standard plastic snow fences such that they can work well along road regions with narrow right of ways.

To assess the efficiency of a snow fence design, it is needed to test the performance of the snow fence in the field and compare its capacity to retain a large volume of snow over a relatively small distance from the fence with that of other designs. The most critical step of such a fence monitoring program is to determine the volume of snow retained by the fence after major snow storm events. This requires methods to determine the ground profile and the snow profiles in the fence vicinity. Information on the temporal evolution of the volume of snow retained by the fence over long periods of time (e.g., over a whole winter season) cam also provide lots of useful information to assess the overall performance of the fence design that is tested.

1.4 Research Goals and Objectives

The first goal of the present study is to investigate the physics of turbulent flow past a 2D porous vertical plate attached to or situated in the vicinity of a horizontal surface. This is because this somewhat simplified flow and geometry set up can be used to better understand flow and wake structure past typical wind fences used in practical engineering

9

applications. In particular, a main objective of the present study is to provide a detailed description of the unsteady wind loads on the plate, vortical structure of the turbulent wake, spectral content of the wake, the separated shear layers and of the characteristics of the large-scale vortex shedding behind the plate, if present. The emphasis will be on obtaining information not available from experimental studies of these flows and to perform a systematic study that will allow understanding how each of the main design and flow parameters influences the wake structure past porous plates. As such, the main objectives of the first part of the study dealing with fundamental description of flow and turbulence structure past porous plates are:

- to show 3D LES can accurately predict flow around 2D cylinders and plates

- to systematically investigate the effect of varying the plate porosity, the relative size of the bottom gap G/H and the relative size of the strip holes d/H on the wake structure

- to investigate the effect of the ground roughness on the flow structure

The second goal of this study is to propose a novel methodology involving field monitoring of snow fences, field measurements of the snow deposits and numerical simulations that can be used to improve design of snow fences. As this methodology is expected to be used in consulting, numerical simulations based on Reynolds-Averaged Navier Stokes (RANS) - which are computationally much less expensive compared to LES - will be conducted to help compare the efficiency of different snow fence designs. A major research objective related to the second goal is to apply this method to design lightweight snow fences that can be effectively used to protect roadways against snow drifting in regions with narrow right of ways where standard design snow fences do not work well.

As the assessment of the performance of a fence design is based on the capacity of the fence to retain snow during major snow events, a related objective is to test and assess the accuracy, advantages and disadvantages of various methods that can be used to measure snow profiles in the vicinity of the snow fence. Part of this study, a novel non-intrusive method based on close range photogrammetry will be proposed and tested to determine the temporal evolution of the volume of snow retained by the fence.

1.5 Structure of Thesis

The outline of the thesis is as follows. Chapter 2 provides a summary of previous experimental and numerical studies of flow over vertical solid and porous plates and cylinders situated in the vicinity or in contact with a bottom wall surface. Both fundamental studies of the wake past such obstacles and applied studies related especially to improving the design of Section windbreaks and snow fences are discussed. Chapter 3 describes the numerical modeling approaches based on large eddy simulation (LES) and Reynolds-Averaged Navier Stokes (RANS) used to simulate flow past solid and porous plates and snow fences.

Chapter 4 discusses validation of the LES model for two relevant cases: turbulent flow around a square cylinder in a wide channel and turbulent flow around a solid/porous fence on a flat bed. In the same chapter, the effect of the rectangular cylinder width is investigated by comparing results for a square cylinder with those for of a thin rectangular cylinder of same height. Chapter 5 through Chapter 8 report several parametric studies of flow past high-aspect ratio rectangular barriers based on LES results obtained at relatively low Reynolds number (Re=20,000) at which most of the detailed laboratory investigations of these flows were performed. In each of these parametric studies conducted for both solid

11

and porous barriers, only one of the main geometrical parameters (barrier porosity, bottom gap for both solid and porous barriers, spacing between the rectangular elements forming the porous barrier) is varied. Finally, the effects of bed roughness on the flow past solid and porous barriers are investigated in Chapter 9 by conducting LES simulations in which the bottom surface contains an array of equally-spaced 2D ribs.

Chapters 10 and 11 report on field studies in which the performance of plastic snow fences was monitored over several winter seasons. Chapter 10 presents a novel methodology to improve the design of snow fences based on monitoring of sites containing snow fences, measurements of the snow deposit profiles using various techniques and 2-D RANS simulations used to identify candidates for improved fence designs to be tested in the field. Chapter 11 presents a novel non-intrusive image-based technique that can be used to quantitatively estimate the temporal evolution of the volume of snow trapped by a fence over long periods of time. This technique is based on 3-D close range photogrammetry. The chapter discusses measurement protocols, testing and comparison with accuracy of other methods used to determine the snow deposit profiles in the field.

The main findings of the study are outlined in Chapter 12. Recommendations for future research are also presented in the same chapter.
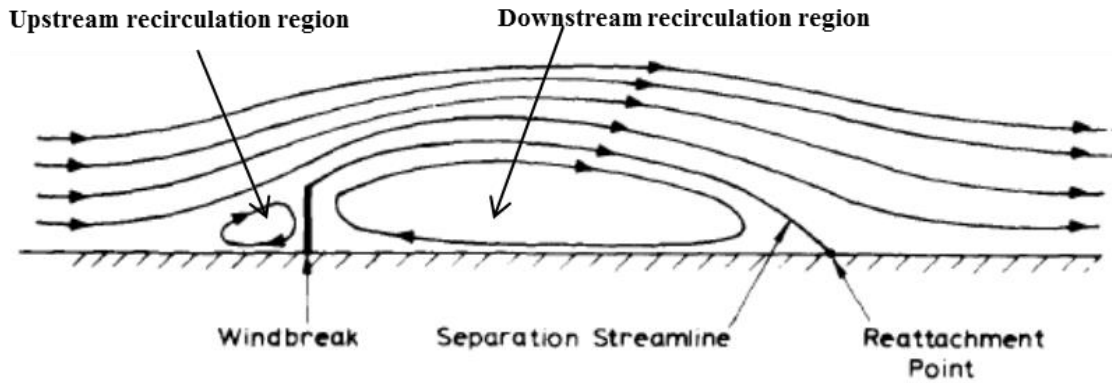
Figure 1.1 Flow including separation and reattachment zone around an obstacle or windbreak (Raine and Stevenson, 1977). Note that for high porosities, upwind and downwind recirculation regions may be absent.

a)   b)
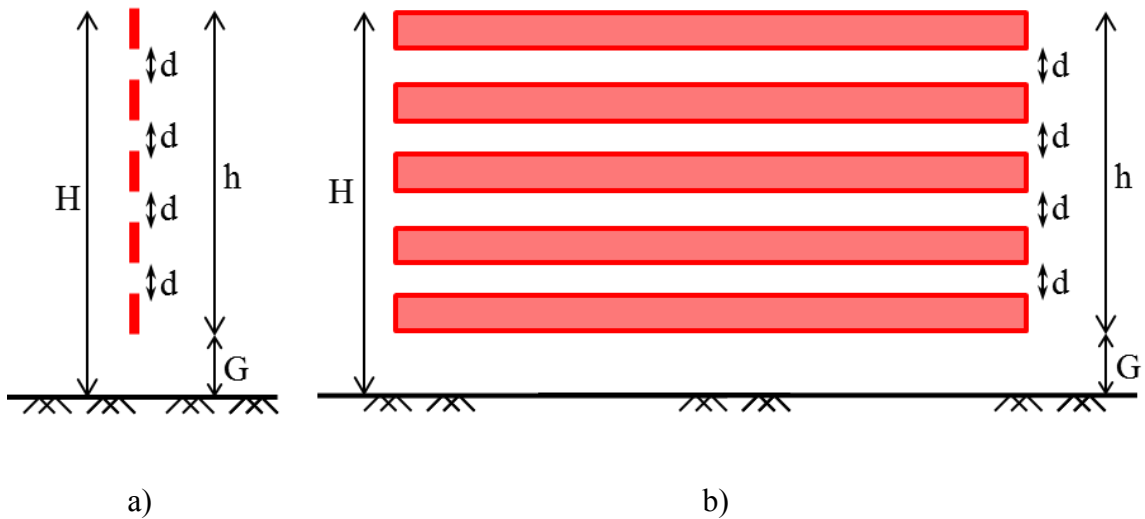
Figure 1.2 Sketch showing main variables characterizing a porous plate; total height of the obstacle (H), net obstacle height (h), bottom gap (G), and hole-size (d): a) side view; b) front view.

Figure 1.3 Shelter (living) fence made from trees (Source: http://creating-a-new-earth.blogspot.com/p/important-hardscaping-terms-definitions.html).

Figure 1.4 Windbreak (living fence) made from trees (Source: http://www.ohiodnr.com/news/mar07/0315windbreakprogram/tabid/18460/Default.aspx).

Figure 1.5 Structural windbreak made from plastic material (Source: http://www.agriflex-fencing.com/windbreak.jpg).

Figure 1.6 Structural sand fence installed along the coast (Source: www.flickr.com/photos/57744973@N00/8171874728).

Figure 1.7 Structural sand fence installed along a highway to minimize sand drifting on the road (Source: http://members.virtualtourist.com/m/p/m/1ed4e5/).
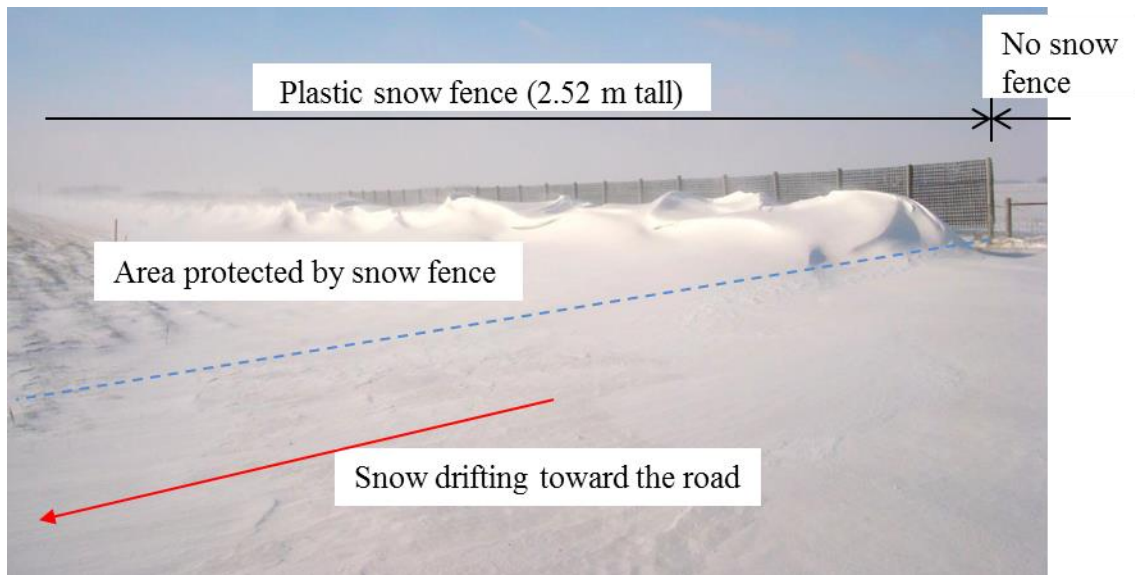
Figure 1.8 Picture illustrating the effect of placing a snow fence close to a road on snow drifting. The unfenced area on the right is subject to significant snow blowing and drifting toward and over the road, leading to the development of a significant snow deposit on the roadway. On the left side, which is protected by a structural snow fence, snow accumulates on the downwind side of the fence but the snow deposit close to the roadway is negligible. The picture was taken on a road near Williams, Iowa, U.S.

CHAPTER 2 LITERATURE REVIEW

2.1 Experimental Studies

A large number of experimental investigations have been conducted to study the flow past surface mounted 2D barriers and porous plates.

Cabron (1957) provides a general classification of windbreaks, which are basically porous barriers mounted on the ground. Windbreaks or wind fences can be constructed from several materials (Sañudo-Fontaned et al., 2011). Besides the traditional wood fences, typical materials for fences include metal rails, plastic nets, polymer rails and woven fabric. Fence materials are attached to supporting structures (e.g., posts) made of steel or wood or by using an especially designed (truss-type) framework set in the ground. Dong et al. (2007) classified structural wind fences into five different types as shown in Figure 2.1 depends on the shape and orientation of solid and void parts of the total fence surface. Heisler and Dewalle (1988) provide a detailed review of the effects of windbreak design on wind flow and wind speed reduction behind the windbreak. Plate (1971) provides a good review of the aerodynamics of shelterbelts, which are a particular type of windbreak barrier.

Flow past thin perforated obstacles (e.g., windbreaks) has been studied experimentally since the 1940s with the goal of finding the optimal fence design that provides maximum protection (e.g., maximum reduction in wind velocity in the case of windbreaks, maximum deposition of snow deposit in the vicinity of the fence in the case of snow fences) at the minimum cost (Plate, 1971). Several experiments were conducted to determine the drag of windbreaks and other obstacles having configurations similar to that of classical windbreaks (e.g., Tani, 1952; Plate, 1964; Hagen and Skidmore, 1971; Castro, 1971). Seigner (1972) estimated experimentally the drag of porous fences and

introduced a more accurate method to calculate the windbreak's drag coefficient. A review of published results shows that the drag coefficient of a fence decreases as the fence porosity increases (e.g., Hoerner, 1965; Seginer, 1972; Wilson, 1985; Guan et al., 2003). This would mean that in principle less porous fences provide a better shelter effect compared to high porosity fences. Hence, solid fences would have the best efficiency. But this is not true if one considers other factors. So, the drag coefficient alone is not able to provide sufficient information for defining the optimal porous fence design. Other factors should be considered to fully characterize the shelter effect created by wind fences.

Most of the published experimental results have shown that the optimal porosity of windbreaks is around 0.3 or 0.4 (Hagen and Skidmore, 1971; Lin et al., 1984; Lee et al., 2002). These results confirm that the shelter efficiency of the windbreak is also determined by other factors besides the degree of wind speed reduction behind the fence. The distribution of the mean velocity fluctuations and the vortical structure of wake flow behind the fence have received increasing attention because of their importance for understanding the flow physics and transport phenomena around porous barriers. Moreover, the passage of large scale eddies near the bed has a significant effect on the bed shear stress, which in turn controls deposition and erosion around the fence (e.g., Hagen and Skidmore, 1971; Bradley and Mulhearn, 1983; Castro and Haque, 1987; Shiau, 1992 and 1995).

Since at least the 1970s, considerable effort has been devoted to studying the wind reduction and turbulence amplification induced by porous fences with the goal of identifying the optimal value of the fence porosity which will maximize the effect which motivated the deployment of the fence. These efforts have included both field measurements and wind tunnel laboratory experiments (e.g., Raine and Stevenson, 1977;

Perera, 1981; Borges and Viegas, 1988; Wilson, 1997; Lee and Kim, 1998 and 1999; Lee and Park, 1999; Dong et al., 2006 and 2007). Relatively few measurements of turbulence characteristics behind shelter fences have been made until recently despite the fact that turbulence and turbulent transport mechanisms are likely to have at least as great of an influence on shelter effectiveness as the mean flow field (Raine and Stevenson, 1977). The earliest experimental studies date back to Arie and Rouse (1956) who used hot-wire probes to analyze the time-averaged velocities and turbulent Reynolds stresses in the separation bubble behind a plate mounted in a flatbed channel.

The earliest experimental investigations of turbulent velocity fluctuations behind porous fences were conducted in the field. Measurements conducted using anemometers provide only a rough estimate of the turbulent kinetic energy because field measurements are often influenced by changing wind direction, atmospheric stability and surface conditions (Bradley and Mulhearn, 1983; Finnigan and Bradley, 1983). On the other hand, measurements conducted in wind-tunnel scaled-model studies allow a better control of the flow conditions during the experiment. Lee and Kim (1999) found that measurements conducted using a hot-wire anemometer (HWA) overestimated the turbulence in the recirculation regions forming around the fence. Perera (1981) and Ranga raju et al. (1988) used a pulsed-wire anemometer (PWA) to conduct measurements within the separated wake flow. Both HWAs and PWAs are intrusive techniques that distort the flow fields and have difficulties measuring turbulent stresses in the near-wake region that is dominated by highly turbulent energetic eddies (Lee and Kim, 1999).

Non-intrusive measurement techniques such as laser Doppler anemometers (LDA) and phase Doppler anemometers (PDA) have also been used to measure mean flow and

turbulent stresses behind fences. These techniques were found to be more accurate compared to intrusive techniques like HWA and PWA. However, all these measurement techniques can provide the time-averaged velocity and turbulent stresses only at discrete measurement points (Lee and Kim, 1999).

Non-intrusive measurement techniques such as particle image velocimetry (PIV) and particle tracking velocimetry (PTV) can provide high-resolution and high-frequency velocity measurements over a certain 2D region. Such techniques have been used only recently to understand turbulence structure behind porous fences. For example, Dong et al. (2007 and 2010) used a two-frame PIV technique to measure the instantaneous velocity fields behind fences with different porosities in a scaled model wind-tunnel experiment. Dong et al. (2007 and 2010) report detailed measurements and analysis of mean velocity, turbulence intensity, vorticity, Reynolds stresses and turbulent kinetic energy as a function of the fence porosity. Similarly Lee and Kim (1999) estimated the mean velocity and turbulent Reynolds stresses in the near-wake region behind porous wind fences using PTV.

2.1.1 Effect of Porosity on Flow past 2D Plates

Though the following discussion refers primarily to porous fences, this type of obstacle is from a fluid mechanics point of view a porous plate mounted vertically on a channel bed. Several studies (e.g., Seginer, 1972; Heisler and Dewalle, 1988; Dong et al., 2007 and 2010) have shown that the fence porosity is the main parameter determining the degree of velocity reduction and turbulence amplification in the wake of long fences (e.g., fences whose length is much larger than their height). The characteristics of the turbulent velocity field behind the fence determines, to a large degree, how many particles of snow/sand will deposit and over what distance significant deposition of particles will occur.

Many investigators (e.g., Perera, 1981; Borges and Viegas, 1988; Wilson, 1997; Lee and Kim, 1998; Lee and Park, 1999; Dong et al., 2006) have tried to make recommendations on optimal fence porosity by measuring and analyzing the mean velocity, turbulent kinetic energy, bed shear stress and sediment susceptibility to wind transport behind such fences. Baines and Peterson (1951) found that the fences should have a porosity of more than 50% to avoid the jet coalescence effect which induces a large amplification of the turbulence behind the fence.

Baltaxe (1967) found a critical porosity of about 35% below which the frequency spectrum of the velocity fluctuations exhibited a marked peak. When the porosity exceeded 35%, this peak was absent and presumably the separation bubble behind the fence was also absent. Apart from the abrupt elimination of the peak in the velocity power spectrum, the energy of the velocity-fluctuations fell off fairly evenly with increasing porosity. These findings are in agreement with the study of de Bray (1957). The absence of a separation bubble for fence porosities, P, larger than 30-35% is consistent with the findings of Castro (1971) who performed two-dimensional simulations to investigate the wake characteristics of perforated plates positioned normal to an air-stream. The simulations showed that the recirculation zone behind the porous plate disappears when the porosity, P, exceeds 30%.

Raine and Stevenson (1977) used the HWA method to measure the velocity and turbulence intensity in the wake of fences with varying porosity. They found that a windbreak of low to medium porosity had better overall mean wind velocity reduction characteristics than a solid one. They found that the 20% porosity fence produced the best overall velocity pattern inside the wake (shelter) region. They also indicated that as the

fence porosity increases there is less shear in the flow at the fence top and thus a weaker streamwise momentum transfer from the displacement flow back into the sheltered region.

Perera (1981) investigated the wake flow of solid and porous fences in a simulated rural atmospheric boundary layer using PWA. His measurements could not detect a recirculation bubble behind the fence for P>30%, which agrees with the results of Castro (1971). Marshall (1967) observed that the area of leeward sheltered ground decreases with decreasing porosity because the minimum leeward wind velocity occurs closer to the barrier.

The experiments of Yaragal et al. (1997) showed that a wind fence with a porosity P=30% had mean pressure fluctuation levels in the downwind region of the fence by around 50% lower compared those observed behind a solid fence. They also found that the reattachment length is close to 26H for fences with P<12.5%. The reattachment length decreased slightly to 25H for P=26%. In agreement with other studies, no reattachment region was detected for a fence with P=60%.

Yaragal et al. (2002) carried out wind tunnel experiments of perforated plates (0%≤P≤50%) to study the effect of porosity on the extent of the reattachment region behind the plates. They provided streamline plots for 6 different porosities. Figure 2.2 visualizes that the Ψ=0 dividing streamline that defines the shape of the separation bubble. For P>30% the bubble does not form. They have also reported the variation of the shape and position of the bubble as a function of the porosity, P (Figure 2.3). It can be seen that, the height of the separated bubble and its length decrease progressively as the porosity increases. The separation bubble vanishes completely for porosity levels greater than 30%.

Corneils W.M. and Gabriels D. (2005) have focused on optimizing the design of windbreaks whose main purpose was to minimize wind-erosion. Their study found that the optimal porosity of such windbreaks is between 20% and 35%. On the other hand, a wind tunnel experimental study of sand fences conducted by Dong et al. (2006) found that fences with porosities between 30% and 60% (depending on the fence height) had the maximum relative threshold wind velocity and maximum effective shelter distance and were the most suitable for controlling wind induced sand erosion. Furthermore Dong et al. (2007) conducted a wind tunnel experiment in which 11 fences with porosities varying from 5% to 90% were tested. According to their study, the optimal porosity which corresponds to a critical porosity above which the bleed flow dominates and below which reversed flow becomes significant is around 20%-30%. In agreement with other studies, Dong et al. (2010) found that the decrease in fence porosity induces a decrease of the mean streamwise velocity behind the fence, but the mean velocity fluctuations in the vertical direction can increase significantly. Their study proposed an optimal fence porosity of about 20% based on the fact that for lower porosities the turbulent intensity, the Reynolds stresses and the vertical velocity fluctuations behind the fence start increasing rapidly with further decrease in the fence porosity.

Wake flow behind dust fences of different porosities has been investigated experimentally by Duan et al. (2011a and 2011b). Their wind tunnel studies concluded that the optimum porosity is between 23% and 32%. The study of Lee and Kim (1999) tried to determine the optimum porosity that reduces wind erosion induced by wind-blown dusts. They investigated the characteristics of the turbulent wake flow behind fences with P=0%, 20%, 40% and 65% using the PTV technique. Experiments were conducted in a

recirculating water channel with uniform approach flow. Their study provided mean velocity and mean turbulent fluctuation profiles at 8 different locations in the fence wake, as shown in Figure 2.4 and Figure 2.5 respectively.

The mean velocity profiles in Figure 2.4 indicate that both the streamwise and the vertical velocity components are a strong function of the fence porosity. The mean velocity profiles recover gradually. The flow achieves equilibrium at a significant distance behind the fence. The velocity profiles recover more quickly as the fence porosity increases. On the other hand, the overall reduction of the streamwise velocity behind the fence increases with decreasing porosity. A recirculating bubble region forms only behind the P=0% and P=20% fences. While for the solid fence the recirculation bubble touches the back of the fence, for P=20% the bubble is shifted in the downstream direction to a location of about x=1H. Furthermore, the maximum reverse velocity behind the P=20% fence is reduced by about 28% compared to the non-porous fence (P=0%). A zone of maximum vertical velocity can be noticed in the near wake region. This zone shifts upwards as the porosity increases and as the distance from the fence increases. In this near-wake region, the vertical velocity decreases as P increases.

The turbulence intensity behind the fence increases as P decreases. However, the P=20% fence has the highest turbulence intensity in the region situated below the fence height, up to about the x=2H location. In the region situated just behind the fence (x<2H), the location of the highest streamwise mean turbulent fluctuations in the upper shear layer shifts down as the porosity increases. The maximum value of mean streamwise velocity fluctuations decreases with increasing porosity. In the shear layer forming at the bottom of the fence, the P=20% fence shows the highest turbulence intensity up to about x=3H. The

effect of the fence holes is to reduce the mean vertical velocity fluctuations. Lee and Kim (1999) concluded that for the sole purpose of velocity reduction, the P=20% fence shows the best performance but the 40% porosity fence has better flow characteristics for abating wind erosion because of smaller turbulence fluctuations as well as large mean velocity reduction among the porous fences used in their study.

In conclusion, most experimental studies (e.g., Baltaxe, 1967; Castro, 1971; Perera, 1981; Ranga raju et al., 1988; Lee and Kim, 1999) found that no well-defined recirculation region (bubble) forms in the wake of the porous fence if the fence porosity is larger than 30%. Most of the experimental studies found that the optimum porosity of the fence is between 20% and 50% depending on the target variables that have to be minimized or maximized to increase fence performance (e.g., Baltaxe, 1967; de Bray, 1957; Castro, 1971; Raine and Stevenson, 1977; Perera, 1981; Ranga raju et al., 1988; Yaragal et al., 1997; Lee and Kim, 1999; Yaragal et al., 2002; Corneils W.M. and Gabriels D., 2005; Dong et al., 2007 and 2010; Duan et al., 2011a and 2011b).

The scatter observed among the experimental results reported by these authors is due in part to differences in the hole-distribution pattern and shape of the tested fences. Therefore there are other important parameters besides the fence porosity that need to consider while optimizing the design of wind fences. Only one research group (Lee and Kim, 1999; Kim and Lee, 2001 and 2002) has conducted systematic experimental investigations of the flow past thin perforated plates (wind fences) with the specific goal of studying the effects of these other parameters.

2.1.2 Effect of Bottom Gap on Flow past Non-porous and Porous Plates and Rectangular Cylinders

The bottom gap is another major parameter which affects the mean flow and turbulence statistics in the near wake region behind rectangular cylinders and plates. Moreover, the large-scale unsteady dynamics of the wake flow can change significantly as the bottom gap increases (Martinuzzi et. al, 2003). The main difference compared with the case when the bottom of the cylinder/plate touches the channel bed is the formation of a bottom shear layer which, in some cases, can interact with the shear layer forming past the top of the cylinder/plate. An excessive bottom gap will significantly increase turbulence intensity in the wake flow region.

Durão et al. (1991) experimentally investigated the mean flow around a square cylinder situated in the vicinity of the channel bed using Laser Doppler Velocimetry (LDV). The bottom gap was varied between 0H (cylinder attached to the bed) and 3.3H. They reported results only for two values of the bottom gap (G=0.5H for which the wake sheds vortices, similar to the case of cylinders situated away from channel boundaries and G=0.25H for which the wake does not shed large-scale vortices), both with Re=1.36x10^4. Sample results are shown in Figure 2.6. They observed that the degree of velocity amplification around the top and bottom faces of the cylinder is comparable for 0.35<G/H<2.5. For the case with G=0.25H, the velocity amplification was larger around the upper face of the cylinder compared to the bottom face. They also found that for G>0.35H the Strouhal number was close to constant (St=0.133) and regular vortex shedding was suppressed for G<0.35H.

Bosch et al. (1996) investigated experimentally the effect of bottom gap on flow past a square cylinder for different values of the bottom gap. In agreement with Durão et

26

al. (1991), they found that the critical value of the bottom gap for suppression of vortex shedding is between G=0.35H and G=0.5H. Martinuzzi et al. (2003) conducted a series of experiments at Re=18,900 for square cylinders. They found that for G<0.3H the lower shear layer reattaches permanently on the channel bed and the large-scale periodic fluctuations are completely suppressed. On the other hand, Panigrahi P. K. (2009) investigated the flow behind surface-mounted detached square ribs using PIV for four different values of the bottom gap (G=0.2H, 0.37H, 0.57H and 1H) at a cylinder Reynolds number of 11,075. He defined three different types of vortex shedding based on the position of the square cylinder from the channel bed: complete suppression of vortex shedding for G=0.2H; transition regime, where channel bed affects the large scale vortex shedding, for G=0.37H and G=0.57H; and vortex shedding regime, in which the effect of channel bed on vortex shedding is negligible, for G=1H.

Most of the experimental investigations of the effect bottom gap were performed with square cylinders. Only a limited number of studies considered rectangular cylinders whose aspect ratios (cylinder height to cylinder thickness) are much larger than 1, which corresponds to wind fences (Abdalla et al., 2009). Cho (1996) briefly investigated the wake flow behind a porous fence with a bottom gap. He discovered that by using a wind fence with a bottom gap the shear stress in the far wake region was reduced with respect to the case the bottom gap was not present. However, this study was too limited to fully understand the effect of the bottom gap on the near wake flow behind porous fences. To maximize snow storage capacity of structural snow fences, most conventional snow fence designs generally recommend G=0.1H.

Kim and Lee (2002) performed a detailed study of the effect of the bottom gap for porous fences with P=38.5%. They studied the characteristics of the wake flow behind fences with bottom gaps of 0H, 0.1H, 0.2H, and 0.3H based on PTV measurements performed in a recirculating water channel. They measured the mean velocity (streamwise and vertical) and the mean velocity fluctuations (streamwise and vertical velocity components) at a number of streamwise locations, as shown in Figure 2.7 and Figure 2.8 respectively.

For small values of G/H, the mean streamwise velocity inside the gap increases as the bottom gap increases. However, the maximum streamwise velocities are nearly unchanged if the bottom gap is larger than 0.2H-0.3H (Figure 2.7a). Their study found that the mean velocity reduction along the height of the fence is nearly independent of the gap size for the near-wake region (x<3H) and that the length of the nearly uniform velocity profile region along the fence height reduces in the downstream direction for x>3H. Negative values of the mean vertical velocity are present inside the bottom gap region for the highest gap size G=0.3H (Figure 2.7b). As one moves downstream, the difference between the vertical velocity profiles for different gap sizes is reduced until x=3H. However, as the flow travels further downstream (x>3H), the difference increases again. The shear layers developing from the fence top and the fence bottom begin to interact with each other at around x=4H for the case with G=0.3H.

In the upper shear layer, the maximum streamwise mean velocity fluctuations have similar values irrespective of the gap size. The location of local maximum mean velocity fluctuations shifts upwards with increasing G. In the lower shear layer, the maximum turbulence intensity increases with increasing G. As the flow moves downstream of the

fence, the region of large turbulence intensity expands because of the increase in the shear layer width. For G=0.1H, the profile of the mean streamwise velocity fluctuations is close to that observed for G=0H at x=5H (Figure 2.8a). Therefore, behind the fence, the distribution of the streamwise turbulence intensity profiles for G=0.1H is similar to that for G=0H. For G=0.2H and G=0.3H, the maximum mean streamwise velocity fluctuations have similar values in the upper and lower shear layers. Within the lower shear layer, the maximum turbulence intensity for G=0.2H is pretty close to that for G=0.3H at all streamwise locations downstream of the fence. In the upper shear layer, there is not much difference in the profiles of the mean vertical velocity fluctuations as the gap varies, and the maximum turbulence intensity has the similar values regardless of the height of the value of G. In the lower shear layer, only for G=0.3H large values of the mean vertical velocity fluctuations are observed up to x=3H. For x>3H, the maximum value of the mean velocity fluctuations increases as the gap increases.

Kim and Lee (2002) concluded that the G=0.1H case performed the best among the designs tested because the turbulence intensity profile for G=0.1H becomes similar to that of a no-gap fence (G=0H) in the wake region and because the mean velocity is significantly reduced in the near wake region. Therefore their main recommendation was to use of a bottom gap of height equal to 10% of the fence height for fences with porosity close to 40%.

2.1.3 Effect of Hole Size on Flow past Porous Plates

Perera (1981) mentioned that the shape of the hole in a fence was a less important factor compared to other parameters affecting the wake-flow characteristics. However, Raine and Stevenson (1977) claimed that fine holes would be more efficient in maintaining

29

a low mean turbulence level behind the porous fence. On the other hand, the scatter in the value of the critical porosity reported by many authors based on their experimental results could be due to differences in the shape, arrangement and size of the fence holes.

Kim and Lee (2001) carried out experiments in a recirculating water channel with uniform approaching flow to investigate the effect of hole-size on the wake flow behind porous fences. Three fences with hole diameters of d=1.4, 2.1 and 2.8mm having the same porosity (P=38.5%) were tested. PTV was used to measure the mean velocity and turbulent intensity at four different downstream locations, as shown in Figure 2.9 and Figure 2.10 respectively.

The fence with smallest hole-diameter (d=1.4mm) showed the largest reduction of streamwise velocity behind the fence. The variation of the reduction of the streamwise velocity with d was not monotonic, as the d=2.1mm fence showed the smallest streamwise velocity reduction instead of the d=2.8mm fence (Figure 2.9a). The case with d=1.4mm showed the largest values of the vertical velocity among the three cases. The d=2.1mm and d=2.8mm cases produced similar vertical velocity profiles (Figure 2.9b).

The maximum turbulence intensity (both streamwise and vertical mean velocity fluctuations) peaks in the shear layer originating at the top of the fence (Figure 2.10). The maximum values of the mean streamwise and vertical velocity fluctuations for the fences with d=1.4mm and d=2.8mm are close to each other. For x>3H, the difference in turbulence levels between d=2.1mm case, which is characterized by lower turbulence intensities, and other two cases increases.

They found that some of the wake features of the fence with the smallest hole-diameter (d=1.4mm) are similar to those they observed for low porosity fences (e.g., Lee

and Kim, 1999) though the porosity is same as for the other 2 fences (d=2.1 and 2.8mm). This is because of the blockage of the incoming flow approaching the fence increases with decreasing hole-diameter. The fence with d=2.8mm shows the greatest velocity reduction and the highest turbulence intensity in the near wake. Jet coalescence and mixing of bleed flow are stronger for the fence with d=2.8mm compared to the fence with d=2.1mm, even though both fences have the same porosity (P=38.5%). In summary, the study of Kim and Lee (2001) showed that the upwind flow retardation decreases as the hole-size, d, increases. However, as the hole-size increases, jet coalescence and the bleed flow mixing become more active.

Huang et al. (2012) conducted an experiment in a wind tunnel with the primary purpose of obtaining validation data for their numerical study on flow past non-uniform fences. Though they conducted only one experiment for a fence with P=30% (Figure 2.11), they varied the fence hole-size in numerical simulations with the aim of testing 5 different sets of fence design which have a different porosity in their upper half compared to their lower half (Figure 2.12i). Unfortunately, they did not discuss in any detail the effect of fence hole-size on the flow past porous fences.

2.1.4 Effect of Bed Roughness on Flow past Porous Plates

Most of the lab experiments of flow past wind fences were conducted in channels with a smooth bed. Experimental investigations conducted with a rough bed are very limited despite the fact that in most practical applications the incoming flow develops over a rough bottom boundary (e.g., due to vegetation). Huang et al. (2012) performed a wind tunnel experiment to obtain validation data for a numerical study of flow behind porous fences with non-uniform porosity. In their experiments, arrays of identical 2D ribs

31

(roughness elements) were installed at the channel bed in between the inlet of the wind tunnel and the fence, as shown in Figure 2.11. However the effect of varying the bed roughness on the flow generated around the fence was not studied. The purpose of conducting the experiment with the rough bed was to create an incoming mean velocity profile that is close to those measured in thermally neutral atmospheric boundary layers.

2.2 Numerical Studies

Most previous numerical studies used steady RANS models with wall functions to investigate flow around surface mounted obstacles including porous fences/plates and windbreaks. The use of wall functions reduces the mesh size requirements and increases the robustness of the solver. However, wall function method assumes that the law of the wall is valid near all the solid boundaries within the flow domain. The presence of separation and strong adverse pressure gradients makes the use of the wall function approach questionable to accurately predict flow past surface mounted obstacles. A better option is to use RANS models with near wall modeling capabilities. Unfortunately no such RANS studies of flow past porous fences and windbreaks were yet performed. Furthermore, unsteady flow features such as vortex shedding in the separated shear layer (SSL) forming at the top edge of the fence and in the fence wake, vortex merging and the interaction between large-scale coherent structures play an important role in the flow physics and in the transport, entrainment and deposition of particulates (e.g., snowflakes) around the fence. The effect of the large scale turbulence cannot be accurately captured with a steady RANS model. Thus, the use of this approach to understand the flow physics is very limited.

A better option is the use of time-accurate RANS (URANS) models that can partially overcome some of the aforementioned limitations of steady RANS models. Although these models can capture at least some of the large-scale unsteadiness and were shown to give more accurate results compared to the steady RANS models, they are still not very successful in predicting important aspects of massively separated flows past surface mounted obstacles and flow past porous obstacles where thin unsteady SSLs are generated as the flow is advected through the holes of the fence.

Eddy resolving techniques such as Direct Numerical Simulation (DNS), large Eddy Simulation (LES) and hybrid RANS-LES methods like Detached Eddy Simulation (DES) are more appropriate to be used for the numerical prediction of flow past surface-mounted solid and porous obstacles. In eddy-resolving simulations, the large-scale structures are computed while small-scale are modeled. The rationale behind this approach is based on two observations: most of the turbulent energy is contained in the larger flow structures and the small-scale structures are more isotropic and universal, thus easier to model using a sub-grid scale model. Such 3D simulations provide not only a more accurate description of the mean flow and turbulent statistics compared to RANS and URANS, but also capture the unsteady dynamics of the large scale turbulence in the flow (Rodi et al., 2013). This allows a better understanding of the complex interactions of large-scale structures and of their role in the transport of particulates (Baetke and Werner, 1990).

Before reviewing below mostly numerical investigations of flow past surface mounted porous fences (high aspect ratio porous rectangular cylinders), one should also mention several numerical studies of the simpler case of turbulent flow past a surface mounted low-aspect-ratio solid rectangular cylinder (e.g., Yang and Ferziger, 1993;

33

Acharya et al., 1994; Lee and Bienkiewicz, 1997; Hwang et al., 1999; Lohász et al., 2006; Chen and Jiang, 2009). Such studies used RANS, URANS, DNS and LES to investigate the turbulent wake past the solid obstacle. They showed the superiority of DNS and LES over RANS approaches.

2.2.1 Studies using Steady RANS Models

Most numerical studies on flow past porous fences using RANS employed variants of the k-ε model. The standard k-ε, the RNG k-ε and the realizable k-ε models (e.g., Wilson, 1985; Patton et al., 1998; Santiago et al., 2007) are among the most popular ones. In general, the RNG k-ε and realizable k-ε turbulence models showed better performance compared to the standard k-ε model, especially in the far wake of the fence.

Among the earliest RANS studies of flow past a windbreak are the ones conducted by Wilson (1985), Wang and Takle (1995), Wilson and Mooney (1997), Wilson and Yee (2003) and Wilson (2004) found that the use of different RANS closures results in substantial differences in the mean flow field and turbulence statistics predicted by the simulations around the windbreak.

Similar RANS studies were conducted by Lee and Lim (2001) and Li et al. (2007) to study the sheltering effect of a wind fence place upwind of a building or other obstacle. For example, Lee and Lim (2001) performed 2D RANS simulations using the RNG k-ε model to study the flow past a 2D triangular prism situated behind a porous fences. They conducted CFD simulations for different values of fence porosity, fence height and distance between the fence and the prism. Their results showed that using a fence with a porosity between P=30% and P=50% induces the maximum reduction of the mean pressure force acting on the prism. Li et al. (2007) conducted a similar investigation of the sheltering

effects of placing a windbreak on an outdoor open space containing a building downwind of the fence. Results using several turbulence models (standard k-Ɛ, RNG k-Ɛ and k-Ɛ two-layer) and discretization schemes were compared. They mentioned that the k-Ɛ two-layer model is the one which overall gave the best results. Their study found that the distance between the windbreak and building is an important variable that together with the porosity of the windbreak determine the degree of wind speed reduction around the building for cases when the windbreak is situated at less than 5H (H=height of the windbreak) from the building. One important conclusion of their study was that high-density windbreaks with P=20–30% should be used for cases when the building is situated at a short distance from the windbreak.

The flow past windbreaks was also studied by Santiago et al. (2007) using three different RANS models (standard k-Ɛ, RNG k-Ɛ and realizable k-Ɛ). They simulated windbreaks with a porosity between P=0% and P=50%. They found that windbreaks with P=35% give the best sheltering effect.

Bitog et al. (2009) utilized the renormalization group (RNG) k-Ɛ CFD model to investigate how wind velocity is affected by wind fence design and in particular by fence height. Based on their simulation results they recommended using a fence with P=20%. Saif et al. (2010) investigated the aerodynamics of wind flow behind wind fences of different designs. The RNG k-Ɛ turbulence model was used. They considered fences with a uniform porosity over the fence height, fences with a different porosity over the upper half fence height and the lower half fence height and fences with different porosities over each third of the fence height. The base case was that of a fence of uniform porosity with P=30%. The study found that a non-uniform fence design with a lower half fence porosity

35

$\mathcal{E}_L$=20% and an upper half porosity $\mathcal{E}_U$=40% gives the best results in terms of the degree of reduction of wind velocity magnitude over relatively large distances from the fence.

Cong et al. (2011) conducted numerical simulations using RNG k-$\mathcal{E}$ turbulence model to check the effectiveness of porous fences in reducing dust emissions. Their study showed that the dust emissions decrease dramatically due to the presence of a porous fence compared to the case when no fence is present (Figure 2.13).

2.2.2 Studies using Time Accurate Simulations

Najjar and Vanka (1993) conducted time-accurate numerical simulations of flow past a normal solid plate placed in a uniform flow. They solved the time-dependent 2D RANS equations with an upwind-biased finite-difference scheme. Simulations were conducted at several low Reynolds numbers between Re=25 and Re=500. The results showed that the separated flow remained steady for Re<150. For Re>150, they observed unsteady vortical structures developing from the SSL. Furthermore, unsteady separation characterized by vortex formation, coalescence, and shedding were observed for Re>250.

A finite-volume Eulerian-Eulerian RANS numerical model (2D and 3D) was developed by Alhajraf (2004) to simulate particles drifting around porous barriers. A convection-diffusion transport equation was solved in a time-accurate way for the particle volume fraction. Two types of applications were considered in the study. The first one was the study of the snow drift around a single row fence. The second one was the study of sand drift around a double row fence.

2.2.3 Studies using LES/DNS Models

Relevant LES studies of flow past solid obstacles mounted on a flatbed were reported, among others, by Rodi (1997), Rodi et al. (1997), Shah and Ferziger (1998) and Krajnovic and Davidson (2002).

Orellano and Wengle (2000) conducted 3D DNS and LES of turbulent flow past a solid plate (P=0%) at Re_H=3,000. For DNS, the computational domain size was 39Hx6Hx5H and 51.6 million (896x192x300) grid points were used. The LES was conducted in a domain of 32.2Hx6Hx5H with only 1.67 million (236x96x74) grid points. So LES was about 20 times less computationally expensive than DNS. Figure 2.14 shows sample visualization of the coherent structures in the flow in a streamwise vertical plane. Two additional cases with forcing were conducted at the same Reynolds number (Re_H=3,000) with the aim of controlling the size of the mean separation bubble in the wake flow behind the barrier. In the case when a high-frequency forcing with a Strouhal number St=0.6 was applied, they observed that the re-attachment length of mean flow was reduced by 10% compared to the reference case. In the case where a low-frequency forcing with St=0.08 was applied, a much stronger reduction of the bubble reattachment length (36%) was observed. The simulations also showed that the case with a low-frequency forcing exhibited an interesting feature. Large-scale structures were created in front of the fence, rolled over the fence without any significant disturbance and then rolled downstream while further growing in size until the height of the separation zone behind the fence was filled by these structures. LES was also performed with no forcing and with forcing at a higher Reynolds number (Re_H=10,500). About 5.76 million (400x96x150) grid points were used to mesh the computational domain of size 37Hx6Hx6.75H. In agreement with the results of experiments conducted by Siller and Fernholz (1997) for similar flow conditions,

Orellano and Wengle (2000) show that for Re_H=10,500 the optimum forcing Strouhal number is related to the low-frequency movement of the entire separation bubble and not to the instability mode of the SSL.

As the presence of a rough bottom surface can influence the flow past the porous fence, it is also relevant to briefly mention the study of Ikeda and Durbin (2007) that performed 3D DNS of fully turbulent flow in a rib-roughened periodic channel. An array of 2D square ribs was placed at the channel bottom (see Figure 2.15). The spacing between the ribs was 9H, where H is the rib height. Their study showed that a logarithmic layer exists for y≥2H. However, in the roughness sub layer, they observed a significant turbulent energy flux. A high-energy region was generated by the irregular turbulent motions just above the roughness elements. This shows the advantage of performing eddy resolving numerical simulations that resolve the roughness elements. Though computationally much more expensive, such an approach can help understanding the effect of bed roughness on the flow past a porous fence situated in its vicinity.

Fang and Wang (1997) performed 2D LES on flow past wind fences using a Standard Smagorinsky sub-grid scale model. The fence bottom was G/H=0.1 in all their simulations which were conducted with Re=40,000. A $1/7^{th}$ power law distribution of velocity profile was assumed for the approaching flow with a relative boundary layer thickness δ/H=3. Their study examined the effects of varying the fence porosity (P=10%, 20%, 30% and 40%) on the wake flow and the extent of the separation bubble behind the fence. In a second series of simulations they investigated the effect of boundary layer thickness (δ/H was varied between 1 and 4) for fences with P=30%. They found that as δ/H increases, the magnitude of the speed in the high-speed region decreases and the

streamwise drag on the fence is reduced. Unfortunately, the 2D computational domain (26Hx10H) was discretized using only 100x30 grid points. So, it is not clear how accurate the statistics calculated from their LES are.

Huang et al. (2012) performed 2D LES with a dynamic subgrid-scale model to study the flow past a porous wind fence. A finite volume scheme was used to discretize the governing equations for a weakly compressible-flow. The size of the computational domain was 40Hx10H. A power-law velocity profile was applied at the inflow. No-slip boundary conditions were used at the bottom wall and on the surface of the porous fence. Their simulation tried to replicate a wind tunnel experiment with a non-uniform porous fence placed on a rough surface (see Figure 2.11). The LES was performed without any roughness elements on the bottom surface. Additionally, LES was used to investigate the performance of different designs for fences with non-uniform porosity over the lower half (ε_L) and upper half (ε_U) of the fence height (see Figure 2.12i). In all the cases the porosity was less than 30%. As shown by the results in Figure 2.16, a recirculation region was observed behind all the designs tested. The study tried to determine the optimal design of a porous fence. A shelter parameter called the Protection Index (PI) was used to quantify the sheltering effect of the fence. The value of PI is evaluated based on the surface of the region contained in between a contour line corresponding to a given u/u_0 value (u is the mean streamwise velocity and u_0 is the uniform inlet velocity) and the ground. Results in Table 2.1 show the values of $PI_{0.1}$, $PI_{0.3}$ and $PI_{0.5}$, calculated for u/u_0=0.1, 0.3 and 0.5 respectively. The study found that for non-uniform porous fences with $\varepsilon_L<\varepsilon_U$, PI decreases compared to the value obtained for a fence with $\varepsilon_L=\varepsilon_U$. Moreover, they found that non-uniform porous fences with $\varepsilon_L>\varepsilon_U$ effectively enhance the sheltering effect compared with

the case of a fence with $\varepsilon_L=\varepsilon_U$. The study found that the porous fence with $\varepsilon_L=30\%$ and $\varepsilon_U=0\%$ gave the best sheltering among the designs that were tested.
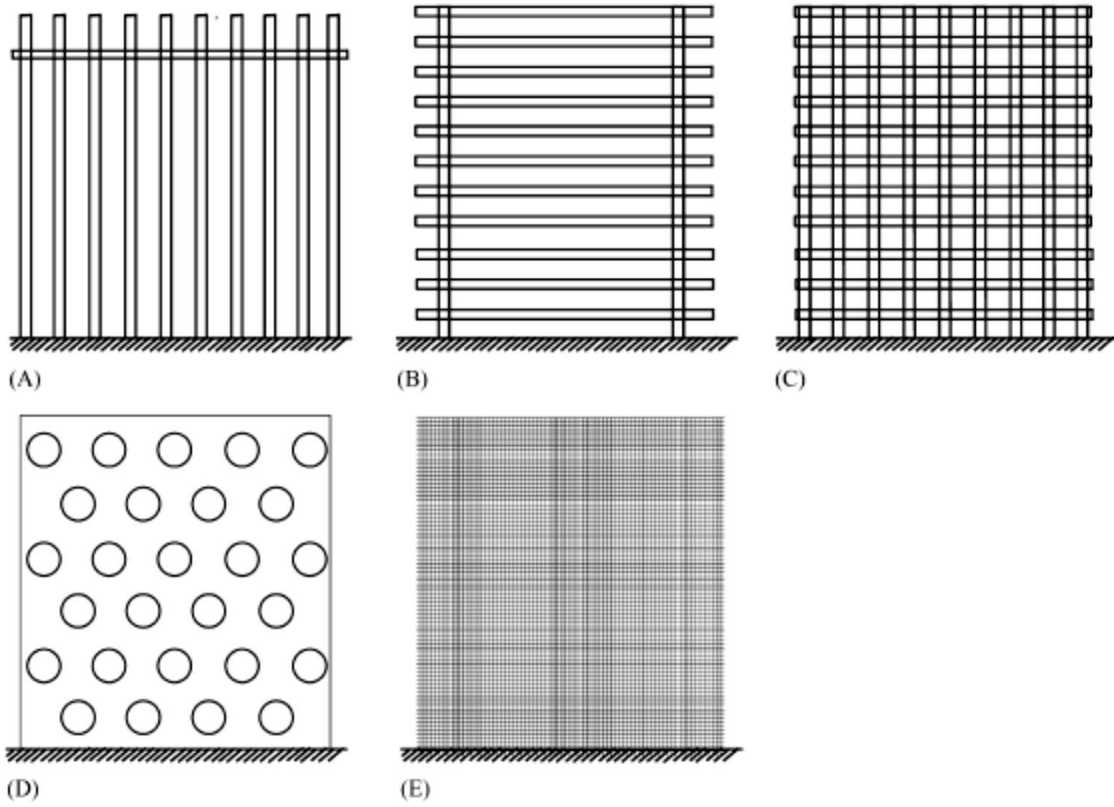
Figure 2.1 Types of structural wind fences: (A) upright fence; (B) horizontal fence; (C) gridded fence; (D) holed-plank fence; (E) wind screen. From Dong et al. (2007).
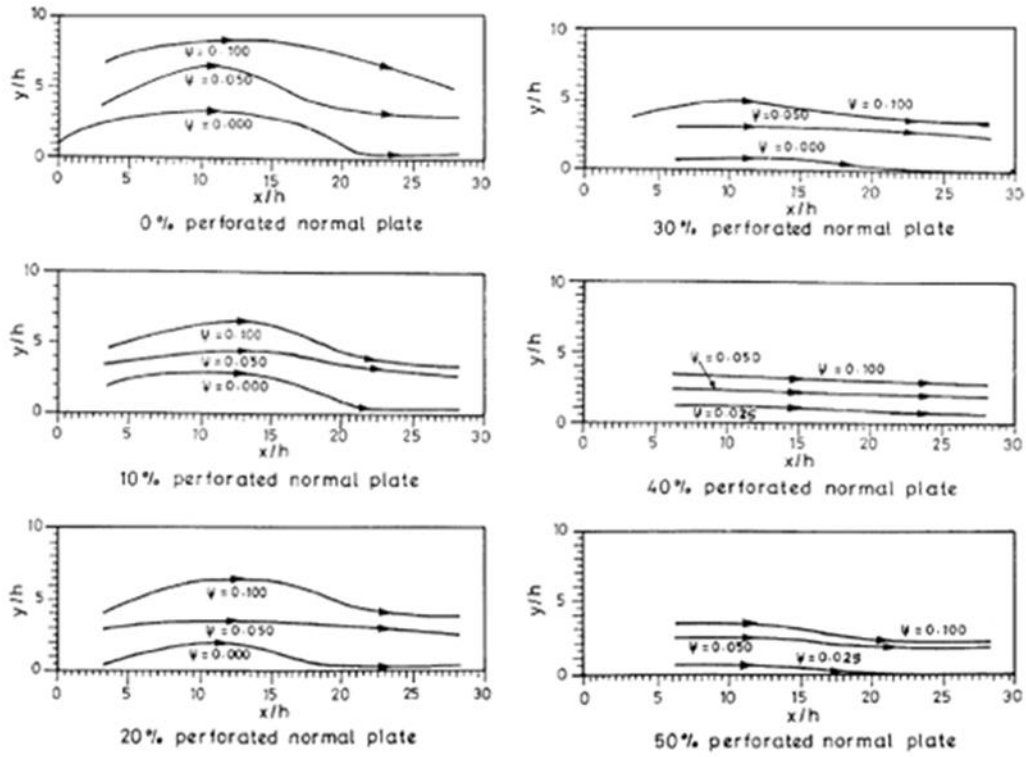
Figure 2.2 Effect of plate porosity on 2D streamline patterns in the near wake. From Yaragal et al. (2002) where Ψ=0 streamline defines the shape of the separation bubble.
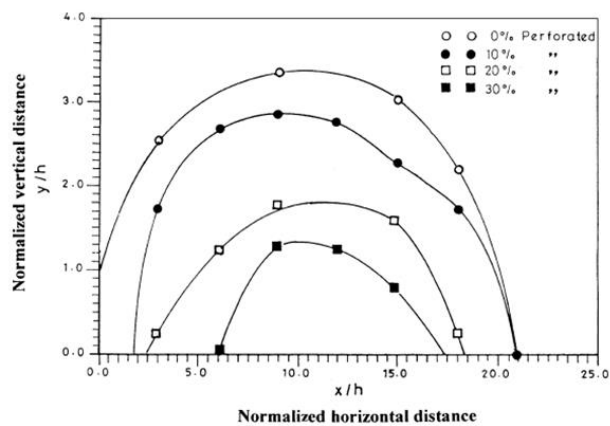
Figure 2.3 Effect of plate porosity on the dimensions and position of the separation bubble behind the plate. From Yaragal et al. (2002) where h is the plate height.
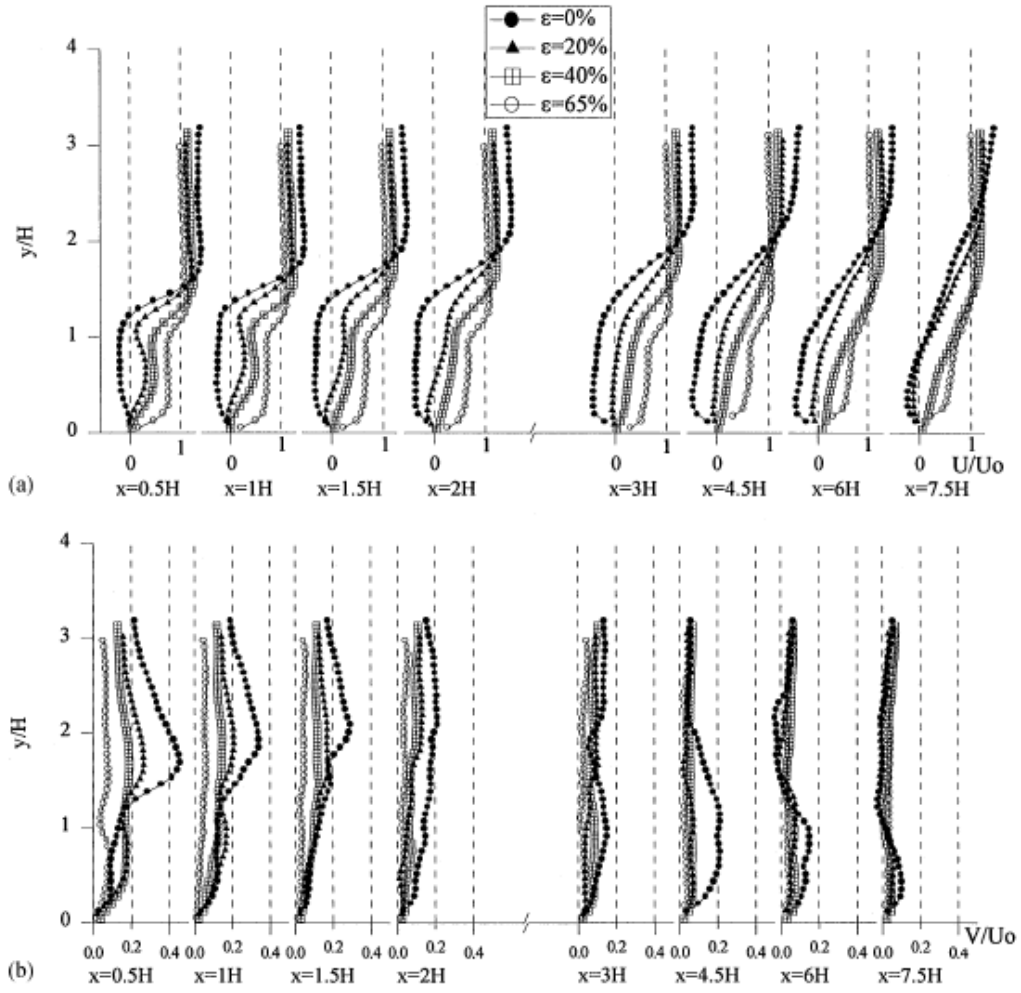
Figure 2.4 Vertical variation of velocity profiles: a) mean streamwise velocity (U); b) mean vertical velocity (V). From Lee and Kim (1999) where U0 is the incoming flow velocity, H is the fence height and ε is the fence porosity.
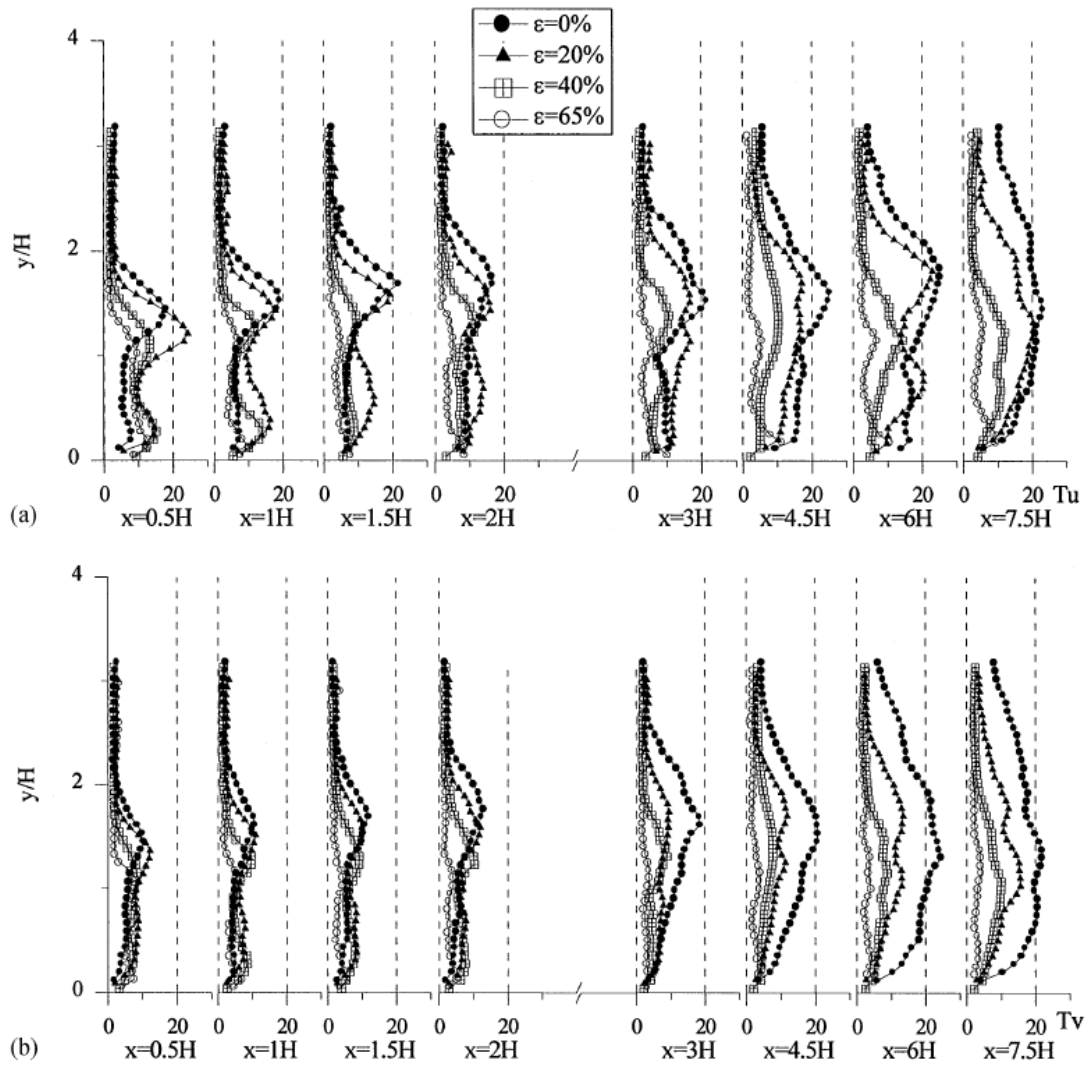
Figure 2.5 Vertical variation of mean velocity fluctuations: a) streamwise turbulence intensity (Tu = rms values of streamwise velocity fluctuations); b) vertical turbulence intensity (Tv = rms values of vertical velocity fluctuations). From Lee and Kim (1999) where H is the fence height and ε is the fence porosity.
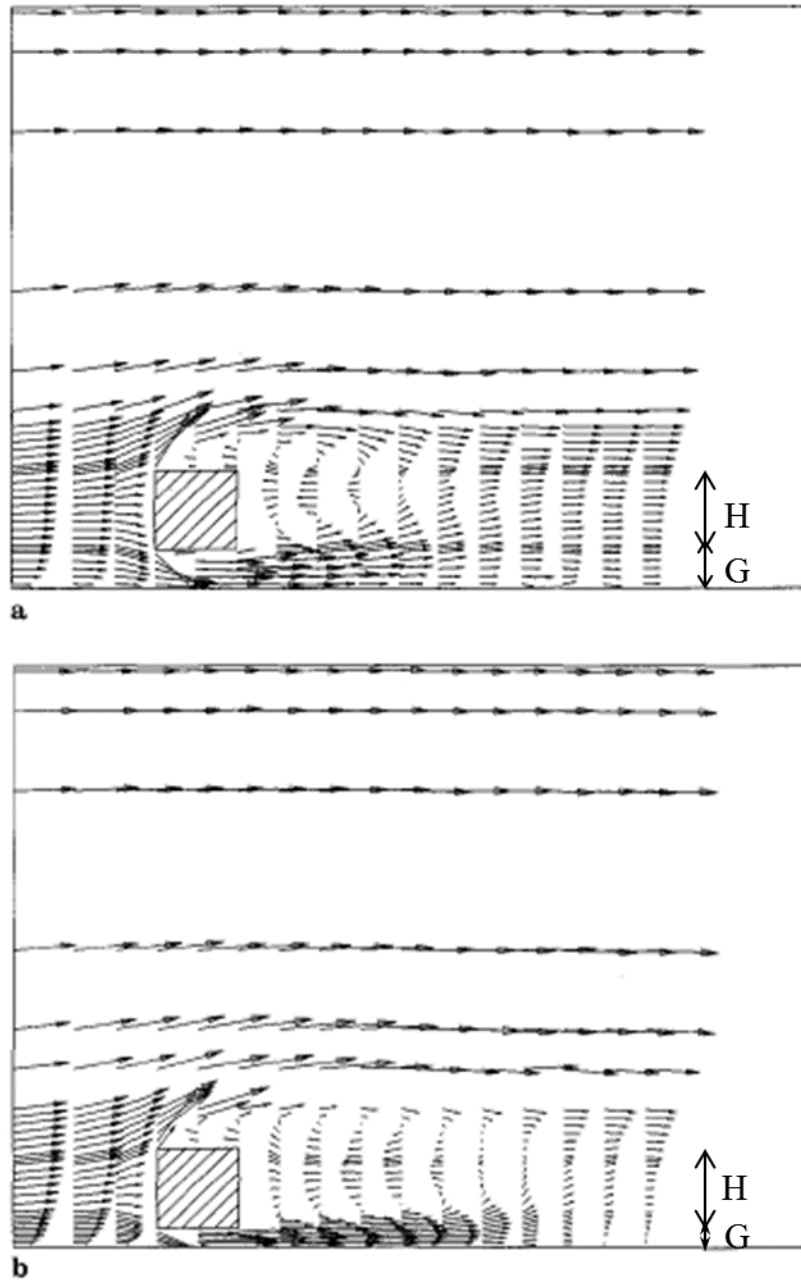
Figure 2.6 Mean flow structure around a square cylinder situated in the vicinity of the channel bed: a) G/H=0.5; b) G/H=0.25. From Durão et al. (1991) where H is the cylinder height and G is the bottom gap.
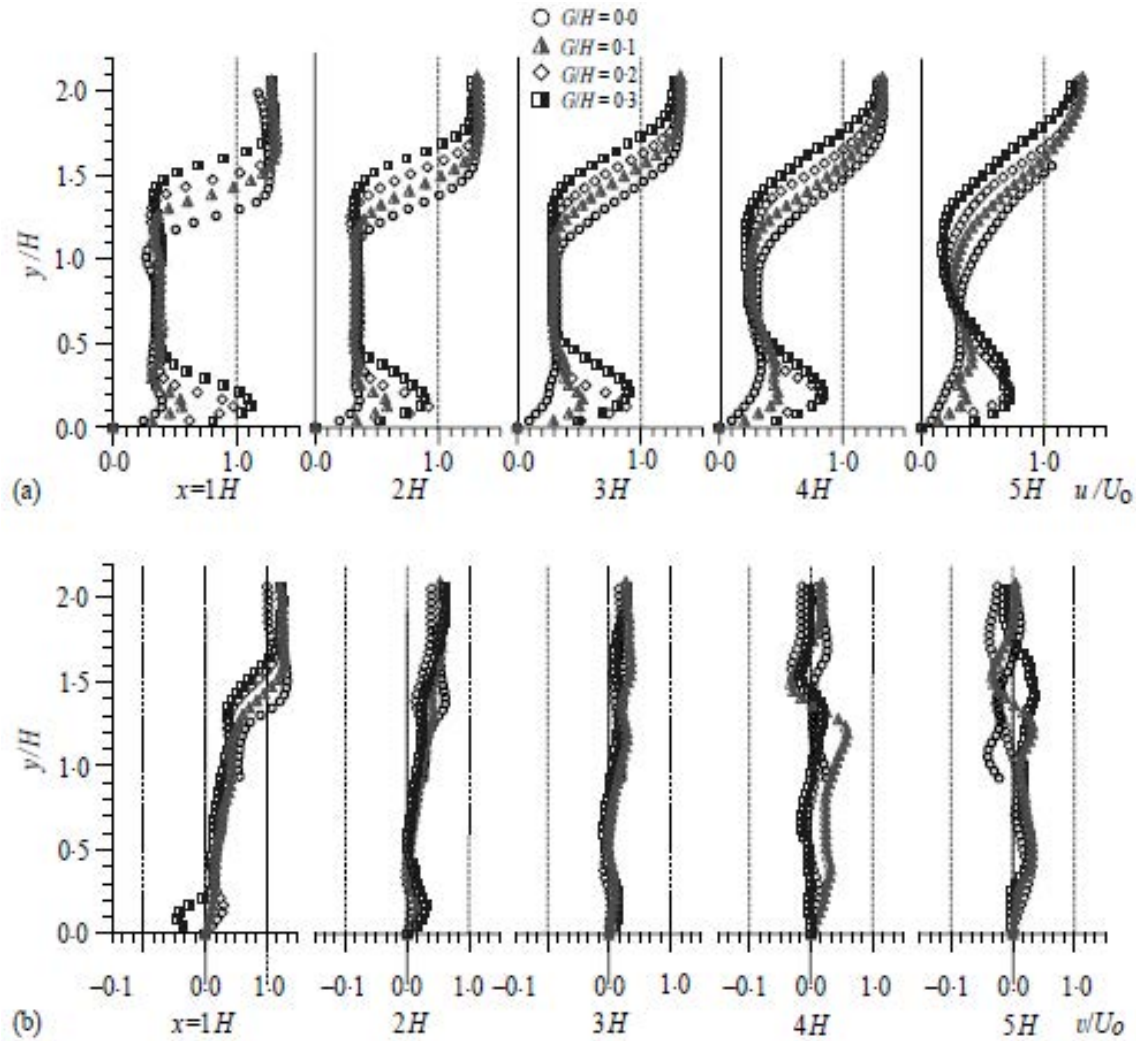
Figure 2.7 Vertical variations of: a) mean streamwise velocity (u) profile; b) mean vertical velocity (v) profile. From Kim and Lee (2002) where U_0 is the incoming flow velocity, H is the height of the fence and G is the bottom gap.
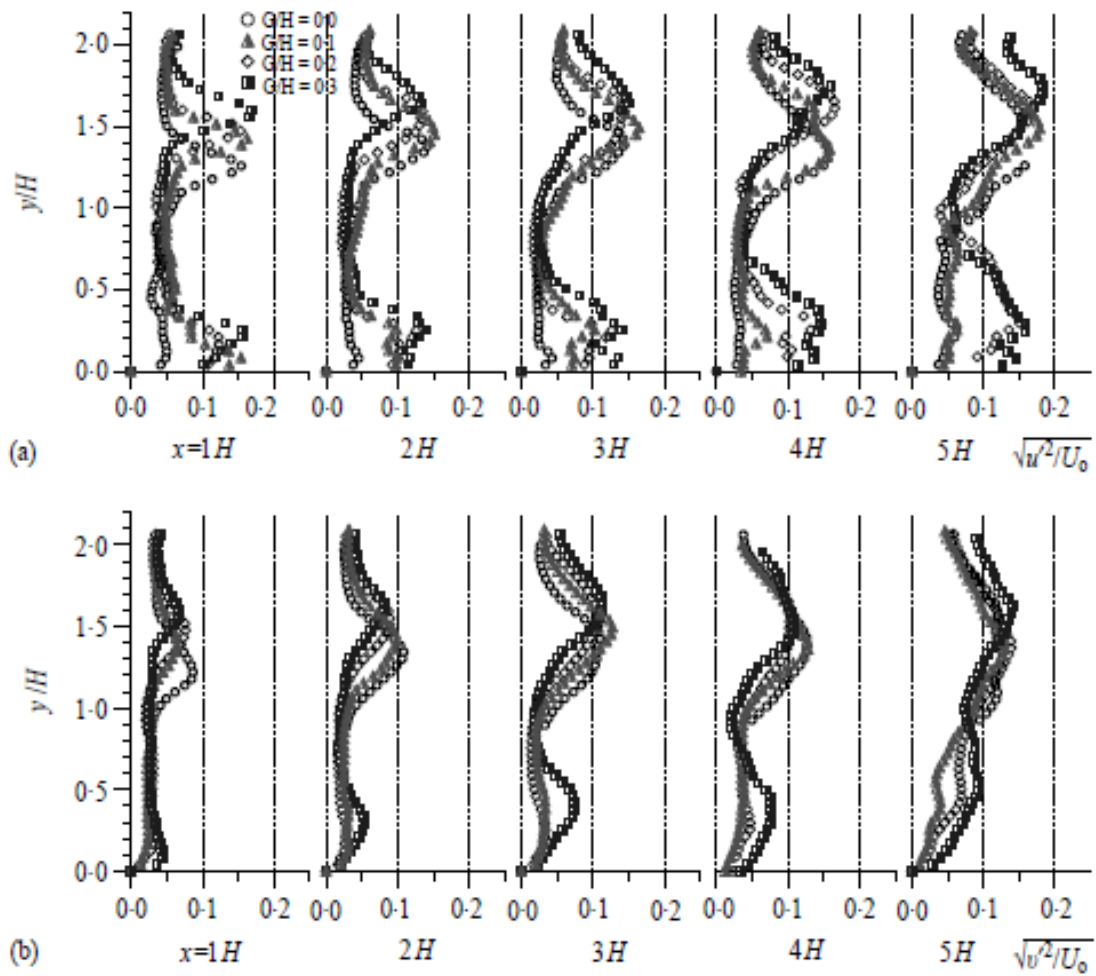
Figure 2.8 Vertical variations of mean turbulent velocity fluctuation profiles: a) streamwise component; b) vertical component. From Kim and Lee (2002) where u' denotes the streamwise velocity fluctuation and v' denotes vertical velocity fluctuation, U_0 is the incoming flow velocity, H is the height of the fence and G is the bottom gap.
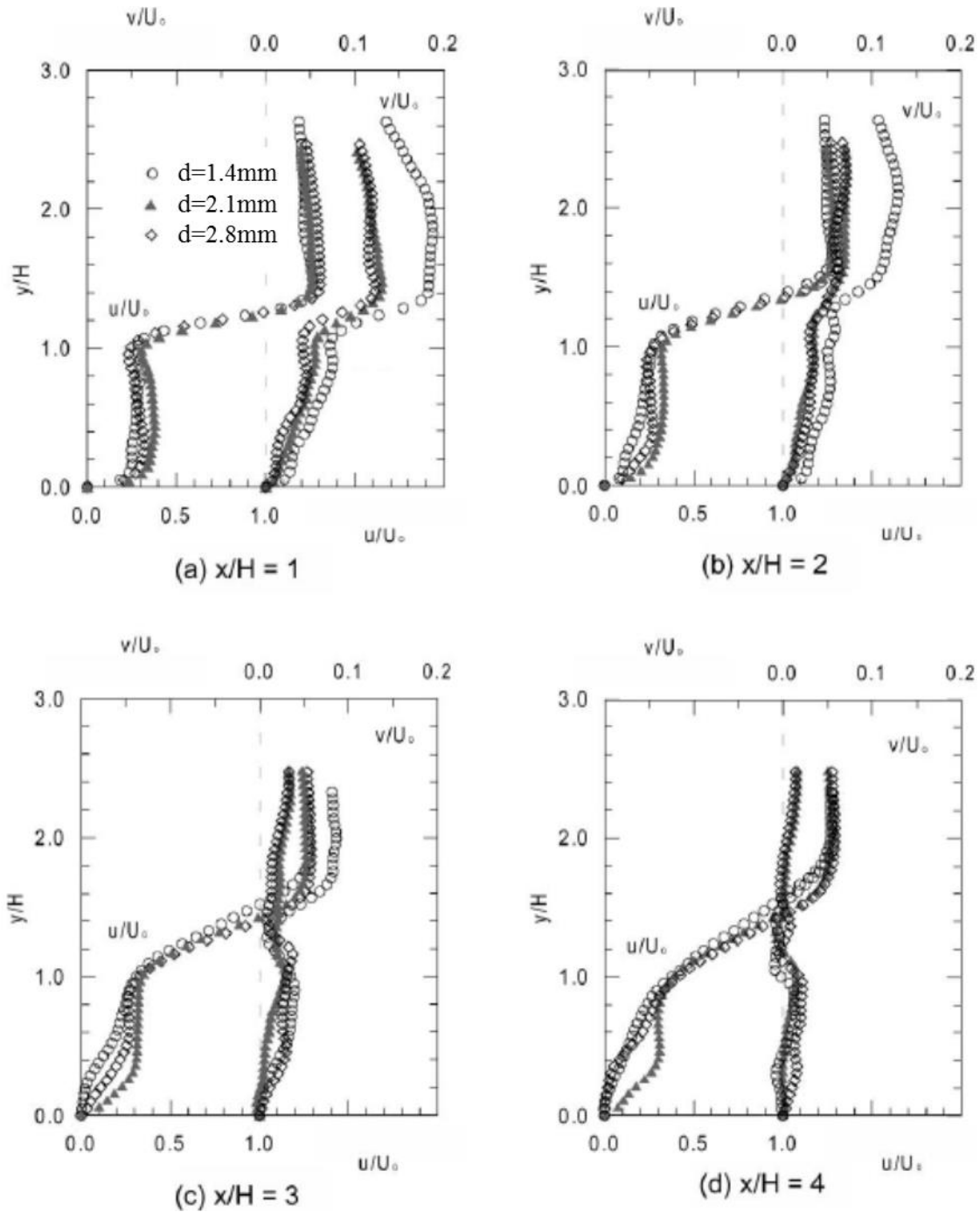
Figure 2.9 Mean streamwise velocity (u/U_0) and vertical velocity (v/U_0) profiles in the wake of a porous fence (P=38.5%) with varying hole diameters d=1.4mm, d=2.1mm and d=2.8mm. From Kim and Lee (2001), where U_0 is the incoming flow velocity, H is the height of the fence and d is the diameter of the hole.
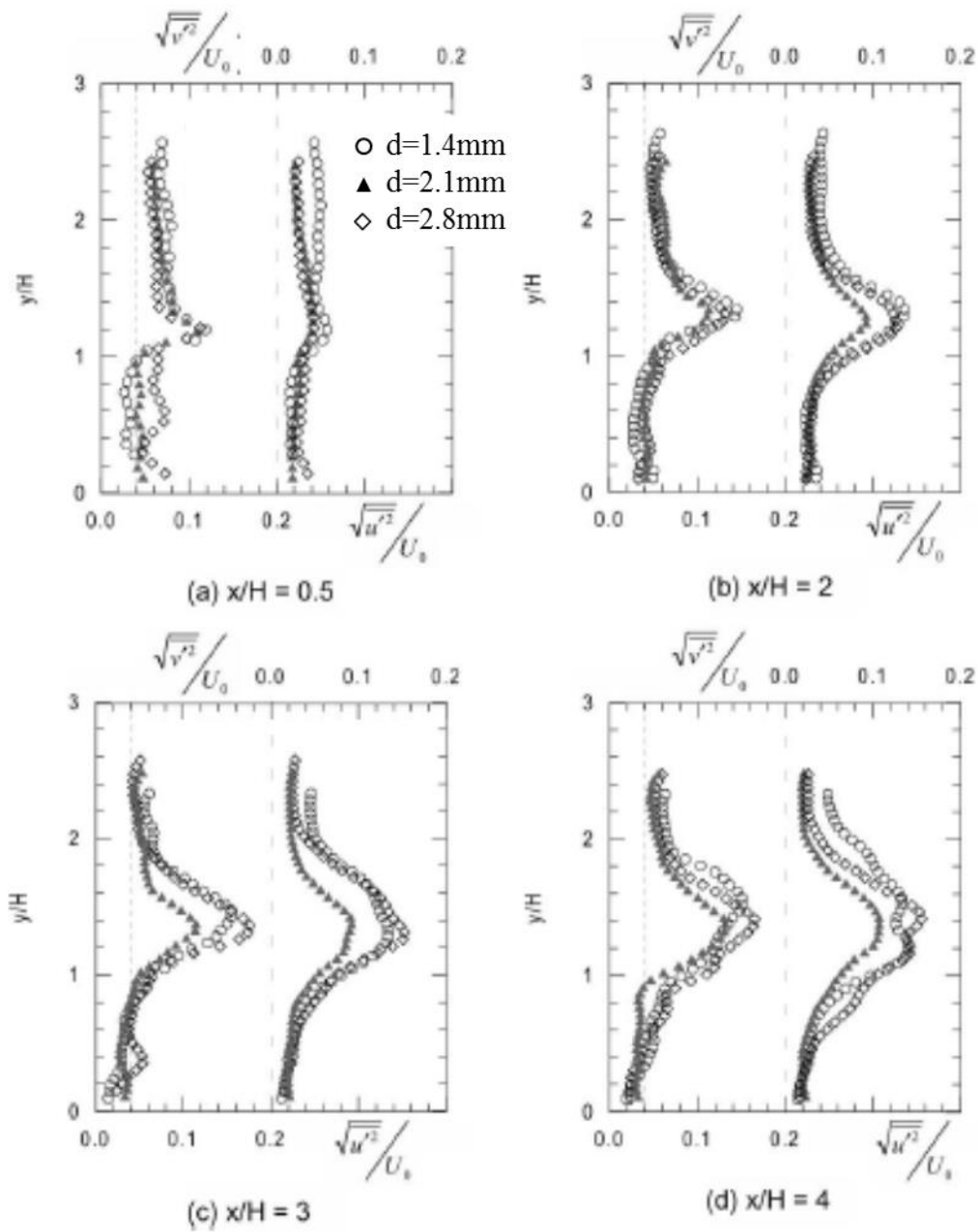
Figure 2.10 Vertical variations of the nondimensional rms values of streamwise velocity fluctuations and vertical velocity fluctuations. From Kim and Lee (2001), where U_0 is the incoming flow velocity, H is the height of the fence and d is the diameter of the hole.
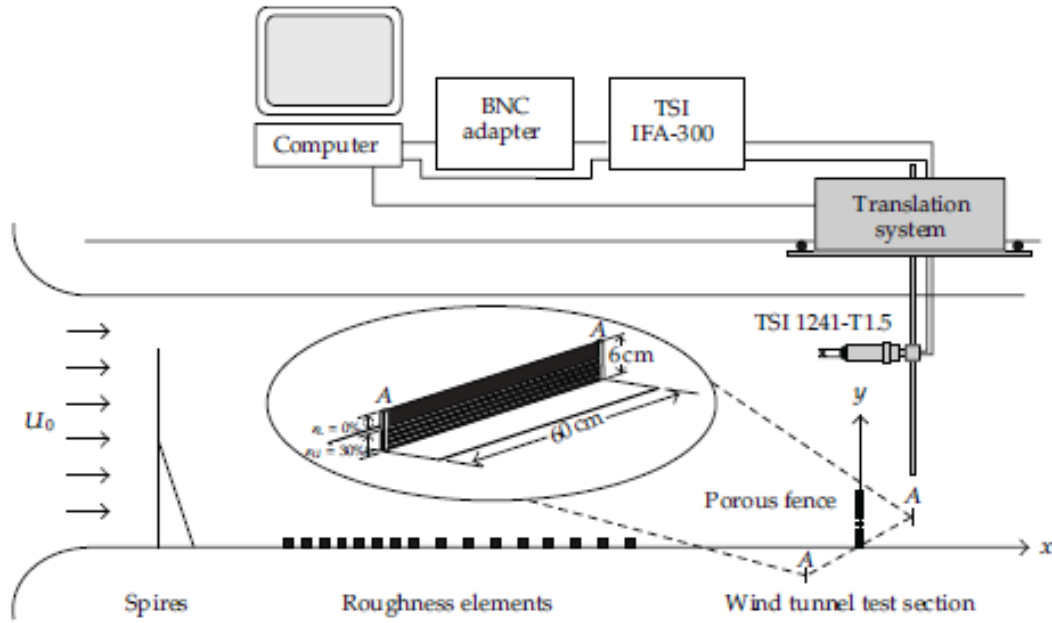
Figure 2.11 Schematic diagram of experimental set-up used by Huang et al. (2012) to study wake flow past porous fences containing 2 regions with different mean porosities, where u_0 is the uniform inlet velocity, lower half fence porosity $\varepsilon_L=30\%$ and upper half fence porosity $\varepsilon_U=0\%$.
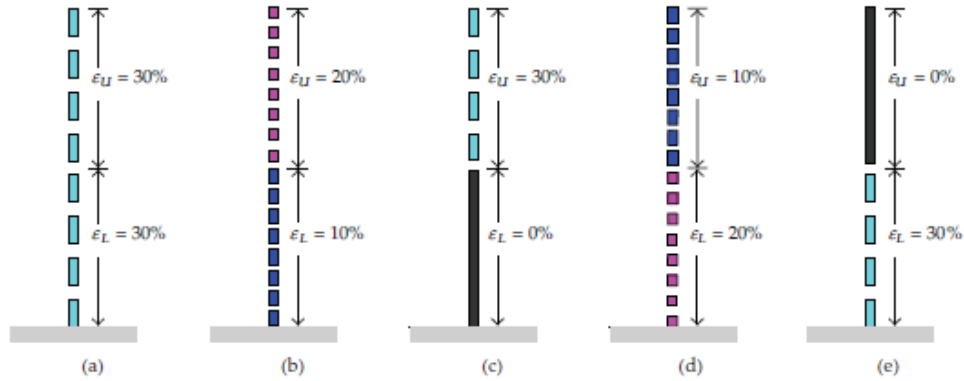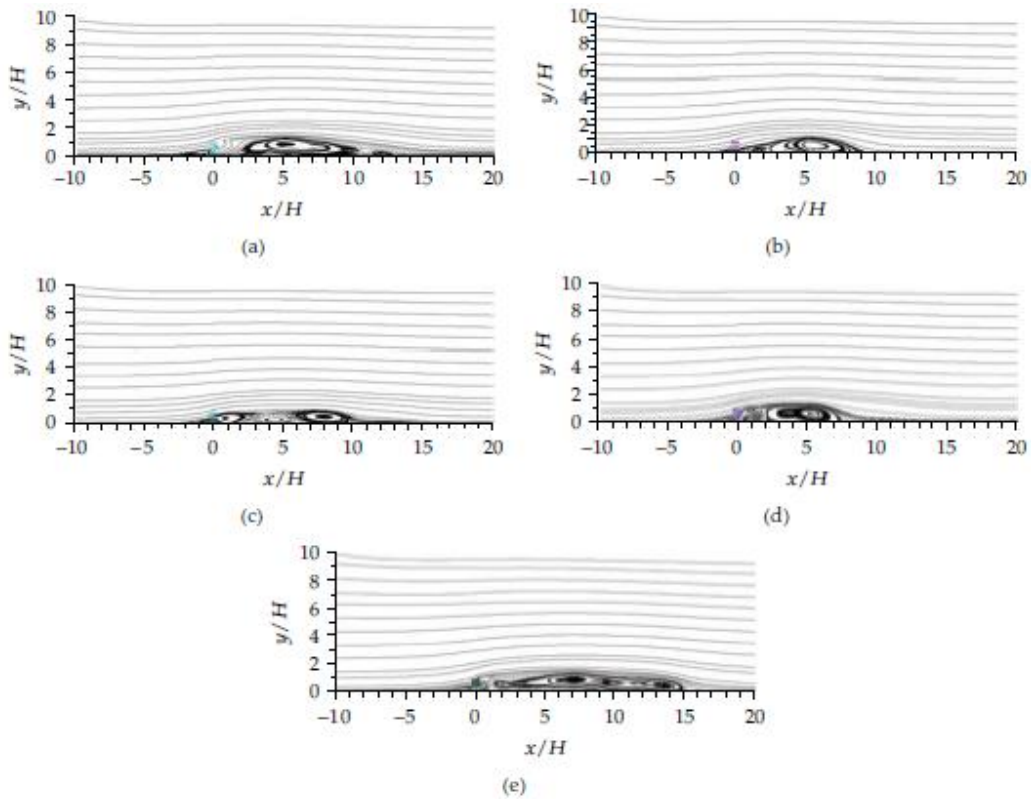
Figure 2.12 Mean streamline patterns around the fence design studied by Huang et al. (2012), where H is the total height of the fence; i) sketch of fence design indicating the mean porosity value within the lower half of the fence (ε_L) and the mean porosity value within the upper half of the fence (ε_U) of the fence; ii) 2D mean streamline patterns for the five designs tested.
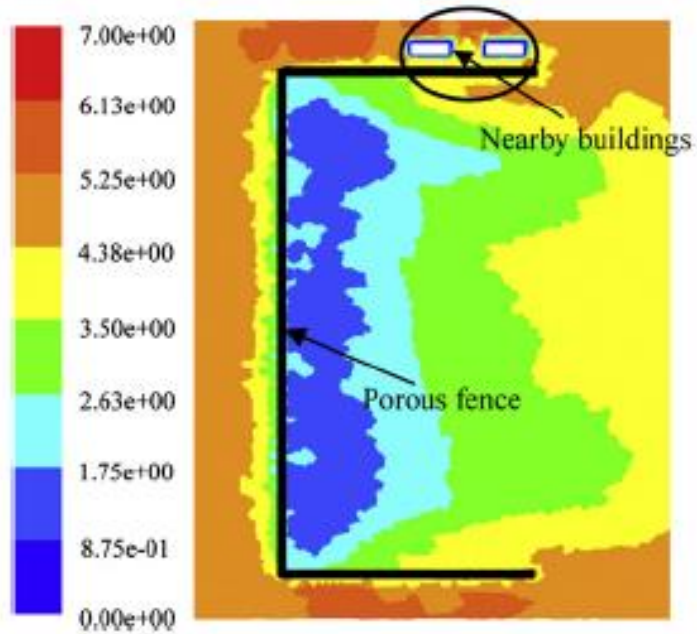
Figure 2.13 Top view of the mean velocity magnitude (unit: m/s) contours in a region containing buildings protected by a porous fence. The fence position is shown in black. The wind direction is from left to right. From Cong et al. (2011).
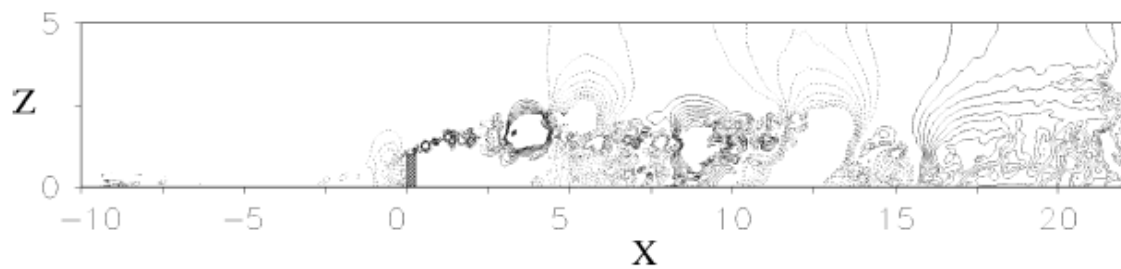
Figure 2.14 Iso-lines of pressure fluctuations used to visualize the growth of the vortical structures in the SSL and wake flow behind a solid plate in an instantaneous flow field obtained from DNS. From Orellano and Wengle (2000).
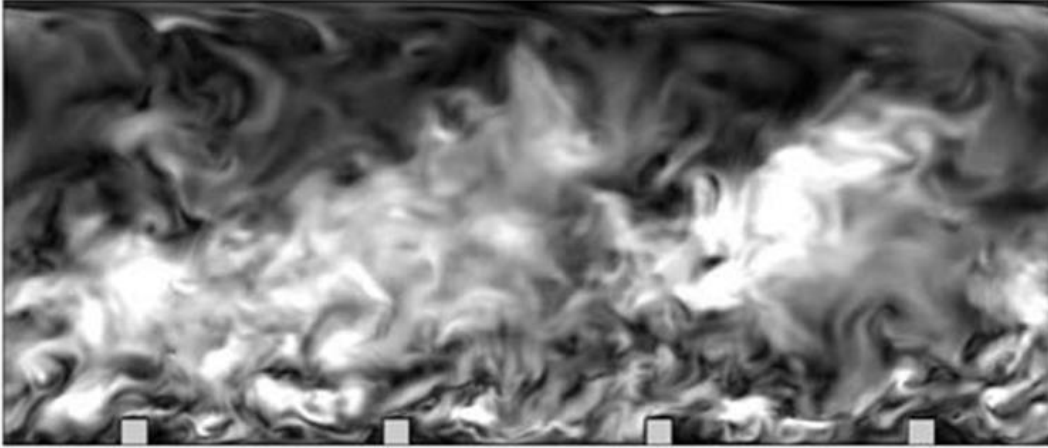
Figure 2.15 Instantaneous velocity fluctuations in a channel flow (DNS simulation) in which an array of identical square cylinders (roughness elements) was placed at the channel bottom. From Ikeda and Durbin (2007).
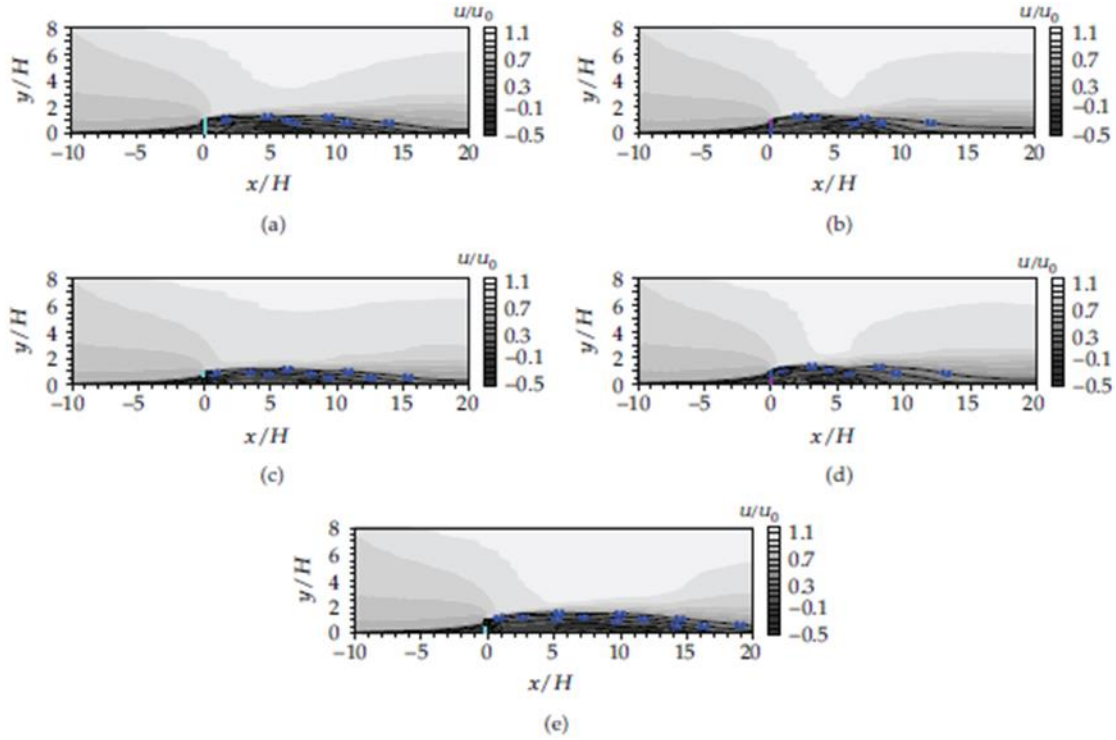
Figure 2.16 Contour plots of the mean streamwise velocity around a non-uniform porous wind fence. Results are shown for five designs: a) ε_L=30%, ε_U=30%; b) ε_L=10%, ε_U=20%; c) ε_L=0%, ε_U=30%; d) ε_L=20%, ε_U=10%; e) ε_L=30%, ε_U=0%, where ε_L is the porosity of the lower half of the fence and ε_U is the porosity over the upper half of the fence, u is the mean streamwise velocity and u_0 is the uniform inlet velocity. From Huang et al. (2012).

Table 2.1 Protection Index (PI) values predicted by Huang et al. (2012) representing areas under contours line u/u_0=0.1, 0.3 and 0.5 behind a porous fence with nonuniform porosity (see also Figure 2.16).

Protection Index (H^2)	Case				
	a	b	c	d	e
$PI_{0.1}$	9.44	7.44	8.56	7.78	14.49
$PI_{0.3}$	16.67	13.05	13.63	14.26	21.33
$PI_{0.5}$	22.97	21.92	20.96	24.06	28.37

CHAPTER 3 NUMERICAL SOLVER

3.1 Introduction

Most predictions of engineering flows are obtained using the so-called Reynolds Averaged Navier-Stokes (RANS) approach in which the effect of most of the scales (eddies, vortices) on the mean flow is accounted for via a (RANS) turbulence model. By contrast, in the Large Eddy Simulation (LES) approach, the dynamically important scales in the flow are directly computed, and only the effect of the (filtered) smaller scales on the (resolved) larger scales is modelled. Both types of numerical methods were employed in this study. LES is the most advanced modelling tool currently available for prediction of realistic complex flows. 3D LES generally provides more detailed information compared to experiments (e.g., in terms of the dynamics, shape and position of the energetically important large-scale turbulent structures in the flow) and allows estimating variables that are very difficult to estimate from experiments (e.g., boundary shear stresses, pressure fluctuations on solid surfaces, drag forces on individual elements, etc.). However, LES is computationally much more expensive compared to RANS. This is why, RANS is still used for practical applications (e.g., for design) in most cases.

The flow and turbulence structure around 2D vertical solid and porous plates situated at or in the vicinity of a horizontal no-slip surface was investigated based on results of 3D LES. The goal was to use these simulations to supplement information on the flow physics already available from experimental studies and to focus on fundamental aspects of this particular type of flow past solid and porous obstacles. The second part of the study was motivated by the need to improve the design of snow fences deployed in the vicinity of roads. Because the design methodology proposed in the present study relies on performing a relatively large number of simulations for fences placed in a realistic

environment (e.g., using a realistic topography, for high winds which correspond to flows with very high Reynolds numbers, outside of the range where well resolved LES is computationally feasible), the RANS approach was preferred for the second part of the study. RANS predictions of the mean flow and other parameters required by the design methodology are sufficiently accurate. Commercial software called STAR-CCM+ was used to perform the 2D RANS simulations.

3.2 Large Eddy Simulation Model

In LES, the unsteady, three-dimensional Navier–Stokes equations are spatially filtered, the resolved scales of motion are directly computed, and the influence of the filtered scales on the resolved scales is modelled. Spatial filtering (denoted by the "~") of the Navier-Stokes equations with a filter that commutes with the spatial and temporal derivatives yields the filtered Navier-Stokes equations used in LES:

$$\frac{\partial \widetilde{u}_i}{\partial x_i} = 0 \tag{3.1}$$

$$\frac{\partial \widetilde{u}_i}{\partial t} + \frac{\partial \widetilde{u}_i \widetilde{u}_j}{\partial x_j} = -\frac{\partial \widetilde{p}}{\partial x_i} + \nu \frac{\partial^2 \widetilde{u}_i}{\partial x_i \partial x_j} + \frac{\partial \tau_{ij}}{\partial x_j} \tag{3.2}$$

where u_i is the Cartesian velocity component along the i direction, ν is the molecular viscosity, p is the pressure and $\tau_{ij} = \overline{u_i u_j} - \widetilde{u}_i \widetilde{u}_j$ is the subgrid stress. In the following, all of the quantities are grid filtered and the symbol "~" is omitted.

In the case in which an isotropic Smagorinsky-like subgrid-scale (SGS) model is used to estimate the SGS stresses, τ_{ij}, equations 3.1 and 3.2 can be rewritten as:

$$\frac{\partial u_i}{\partial x_i} = 0 \tag{3.3}$$

$$\frac{\partial u_i}{\partial t} + \frac{\partial (u_i u_k)}{\partial x_k} = -\frac{\partial p}{\partial x_i} + \frac{\partial}{\partial x_k}\left[(v + v_{SGS})\left(\frac{\partial u_i}{\partial x_k} + \frac{\partial u_k}{\partial x_i}\right)\right] \tag{3.4}$$

In the governing equation 3.4, the viscosity term contains the extra SGS term because of filtering. Formally, the governing equations in RANS are identical to equations 3.3 and 3.4. The only difference is that in RANS the subgrid-scale SGS viscosity, v_{SGS}, is replaced by the eddy viscosity, v_T, which is estimated using a RANS closure. The equations are solved in nondimensional form. If U and H are the velocity and length scale, respectively, then the nondimensional form of equations (3.3) and (3.4) is the same as the dimensional form except for the molecular viscosity that is replaced by 1/Re, where the Reynolds number is Re=UH/v.

The dynamic isotropic Smagorinsky model (Rodi et al., 2013) was used to estimate the SGS viscosity, v_{SGS}, using:

$$v_{SGS} = C_d \Delta^2 \, |S| \tag{3.5}$$

The dynamic parameter, C_d, is estimated as:

$$C_d \Delta^2 = \frac{1}{2}\frac{L_{ik} M_{ik}}{M_{ik} M_{ik}} \tag{3.6}$$

$$L_{ik} = -\overline{u_i u_k} + \overline{u}_i \overline{u}_k \tag{3.7}$$

$$M_{ik} = \left(\overline{\Delta}/\Delta\right)^2 |\overline{S}|\overline{S}_{ik} - \overline{|S|S_{ik}} \tag{3.8}$$

where '-' denotes a second filter (test filter). The rate of strain tensor and its magnitude are

$$S_{ij} = \frac{1}{2}\left(\frac{\partial u_i}{\partial x_j} + \frac{\partial u_j}{\partial x_i}\right) \text{ and } |S| = 2\sqrt{S_{ij} S_{ij}} \; .$$

The use of the dynamic Smagorinsky model as opposed to the classical constant coefficient Smagorinsky model, and of grids that resolve the viscous sublayer have several important advantages. It eliminates the need to specify the value of the model constant, C_d, which becomes a function of space and time and is calculated from the resolved variables (velocity components) without any empirical input. The use of a dynamical model also eliminates the need to use empirical near-wall corrections (e.g., Van Driest damping functions), as the governing equations are integrated up to the wall ($\Delta n_1^+ \sim 2$, where $n^+ = nu_\tau/\nu$ and u_τ is the friction velocity) and the model coefficient decays automatically to zero as the solid boundary is approached.

The numerical solver used to perform the LES simulations is a finite-volume non-dissipative viscous flow solver. A detailed description of the code and computational technique is available in Pierce and Moin (2001). The code solves the conservative form of the incompressible Navier-Stokes equations on non-uniform Cartesian meshes. The numerical algorithm (fractional step) uses a staggered conservative space-time discretization with a semi-implicit iterative method to advance the equations in time such that it is second order accurate in both space and time. A Poisson equation is solved for the pressure using multigrid. The algorithm discretely conserves energy (Mahesh et al., 2004) and uses strictly non-dissipative (central) discretization to solve for the momentum and pressure. The features ensure robustness at relatively high Reynolds numbers in the LES regime. All operators are discretized using central discretization except the convective terms in the scalar transport equations for which the QUICK scheme is used. The code is parallelized using MPI. Time discretization is achieved using a Crank Nicholson scheme for the convective and viscous operators in the momentum (predictor step) equations. The

58

system resulting due to the implicit time discretization solved using the SOR method. A blanking technique is used to conduct simulations in domains of complex shape (e.g., containing obstacles).

Channel flow simulations are conducted with either an imposed steady velocity profile at the inlet or with fully developed turbulent flow containing turbulent fluctuations obtained from a precursor LES of channel flow with periodic boundary conditions in the streamwise direction. Periodic boundary conditions are imposed in the spanwise (z) direction. All solid surfaces (e.g., surface of fence elements, ground surface) are treated as no slip surfaces. The mesh in the wall normal direction was sufficiently fine for all solid surfaces such that no wall functions were used. At the outflow, a convective boundary condition that allows coherent structure to exit domain without introducing spurious oscillations is used (Rodi et al., 2013).

Details of the numerical method and description of validation studies conducted for constant density and stratified flow in channels with flat and deformed bed are given in Chang et al. (2006 and 2007), Ooi et al. (2009), Gonzales-Juez et al. (2010), Tokyay et al. (2011) and Chang and Constantinescu (2013). In particular, the code was validated for prediction of 2D channel flow, flow in channels containing dunes at the bottom surface, channel flow containing a 2D bottom cavity, bottom propagating gravity currents in straight channels, interaction of a gravity current with a bottom obstacle or with an obstacle placed in the vicinity of the channel bed. In particular, the LES model was shown to correctly predict the temporal variation of the forces induced on isolated cylinders placed in a channel (Gonzales-Juez et al., 2010).

Most of the 3D numerical simulations were run on 64 processors of high-performance PC clusters at the TRACC facility of the Argonne National Laboratory.

3.3 Reynolds Averaged Navier-Stokes Model

The RANS numerical simulations of the airflow past porous snow fences situated in the vicinity of roadways were performed using the Computational Fluid Dynamics (CFD) package STAR-CCM+, developed by CD-Adapco. This CFD software contains an advanced mesh generator with automatic mesh refinement capabilities that offers lots of flexibility in terms of resolving the boundary layers close to solid surfaces in very complex domains.

The governing Navier Stokes equations are discretized in conservative form:

$$\frac{\partial}{\partial x_i}(\rho u_i) = 0 \tag{3.9}$$

$$\frac{\partial}{\partial t}(\rho u_i) + \frac{\partial}{\partial x_i}(\rho u_i u_k) = -\frac{\partial p}{\partial x_i} + \frac{\partial}{\partial x_j}\left[(\mu + \mu_t)\left(\frac{\partial u_i}{\partial x_j} + \frac{\partial u_j}{\partial x_i}\right)\right] \tag{3.10}$$

where u_i is the Cartesian time-filtered velocity component along the i direction, ν is the molecular viscosity, p is the pressure, ρ is the density and μ and μ_t are the dynamic and turbulent (RANS) viscosity, respectively. The governing equations 3.9 and 3.10 are formally identical to equations 3.1 and 3.2 in which the space filtered was replaced by a time filter. The time filtering of the nonlinear convective term results in the Reynolds stress term which is modelled using an eddy viscosity RANS model. The k-ε turbulence model (k is the turbulence kinetic energy and ε is the turbulent dissipation rate) was used to account for turbulence effects and to estimate the eddy viscosity:

$$\mu_T = \rho C_\mu \frac{k^2}{\varepsilon} \tag{3.11}$$

The transport equations used to calculate k and ε are:

$$\frac{\partial}{\partial t}(k) + \frac{\partial}{\partial x_i}(u_i k) = \frac{\partial}{\partial x_j}\left[\frac{1}{\rho}(\mu + \frac{\mu_t}{\sigma_k})\left(\frac{\partial k}{\partial x_j}\right)\right] + G - \varepsilon$$

(3.12)

$$\frac{\partial}{\partial t}(\varepsilon) + \frac{\partial}{\partial x_i}(u_i \varepsilon) = \frac{\partial}{\partial x_j}\left[\frac{1}{\rho}(\mu + \frac{\mu_t}{\sigma_\varepsilon})\left(\frac{\partial \varepsilon}{\partial x_j}\right)\right] + C_{\varepsilon 1}\frac{\varepsilon}{k} - C_{\varepsilon 2}\frac{\varepsilon^2}{k}$$

(3.13)

where G is the turbulence production term and the model coefficients have the following values:

$$\sigma_k = 1.0 \quad \sigma_\varepsilon = 1.3 \quad C_{\varepsilon 1} = 1.44 \qquad C_{\varepsilon 2} = 1.92 \qquad C_\mu = 0.09$$

(3.14)

The two-layer k-ε model was used in the present RANS simulations, in which the mesh was sufficiently fine to resolve the flow within the viscous sublayer. The flow domain is divided into two regions: an inner layer where a one-equation turbulence model is used and an outer layer where the above (high-Reynolds-number) version of the k-ε model is used. The inner-layer model solves only the k-equation 3.12 while the ε equation is replaced by

$$\varepsilon = \frac{k^{3/2}}{l_\varepsilon}$$

(3.15)

The eddy viscosity in the inner layer is obtained from

$$\mu_T = \rho C_\mu \sqrt{k} l_\mu$$

(3.16)

instead of equation 3.13. Here l_ε and l_μ are length scales which are a function of the turbulence Reynolds number, $R_T = \frac{\sqrt{k}n}{v}$. Their expressions are:

$$l_\mu = C_1 n\left[1 - \exp\left(-\frac{R_T}{A_\mu}\right)\right]$$

(3.17)

$$l_\varepsilon = C_1 n \left[1 - \exp\left(-\frac{R_T}{A_\varepsilon} \right) \right]$$
(3.18)

where n is the normal distance from the (nearest) wall, $C_1 = \kappa C_\mu^{-3/4}$, so as to obtain a smooth eddy-viscosity distribution between the inner and the outer layers, $\kappa = 0.418$ is the von Karman constant, $A_\varepsilon = 2C_1$ and $A_\mu = 70$. Besides its robustness, an advantage of the two-layer model is that it does not require a boundary condition for ε at the wall.

In the constant-density RANS simulations performed in the present study, the diffusion terms were discretized using a second-order-accurate central scheme and the convective terms were discretized using the second-order upwind scheme. The first-order upwind scheme was used to discretize the convective terms in the transport equations for the turbulence variables. As only steady state RANS simulations were performed, the unsteady term in the momentum equations and in the transport equations for the turbulent variables was equal to zero. The segregated flow solver uses a cell-centered finite-volume method in which the gradients of the variables are computed by means of Green-Gauss' theorem. The SIMPLE algorithm was used to solve the discretized Navier-Stokes equations.

Similar to the 3D LES simulations discussed in the previous subsection, an important feature of the RANS simulations of airflow past porous snow fences is that the solid elements forming the porous fence are resolved by the mesh. This is a much more correct treatment compared to the common procedure in which a layer of uniform porosity is defined at the location of the fence. Of course, generating a high quality mesh is much more difficult given the presence of very thin solid elements. But the details of the airflow through the fence and the influence of porosity on the wake flow downwind of the fence

are more correctly simulated. In this regard, the use of the local mesh refinement procedure available in the grid generator integrated with STAR CCM+ was critical to generate a high quality mesh.

A slip (symmetry) boundary condition was used at the top boundary for the velocity. The bottom boundary and the fence surfaces were treated as no-slip (zero velocity) boundaries. The turbulent kinetic energy was set equal to zero at these boundaries. A standard mass outflow boundary condition was used at the downstream boundary. The turbulence variables were extrapolated at the exit and on the top boundary. The distributions of the mean velocity and turbulent quantities in the inflow section were obtained from a preliminary simulation of the flow in a straight channel of identical height with periodic conditions in the streamwise direction. This is standard treatment for this type of problems (e.g., see Kirkil and Constantinescu, 2009; Constantinescu et al., 2011). The simulations were started with a zero velocity field in the interior of the domain and with small values for k and ε. As steady-state simulations were conducted, the initial conditions did not affect the final steady solution.

In all simulations, the inlet section was situated far enough from the region where the presence of the snow fence disturbs the incoming flow field. To also mimic conditions encountered in the field, the incoming flow was assumed to be fully turbulent. The distributions of the mean velocity and turbulent quantities in the inflow section were obtained from a preliminary simulation of the flow in a straight channel of identical height with periodic conditions in the streamwise direction. A slip boundary condition was used at the top boundary. The bottom boundary and the fence surfaces were treated as no-slip

boundaries. A standard mass outflow boundary condition was used at the downwind boundary.

CHAPTER 4 ASSESMENT OF THE CAPABILITIES OF THE LES SOLVER TO
PREDICT FLOW PAST SOLID AND POROUS CYLINDERS

4.1 Introduction

The LES solver (see section 3.2) was already used to predict constant-density
turbulent flow in straight channels with flat and deformed bed containing dunes or bottom
cavities (e.g., see Chang et al., 2006; Chang and Constantinescu, 2013), ejection of heavier
contaminants from bottom cavities (Chang et al., 2007) and propagation of gravity currents
in channels with a flat bottom or a bottom containing ribs or dunes (Ooi et al., 2009; Tokyay
et al., 2011 and 2012). These simulations were conducted at moderate Reynolds numbers,
similar to the numerical simulations that will be performed in the present study. For all
these test cases, LES predictions of the mean flow and turbulence statistics were found to
be in good agreement with experimental data.

The main objective of this chapter is to further evaluate the accuracy of the LES
solver to predict flow past rectangular cylinders and porous barriers. The present chapter
reports comparison with experimental data for two test cases: flow past a square cylinder
placed at mid channel height and flow past a thin porous plate situated in the vicinity of
the channel bed. As barriers usually resemble high-aspect-ratio rectangular cylinders, the
present chapter also discusses how the width of the cylinder affects the mean flow,
turbulence statistics and wake vortex shedding by comparing results for a square cylinder
and for a high-aspect-ratio rectangular cylinder of same height.

4.2 Flow past a Solid Rectangular Cylinder

LES was used to simulate flow past a 2D square cylinder and flow past a high-
aspect ratio rectangular cylinder (thin vertical plate). In both cases, the cylinder height H
and the incoming flow velocity, U_0, were the same. The cylinder Reynolds number,

Re=U_0H/ν, was equal to 21,400. The flow conditions are those considered in the experiments conducted by Lyn et al. (1995) for a square cylinder. The same test case was simulated using LES by Wang and Vanka (1996) and by Srinivas et al. (2006). These experimental and numerical data are used to validate present LES results for the flow past a 2D square cylinder.

4.2.1 Simulation Setup

The computational domain used in the 3D simulation of flow past a square cylinder is shown in Figure 4.1. The computational domain used in the simulation of flow past a high-aspect-ratio rectangular cylinder was similar. The high-aspect-ratio rectangular cylinder will be referred as a (vertical) plate. The thickness (width) of the cylinder was 0.02H. In both simulations, the x-axis was aligned with the incoming flow direction and the z-axis was parallel to the cylinder axis (spanwise direction). The origin of the x and y axes was situated at the center of the 2D cylinder (Figure 4.1). The cylinder height H was used as the length scale. The uniform incoming flow velocity U_0 was used as the velocity scale.

The length and the height of the computational domain were 35H and 14H respectively. In both simulations, the cylinder was located at a distance of 10H downstream of the inflow section. The length of the cylinder in the spanwise direction was equal to 3.5H. The length of the square cylinder was 9.75H in the experiment of Lyn et al. (1995) and 3.15H in the LES of Wang and Vanka (1996). For simulations of flow past 2D cylinders conducted with periodic boundary conditions in the spanwise direction, a width of the domain of about 3H is considered sufficient for the mean flow and turbulence statistics to be independent of the spanwise length of the domain. The blockage ratio (0.07)

66

was identical to the one in the experiment of Lyn et al. (1995). The blockage ratio was slightly smaller (0.05) in the LES performed by Wang and Vanka (1996).

The mesh in a streamwise-vertical (z=constant) x-y plane is shown in Figure 4.2 for the square cylinder case. The computational domain contains around 51 million hexahedral elements (832x640x96). The mesh is uniform along the z direction. Grid points are clustered around the x=constant and y=constant locations corresponding to the edges of the cylinder to resolve the attached boundary layers on these surfaces. The mesh used for the simulation of flow past the 2D plate is very similar in terms of the number of mesh points used in each direction and the grid spacing near and away from the plate's surfaces.

A minimum grid spacing ($y^+=u_\tau y/\nu$) of about 2 wall units (assuming $u_\tau/U_0=0.05$) was used in the wall normal direction near the no-slip surfaces of the cylinder/plate. This corresponded to a length of the cell of about 0.002H in the wall normal direction close to each face of the cylinder. Away from the cylinder/plate, the dimensions of the 3D cells were increased to about 0.06Hx0.05Hx0.04H.

The time step used in the simulations was $0.0006H/U_0$. The simulations were run for $70H/U_0$ time to eliminate the transients. Statistics were then collected over an additional $70H/U_0$. When calculating the mean flow and turbulence statistics, the averaging was done over time and the spanwise direction, as the mean flow is two-dimensional. 3D velocity fields were saved every $0.25H/U_0$. Statistics were checked for convergence.

At the inflow section, steady uniform flow with streamwise velocity U_0 was applied. The mean velocities in the other two directions were set to zero. No resolved turbulence was added through the inflow section. At the outflow, a convective boundary condition that allows the vortical structures to exit the domain in a time accurate way and

without producing unphysical oscillations was used (Rodi et al., 2013). This is standard treatment for boundaries through which large-scale turbulence is exiting the computational domain. As the flow was assumed to be homogeneous in the spanwise direction, periodic boundary conditions were used for the lateral surfaces. A symmetry (free slip) boundary condition was used on the top and bottom surfaces. No-slip boundary conditions were used on the solid surfaces of the cylinder/plate. These boundary conditions are similar to those used by Wang and Vanka (1996) in their LES of flow past a square cylinder.

4.2.2 Validation

Figures 4.3 through 4.7 compares the time-averaged vertical profiles of the mean velocity components and Reynolds stresses predicted by the present simulation of flow past a square cylinder to the corresponding experimental results of Lyn et al. (1995), the 3D LES results of Wang and Vanka (1996) and the 3D LES results of Srinavas et al. (2006). The profiles are compared at three different streamwise locations situated at x=1H, 1.5H and 5H from the center of the square cylinder. Only half of the domain is shown (y>0), as the mean flow is symmetrical with respect to the centerline of the cylinder (y=0H). The results from the present simulation, in general, were in good agreement with the previous experimental and LES results.

Figures 4.3 and 4.4 compare the time-averaged streamwise and vertical velocity profiles. As the flow is advected past the cylinder, two symmetrical counter rotating vortices form at the back of the cylinder. The mean streamwise velocity decreases in the wake of the cylinder with the maximum reduction occurring at the centerline. The flow recovers slowly toward the free stream value as one move away from the centerline. For the same reasons, the vertical velocity becomes non-zero in the wake of the cylinder, but

because of the flow symmetry the mean vertical velocity is equal to zero at the centerline. Values of the vertical velocity as high as $0.4U_0$ are observed in the wake at x=1H. The vertical location, at which the maximum vertical velocity occurs, increases with the distance from the cylinder due to the increase in the width of the wake. However, by x=5H the vertical velocity component is negligible at all vertical locations. That is not the case for the streamwise velocity deficit, which is still significant at x=5H.

The level of agreement between LES and experiment is good. Some differences are observed in the profiles of u at x=1.5H where the wake flow recovers faster in LES compared to experiment. LES also does not capture very accurately the low vertical velocities close to the channel centerline over the upwind part of the wake. Unfortunately, no detailed information is provided on the error of the measurements. However, an important observation is that the predictions given by the three LES are very close to each other despite the fact that the numerics in the three LES solvers are different.

The general level of agreement between the three LES and between LES and experiment is similar for the normal Reynolds stresses in the streamwise and vertical directions and for the primary Reynolds shear stress. The comparison is provided in Figures 4.5 to 4.7. The flow in the near wake is highly anisotropic as shown by the different distributions of the normal stresses in the region where turbulence intensity is high. Interestingly, LES captures very well the variation of the normal stresses at all locations. The peak streamwise normal stresses occur in the separated shear layer forming on the sides of the square cylinder via production by mean shear. As one moves away from the back of the cylinder the peak moves closer to the centerline. The vertical normal stresses remain low within the separated shear layer as the vortex tubes advected within this layer

69

follow a trajectory that is fairly parallel to the streamwise direction, rather the largest values occur close to the centerline in the region where the separated shear layers on the two sides of the cylinders interact to form the large scale billow vortices. This happens around x/H=1.5. Then the peak centerline values decay monotonically with the distance from the cylinder.

The agreement between LES and experiment for the normal Reynolds stresses is better than that observed for the mean velocities. Larger differences between LES and experiment are observed for the primary mean shear stress. The largest error occurs near the centerline at x/H=1.5 where LES predict a rapid increase of the primary shear stress away from the centerline while measurements indicate the shear stress remains very low until y/H=0.4. The levels of the shear stress are negligible by x=5H at all y locations. Again, the Reynolds stresses predictions of the three LES are very close at all three streamwise locations. Errors are marginally larger in the LES results of Srinivas et al. (2006) for the vertical normal stresses at x=5H and for the primary shear stress at x=1H.

4.2.3 Flow Structure

In this section the effect of the cylinder width on the wake and forces induced on the rectangular cylinder is analyzed by comparing the instantaneous and mean flow fields and turbulence statistics for the case of a square cylinder (width equal to 1H) and of a vertical plate (width equal to 0.02H) of equal height (H).

4.2.3.1 Instantaneous Flow Fields

As the flow is homogeneous in the spanwise direction, we will analyze flow structure only in a streamwise-vertical x-y plane.

The streamwise velocity fields in Figure 4.8a and 4.9a show that the wake assumes an undulatory shape in both cases. The undulatory shape is induced by the wake billow vortices shed at the back of the obstacle (square cylinder/vertical plate) dur to the interaction of the separated shear layers forming at the upstream edges of the square cylinder and respectively at the extremities of the vertical plate. As a result of the difference in the obstacle geometry, the orientation of the SSLs in the two cases is different. Moreover, the SSLs penetrate further downstream from the back of the obstacle in the case of a vertical plate. Still, as explained below, the mechanism responsible for the formation of the wake roller vortices is essentially the same in the two cases.

The instantaneous spanwise vorticity fields in Figure 4.8b show a strong amplification of the vorticity in the separated shear layers (SSLs) forming on the two sides of the square cylinder and an acceleration of the streamwise flow on the outer side of the SSLs. As expected for flow past 2D bluff bodies, the wake contains large scale roller vortices and assumes an undulatory shape. The roller vortices forming the von Karman vortex street are shed from the back of the cylinder as a result of the interaction of the SSLs forming on the two sides of the cylinder. These SSLs originating at the upwind edges of the cylinders where the flow separates extend over the whole lateral side of the cylinder and past it. Strongly coherent eddies forming because of the KH (Kelvin-Helmholtz) instabilities are shed inside the SSLs. As the downwind end of one of the SSLs curves toward the centerline (e.g., the left side SSL in Figure 4.8b), eddies advected in the other SSL rather then moving downwind are diverted toward the back of the cylinder where they merge to form a larger (roller) vortex. When the circulation of the roller vortex is sufficiently high the roller detaches from the back of the cylinder and pushes the (left) SSL

71

away from the centerline. Once this happens, the other SSL moves toward the centerline and a new roller with an opposite sense of rotation to the previous one starts forming. One should also notice that during each cycle that results in the formation of a new roller, the SSLs on the two sides of the cylinder change their orientation. At times they are attached to the lateral side of the cylinder, while at other times they detach close to the upwind edge of the cylinder. The wake vortices are region of low pressure.

The 2D streamline patterns in Figure 4.10a show the new roller vortex forming at the back of the square cylinder and the previously shed vortex whose axis is situated close to x/H=2 that moves away from the cylinder. Results for the vertical pate in Figure 4.11 are qualitatively very similar. The only difference is that the size of the region at the back of the obstacle where the billows form is larger in the case of a vertical plate. In the case of a square cylinder recirculation regions form in between the SSLs and the lateral edges of the square cylinder. The position of the roller vortices away from the cylinder can be visualized using pressure contours, as the pressure in the core of strongly coherent vortices is expected to be lower compared to the surrounding flow. The solid lines in Figures 4.8 through 4.11 correspond to a line of constant low pressure. The cores of the rollers also correspond to the regions where neighboring patches of high and low streamwise velocities are present. The pressure isocontour line in Figures 4.8 and 4.9 shows that the wake vortices are situated in the regions where the undulatory wake approaches the symmetry line. In those regions the rotational movement of the vortex is superimposed to the mean streamwise velocity at that location and results in the increase of the total streamwise velocity over part of the core with respect to the mean streamwise velocity at that location

72

(red patches) and a decrease of the total streamwise velocity over the other part of the core (blue patches).

The coherence of the rollers shed behind the square cylinder and the vertical plate is larger than the one generated behind a circular cylinder. This is because of the stronger velocity acceleration induced on the sides of the rectangular cylinder by the diverted flow. The degree of frontal bluffness of the square cylinder and vertical plate of equal height is basically the same.

The roller vortices are stretched by the 3D turbulence (e.g., see Figure 4.12 where the Q criterion was used to visualize the eddy content of an instantaneous flow field) but they maintain their coherence in the near wake region (e.g., see patches of concentrated positive and negative vorticity in Figure 4.8b). Besides the smaller scale 3D turbulence, larger, predominantly streamwise oriented, eddies are sometimes observed in the instantaneous flow fields (e.g., see Figure 4.12). These eddies are due to a secondary instability generated by the interaction of the core of neighboring rollers that generates smaller streamwise vortices connecting the rollers. These vortices are sometimes called finger vortices.

Despite the fact that the mean flow is two-dimensional, the formation of energetic smaller-scale 3D eddies induces significant spanwise velocities in the instantaneous flow fields, as also observed from Figure 4.10b and 4.11b where the magnitude of the maximum spanwise velocities are close to $0.7U_0$. Interestingly regions of high positive spanwise velocity are situated in the vicinity of regions with high negative spanwise velocity. This is true especially in the regions connecting spanwise oriented roller vortices. This suggests that the elongated regions of positive and negative velocity magnitude are induced by the

secondary streamwise oriented finger vortices connecting successively shed roller vortices. The core of the roller vortices is also generally split into two regions containing positive and negative spanwise velocity, which suggests that the roller vortices also transport momentum in the spanwise direction. So, significant mass and momentum transport occurs in the spanwise direction in the wake of 2D rectangular cylinders. The overall magnitude levels of the spanwise velocity are somewhat larger in the case of a vertical plate.

The temporal evolution of the lift coefficients for flow past a square cylinder is shown in Figure 4.14. It clearly shows the lift oscillations are quasi regular and the oscillations occur with a period of about $7H/U_0$. Table 4.1 summarizes the predicted values of the mean drag and lift coefficients and their root-mean-square fluctuations by the present LES, experiments and other LES studies of flow past square cylinders at comparable Reynolds numbers. As expected, the mean of the lift coefficient predicted by the present LES is close to zero ($\overline{C}_L$=0.008). The average value of the drag coefficient is 2.11, which is close to the measured values ($\overline{C}_D$=2.0-2.15 for Re~20,000) obtained from experiments conducted for square cylinders (e.g., Lindsey, 1938; Bearman and Obasaju, 1982; Norberg, 1993; Lyn et al., 1995). The Strouhal number corresponding to the large scale oscillations of C_L is 0.132, in excellent agreement with other experimental and numerical studies conducted at similar cylinder Reynolds numbers. The root-mean-square fluctuations of the drag coefficient predicted by the present LES is 0.21. This value is close to the one predicted by other LES. The predicted value of the root-mean-square fluctuations of the lift coefficient (1.5) is slightly larger than the one predicted by the other LES investigations.

Table 4.2 summarizes the predicted values of the mean drag coefficients and their root-mean-square fluctuations by the present LES. Also included are the values of the mean

drag and the Strouhal number associated with the dominant oscillations of the force on the vertical plate estimated from an experiment of flow past a vertical plate conducted by Fage and Johansen (1927) and Kiya and Matsumura (1987). The time averaged value of the drag coefficient predicted by LES is 2.17, which is close to the measured value (Fage and Johansen, 1927, $\bar{C}_D$=2.13). This value is only slightly larger than the one predicted by LES in the case of a square cylinder ($\bar{C}_D$=2.11). The Strouhal number increases slightly from 0.132 for a square cylinder to 0.142 for a flat plate. Interestingly, while the rms of the drag coefficient is about the same for the square cylinder and for the vertical plate, the rms of the lift coefficient is by about 50% larger for the square cylinder case. This is because probably because the ends of the SSLs that are curving toward the other side of the obstacle are closer to the back of the obstacle in the case of a square cylinders. Thus, the wake rollers form at a smaller distance from the back of the cylinders and their effect on the lift force as they move away from the back of the obstacle is larger in the case of a square cylinder.

Figure 4.15 shows the time series of the vertical velocity and its power spectrum at a point situated inside the near wake region for the square cylinder case. The position of point 4 is shown in Figure 4.13. The spectrum displays a -5/3 inertial subrange. The large scale oscillations of the vertical velocity in the velocity time series at point 4 (Figure 4.15a and 4.16) can also serve to identify the times when a roller vortex is advected through that location. The peak frequency at St=fH/U_0=0.132 in Figure 4.15b corresponds to the frequency of passage of the roller vortices. The dominant shedding frequencies can also be inferred directly from the time series in Figures 4.15a and 4.16 for the two cases.

Besides the dominant frequency associated with the shedding of roller vortices, time series and power spectra of velocity at points situated inside the SSLs display additional energetic frequencies corresponding to the advection of energetic KH eddies within the SSLs. Figure 4.17 shows the streamwise and vertical velocity time series for validation case at point 2, which is located in one of the SSLs of the square cylinder (see also Figure 4.13). The range of energetic frequencies associated with the formation of vortex tubes in the SSLs is about St=1-1.5 for both cases (e.g. see velocity time series at point 2 in Figure 4.17 situated in the SSL of the square cylinder).

4.2.3.2 Mean Flow and Turbulence Statistics

In the mean flow, a recirculation eddy attached to the lateral edge of the square cylinder forms on the inner side of the SSL (Figure 4.18a). The outer side of the SSL is bordered by the region where the diverted flow accelerates as it passes the cylinder. Two additional symmetric recirculation eddies are present at the back of the square cylinder. In the case of the vertical plate, only a pair of recirculation eddies form at the back of the obstacle. The length of the recirculation bubbles at the back of the obstacle is 2.2H for the vertical plate and only 0.6H for the square cylinder. The main reason for this reduction is that the SSL originate at the upstream corners of the square cylinder and they curve quickly toward the back of the obstacle. In the case of a square cylinder, the SSLs are approximatively parallel to the lateral edges of the square cylinder and the spanwise vorticity magnitude inside the SSL decays fast past the downstream face of the obstacle (x>0.5H, see Figure 4.20b). By contrast, in the case of a vertical plate the SSLs move away from the symmetry plane until close to x/H=1 before starting curving toward the back of the obstacle (Figure 4.21b)

76

The streamwise velocity magnitude is very low inside the recirculation bubbles forming behind the obstacle (Figures 4.18b and 4.19b). These recirculation bubble approximately corresponds to the regions where eddies originating in the SSLs penetrate behind the cylinder and roller vortices form.

As expected, the maximum mean pressure in the flow is observed close to the center of the upwind face of the cylinders where the incoming flow decelerates fast. The stagnation pressure distribution on the upstream face of the obstacle is about the same in the two cases given that the shape, orientation and width of the upstream face of the obstacle are the same. The lowest pressure values are observed in the recirculation eddies at the back of the obstacle and also inside the recirculation bubbles forming close to the lateral edges of the square cylinder (see Figure 4.20a and 4.21a).

The advection of KH eddies within the upwind and downwind part of the SSLs generates a large amplification of the streamwise mean velocity fluctuations $\overline{u'^2}/U_0^2$ in Figure 4.22a. The lateral movement of the SSLs is a second reason for the amplification of $\overline{u'^2}/U_0^2$ at the back of the square cylinder. The amplification of $\overline{u'^2}/U_0^2$ inside the SSLs and in the region where the SSLs curve toward the back of the obstacle is smaller in the case of the vertical plate (Figure 4.23a). However, in both cases $\overline{u'^2}/U_0^2$ starts decreases sharply for x/H>2.0.

The effect of the obstacle width on the mean vertical velocity fluctuations (Figure 4.22b and 4.23b) is very small. For both cases, the largest amplification occurs close to the symmetry plane (y/H=0) between x/H=1 and x/H=2.5. Note that the back of the obstacle is situated at x/H=0.5 for the square cylinder and at x/H=0 for the vertical plate. So the region situated just behind the vertical plate is subject to lower levels of $\overline{v'^2}/U_0^2$ compared

to the corresponding region situated at the back of the square cylinder. The newly formed highly-coherent roller vortices detaching from the back of the cylinders are passing through this region. The vertical velocity changes sign during the passage of the counter-rotating roller vortices that are generated from each of the two SSL (e.g., see Figure 4.8b). This explains the large amplification of the vertical velocity fluctuations in this region.

Though the mean spanwise velocity fluctuations (Figure 4.22c and 4.23c) are amplified with respect to the background turbulence inside the SSLs and the near wake, the average level of amplification is several times lower than the peak levels observed for the streamwise and vertical velocity fluctuations. Though the distributions of $\overline{w'^2}/U_0^2$ are qualitatively similar in the two cases in terms of the shape of the region of high amplification of the mean spanwise velocity fluctuations and its streamwise extent (x/H≈3 in both cases), the average levels of $\overline{w'^2}/U_0^2$ within this region are about 150%-200% larger in the vertical plate case. This result is consistent with the distributions of the spanwise vorticity in the instantaneous flow fields. A possible reason is the larger coherence of the finger vortices forming in the wake of the vertical plate.

Consistent with the distributions of the mean streamwise and vertical velocity fluctuations, the TKE (Figure 4.24a and 4.25a) shows the largest amplification between x/H=1 and x/H=2.5 in the region where the newly formed wake rollers start moving away from the back of the obstacle. For the reasons explained before (e.g., penetration length of the SSLs past the downstream face of the obstacle), the TKE amplification close to the back of the vertical plate is smaller than the one observed at the back of the square cylinder.

The magnitude of the primary Reynolds shear stress (Figure 4.24b and 4.25b) is also the largest in the region where the downwind part of the SSLs is subject to oscillatory

lateral motions that results in the formation of the wake rollers. The levels of $\overline{u'v'}/U_0^2$ within this region are by about 30% higher for the square cylinder.

Finally, the distribution of the nondimensional mean pressure fluctuations in Figure 4.24c shows that in the case of a square cylinder the largest amplification occurs in the region where strongly coherent KH vortices are advected in the vicinity of the lateral edges of the square cylinder. Smaller levels of amplifications are also observed in the near-wake region starting at about 0.5H from the back of the square cylinder. The region of fairly large values of the mean pressure fluctuations observed over the upwind part of the near wake is induced by the passage of the roller vortices before the core of these vortices become very large and start losing their coherence due mainly to vortex stretching. In the case of a vertical plate (Figure 4.25c), the largest values of the mean pressure fluctuations are observed behind the plate. It is interesting to note the regions of high TKE do not necessarily correspond with regions of the mean pressure fluctuations.

4.3 Flow past a Partially Porous Plate

The second validation case corresponds to flow past a plate with non-uniform porosity placed over a flat bed. The lower half of the plate has a porosity P=30% while the upper half is solid (P=0%). The simulation was conducted at a Reynolds number of 41,000 defined with the cylinder height, H and the incoming flow velocity, U_0. The flow conditions are those considered in the experiment conducted by Huang et al. (2012). The same test case was also simulated using LES by Huang et al. (2012). Besides discussing the level of agreement between the present LES predictions with the experiment and LES of Huang et al. (2012), this section provides a discussion of the flow past a plate of nonuniform porosity.

The computational domain and the plate geometry used in the 3D simulation are shown in Figures 4.26a and 4.26b respectively. The x-axis is aligned with the incoming flow direction and the z-axis is parallel to the plate's axis (spanwise direction). The length and the height of the computational domain are 40H and 10H respectively. The porous plate is located at a distance of 10H from the inflow section. The length of the porous plate in the spanwise direction is 3.5H. The length of the porous plate was 10H in the experiment of Huang et al. (2012). For simulations of flow past cylinders conducted with periodic boundary conditions in the spanwise direction, a width of the domain of about 3H is considered sufficient for the mean flow and turbulence statistics to be independent of the spanwise length of the domain. The LES of Huang et al. (2012) was performed in 2D. The blockage ratio in the present 3D LES is identical (0.1) to the one in the experiment and LES performed by Huang et al. (2012). The design of the nonuniform porous fence (Figure 4.26b) is identical to that used in experiment and the 2D LES of Huang et al. (2012). The bottom gap is equal to zero (G=0) and the plate width is 0.02H.

The mesh in a streamwise-vertical x-y plane is shown in Figure 4.27a. The computational domain contains close to 47 million grid points (960x768x64). The mesh is uniform along the z direction. Grid points are clustered around the x=constant and y=constant locations corresponding to the edges of the solid elements of the plate (see Figure 4.27b). This is needed to resolve the attached boundary layers on these surfaces. A minimum grid spacing ($n^+=u_\tau n/\nu$, where n is the wall normal direction) of about 2 wall units (assuming u_τ/U_0=0.05) was used in the wall normal direction near the no-slip solid surfaces of the plate. This corresponded to a length of the cell of about 0.001H in the wall

normal direction. Away from the plate, the dimensions of the 3D cells were increased to about 0.08Hx0.08Hx0.05H in the x, y and z directions, respectively.

The time step used in the simulation was $0.0005H/U_0$. The simulation was run for $80H/U_0$ time to eliminate the transients. Statistics were then collected over an additional $80H/U_0$. When calculating the mean flow and turbulence statistics, the averaging was done over time and the spanwise direction, as the mean flow is two dimensional. To calculate statistics, 3D velocity fields were saved every $0.25H/U_0$.

The distributions of the mean velocity and turbulent quantities at the inflow section were obtained from a preliminary simulation of flow in a straight long channel of identical height to that of the channel containing the porous plate but with periodic conditions in the streamwise direction for the velocity components. This is standard treatment for this type of problems (Kirkil and Constantinescu, 2009; Constantinescu et al., 2011). A no-slip boundary condition was used at the bottom boundary (channel bed) and on all the solid surfaces of the porous plate. At the outflow, a convective boundary condition that allows the vortical structures to exit the domain in a time accurate way was used (Rodi et al., 2013). This is standard treatment of boundaries through which large-scale turbulence is exiting the computational domain. As the flow was assumed to be homogeneous in the spanwise direction, periodic boundary conditions were used for the lateral surfaces. A symmetry (free slip) boundary condition was used on the top surface of the domain. These boundary conditions are similar to those used by Huang et al. (2012).

4.3.2 Validation Results

The vertical variation of the nondimensional mean streamwise velocity, $\bar{u}/U_0$, is compared in Figure 4.28 with experimental hot-wire anemometer measurements and

results of 2D LES, both conducted by Huang et al. (2012). The comparison is shown at eight streamwise locations situated between 1H and 25H downwind of the plate. As expected, close to the porous plate (x=1H and x=2H profiles in Figure 4.28), the streamwise velocity is larger in the region with y<0.5H (P=30%) than in the region defined by 0.5H<y<1H (P=0%). This happens because the upper half of the plate is solid while a bleeding flow is present for y<0.5H. The flow recovers slowly as one moves downwind. At x=3H the streamwise velocity is close to zero for 0<x/H<1. Downstream of the location where the flow reattaches to the bed surface (x/H=9), the streamwise velocity profile increases monotonically with the distance from the bed within the wake region.

Overall, present 3D LES predictions of the streamwise velocity profiles are in very good agreement with the experimental data. Moreover, the agreement with the experimental data is clearly better than the one showed by the 2D LES of Huang et al. (2012). In particular, 3D LES better captures the streamwise velocity variation within the wake region at sections situated close to the plate. 2D LES underpredicts the bleeding flow at x=1H close to the bed and then slightly overpredicts the streamwise velocity near the boundary between the wake flow and the outerflow. Unfortunately no measurements of the Reynolds stresses were reported to assess the capabilities of 3D LES to predict the turbulence statistics.

4.3.3 Flow Structure

4.3.3.1 Instantaneous Flow Fields

As the flow is homogeneous in the spanwise direction, the flow structure will be analyzed only in a streamwise-vertical x-y plane. The instantaneous spanwise vorticity in Figure 4.29 shows a strong amplification of the vorticity in the separated shear layer (SSL)

forming at the upper extremity of the porous plate as well as in the vicinity of the lower part of the plate where strong jets penetrating the porous region generate turbulence and vorticity. In the flow field shown in Figure 4.29, the flow appears to reattach around $x/H=14$. The width of the SSL does not increase monotonically with the distance from the plate. As shown by the 2D streamline patters in Figure 4.30a, besides the vortex tubes forming in the upstream part of the SSL, several eddies are present within the main recirculation flow eddy that extends up to $x/H=14$. Then the streamlines diverge again and the wake width increases again. Over this part of the wake, the eddy content and the associated high vorticity are high starting close to the bed. By contrast, except for the upstream part of the bleeding flow penetrating through the lower part of the fence, the vorticity levels are much lower within the main recirculation region compared to those inside of the SSL.

As the mean spanwise velocity is equal to zero, the distribution of the spanwise velocity in Figure 4.30b is a good indication of the three dimensionality of the flow. Several regions of high and low spanwise velocity are observed inside the flow domain downstream of the porous plate. The spanwise velocity magnitude inside these regions is over $0.3U_0$ which means that the spanwise momentum transport is very significant. These values are more than one order of magnitude higher than the spanwise velocities occurring in the fully developed turbulent flow approaching the porous plate. Moreover, the largest regions of high spanwise velocity magnitude are situated within the SSL. Generally one region of high positive spanwise velocity is situated in the vicinity of a region of high negative spanwise velocity. This suggests that the transfer of momentum in the spanwise direction is fairly local and driven by the large scales contained inside the SSL. Such regions are

observed even downstream of the location where the SSL touches the channel bed (x/H=12-14).

The temporal evolution of the drag coefficient for the porous plate is shown in Figure 4.31. Table 4.3 summarizes the predicted values of the mean drag coefficient ($\overline{C_D}$=0.93) and the root-mean-square fluctuations of the drag coefficient (C_D^{rms} =0.08). As seen from Figure 4.31, the oscillations of the drag coefficient are characterized by a fairly broad range of energetic frequencies. No dominant frequency was identified. The experimental and LES studies by Huang et al. (2012) do not report the values of these variables.

4.3.3.2 Mean Flow and Turbulence Statistics

In the mean flow, besides the SSL originating at the top of the plate, a second, shorter, SSL of opposite vorticity forms at the boundary between the solid and porous part of the vertical plate. The interaction of the second SSL with the main SSL may induce the formation of the large scale eddies observed in the instantaneous vorticity field in Figure 4.29. The mechanism is somewhat similar to that that results in the formation of wake roller past 2D bluff cylinders expect that here one SSL is much stronger than the other. As a result, when the second SSL gets closer to the main SSL, vorticity cancelation occurs and the thickness of the main SSL decreases. This may be the main reason for the large scale variation in the thickness of the main SSL observed in Figure 4.29.

Also visible in Figure 4.32a are the jets forming in between the solid elements of the porous plate and the presence of a near bed region of negative vorticity that is induced by the interaction of the second SSL with the bed surface. In the mean flow, the main recirculation eddy contains only two main secondary eddies. The first one corresponds to

84

the recirculation bubble forming at the back of the upper solid portion of the plate. Most of the bleeding flow is first advected downwards toward the bed surface and from there upwards into the SSL around x/H=2.5 (see also the contours of the mean vertical velocity in Figure 4.33b). The second bubble extends from x/H=2.5 until x/H=9.0 where the SSL attaches to the bed. The flow in the wake remains fairly parallel to the bed until x/H=14 after which the streamlines diverge slowly away from the bed surface. As shown in Figure 4.33a, the streamwise velocity magnitude inside the two recirculation bubbles is low compared to that in the surrounding wake flow. Consistent with the 2D streamline patterns, the patch of higher streamwise velocity magnitude originating on the porous side of the plate penetrates up to x/H≈2.

The pressure distribution around the partially porous plate resembles that one would expect for a solid plate, especially on its upstream side. The jets forming in between the solid elements of the porous part of the plate induce a region of very low pressure. Still the mean pressure decay between the upstream and downstream faces of the partially porous plate is less than the one that would be observed around a solid plate of equal height.

As expected, the large shear induced by the small but strong flow jets forming over the lower porous part of the plate induce a small region of high mean velocity fluctuations in all three directions (Figure 4.34). The mean velocity fluctuations are relatively low within the recirculation bubble situated between x/H=2 and x/H=8 as well as the smaller bubble forming behind the solid part of the plate. As expected they peak inside the upstream side of the main SSL before it first attaches to the channel bed. Though the mean streamwise velocity fluctuations are at most locations larger than the ones in the other two

directions and they decay at a slower rate after the SSL attaches, the overall patterns and levels are fairly similar for the mean velocity fluctuations in the three directions.

The upstream part of the main SSL is a region of high magnitude of the TKE and mean pressure fluctuations (Figures 4.35a and 4.35c). The same is true for the region containing the jets penetrating through the porous part of the plate. After some decay in the region where the SSL attaches to the bed and moves parallel to the bed, the TKE and mean pressure fluctuations increase again in the region (x/D>14) where the large scale turbulence inside the SSL starts moving away from the bed. It is possible that vortex breakdown phenomena are inducing this behavior of the region containing energetic vertical eddies after the main SSL first touches the bed surface.

4.4 Conclusions

The two validation cases considered in this chapter showed that 3D LES solver can accurately capture the mean velocity and turbulence statistics in the wake of solid and partially porous rectangular cylinders both for cases when large scale shedding is present in the wake as well as for cases when the rectangular cylinder (partially porous plate) is mounted on a flat surface. In the case of the flow past a square cylinder, the mean velocity, turbulent Reynolds stresses, mean values of the lift and drag coefficients and their root mean square fluctuations predicted by the present LES were found to be in good agreement with the experimental results (e.g., Lyn et al., 1995) and the LES of Wang and Vanka (1996) and Srinivas et al. (2006). In the case of flow past a partially porous vertical plate, LES was found to correctly predict the strength of the bleeding flow through the lower porous part of the plate and the streamwise location at which the mean flow past the top

side of the plate attaches to the bed surface as well as the streamwise velocity profiles in the wake.

Comparison of solutions obtained for the flow past a square cylinder and past a vertical (high aspect ratio rectangular cylinder) plate of same height allowed understanding how the obstacle width affects the characteristics of the wake flow and turbulence, mean drag forces on the obstacle and their rms fluctuations.

The validated LES solver will be used in the following chapters to perform a series of simulations that will allow understanding the effects of varying some of the main geometrical parameters (e.g., porosity, ratio of bottom gap to fence height, ratio of mean fence opening to fence height) that determine the design of plates used as fences in various practical applications.
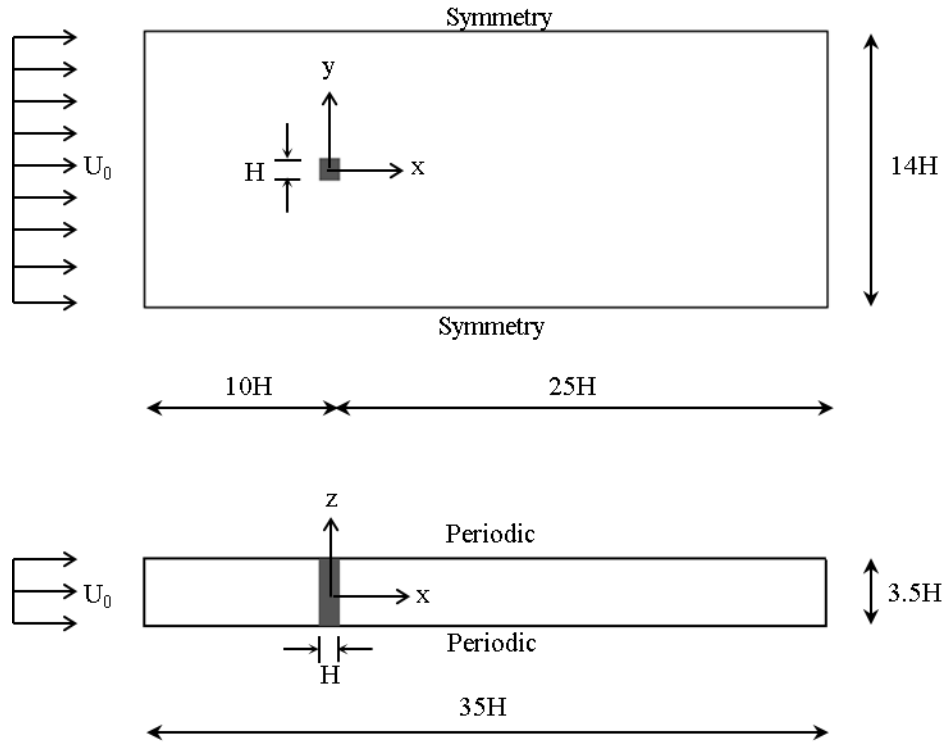
Figure 4.1 Computational domain used to simulate for past a 2D square cylinder. The cylinder is placed at mid channel height. Computational domain and boundary conditions are identical for the simulation of flow past a vertical 2D plate of width 0.02H.
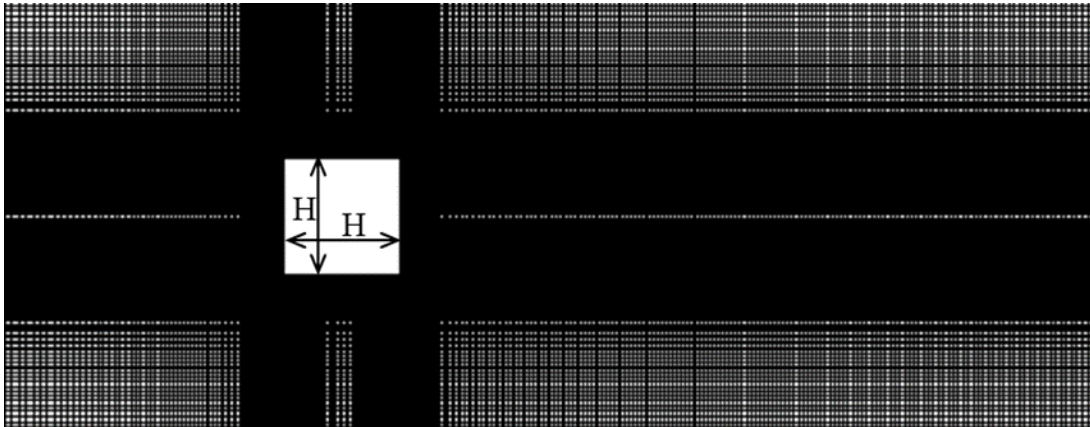
Figure 4.2 View of the computational domain used to simulate flow past a 2D cylinder. The mesh is shown in a streamwise-vertical (x-y) plane.
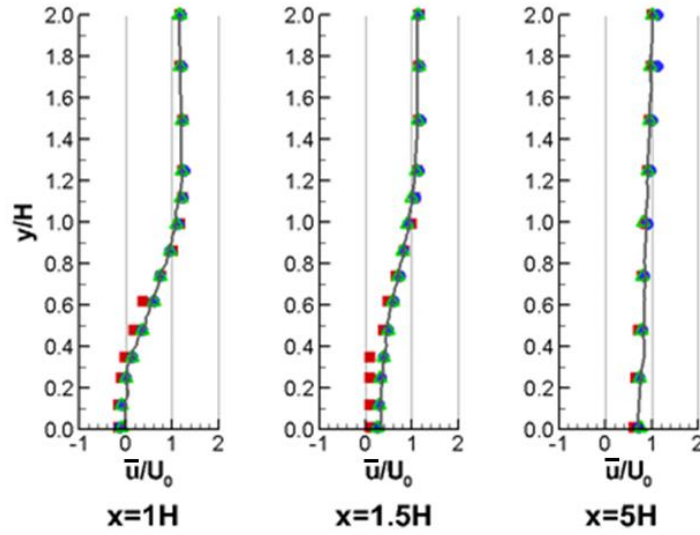
Figure 4.3 Time-averaged streamwise velocity profiles for flow past a square cylinder:
(———) LES results, present study, (■) Experimental results of Lyn et al. (1995), (△)
LES results of Wang and Vanka (1996) and (●) LES results of Srinivas et al. (2006).
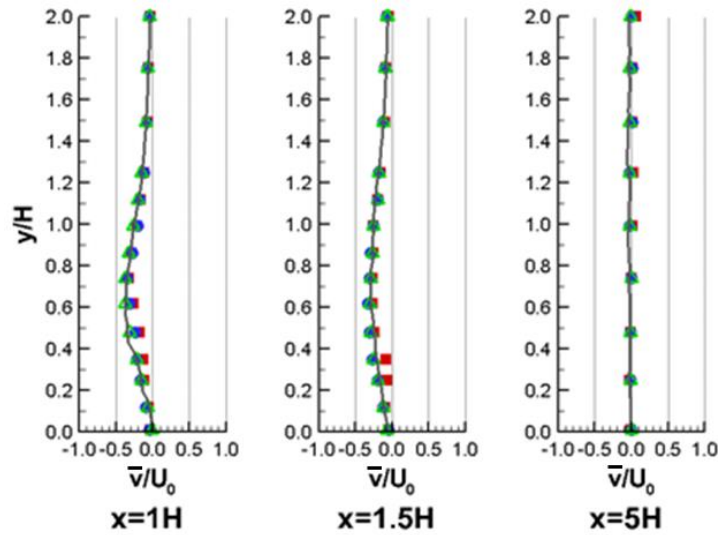
Figure 4.4 Time-averaged vertical velocity profiles for flow past a square cylinder:
(———) LES results, present study, (■) Experimental results of Lyn et al. (1995), (△)
LES results of Wang and Vanka (1996) and (●) LES results of Srinivas et al. (2006).
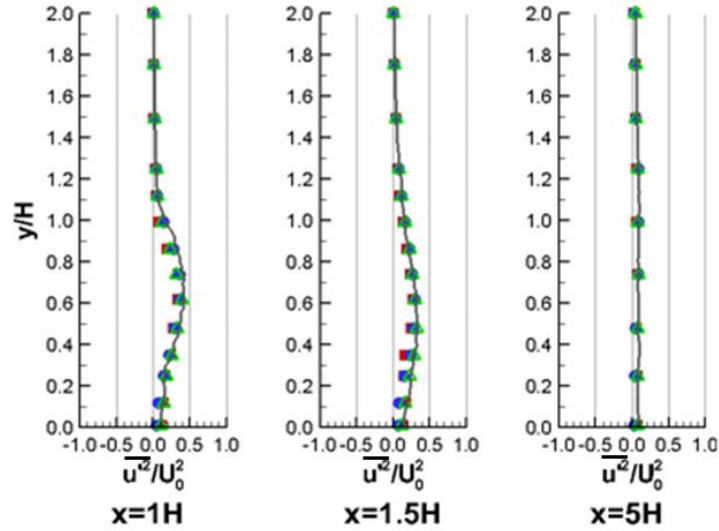
Figure 4.5 Time-averaged streamwise normal Reynolds stress profiles for flow past a square cylinder: (———) LES results, present study, (■) Experimental results of Lyn et al. (1995), (△) LES results of Wang and Vanka (1996) and (●) LES results of Srinivas et al. (2006).
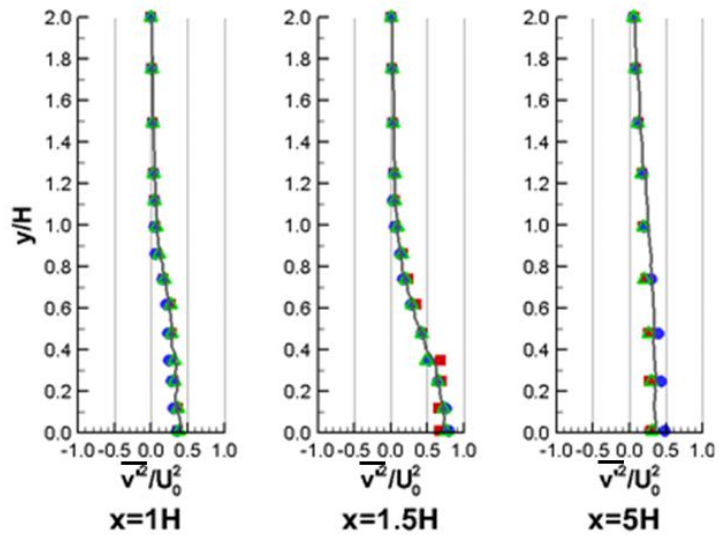
Figure 4.6 Time-averaged vertical normal Reynolds stress profiles for flow past a square cylinder: (———) LES results, present study, (■) Experimental results of Lyn et al. (1995), (△) LES results of Wang and Vanka (1996) and (●) LES results of Srinivas et al. (2006).

90
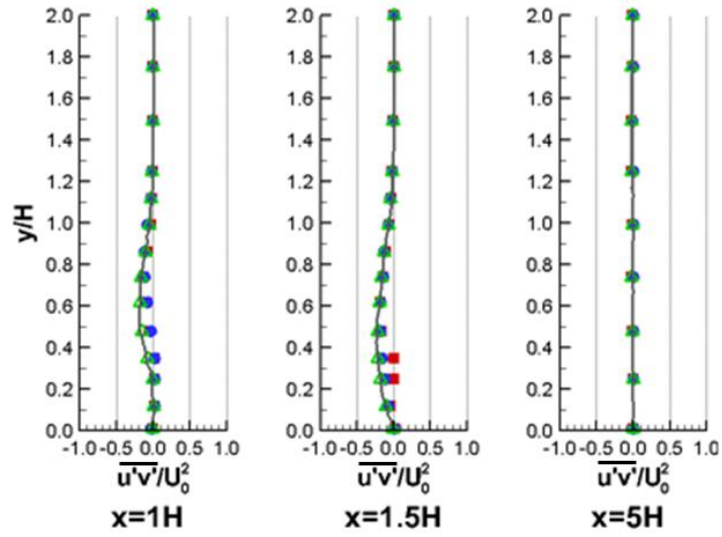
Figure 4.7 Time-averaged Reynolds shear stress profiles for flow past a square cylinder: (——) LES results, present study, (■) Experimental results of Lyn et al. (1995), (△) LES results of Wang and Vanka (1996) and (●) LES results of Srinivas et al. (2006).
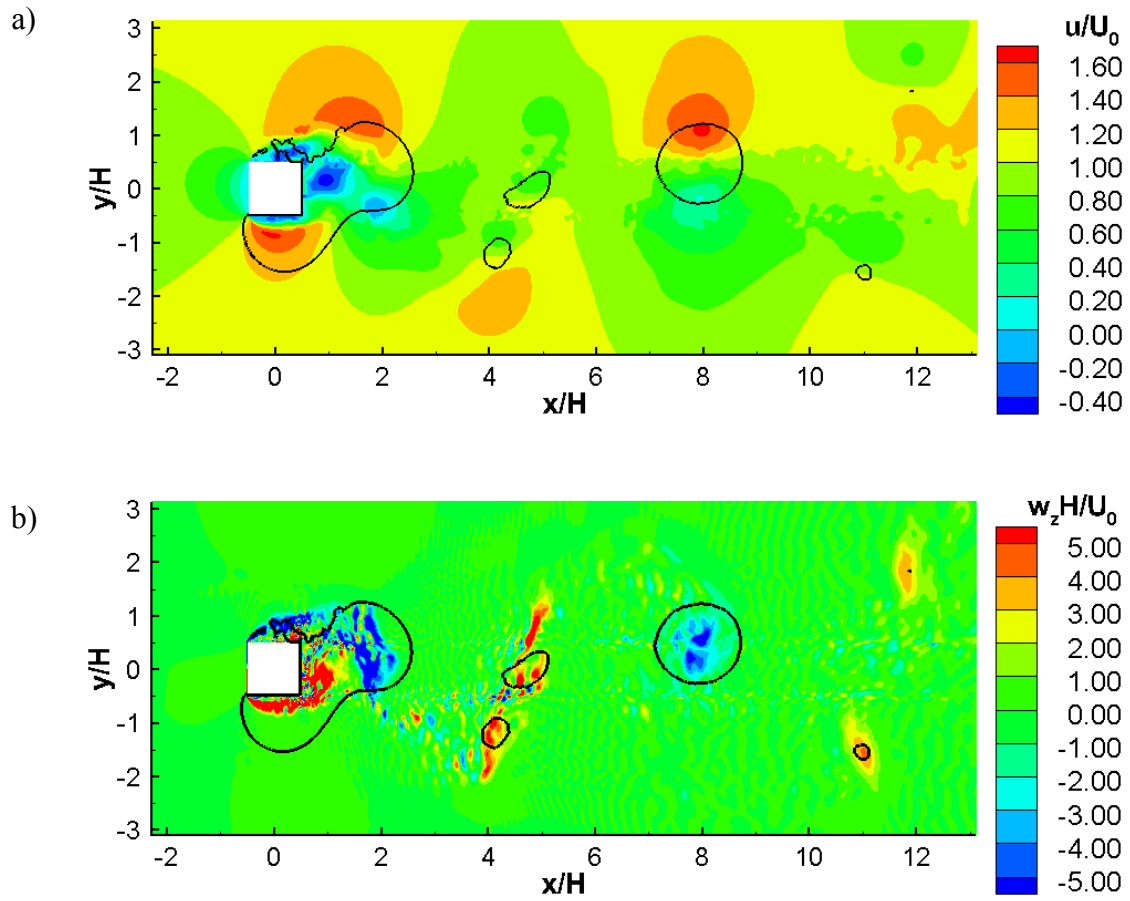
Figure 4.8 Visualization of instantaneous flow past a square cylinder: a) streamwise velocity; b) spanwise vorticity; (black line indicates the P=-0.5(ρU_0^2) iso-line).
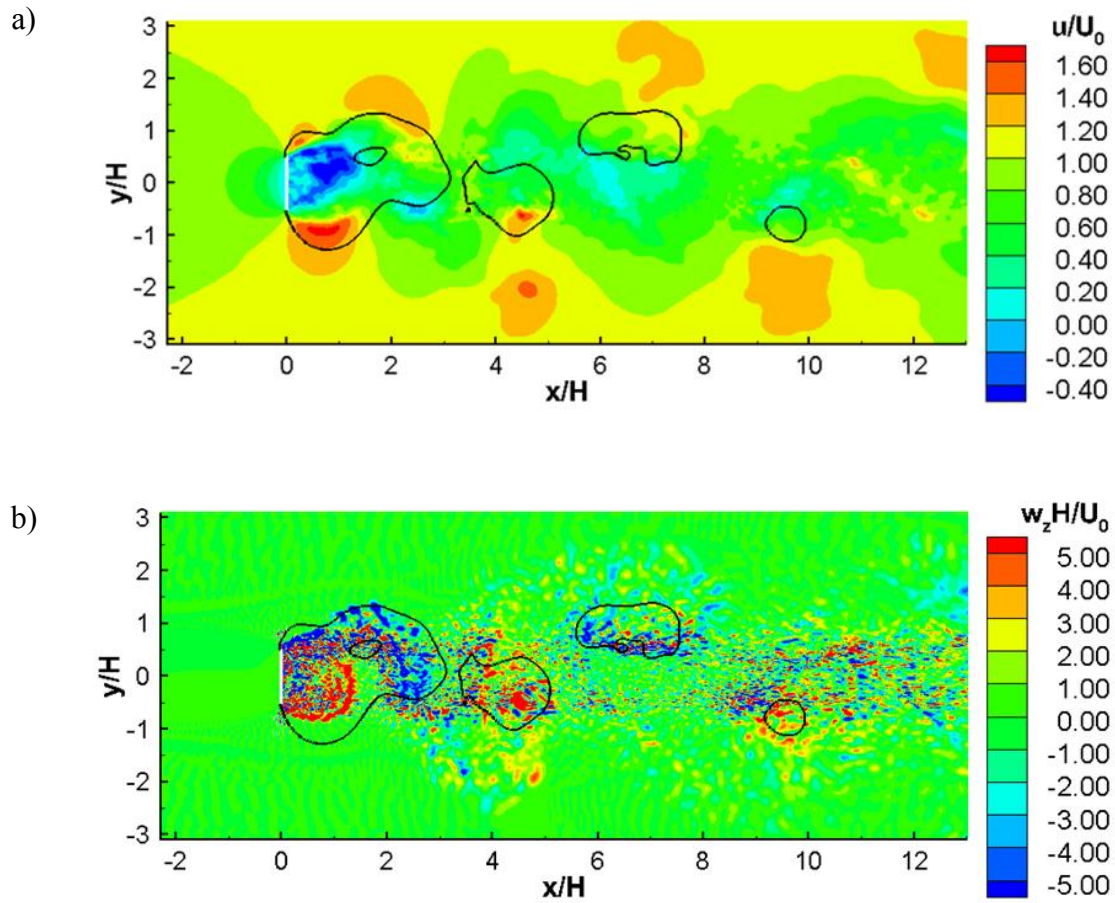
Figure 4.9 Visualization of instantaneous flow past a vertical plate: a) streamwise velocity; b) spanwise vorticity; (black line indicates the P=-0.5(ρU02) iso-line).
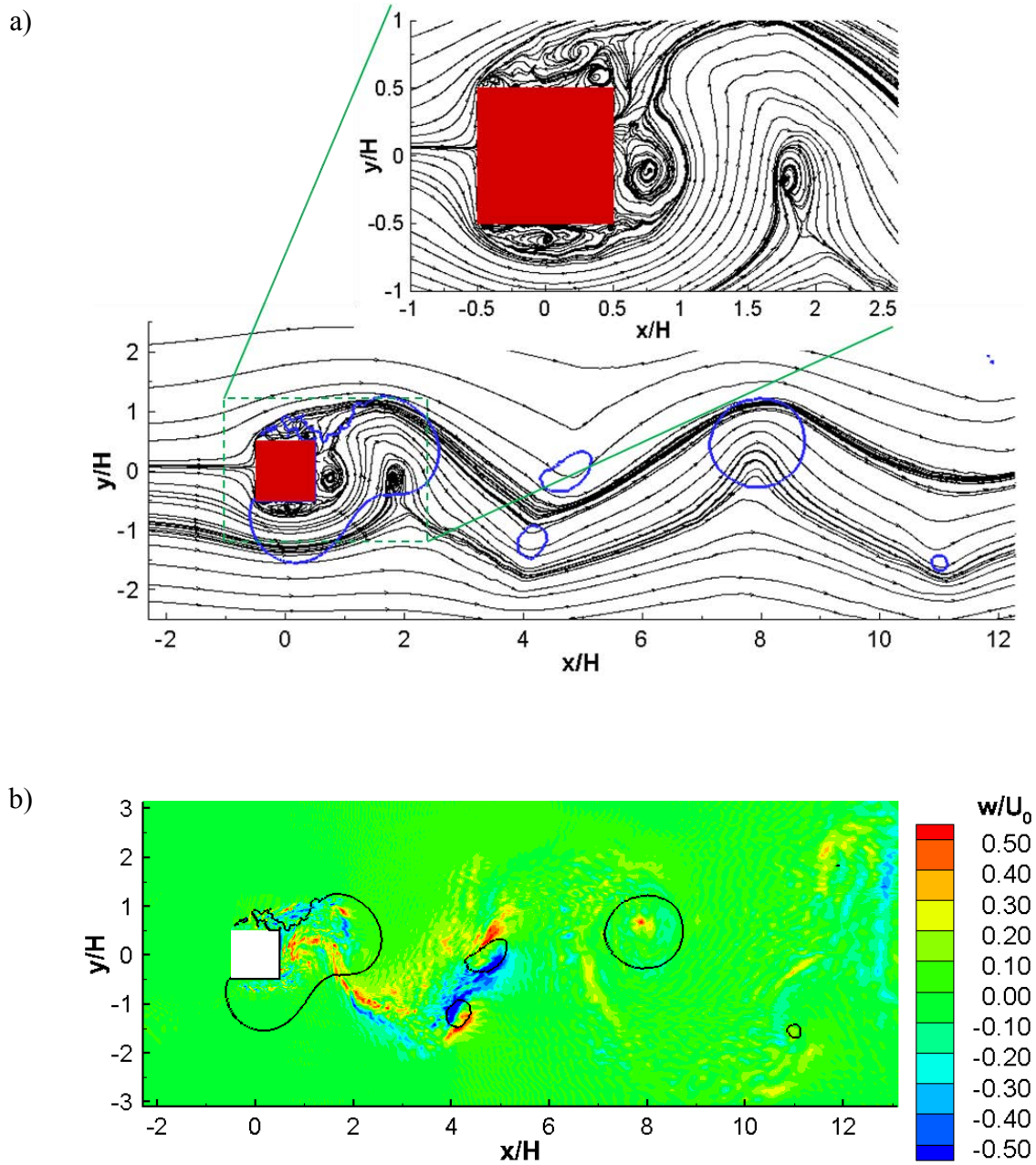
Figure 4.10 Visualization of instantaneous flow past a square cylinder: a) stream lines; b) spanwise velocity; (black and blue lines indicate the P=-0.5(ρU_0^2) iso-line).

a)

b)

Figure 4.11 Visualization of instantaneous flow past a vertical plate: a) stream lines; b) spanwise velocity; (black and blue lines indicate the $P=-0.5(\rho U_0^2)$ iso-line).
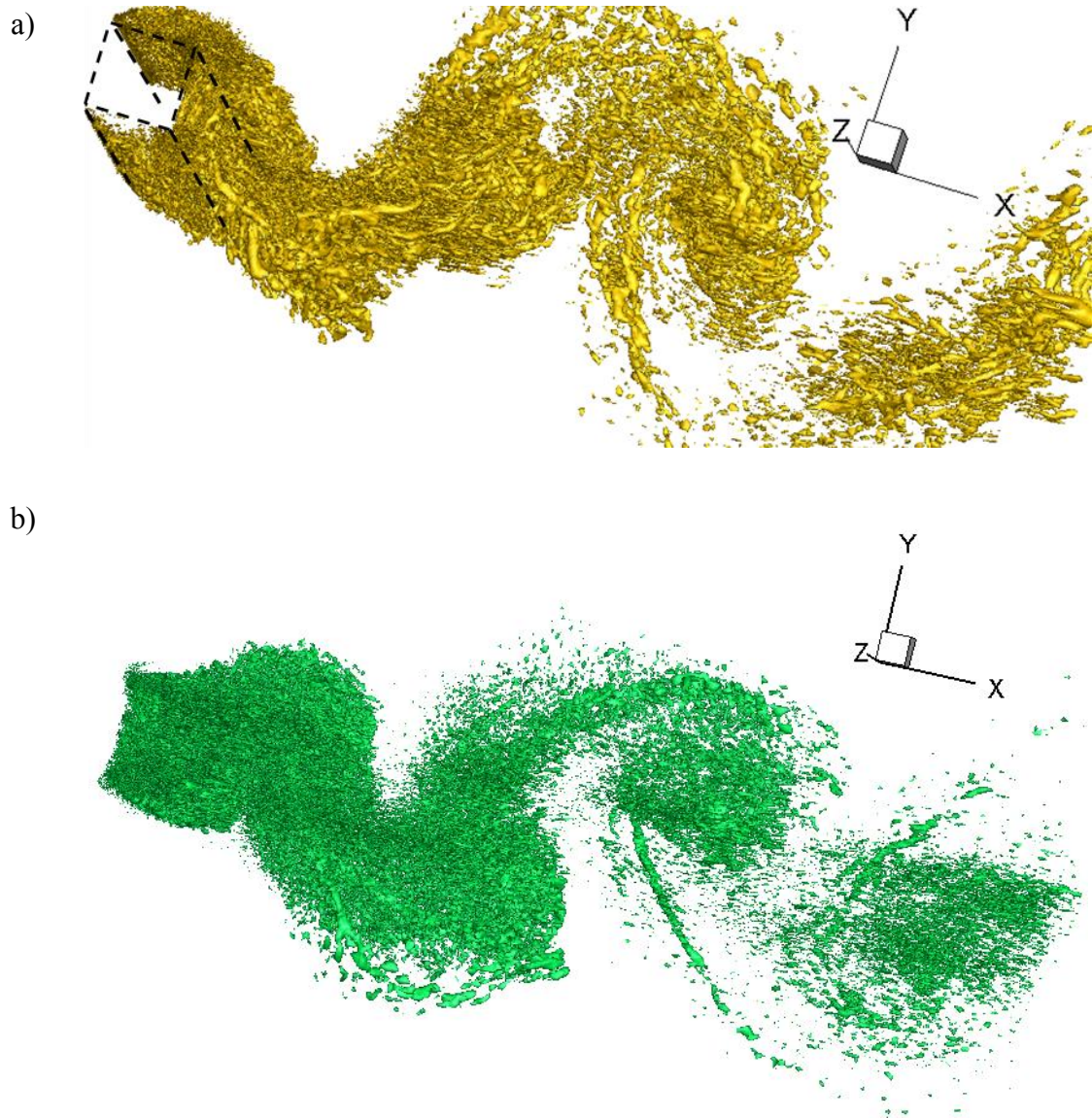
Figure 4.12 Visualization of 3D instantaneous vortical structures using the Q-criterion: a) square cylinder; b) vertical plate.
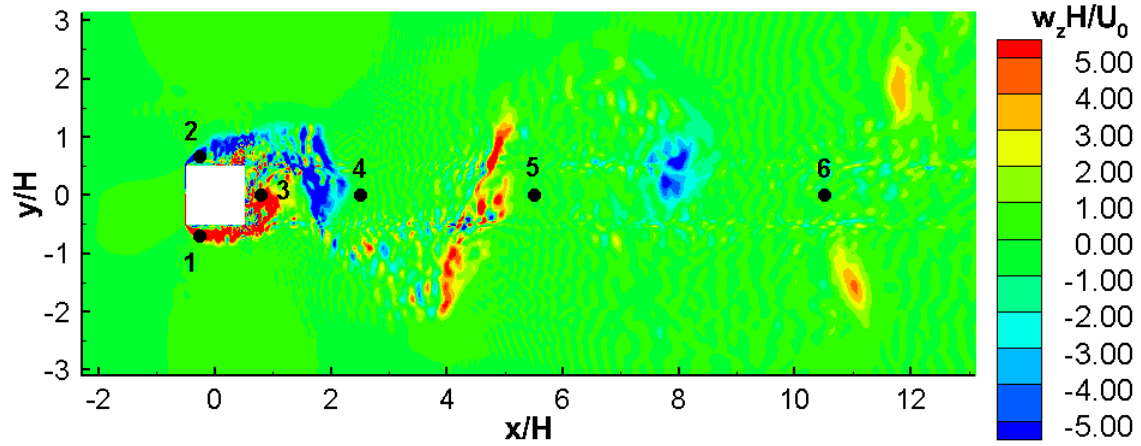
Figure 4.13 Locations of points used for spectral analysis of the flow past a square cylinder. Also shown is the instantaneous spanwise vorticity.
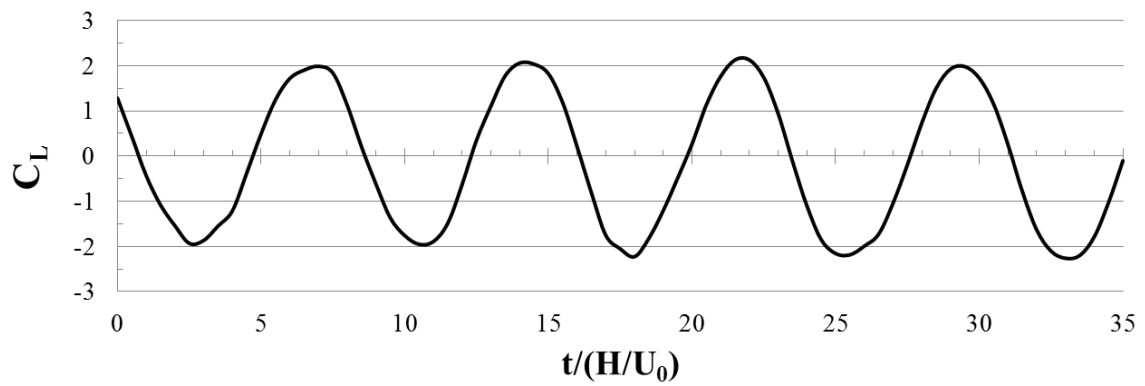
Figure 4.14 Time history of the lift coefficient for flow past a square cylinder.
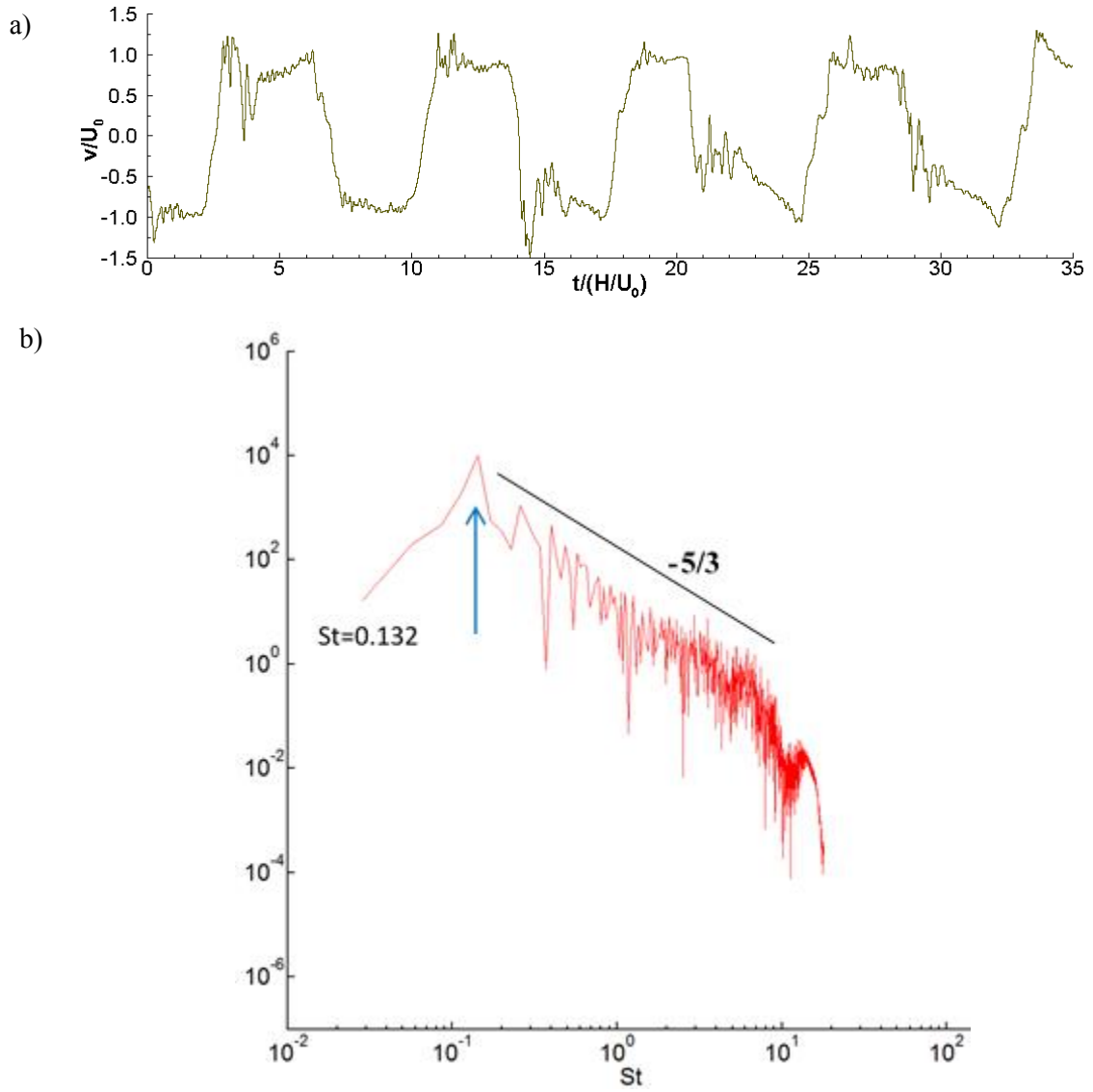
Figure 4.15 Time series (a) and power spectra (b) of vertical velocity at point 4 located in the near wake region (x=2.5H, y=0H, z=0H) of the square cylinder.
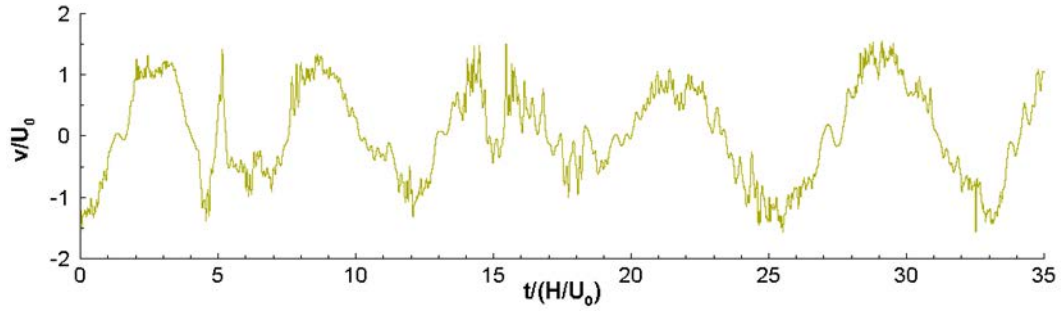
Figure 4.16 Time series of vertical velocity at point 4 located in the near wake region (x=2.5H, y=0H, z=0H) of the vertical plate.
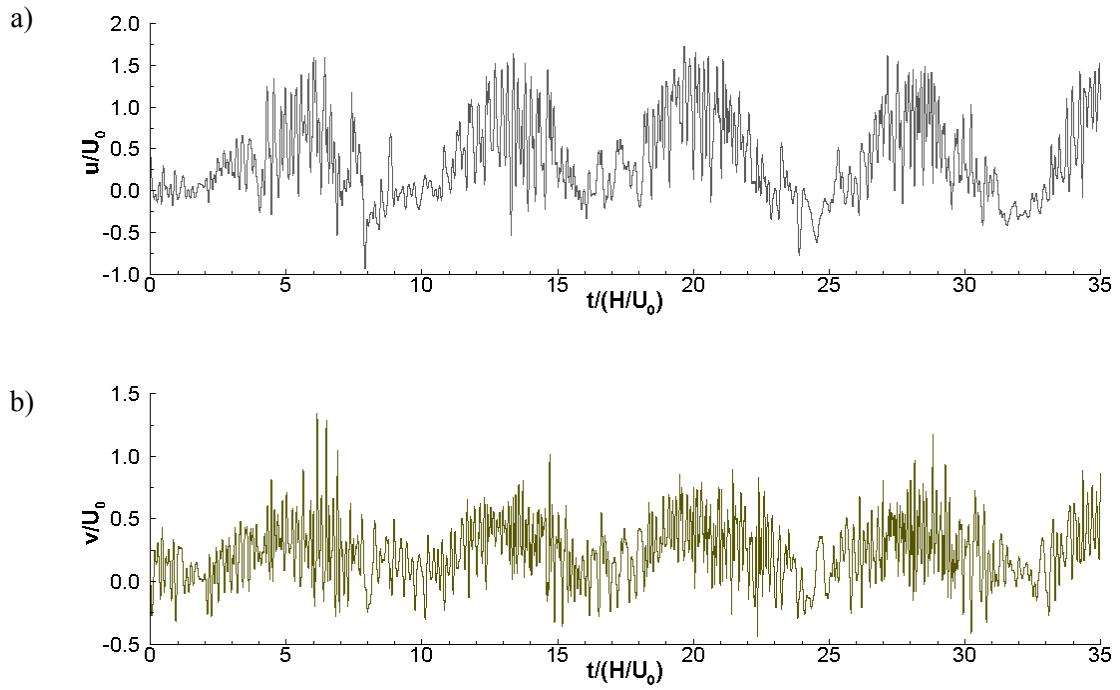
Figure 4.17 Time series of the streamwise velocity (a) and vertical velocity (b) at point 2 located in the upper shear layer (x=-0.27H, y=0.67H, z=0H) of the square cylinder case.
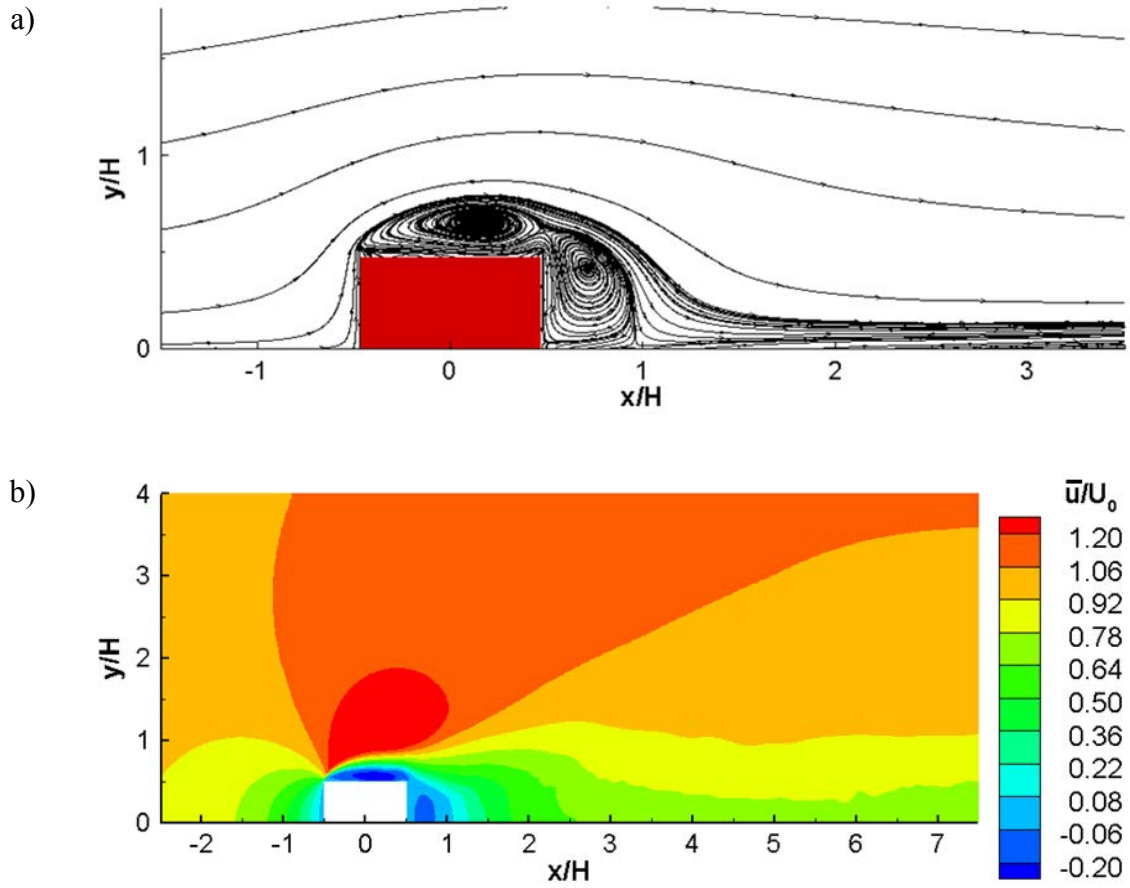
Figure 4.18 Visualization of the mean flow around the square cylinder: a) 2D stream lines superposed on spanwise vorticity; b) streamwise velocity.

a)

b)
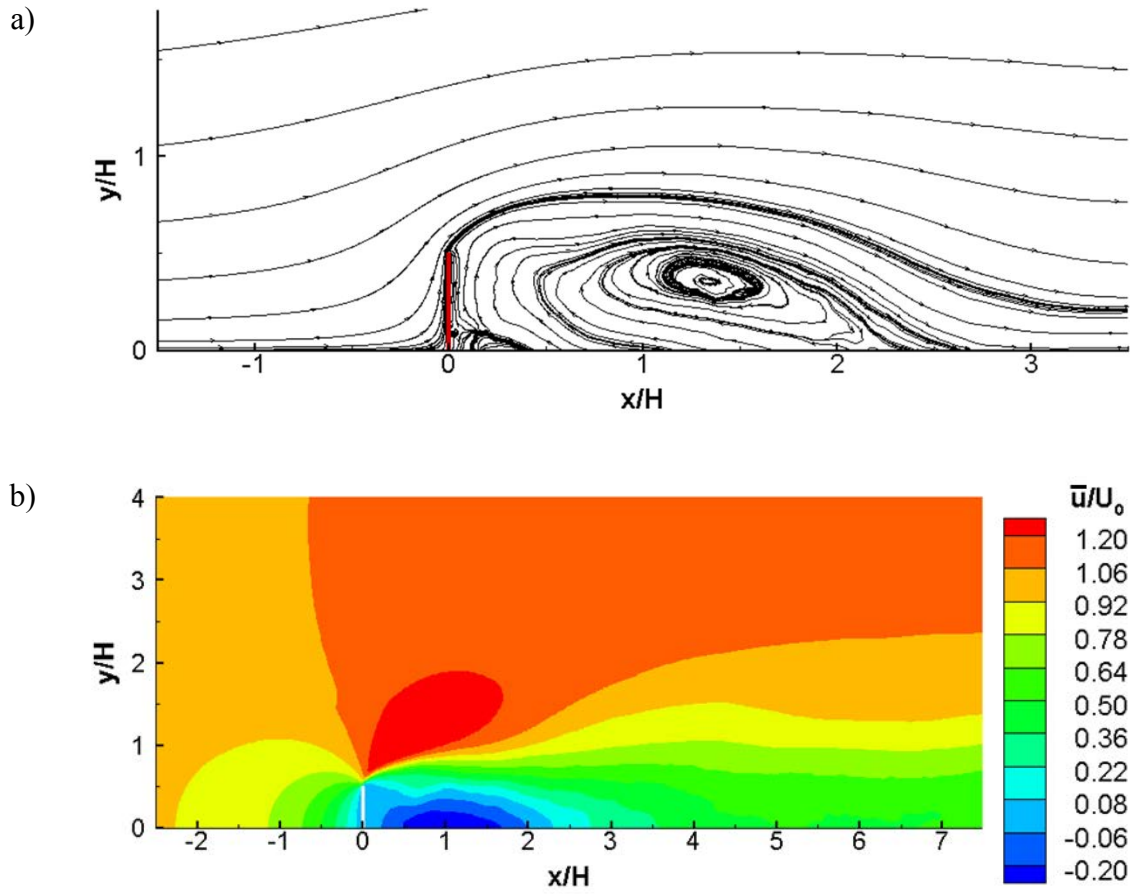
Figure 4.19 Visualization of the mean flow around the vertical plate: a) 2D stream lines superposed on spanwise vorticity; b) streamwise velocity.
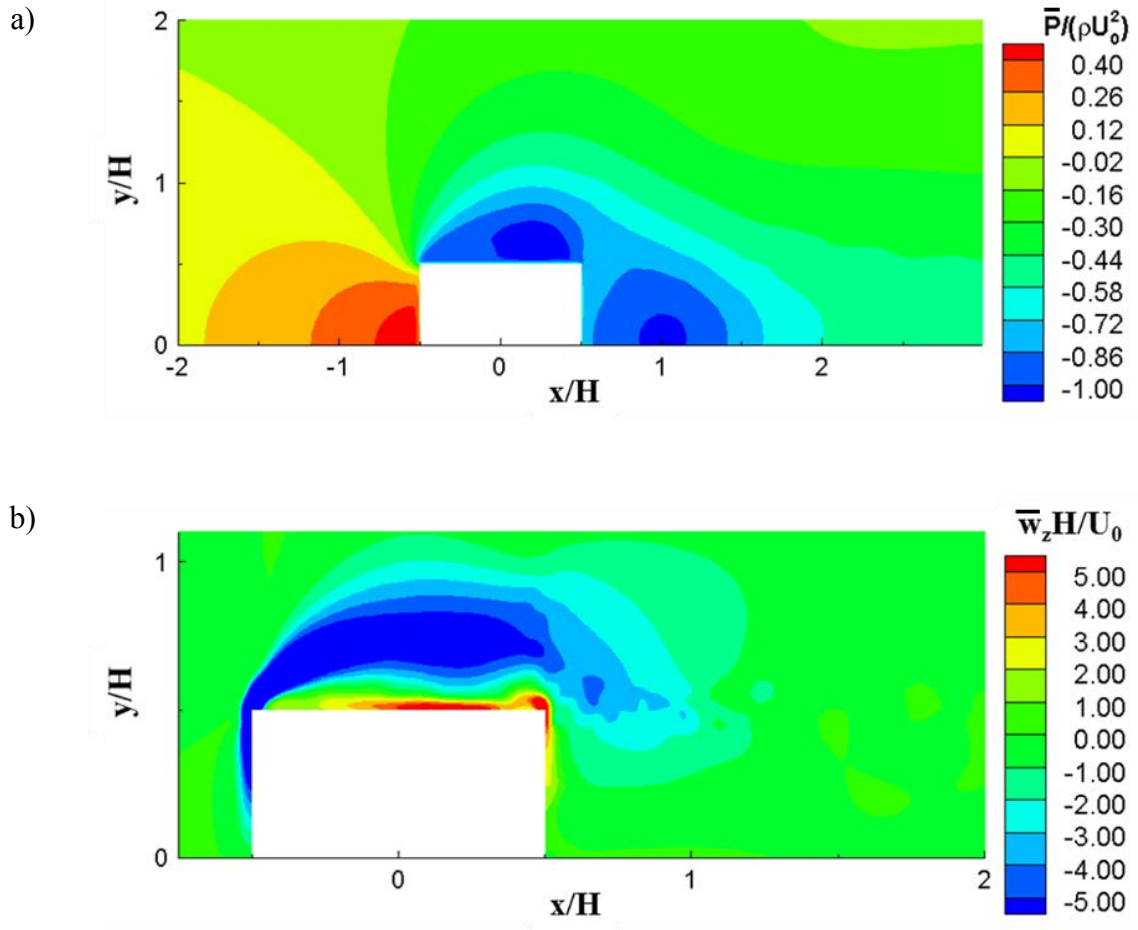
Figure 4.20 Visualization of the mean flow close to the square cylinder using: a) pressure contours; b) spanwise vorticity contours.

a)

b)
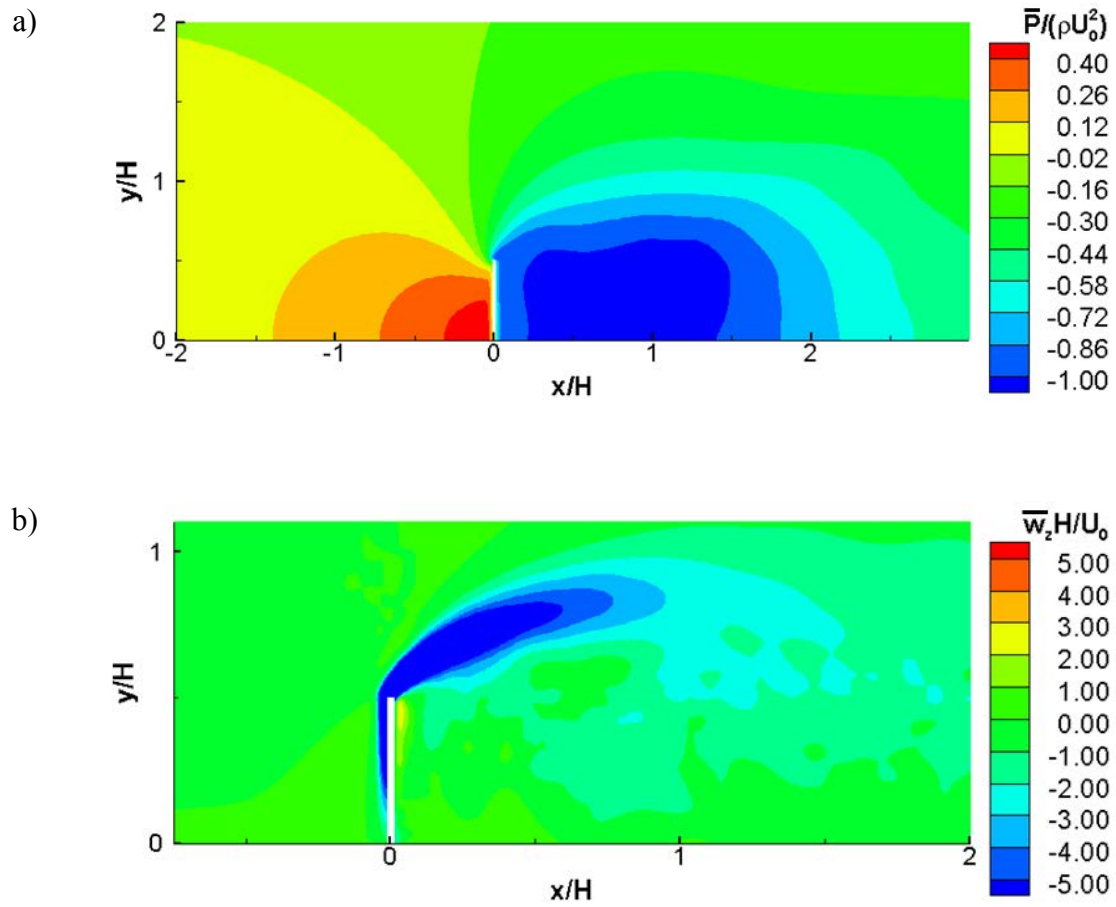
Figure 4.21 Visualization of the mean flow close to the vertical plate using: a) pressure contours; b) spanwise vorticity contours.
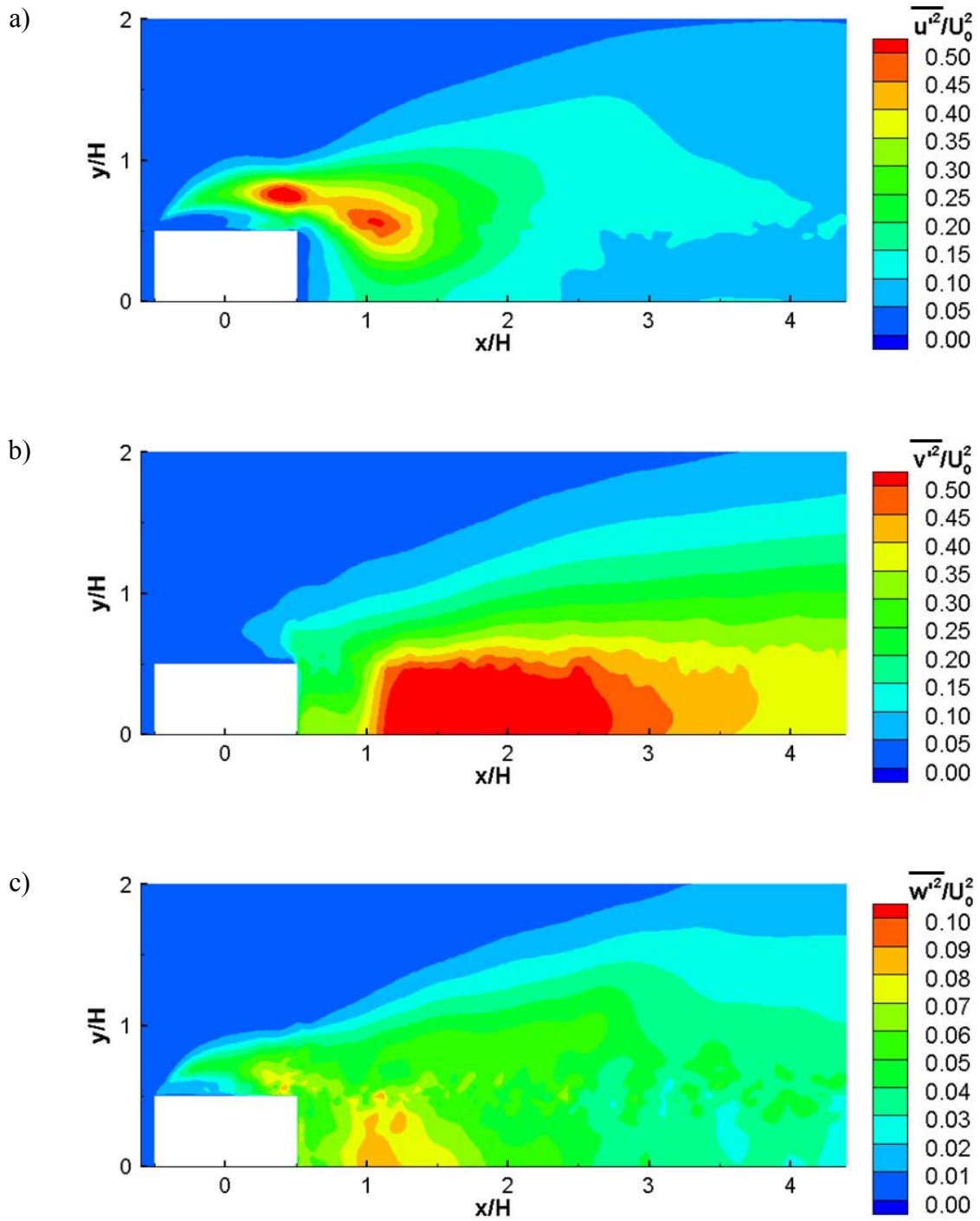
Figure 4.22 Visualization of the mean velocity fluctuations for flow past a square cylinder: a) mean streamwise velocity fluctuations; b) mean vertical velocity fluctuations; c) mean spanwise velocity fluctuations.
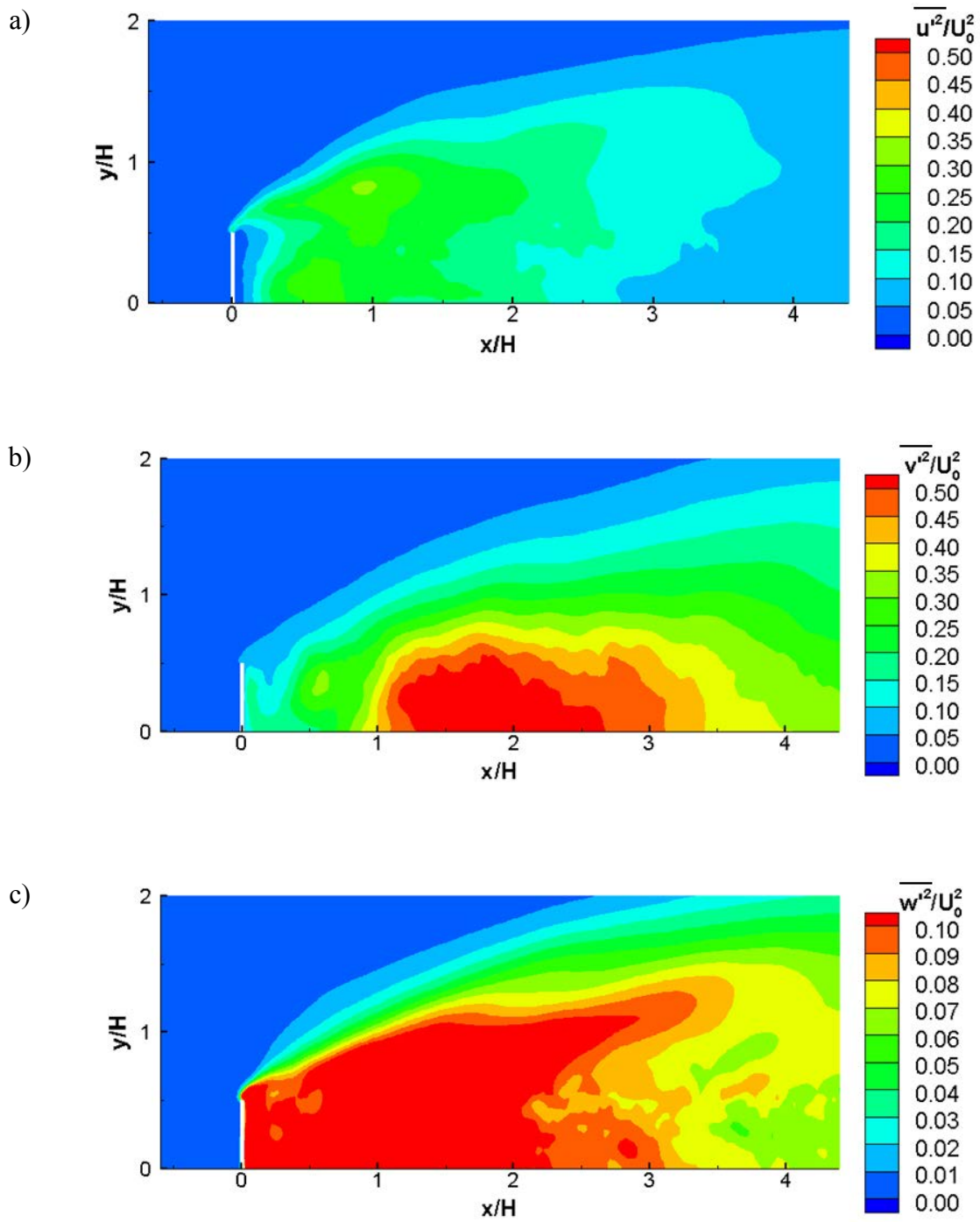
Figure 4.23 Visualization of the mean velocity fluctuations for flow past a vertical plate:
a) mean streamwise velocity fluctuations; b) mean vertical velocity fluctuations; c) mean
spanwise velocity fluctuations.
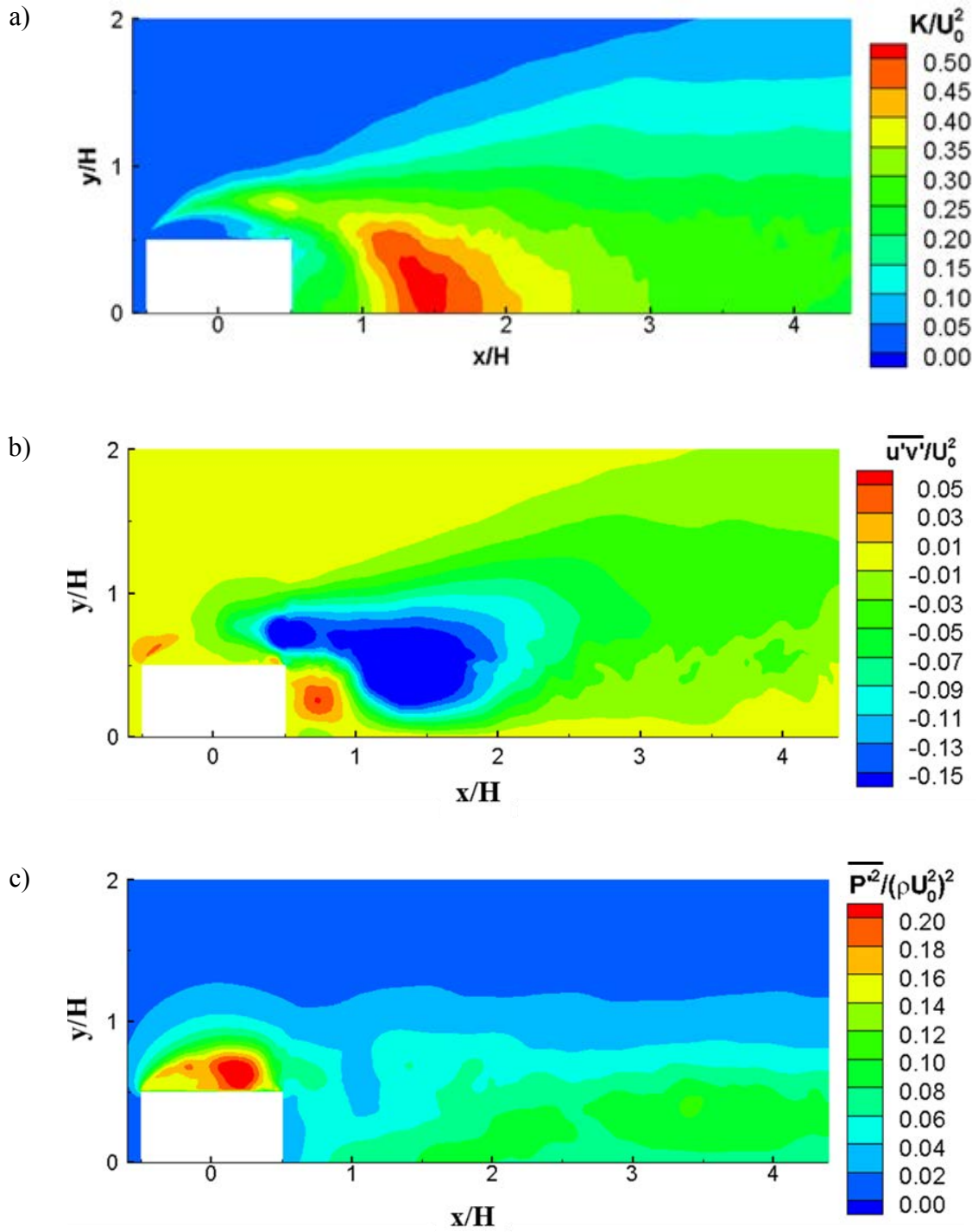
Figure 4.24 Nondimensional turbulence statistics for flow past a square cylinder: a) turbulent kinetic energy; b) primary Reynolds shear stress; c) mean pressure fluctuations.
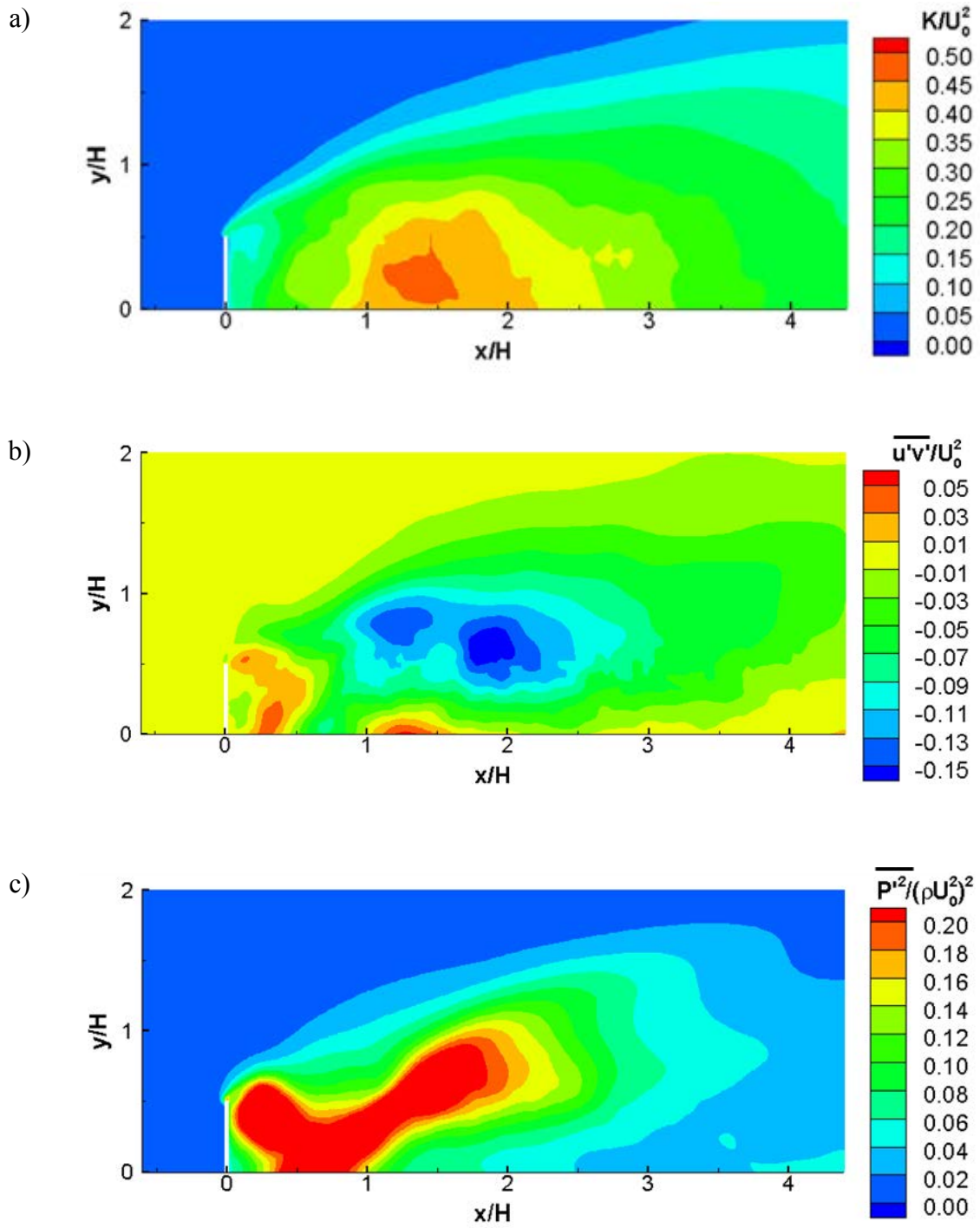
Figure 4.25 Nondimensional turbulence statistics for flow past a vertical plate: a)
turbulent kinetic energy; b) primary Reynolds shear stress; c) mean pressure fluctuations.
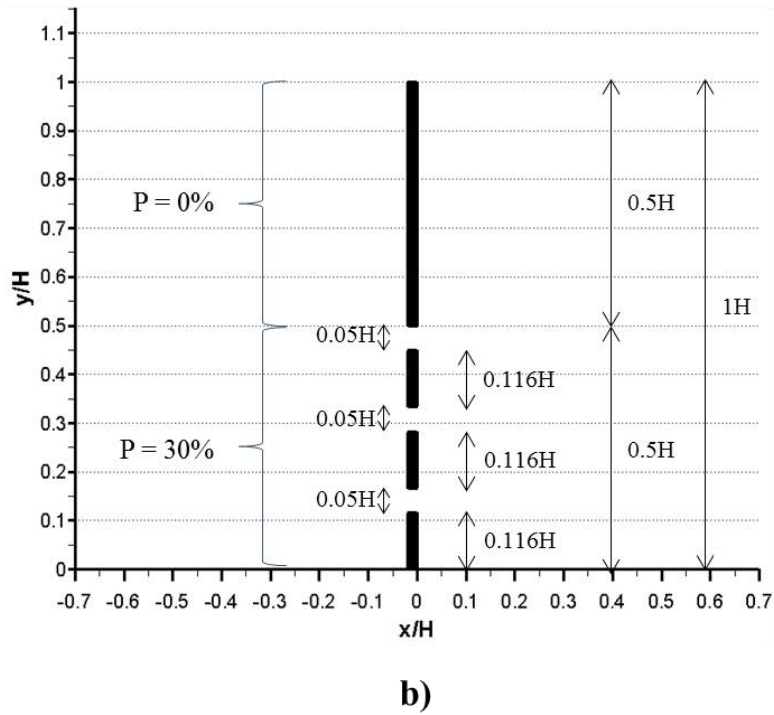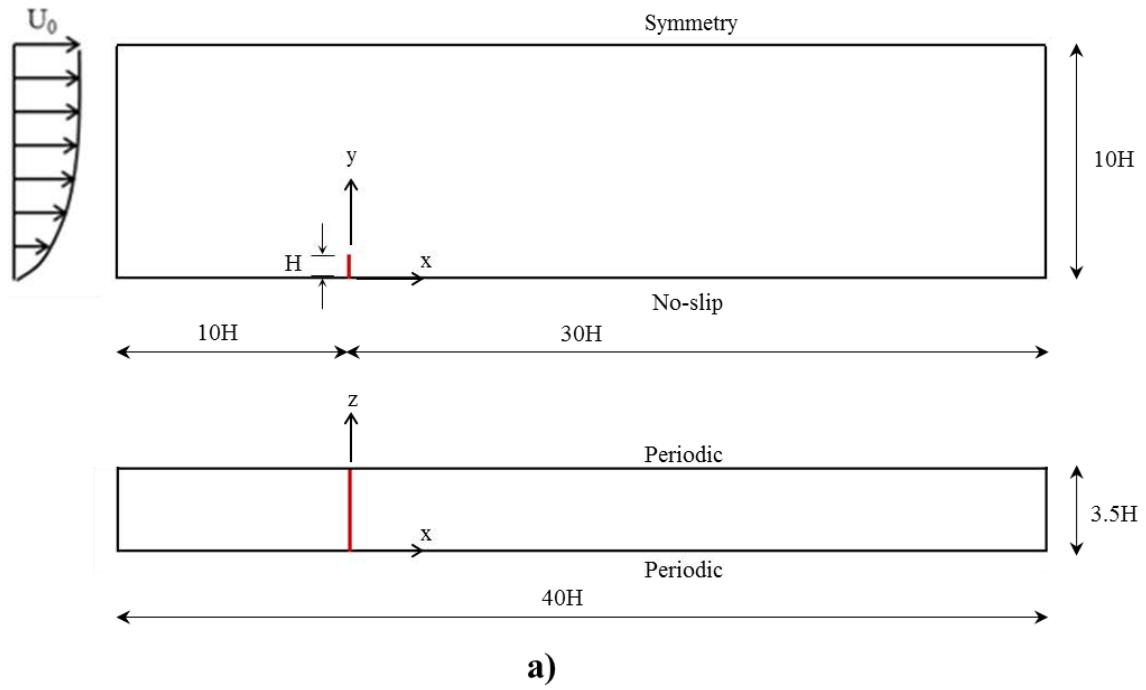
Figure 4.26 Computational domain (a) and main geometrical dimensions of the porous plate (b) used to simulate flow past a porous plate mounted on a flat bed.

a)

0.02H
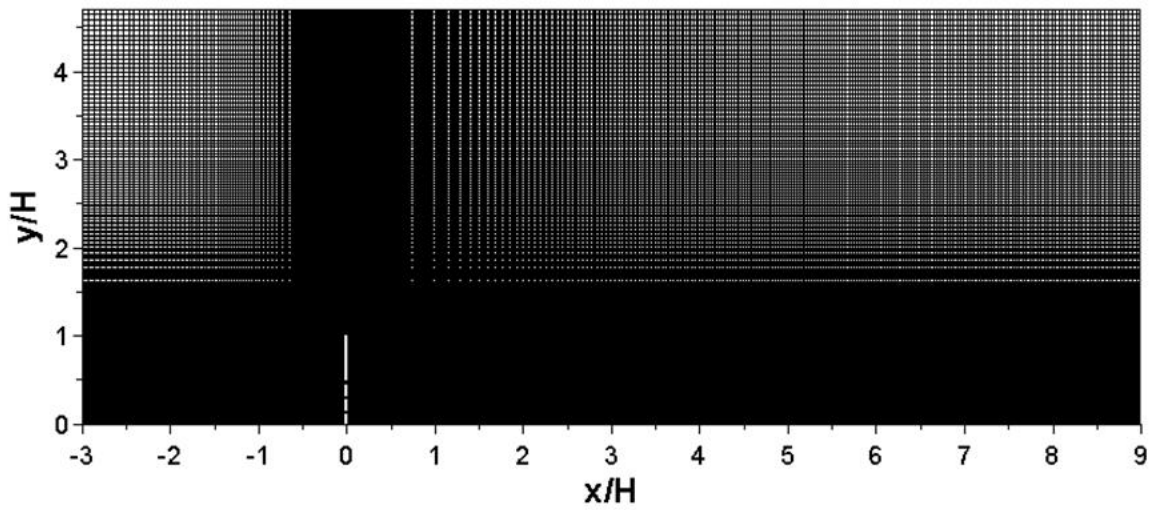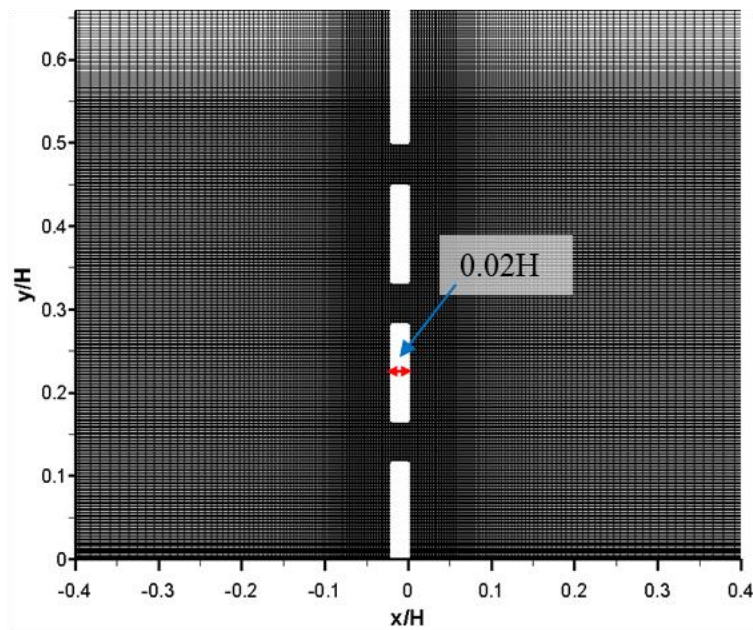
b)

Figure 4.27 View of computational domain and mesh used to simulate flow past a porous plate mounted on a flat bed. a) Mesh in a vertical x-y plane; b) Detail view of the mesh around the porous plate.
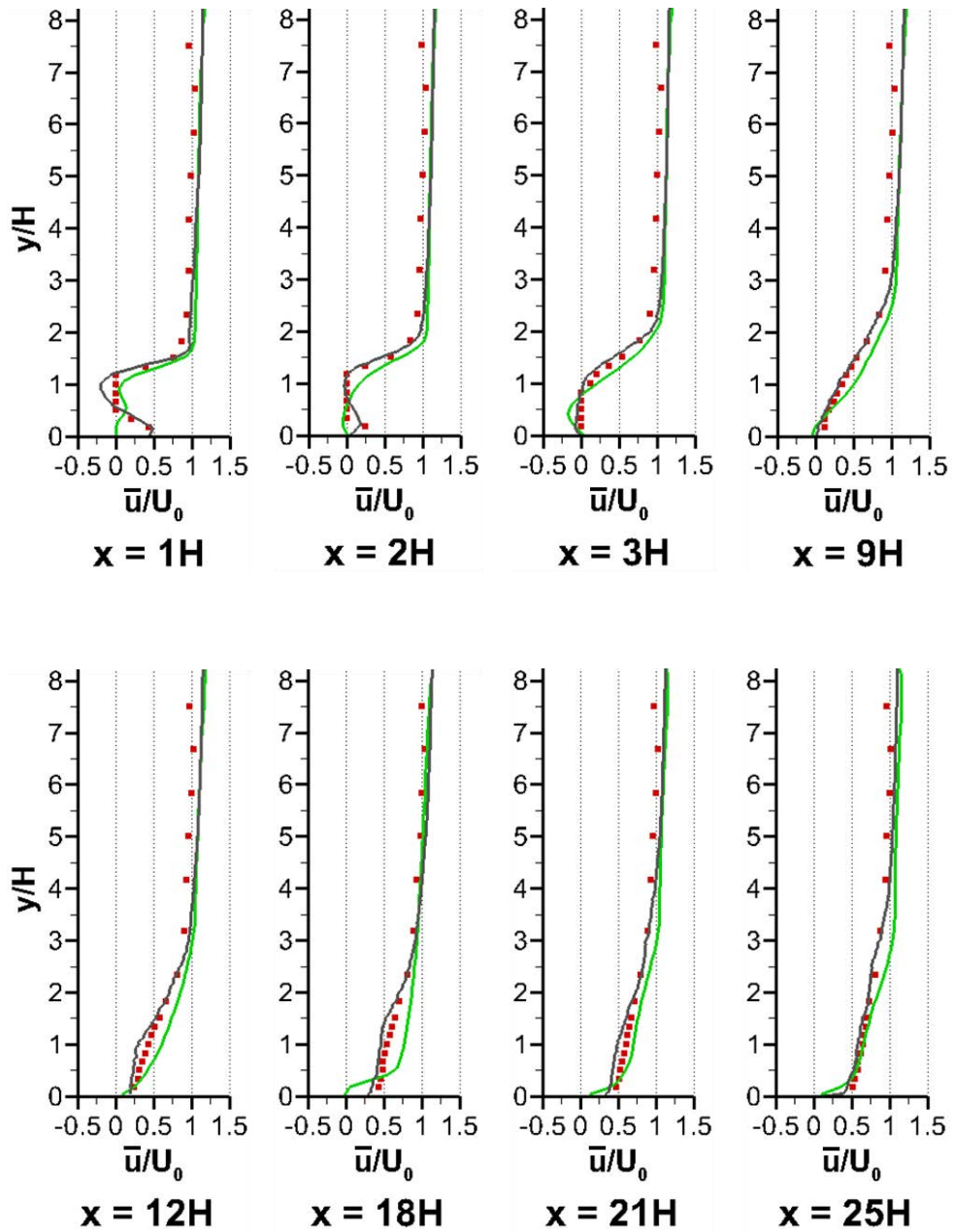
Figure 4.28 Time-averaged streamwise velocity profiles: (———) LES results, present study, (■) Experimental results of Huang et al. (2012) and (———) LES results of Huang et al. (2012).
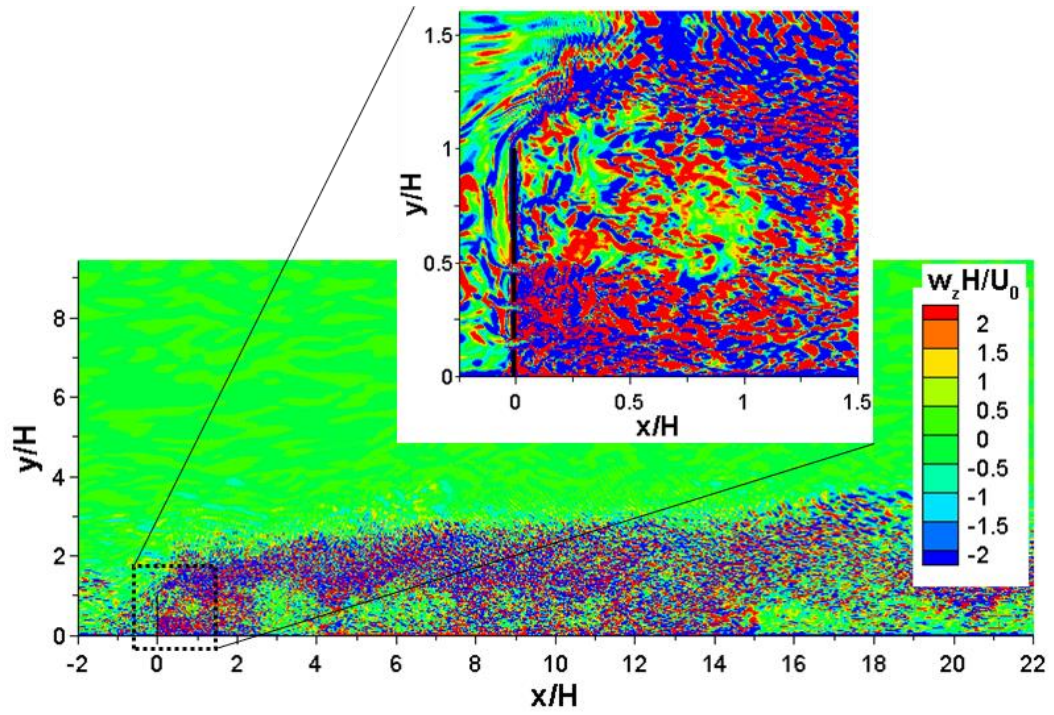
Figure 4.29 Visualization of the instantaneous flow past a porous plate mounted on a flat
bed using spanwise vorticity contours.

a)

b)
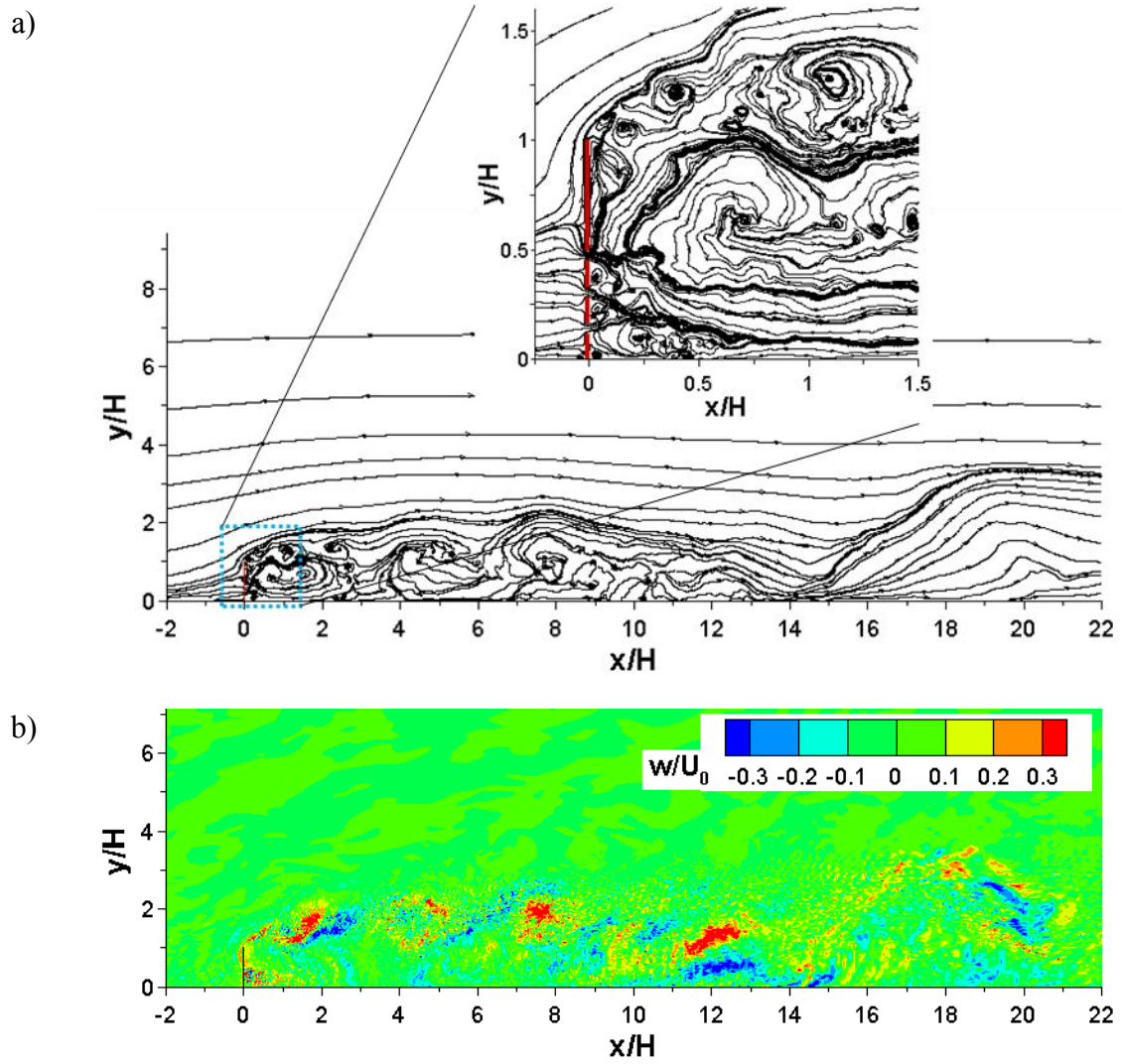
Figure 4.30 Visualization of the instantaneous flow past a porous plate mounted on a flat bed using: a) 2D stream lines; b) spanwise velocity.
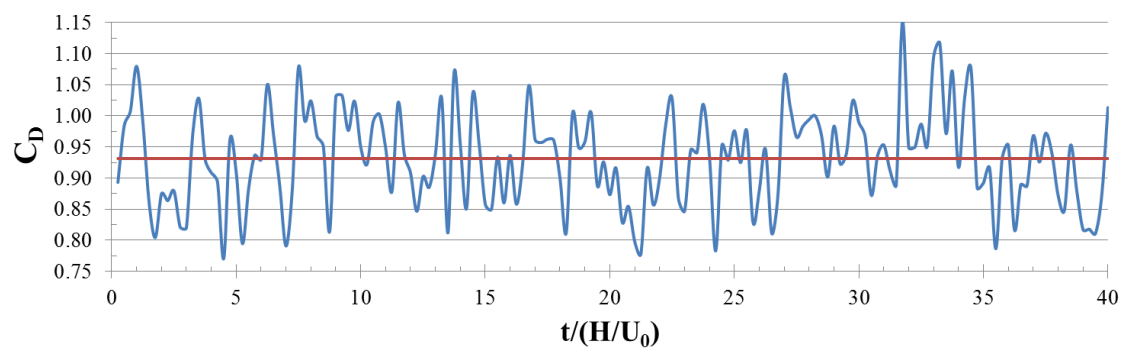
Figure 4.31 Time history of the drag coefficient for the porous plate.

112
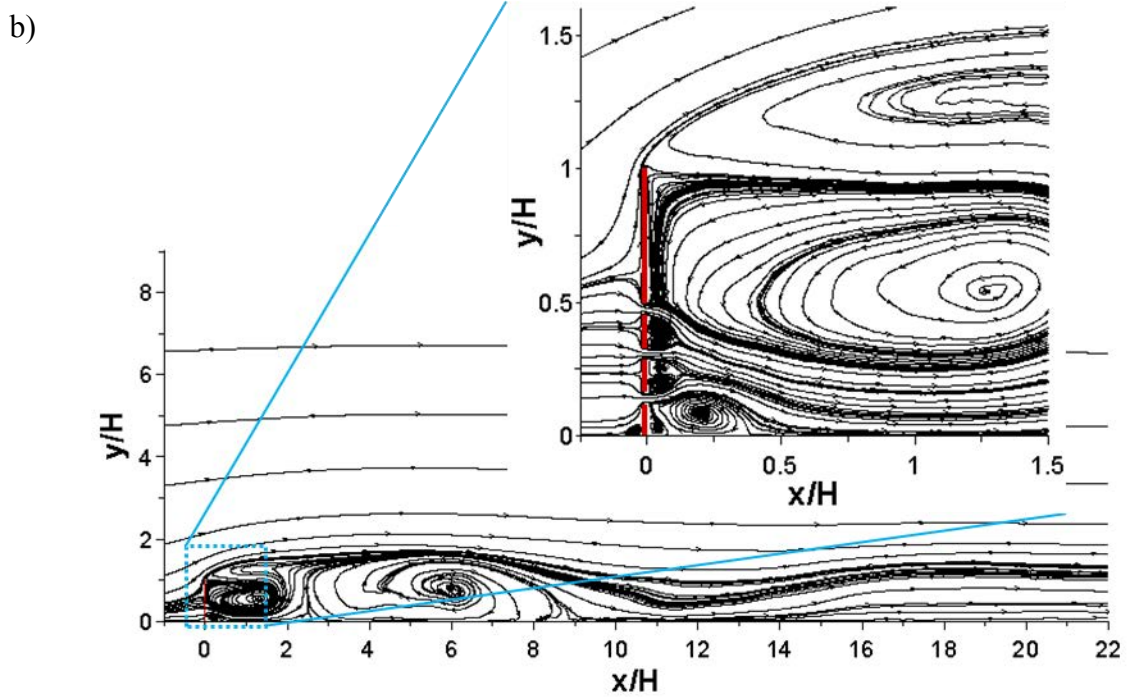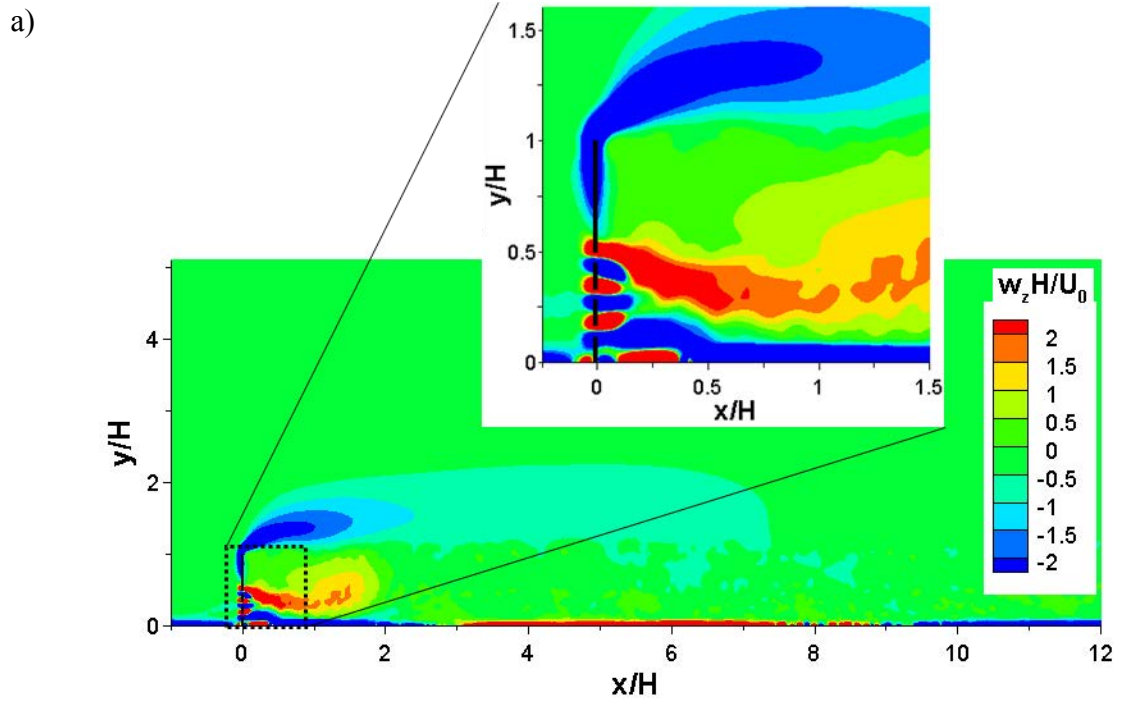
Figure 4.32 Visualization of the mean flow around the porous plate: a) spanwise vorticity; b) 2D streamline patterns.

a)

b)

c)
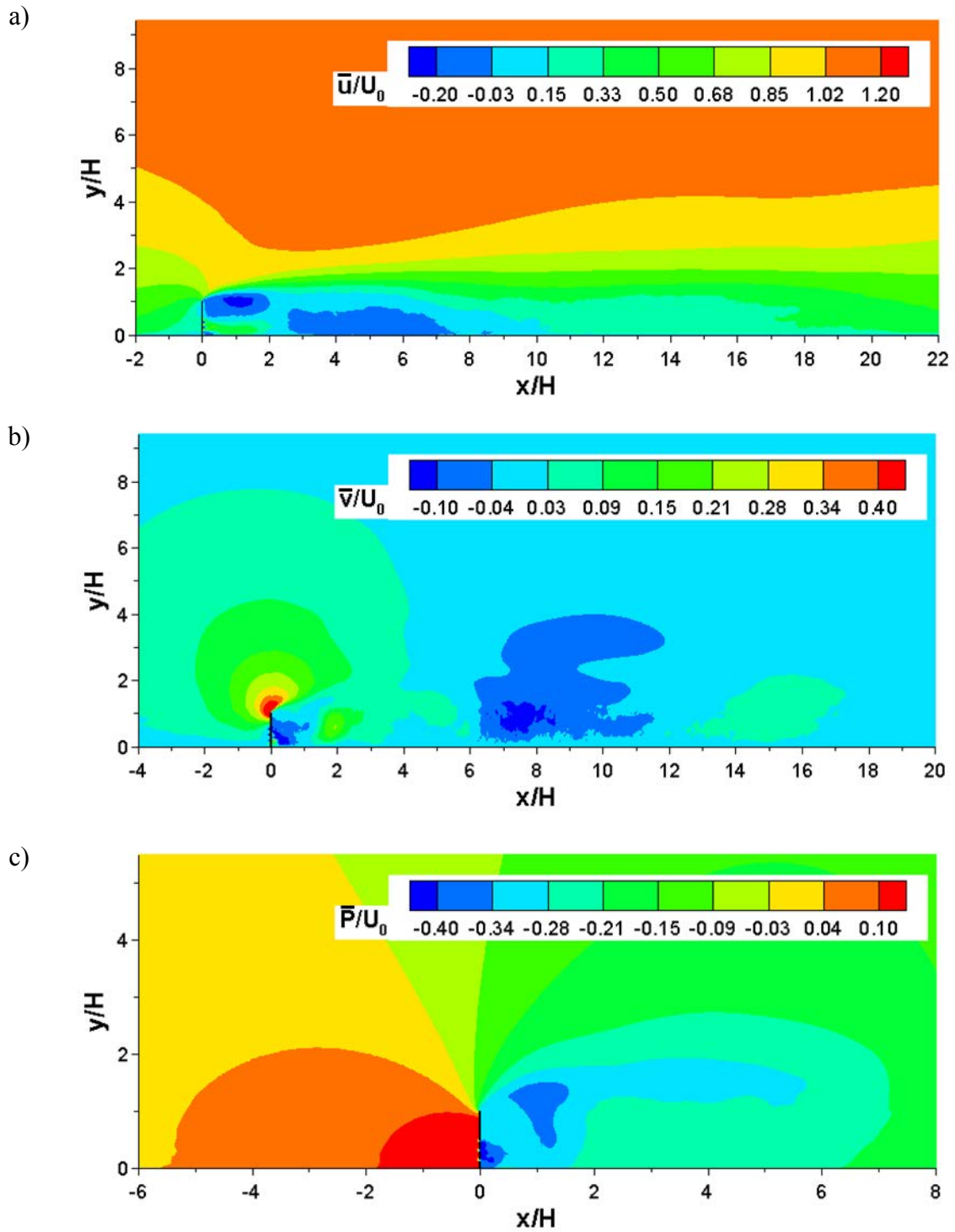
Figure 4.33 Visualization of the mean flow close to the vertical plate: a) streamwise velocity; b) vertical velocity; c) pressure.

114
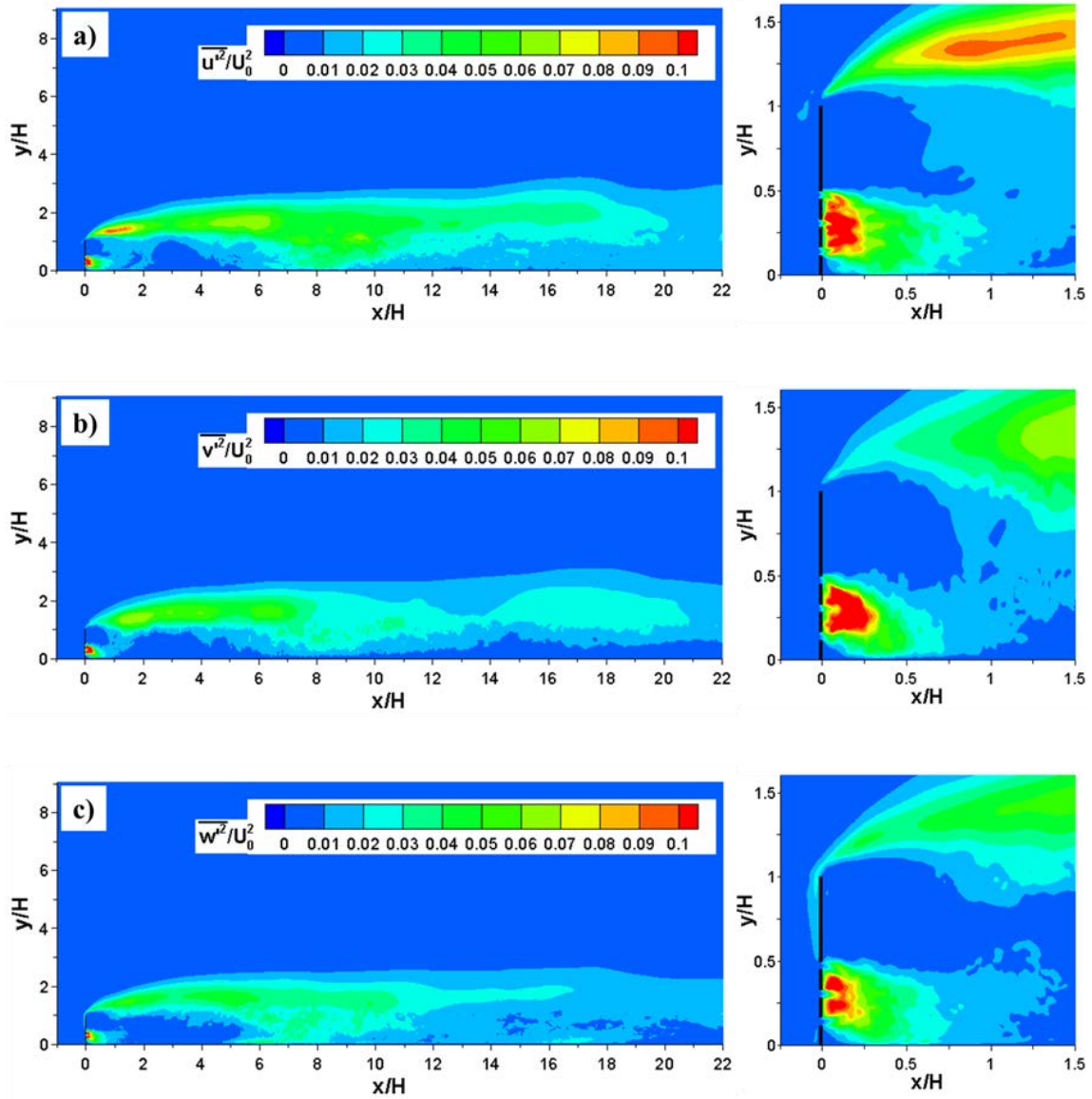
Figure 4.34 Visualization of the mean velocity fluctuations for flow past a porous plate mounted on a flat bed: a) mean streamwise velocity fluctuations; b) mean vertical velocity fluctuations; c) mean spanwise velocity fluctuations.
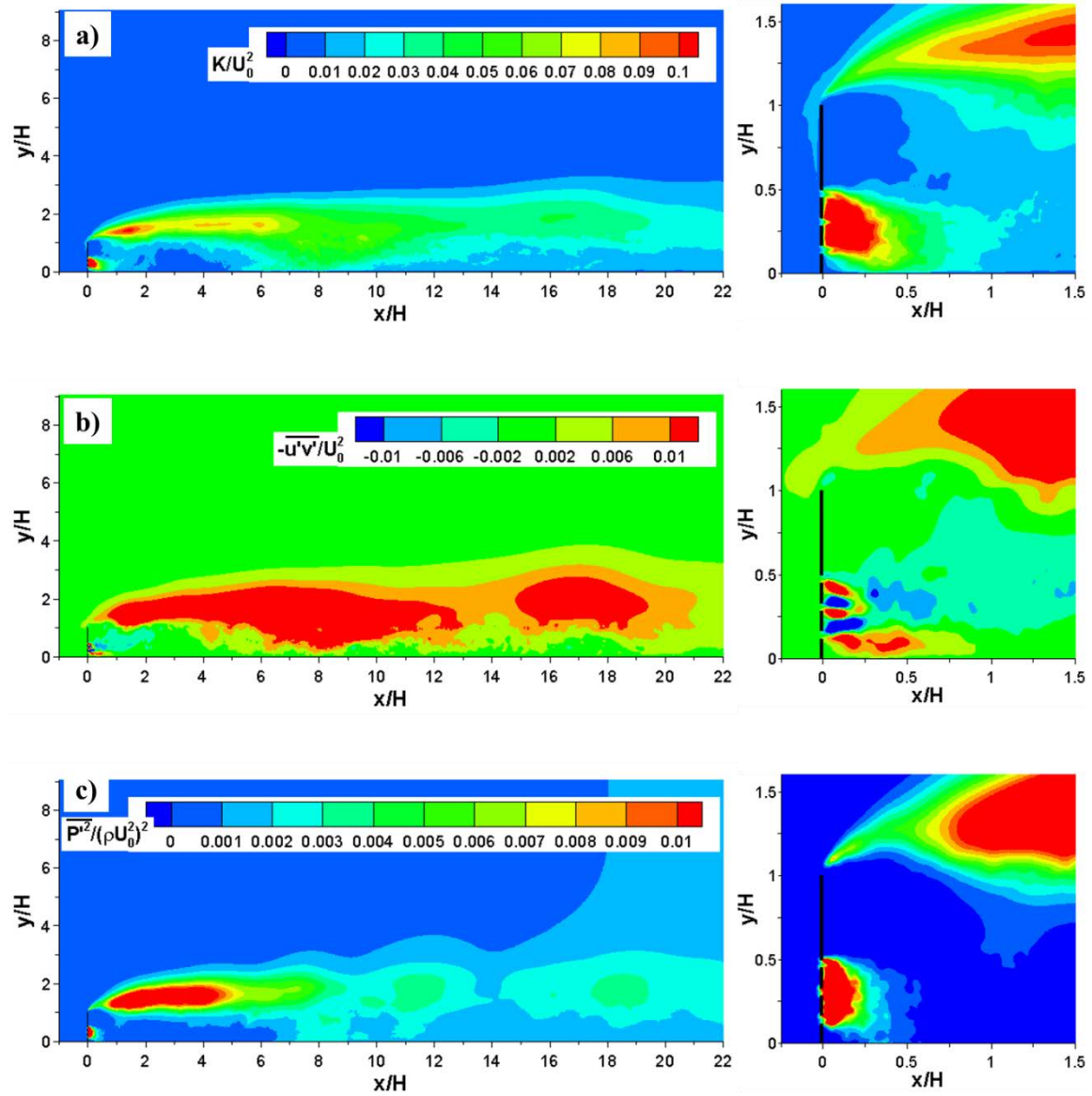
Figure 4.35 Nondimensional turbulence statistics for flow past a porous plate mounted on a flat bed: a) turbulent kinetic energy; b) primary Reynolds shear stress; c) mean pressure fluctuations.

Table 4.1 Flow past a 2D square cylinder. Experimental and LES predictions of the drag and lift coefficients, their rms values and the dominant frequency in the power spectrum of the lift coefficient.

Study	Re	$\overline{C_L}$	$C_L{}^{rms}$	$\overline{C_D}$	$C_D{}^{rms}$	St
Present computation	21,400	0.008	1.50	2.11	0.21	0.132
Lyn et al. (1995)	21,400			2.1		0.132
Wang and Vanka (1996)	21,400	0.04	1.29	2.03	0.18	0.13
Srinivas et al. (2006)	21,400	0.0	1.12	2.14	0.17	0.135
Noda and Nakayama (2003)	68,900		1.18	2.164	0.207	0.131
Durao et al. (1988)	14,000					0.138
Lee (1975)	17,600			2.05		0.122
Norberg (1993)	22,000			2.1		0.13
Bearman and Obasaju (1982)	22,000			2.1		

Table 4.2 Flow past a 2D vertical plate. LES and experimental predictions of the drag and lift coefficients, their rms values and the dominant frequency in the power spectrum of the lift coefficient.

Study	Re	$C_L{}^{rms}$	$\overline{C_D}$	$C_D{}^{rms}$	St
Present computation	21,400	0.93	2.17	0.24	0.142
Kiya and Matsumura (1987)	23,000				0.15
Fage and Johansen (1927)	n/a		2.13		0.146

Table 4.3 Flow past a porous plate mounted on a flat bed. LES predictions of the mean drag and its rms.

Study	Re	$\overline{C_D}$	$C_D{}^{rms}$
Present	41,000	0.93	0.08

117

CHAPTER 5 EFFECT OF VARYING POROSITY ON FLOW PAST A VERTICAL
PLATE

5.1 Introduction

The main objective of this chapter is to use LES to study the effect of varying porosity on

flow past a vertical plate placed on a horizontal and smooth channel bottom surface (zero

bottom gap case). Three simulations are performed with porosities of 0%, 20% and 36%.

A sketch of the (porous) vertical plate used in the three test cases is shown in the Figure

5.1a.

5.2 Simulation Setup

The computational domain used to perform the three 3D simulations is shown in

Figure 5.2a. As in the previously discussed simulations, the x-axis is aligned with the

incoming flow direction and the z-axis is aligned with the vertical direction relative to the

horizontal bottom surface of the channel. The plate height, H, is used as the length scale.

The uniform incoming flow velocity, U_0, is used as the velocity scale.

The Reynolds numbers was kept constant (Re=20,000) in the three simulations. The

thickness of the porous plate is 0.02H. The size of the opening between the solid elements

of the porous plate is d=0.04H for the two test cases where the plate is porous (P=20% and

36%). The (vertical) size of the solid elements is 0.13H for P=20% and 0.06H for P=36%

(see Figure 5.1b).

The length and the height of the computational domain are 35H and 10H

respectively. The plate is located at a distance of 10H from the inflow section. The

spanwise lengths of the computational domain and of the plate are 3.5H. The flow was

assumed to be periodic in the spanwise direction. The blockage ratio is 0.1.

A sample mesh in a streamwise-vertical (z=constant) x-y plane is shown in Figure 5.2b for the P=0% case. The mesh around each individual vertical plate is visualized in Figure 5.1b. The computational domain contains around 19 million grid points (768x384x64) in P=0% case and 25 million (768x512x64) grid points in P=20% and P=36% cases. Discretization along the x and z directions is the same for all cases. Only the discretization along the y axis is changed due to the need to resolve the flow near the edges of the solid elements of the porous plate. The mesh is uniform along the z direction. Grid points are clustered around the x=constant and y=constant locations corresponding to the edges of the solid elements of the plate (see Figure 5.2b) to resolve the attached boundary layers on these surfaces.

When generating the mesh, a minimum grid spacing ($n^+=u_\tau n/\nu$, n is the wall normal direction) of about 2 wall units (assuming $u_\tau/U_0=0.05$) was used in the wall normal direction near the solid surfaces of the vertical plate. This corresponds to a cell size of about 0.002H in the wall normal direction. Away from the plate, the average dimensions of the 3D cells are increased to about 0.07Hx0.06Hx0.05H.

The time step used in simulations was $0.001H/U_0$. The simulations were run for $70H/U_0$ time to eliminate the transients. Statistics were checked for convergence. Statistics were then collected over an additional $70H/U_0$. The full 3D velocity and pressure fields were saved at every $0.25H/U_0$. When calculating the mean flow and turbulence statistics, the averaging was performed over time and the spanwise direction, as the mean flow is 2D. The streamwise vorticity, ω_x, vertical vorticity, ω_y, spanwise vorticity, ω_z, total vorticity magnitude, ω_t, and the turbulent kinetic energy, K, were calculated using the following equations:

$$\omega_x = \frac{\partial w}{\partial y} - \frac{\partial v}{\partial z} \tag{5.1}$$

$$\omega_y = \frac{\partial u}{\partial z} - \frac{\partial w}{\partial x} \tag{5.2}$$

$$\omega_z = \frac{\partial v}{\partial x} - \frac{\partial u}{\partial y} \tag{5.3}$$

$$\omega_t = \sqrt{\omega_x{}^2 + \omega_y{}^2 + \omega_z{}^2} \tag{5.4}$$

$$K = \frac{1}{2}\left(\overline{u'^2} + \overline{v'^2} + \overline{w'^2}\right) \tag{5.5}$$

where u, v, w are the instantaneous velocity components in the streamwise, vertical and spanwise direction, respectively.

The distributions of the instantaneous velocity fields at the inflow section were obtained from a preliminary 3D LES (Re=25,000) of flow in a straight long channel of identical height in which periodic conditions were imposed in the streamwise direction for the velocity components. The channel bottom surface and all the solid surfaces of the porous plate were treated as no-slip. At the outflow, a convective boundary condition that allows the vortical structures to exit the domain in a time accurate way and without producing unphysical oscillations was used (Rodi et al., 2013). This is standard treatment of boundaries through which large scale turbulence is exiting the computational domain. A symmetry (shear-free slip) boundary condition was used at the top boundary. As the flow was assumed to be homogeneous in the spanwise direction, periodic boundary conditions were imposed on the lateral surfaces for all variables.

5.3 Flow Structure

5.3.1 Instantaneous Flow Fields

As the flow is homogeneous in the spanwise direction, the instantaneous flow structure will be analyzed based on the distribution of relevant variables in a streamwise-vertical x-y plane. Figure 5.3 and 5.4 compare the nondimensional distributions of the vorticity magnitude and the spanwise velocity for the P=0%, P=20% and P=36% cases.

In the case of a solid plate, the patches of vorticity advected over the upstream part of the SSL originating at the tip of the plate are stronger (e.g., larger and higher vorticity magnitude patches are observed in the P=0% case between the plate and x/H=10) due to the larger mean vertical shear across the SSL. This is due to the fact that all the incoming flow in the region with y<H is deflected laterally. As it passes the plate, the deflected flow is accelerated on the outer side of the SSL. As a result the turbulence production by mean shear inside the SSL is larger in the P=0 % case.

As the plate porosity is increased, part of the incoming flow penetrates the region behind the plate through the open spaces between the solid elements. This flow will be referred as the bleeding flow. As Table 5.2 shows, the discharge associated with the bleeding flow is increasing monotonically with the plate porosity. Thus, only the remaining part of the incoming flow is deflected laterally past the tip of the plate. Moreover, the size and strength of the flow within the main recirculation bubble decrease monotonically with the increase in the porosity. For the P=36% case, the recirculation bubble occupies only the near bed region behind the plate and the flow on the inner side of the SSL (side closer to the channel bed) is oriented in the streamwise direction. For these reasons, the mean shear across the SSL decreases with the increase in the porosity. This explains the decrease of the coherence of the eddies advected over the upstream part of the SSL as the plate

121

porosity is increased (Figure 5.3). The flow penetrating through the open spaces of the porous plate resembles an array of high speed jets. This explains the generation of patches of high vorticity magnitude behind the plate in the simulations in which the plate is porous.

Given that the mean flow is 2D, the distributions of the spanwise velocity in Figure 5.4 give an indication on the degree of flow three-dimensionality in the SSL and wake. Elongated patches of high positive and negative spanwise velocity are observed in all cases in the wake region. The velocity magnitude inside these patches is of the order of $0.3U_0$, which means that the spanwise transfer of momentum is significant. At most locations a patch of positive spanwise velocity is situated in the immediate vicinity of a patch of negative spanwise velocity. The inclination of these elongated patches with respect to the channel bed decreases as the patches are advected downstream. The streamwise distance from the plate where these patches are present increases with the increase in the plate porosity. For example, such patches are detected around x=2-4H in the P=0% case and around x=12-14H in the P=36% case. Thus, the degree of three dimensionality of the near wake flow decreases as the plate porosity increases. The average angle between these patches and the channel bed decreases with the increase in the plate porosity.

Time series of the velocity and pressure were collected at about 45 points in an x-y plane and at about 210 points in a y-z plane. The positions of the points where time series were collected in an x-y plane for each of three simulations are shown in Figure 5.5. Data were saved over $70H/U_0$ (flow was statistically steady) with a time step of $0.001H/U_0$. The time series at point 10 situated inside the SSL, close to the tip of the plate, and at point 28 situated in the SSL, at about 18H from the plate are compared in Figure 5.6 for the three cases. As expected, the time series at point 10 show the presence of high frequency

fluctuations associated with the formation of the first vortex tubes in the SSL. The time series at point 28 show the presence of a range of lower frequencies associated with the advection of large vertical billows present in the downstream part of the SSL, where the SSL penetrates until the channel bed.

Figures 5.7 to 5.9 show the power spectra of the vertical velocity component at points 10, 28 and 43 for the P=0%, P=20% and P=36% cases, respectively. Point 43 is situated inside the SSL at 22.5H behind the plate.

In the simulations where a recirculation bubble forms just behind the plate and extends up to the SSL (P=0% and P=20% cases, see also Figure 5.15), the power spectra at point 10 contains a range of energetic frequencies, 0.4<St<1.4 with two peak energetic frequencies corresponding to St=0.62 and St=0.85. These two frequencies correspond to the passage frequency of the largest billow vortices contained by the SSL close to the plate. For example, the spanwise vorticity fields in Figure 5.16 visualize the passage of such billow vortices at x/H=3. The period is close 1.15H, which corresponds to St=0.85. As the porosity increases, the energy associated with the two peak energetic frequencies decreases. In the simulation where only a small recirculation bubble forms just behind the fence and the bubble is situated near the channel bed (see also Figure 5.15), the velocity power spectra at point 10 contain a narrower range of energetic frequencies (0.6<St<1) and only one peak frequency (St=0.75). This suggests that the formation of the larger vortical eddies within the upstream part of the SSL is more regular in the higher porosity cases.

As they move away from the plate, the vortical eddies grow in size and at a certain point start interacting with the bed. In the P=0% and P=20% cases where a large recirculation bubble of height comparable to that of the fence forms just behind it, strong

interactions between some of these eddies and the channel bed are observed at the end of the recirculation bubble, around the location where the mean flow reattaches to the bed (e.g., x/H=16 for P=0% and x/H=13 for P=20%). While some of the large eddies pass past the reattachment location with minimal disturbance, the ones having a stronger vertical momentum collapse on the channel bed. As a result some of the vorticity associated with this eddy is entrained into the recirculation bubble and advected upstream toward the SSL. This process results in strong disturbances of the eddies advected in the SSL before the flow reattaches. As some of this additional vorticity merges with an eddy advected in the SSL, a strong increase in the coherence of this eddy is observed. One should also mention that in the P=20% case, some eddies interact first with the bed around x/H=13 and then again around x/H=16.

As shown by the velocity power spectra at points 28 and 43 in Figures 5.7, 5.8 and 5.9, the dominant frequency associated with the passage of the largest billows contained in the SSL shows a non-monotonic variation with the plate porosity. This frequency is close to St=0.08 for the P=0% case. Figure 5.11 illustrates the passage of a large eddy inside the SSL over the x=18H location. The period of passage is close to $12H/U_0$, that corresponds to St=0.08. The same process is illustrated in Figure 5.12 for the P=36% case in which the period of passage is close to $11H/U_0$ at x=18H. This corresponds to a slightly higher Strouhal number (St=0.095). Interestingly, the Strouhal number associated with the passage of eddies in the downstream part of the SSL (St=0.065) is smaller for the P=20% case. Still, velocity power spectra for the P=20% case show a clear peak at St=0.09 at x=9H. It is not clear why this decrease in the average frequency of passage of the large vertical eddies is related to the multiple interactions of these billows with the bed, which

in some cases result in a loss of coherence of such an eddy. Another interesting observation is that the energy associated with the dominant frequency of the passage of the large eddies in the downstream part of the SSL decreases significantly once the bleeding flow through the plate is strong enough to impede the formation of a large recirculating bubble behind it. For example, the energy of the most energetic mode at points 28 and 43 decayed by close to three time as the plate porosity was increased from 0% to 36% (Figures 5.7, 5.9).

Figure 5.13 presents the time history of the streamwise drag coefficient for the plate, C_D, in the three simulations. As the plate porosity is increased above levels where a large recirculation region forms immediately behind the fence, the energy of the higher frequency components increases. When a large recirculation eddy is present behind the plate, low frequency oscillations are present. It is highly possible these oscillations in the streamwise drag force are induced when parts of a large billow collapses on the channel bed in the region where the flow reattaches and part of the billow is injected into the recirculation bubble and from there advected toward the fence. As it reaches the fence, the streamwise force acting on the fence is expected to decay.

As expected, the mean (time-averaged) drag coefficient, $\overline{C_D}$, is decreasing monotonically as the plate porosity is increased (e.g., from 0.78 for P=0% to 0.56 for P=36%, see Table 5.2). This is because, the adverse pressure gradients induced by the plate is decreasing with increasing porosity due to the bleeding flow through the plate. Despite the differences observed in the range of dominant frequencies of C_D, the rms of the drag coefficient fluctuations is increasing with increasing plate porosity (Table 5.2). The rate of increase decreases significantly for P>20%.

5.3.2 Mean Flow and Turbulence Statistics

In all three simulations, the mean flow past the plate contains one or multiple separation bubbles. The main difference in the wake flow structure occurs around plates with a porosity close to 30%. For P<30%, a large separation bubble extending from the bed to the SSL forms. Close to the fence, the separation bubble touches part of the upper part of the fence. For plates with a very low porosity, a smaller recirculation bubble forms in between the main recirculation bubble, the channel bed and the lower part of the fence (e.g., this is the case of a solid plate, P=0% case). As the plate porosity increases, the size of the secondary bubble decreases rapidly because of the bleeding flow penetrating through the fence. The secondary bubble is absent in the P=20% case. In the mean flow, part of the bleeding flow is advected into the SSL, while the remaining part is advected toward the channel bed and from there into the main recirculation bubble. The sketch in Figure 5.14a shows the relative positions of the two recirculation eddies. The length and height of the primary and secondary recirculation bubbles are denoted l_1, h_1 and l_2, h_2, respectively. Their dimensions are given in Table 5.2. The length and height of the main recirculation bubble are decreasing monotonically with the increase in the plate porosity.

For P>30%, the topology of the mean flow is different. The main separation bubble moves away from the fence (e.g., it extends between x=8.5H and x=13H in the P=36% case). Its length and height are smaller compared to cases when the main recirculation bubble is in contact with the plate (Table 5.2). A small separation bubble can still form right behind the plate but this separation bubble is short and its vertical extent represents a small fraction of the fence height. Its height and length are denoted h_3 and l_3 in Figure 5.14b and in Table 5.2.

The distribution of the spanwise vorticity in the mean flow (Figure 5.16) shows that the strength of the upstream part of the SSL and its angle with the streamwise direction are decaying with increasing plate porosity. This is because of the fraction of the incoming flow deflected laterally and the angle of the deflected flow as it passes the plate decay with the increase in the plate porosity. Interestingly, over the downstream part of the SSL (x/H>4), the largest values of the spanwise vorticity are observed for the P=20% case rather than the P=0% case, as one might expect (e.g., see comparison at x/H=12 in Figure 5.16). This is because for a certain range of plate porosities, the flow pattern in the vicinity of the fence is such that a large number of the turbulent eddies associated with the jets forming through the fence openings are advected toward the SSL. Due to the bleeding flow, some of these eddies merge with the large vortical billows advected in the SSL. This is a mechanism that leads to the increase in the coherence of the vortical billows away from the formation region which is not present in the case of a solid plate or in cases when the plate porosity is very low. For very high plate porosities, the deflection of the bleeding flow toward the SSL is very small, so this mechanism for the amplification of the vorticity of the large eddies advected within the SSL does not play an important role. This is because the coherence of the vortical eddies generated by the jets is mostly lost before these eddies get close to the SSL.

The distributions of the mean velocity fluctuations in the three directions (Figures 5.17, 5.18, 5.19) and of the TKE (Figure 5.20) show that the level of amplification of the turbulence inside the SSL decays monotonically with the increase of the plate porosity. This is true for both the upstream and for downstream part of the SSL, after the region of turbulence amplification inside the SSL extends until very close to the channel bed. For

example, comparison of the vertical profiles of the TKE at x=2H in Figure 5.20 show that the peak TKE decreases from $0.042U_0^2$ to $0.027U_0^2$ and to $0.025U_0^2$ as the plate porosity increases from 0% to 20% and then to 36%. As the plate porosity increases, the location where the SSL starts interacting with the bed surface moves away from the plate. For example, based on the distributions of $\overline{u'^2}/U_0^2$ and TKE, this happens at x=4H for P=0%, at x=8H for P=20% and at x=11H for P=36%. Over the downstream part of the SSL, the levels of TKE amplification also decrease with the increase in the plate porosity. For example, the vertical profiles of the TKE at x=12H in Figure 5.20 show that the peak TKE decreases from $0.045U_0^2$ to $0.03U_0^2$ and to $0.019U_0^2$ as the plate porosity increases from 0% to 20% and then to 36%.

Though the mean streamwise velocity fluctuations, $\overline{u'^2}/U_0^2$, are the largest contributor to the TKE inside the SSL, the contributions of the other two components are also significant. This is especially the case for the downstream part of the SSL where the spanwise transport driven by patches of high and low spanwise velocity magnitude increase the degree of three dimensionality of the flow. For all cases, the contributions of the spanwise and vertical components of the mean velocity fluctuations to the TKE are roughly equal. For very high plate porosities, the spanwise component is slightly larger than the vertical component, especially over the downstream part of the SSL.

Besides the SSL, for cases with P>0%, the mean velocity fluctuations are also strongly amplified close to the porous plate due to the turbulence generated by the jets forming as fluid is penetrating through porous plate. However, even for relatively high plate porosities, the streamwise extent of this region is limited (e.g., less than 1H for P=36%).

The largest amplification of the nondimensional mean pressure fluctuations in Figure 5.21 occurs in the downstream part of the SSL, downstream of the location where the region of high mean velocity fluctuations reaches the channel bed. By comparison, the passage of the vortex tubes inside the upstream part of the SSL results in a much smaller level of amplification of the mean pressure fluctuations.

LES has the advantage that it can provide information on the distribution of the friction velocity on the channel bed that is difficult to evaluate from experiments. Knowledge of these distributions allows determination of the spatial extent of the region where the bed friction velocity is affected by the presence of the plate. The value of u_τ/U_0 in the fully developed incoming flow is close to 0.04, consistent with values of the friction coefficient estimated from the Moody diagram at the channel Reynolds number.

It is only for P=0% that u_τ/U_0 approaches this value inside the wake region. This happens around x=10H beneath the main recirculation region. As expected, u_τ/U_0 goes to zero in the region where the near-bed flow changes directions (e.g., at the upstream and downstream boundary of a recirculation eddy that touches the channel bed). As the plate porosity increases, a region of relatively large u_τ/U_0 forms just behind the plate due to part of the bleeding flow that is advected near the channel bed. Downstream of the main recirculation bubble the bed friction velocity starts increasing in a non-monotonic fashion. The rate of increase decreases with the increase in the plate porosity.

5.4 Conclusions

Several 3D LES of flow past a 2D porous vertical plate with a zero bottom gap have been performed at a moderate cylinder Reynolds number (Re=20,000) to study the effects of plate porosity on flow and turbulence structure. The plate porosity was varied between

0% (solid plate) and 36%. The plate porosity was increased by increasing the number of the solid elements of the porous plate, while decreasing their height. The spacing between the solid elements was kept constant (0.04H).

As expected, the mean drag coefficient associated with the streamwise force acting on the plate was found to decay with the increase in the plate porosity because of the increasing bleeding flow that is advected through the porous plate. Meanwhile, the rms of the drag coefficient fluctuations was found to increase with the plate porosity especially for $P \leq 20\%$.

A major change in the mean flow pattern was found to occur for a plate porosity around 30%. For $P < 30\%$, the main recirculation bubble was in contact with the porous plate. For $P \geq 30\%$, the main recirculation bubble formed away from the porous plate and only a small secondary bubble formed close to the channel bed in the immediate vicinity of the plate. The strength of the upstream part of the SSL was found to decay monotonically with the increase in the plate porosity. This happened because of the increase in the level of flow acceleration on the outer side of the SSL which, in turn, induced a larger streamwise velocity gradient across the SSL. The dominant frequencies of the large-scale eddies advected over the upstream part of the SSL were found to be close to constant as long as the main recirculation eddy remained in contact with the plate. For larger porosities, the passage of the eddies become more regular, as the spectrum contained a definite peak frequency. However, the energy associated with these frequencies decayed monotonically with the increase in the plate porosity. The length and height of the main recirculation bubble were found to decay with the increase in the plate porosity. The largest decay is observed when the recirculation bubble starts detaching from the plate.

For all cases, the dominant frequency of the large scale eddies advected over the downstream part of the SSL was close to 0.08-0.1. Still, for the P=20% case, the dominant frequency decayed to 0.065 downstream of the region where the flow reattached to the channel bottom. In general, the dynamics of the billows was found to be strongly affected by their interaction with the channel bed in the region where the flow reattached to the bed. In some cases, as a result of this interaction, part of the vorticity associated with that large eddy was injected into the main recirculation eddy and from there advected toward the plate and the eddies being advected in the upstream part of the SSL. This resulted in further large scale disturbances of the eddies advected over the upstream part of the SSL. A second mechanism that resulted in strong disturbances of the eddies advected over the upstream part of the SSL was due to part of the bleeding flow being diverted toward the SSL. This was particularly evident in the P=20% case.

Large elongated pair of patches of high and low spanwise velocity were found to form along the SSL. As the plate porosity was increased the patches formed at a larger distance from the plate and their angle with the channel bed decreased. All three components of the velocity were found to be significant contributors to the TKE. In all cases the largest contributor was the mean streamwise velocity fluctuations. For large plate porosities, the mean spanwise velocity fluctuations were larger than the mean vertical velocity fluctuations. The TKE was found to decrease monotonically with the increase in the plate porosity over the whole length of the SSL.
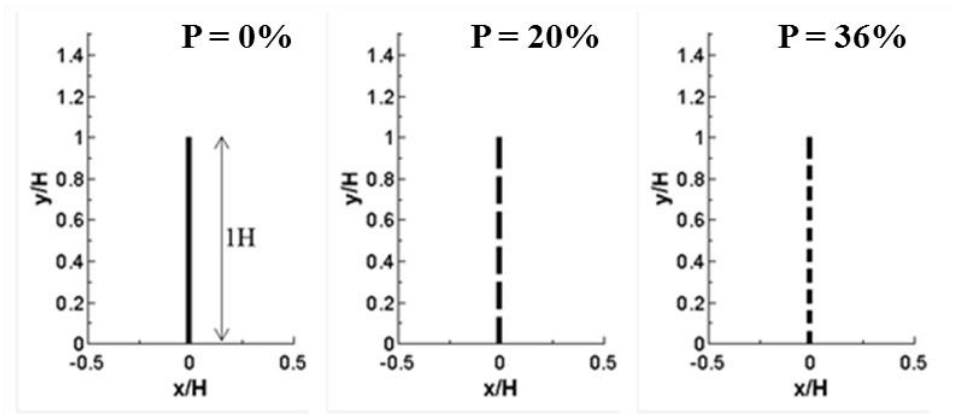
a)
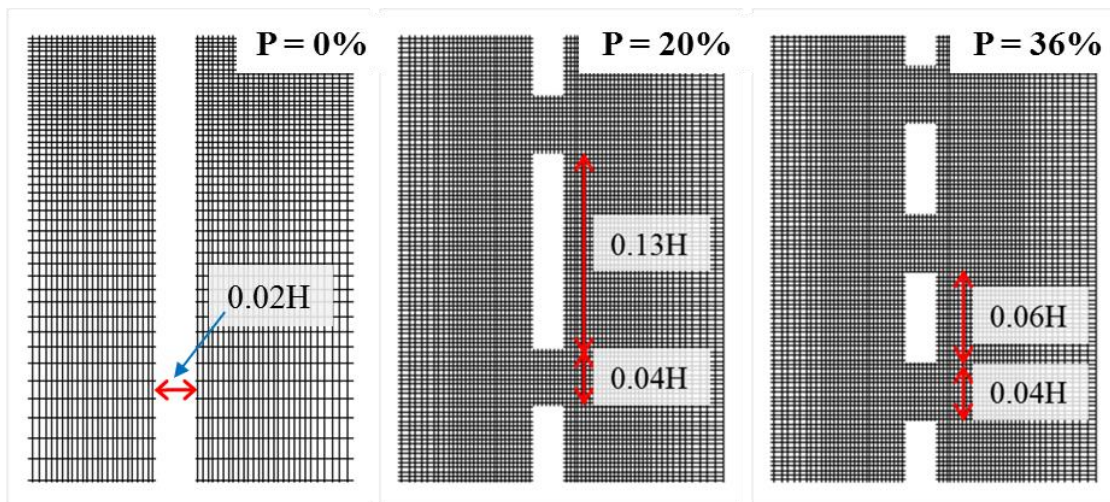
b)

Figure 5.1 Geometrical characteristics of the vertical plate (a) and mesh around the plate (b).
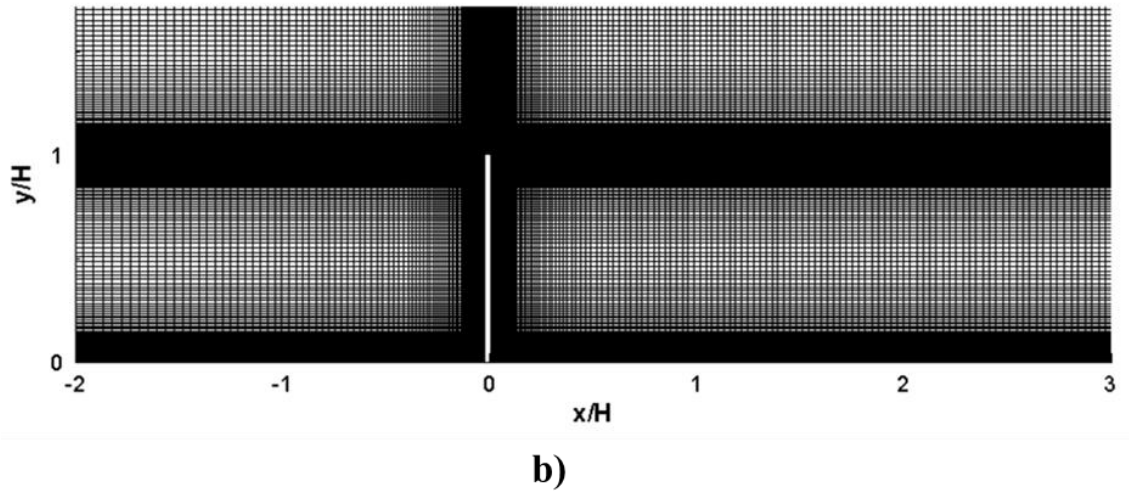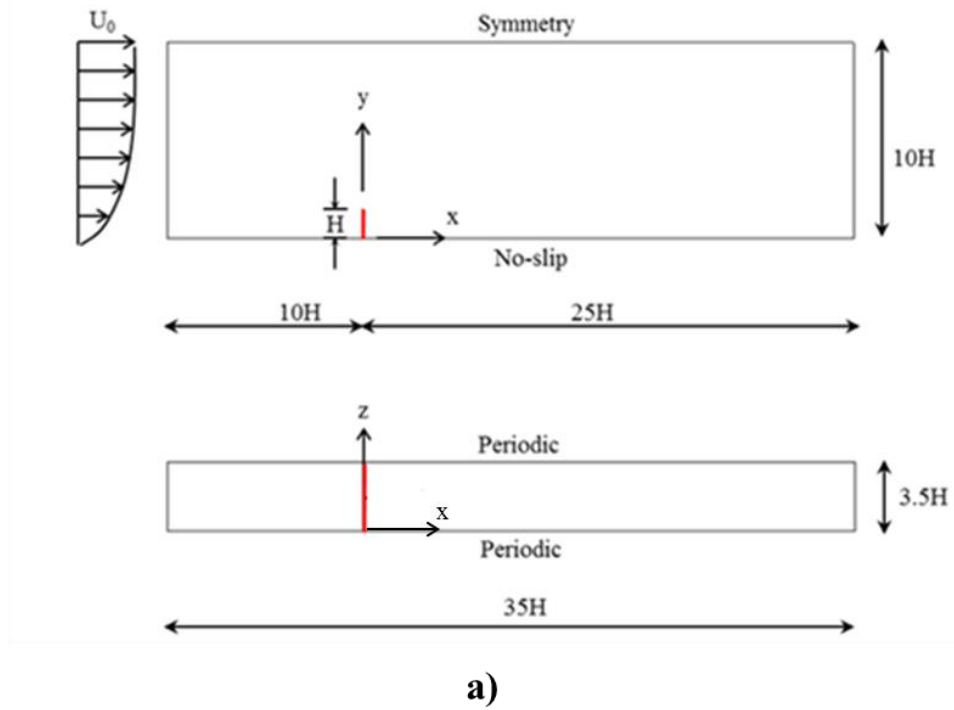
Figure 5.2 Sketch of the computational domain (a) and mesh in a x-y plane (b). The mesh is shown for the P=0% case.
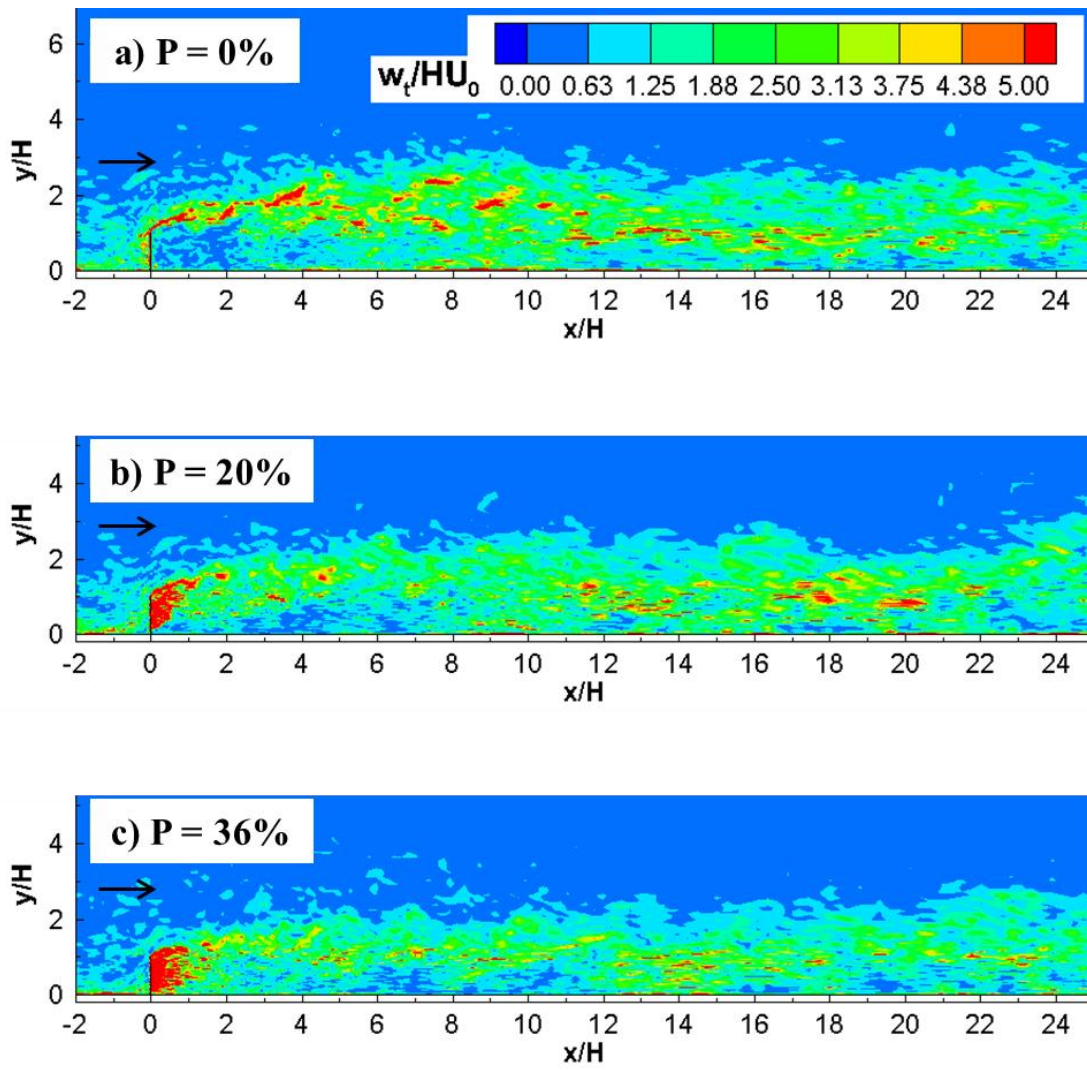
Figure 5.3 Instantaneous total vorticity magnitude, $\omega_t/(H/U_0)$, in an x-y plane.
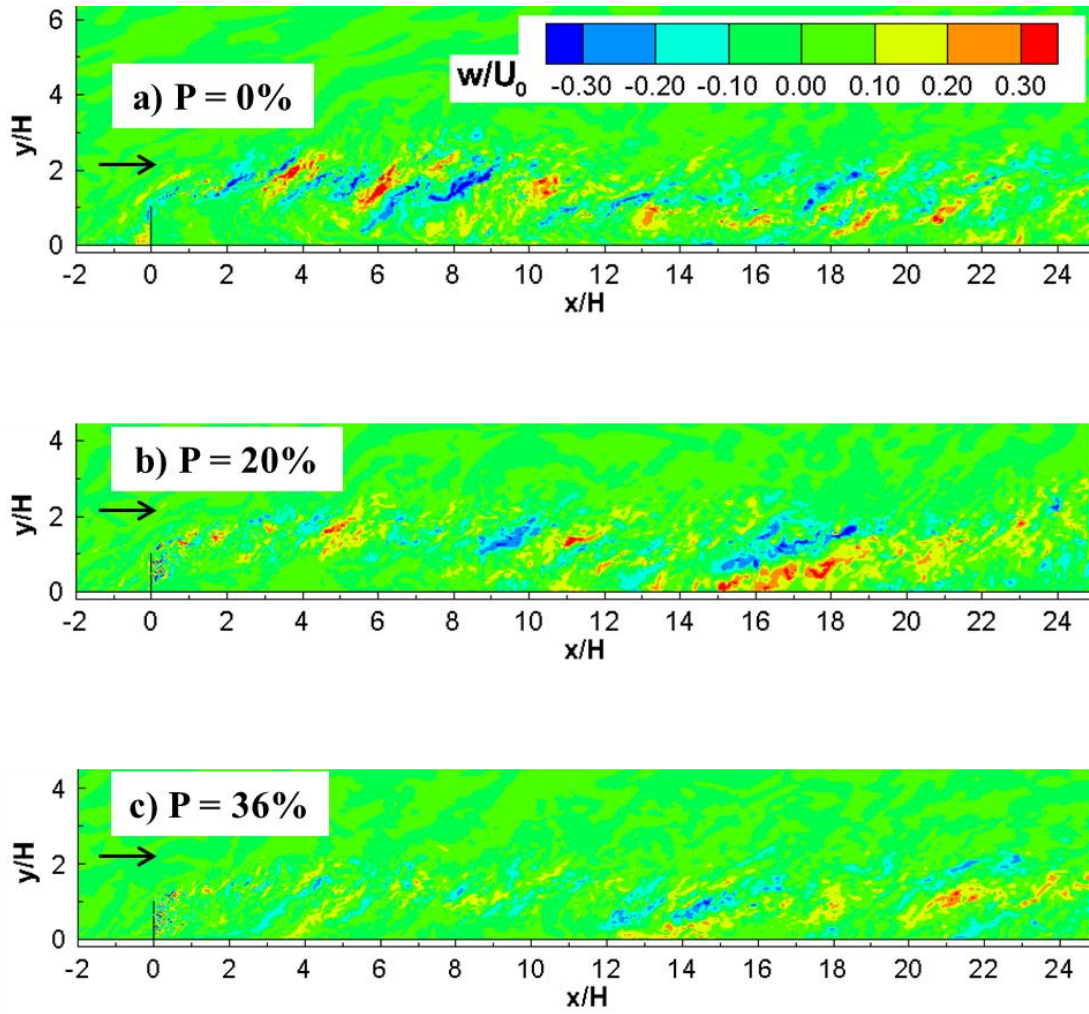
Figure 5.4 Instantaneous spanwise velocity, w/U_0, in an x-y plane.
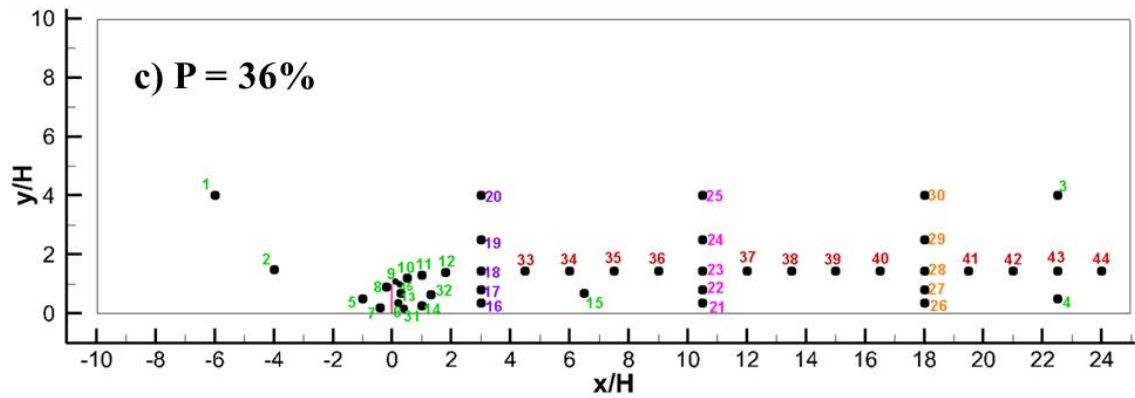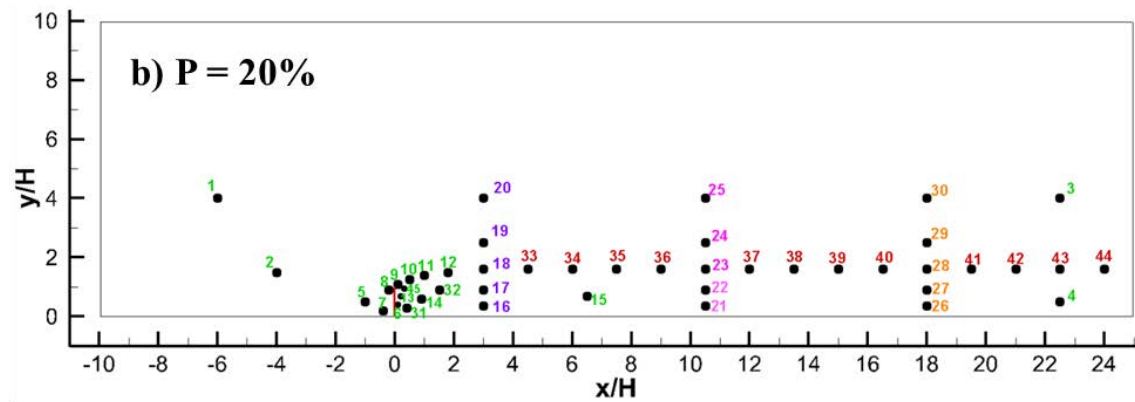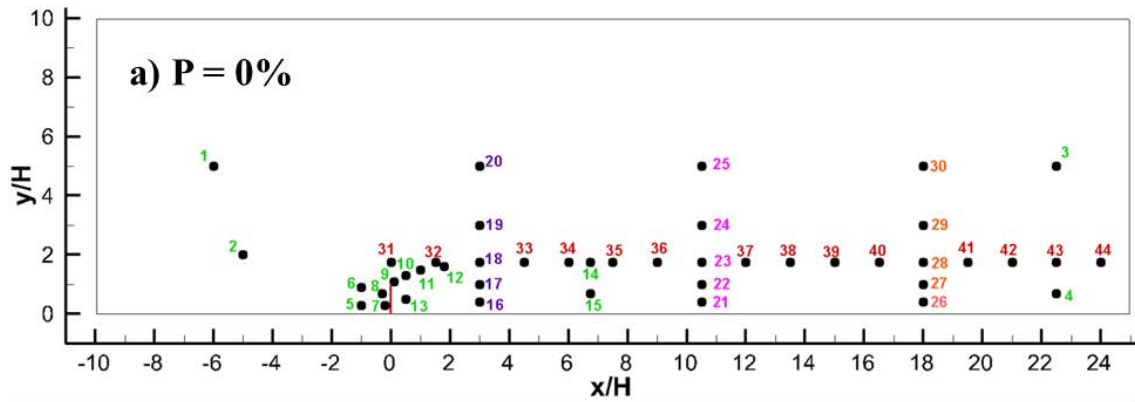
Figure 5.5 Location of points where time series were collected to analyze spectral content of the flow.

a) P = 0%   b) P = 20%   c) P = 36%
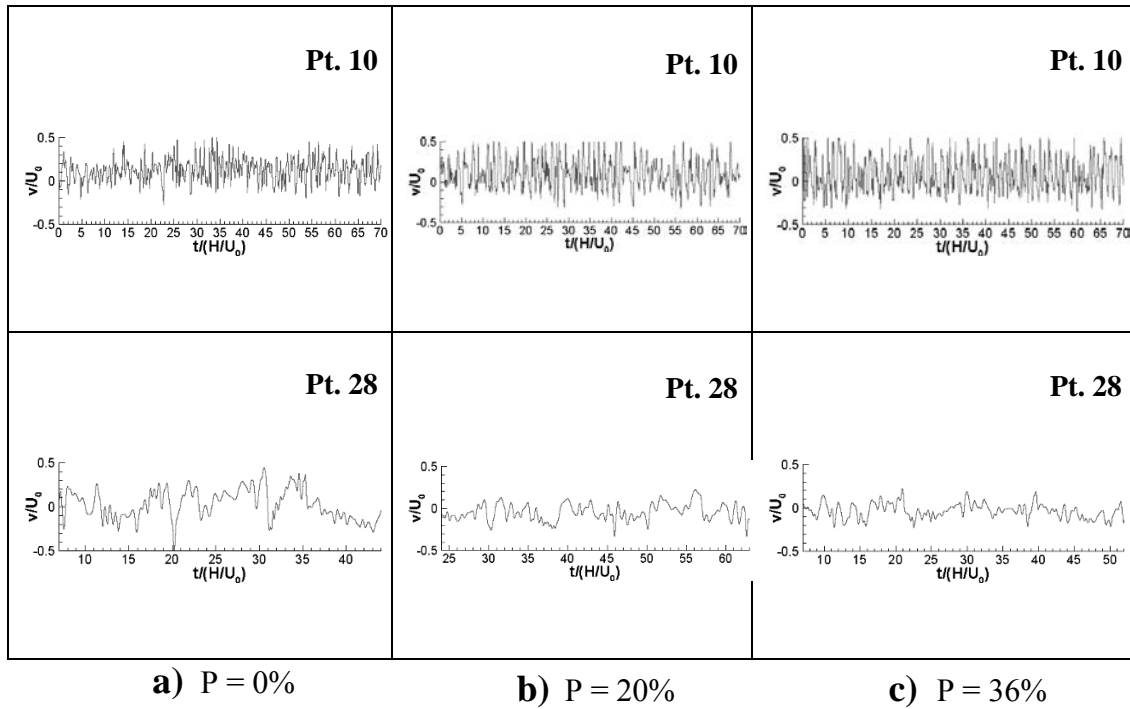
Figure 5.6 Time series of vertical velocity at point 10 (x=0.5H) and point 28 (x=18H). Location of points is shown in Figure 5.5. The spanwise coordinate is z=1.75H (mid length).
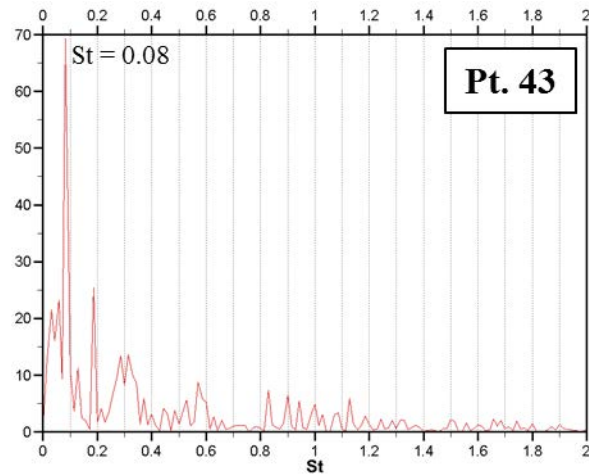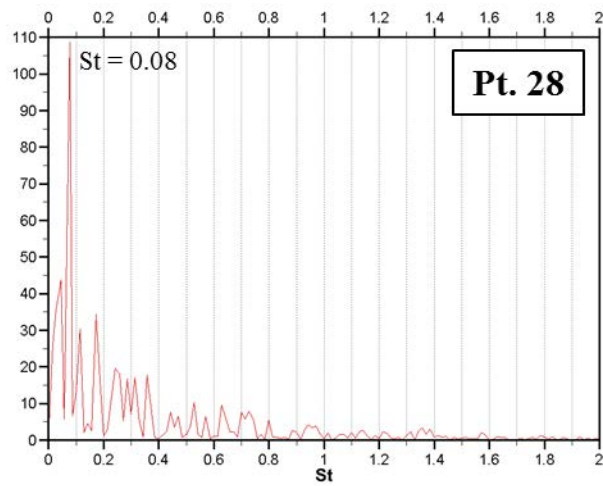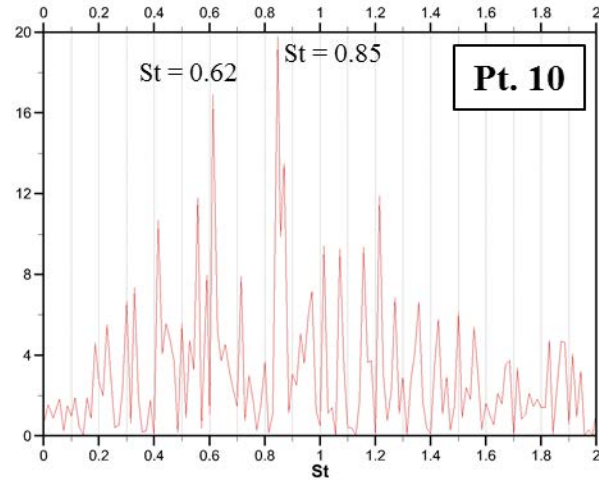
Figure 5.7 Power spectra of vertical velocity for P=0% case at: point 10 (x=0.5H, y=1.3H), point 28 (x=18H, y=1.76H) and point 43 (x=22.5H, y=1.76H). Location of points is shown in Figure 5.5a.

138
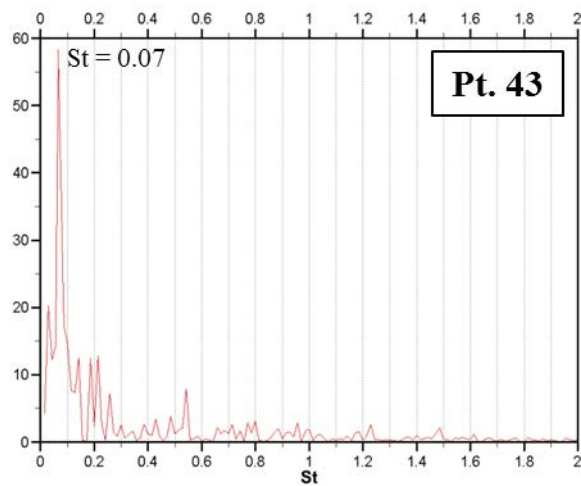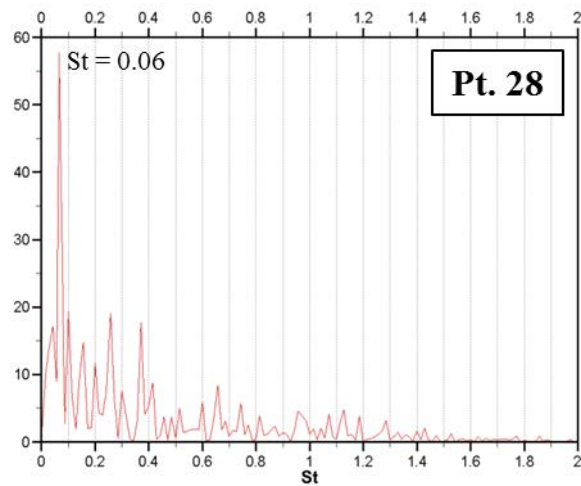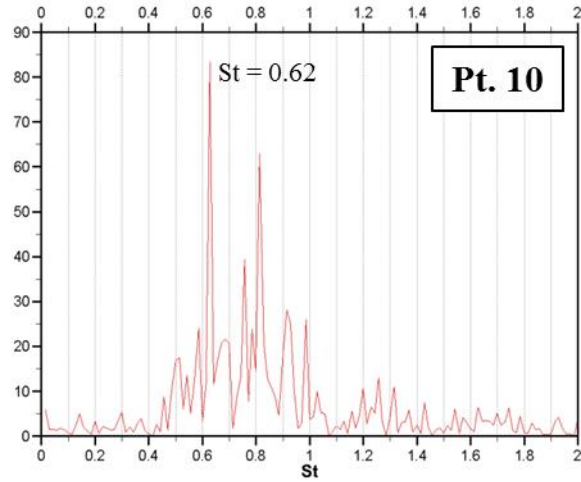
Figure 5.8 Power spectra of vertical velocity for P=20% case at: point 10 (x=0.5H, y=1.3H), point 28 (x=18H, y=1.76H) and point 43 (x=22.5H, y=1.76H). Location of points is shown in Figure 5.5b.
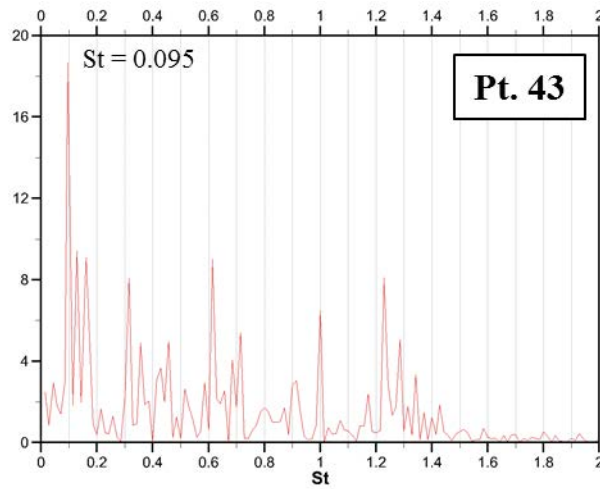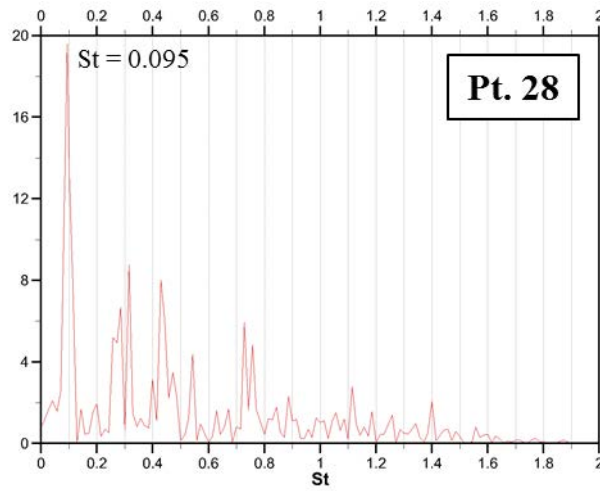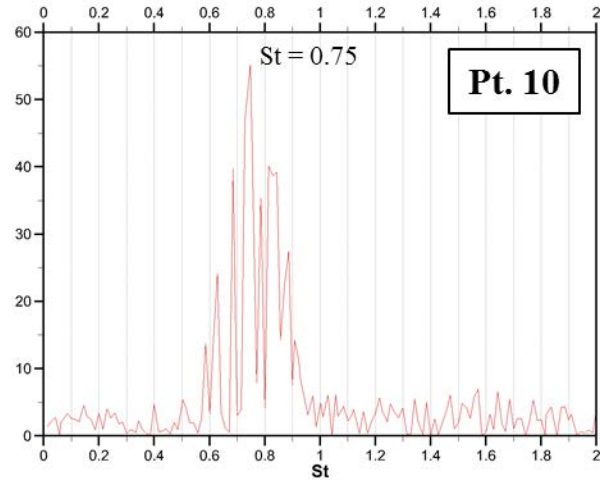
Figure 5.9 Power spectra of vertical velocity for P=36% case at: point 10 (x=0.5H, y=1.3H), point 28 (x=18H, y=1.76H) and point 43 (x=22.5H, y=1.76H). Location of points is shown in Figure 5.5c.

140
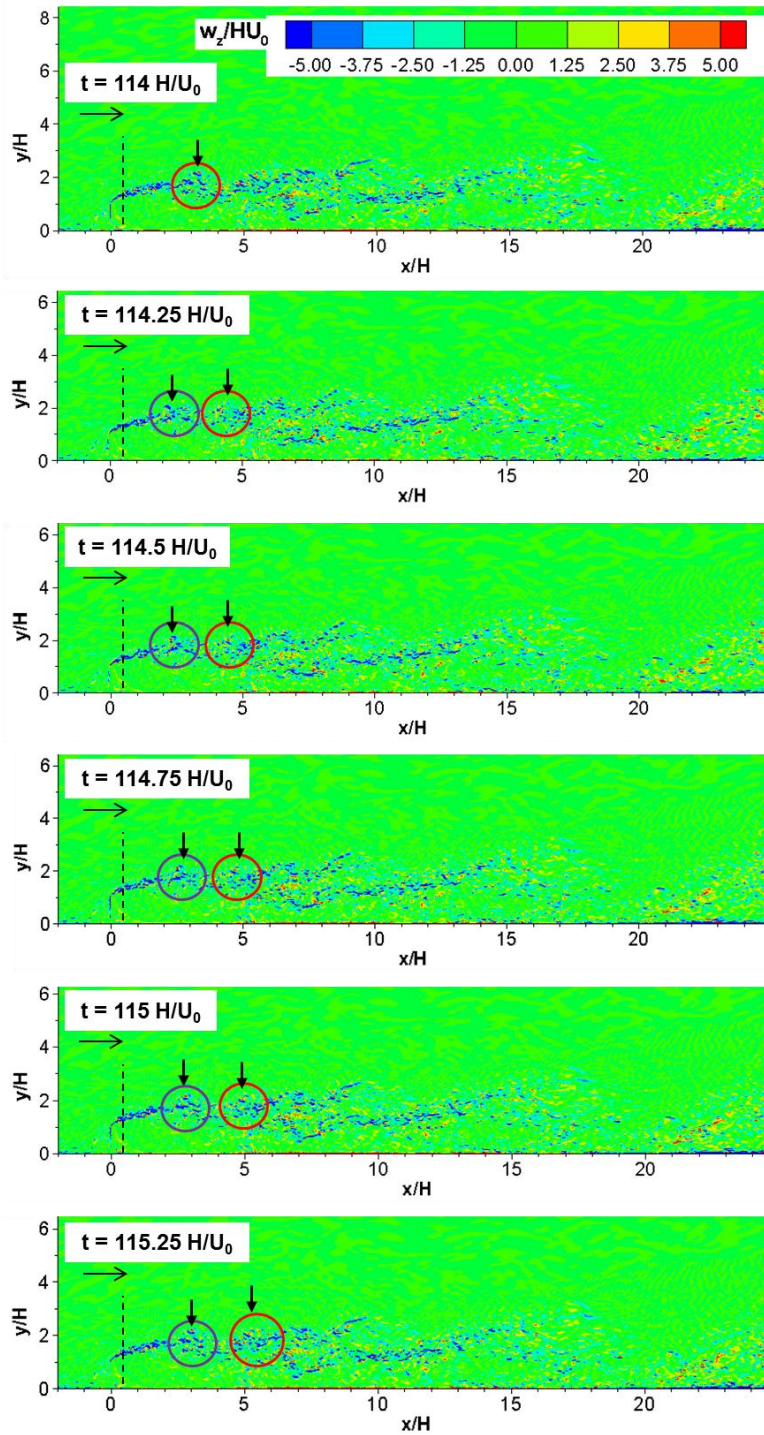
Figure 5.10 Temporal evolution of the spanwise vorticity field in the P=0% case, showing advection of large-scale eddies into the upstream part of the SSL, around x=5H. The two successive eddies are identified using a red and a blue circle. The period of passage of such an eddy is $1.15H/U_0$ corresponding to St=0.85.
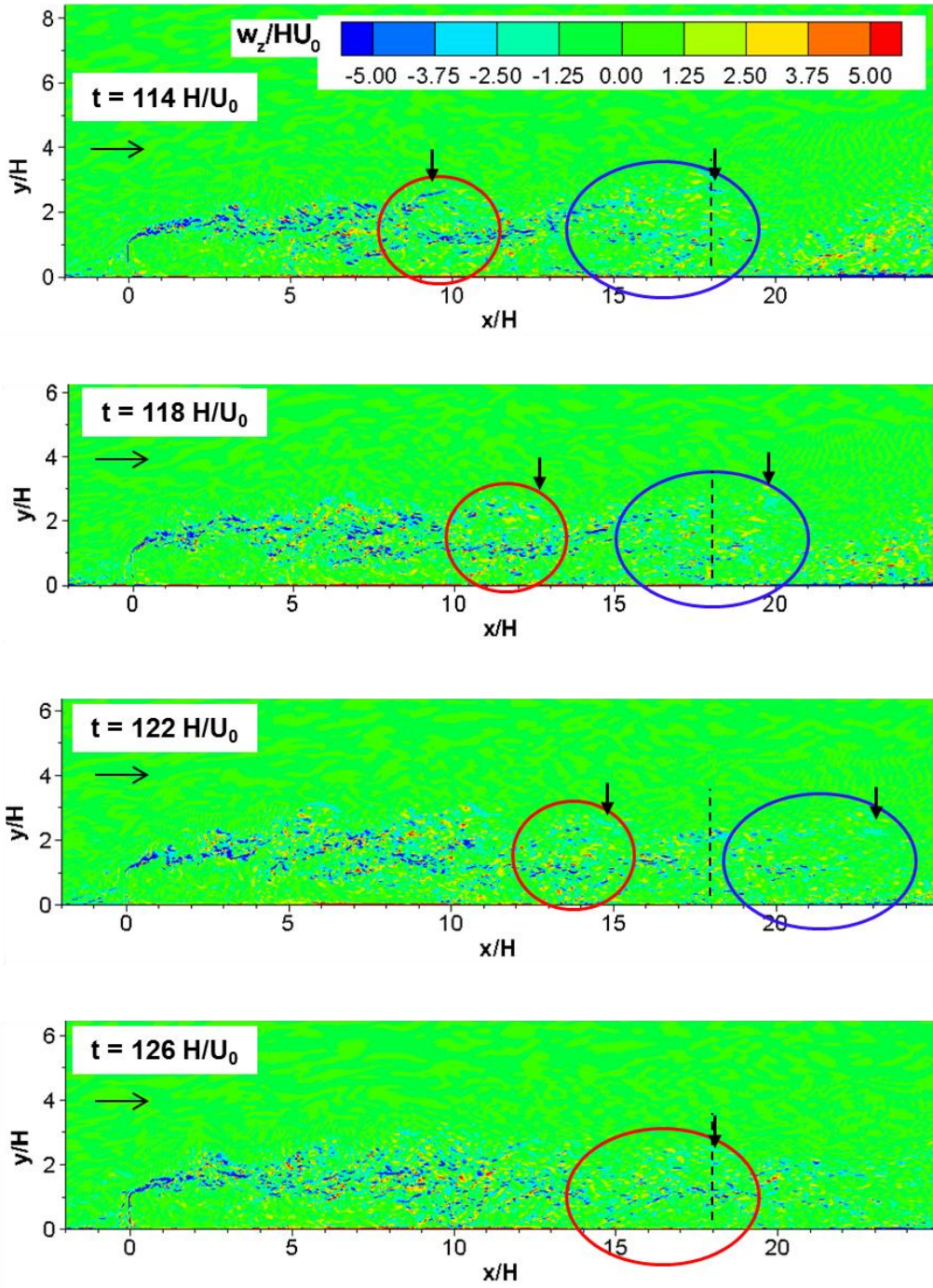
Figure 5.11 Temporal evolution of the spanwise vorticity field in the P=0% case, showing advection of large-scale eddies into the downstream part of the SSL, around x=18H. The two successive eddies are identified using a red and a blue circle. The period of passage of such an eddy is $12H/U_0$ corresponding to St=0.08.
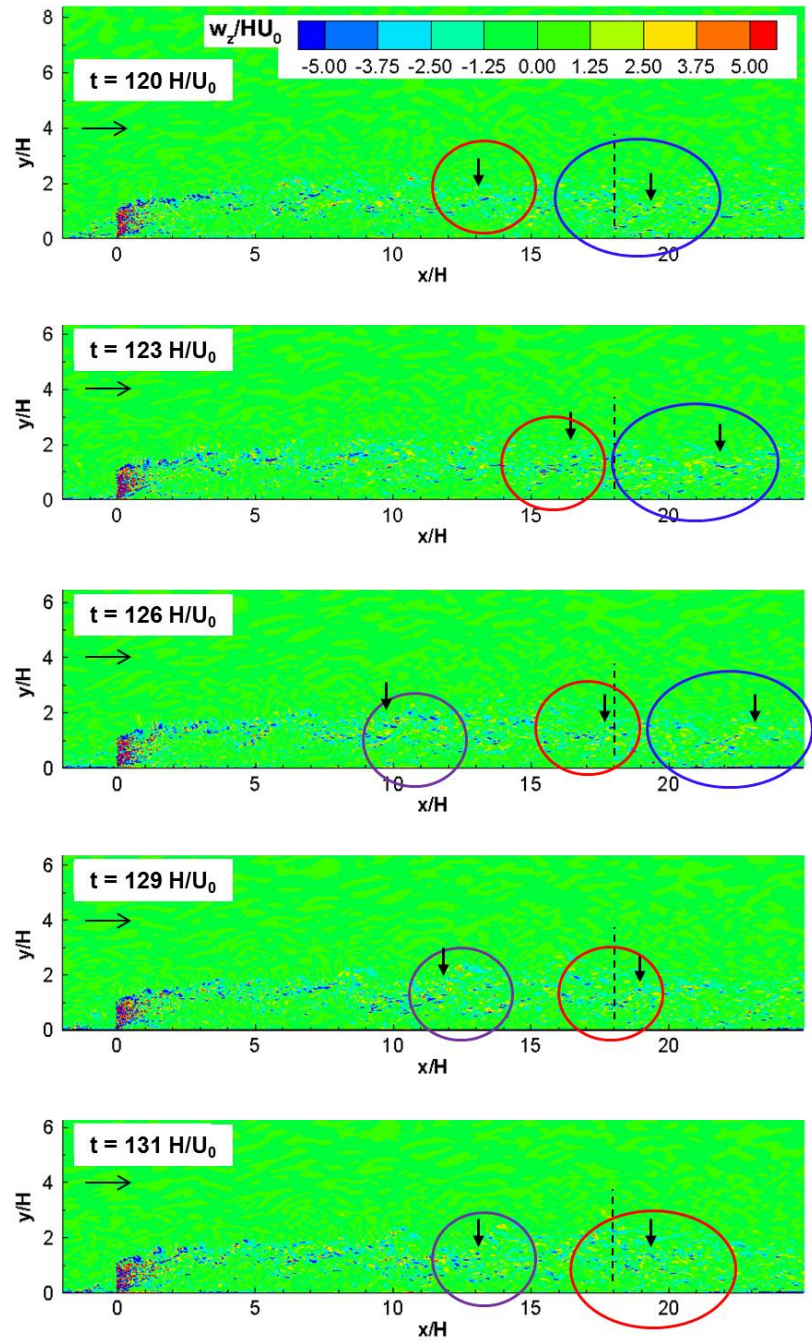
Figure 5.12 Temporal evolution of the spanwise vorticity field in the P=36% case, showing advection of large-scale eddies into the downstream part of the SSL, around x=18H. The two successive eddies are identified using a red and a blue circle. The period of passage of such an eddy is $11H/U_0$ corresponding to St=0.095.
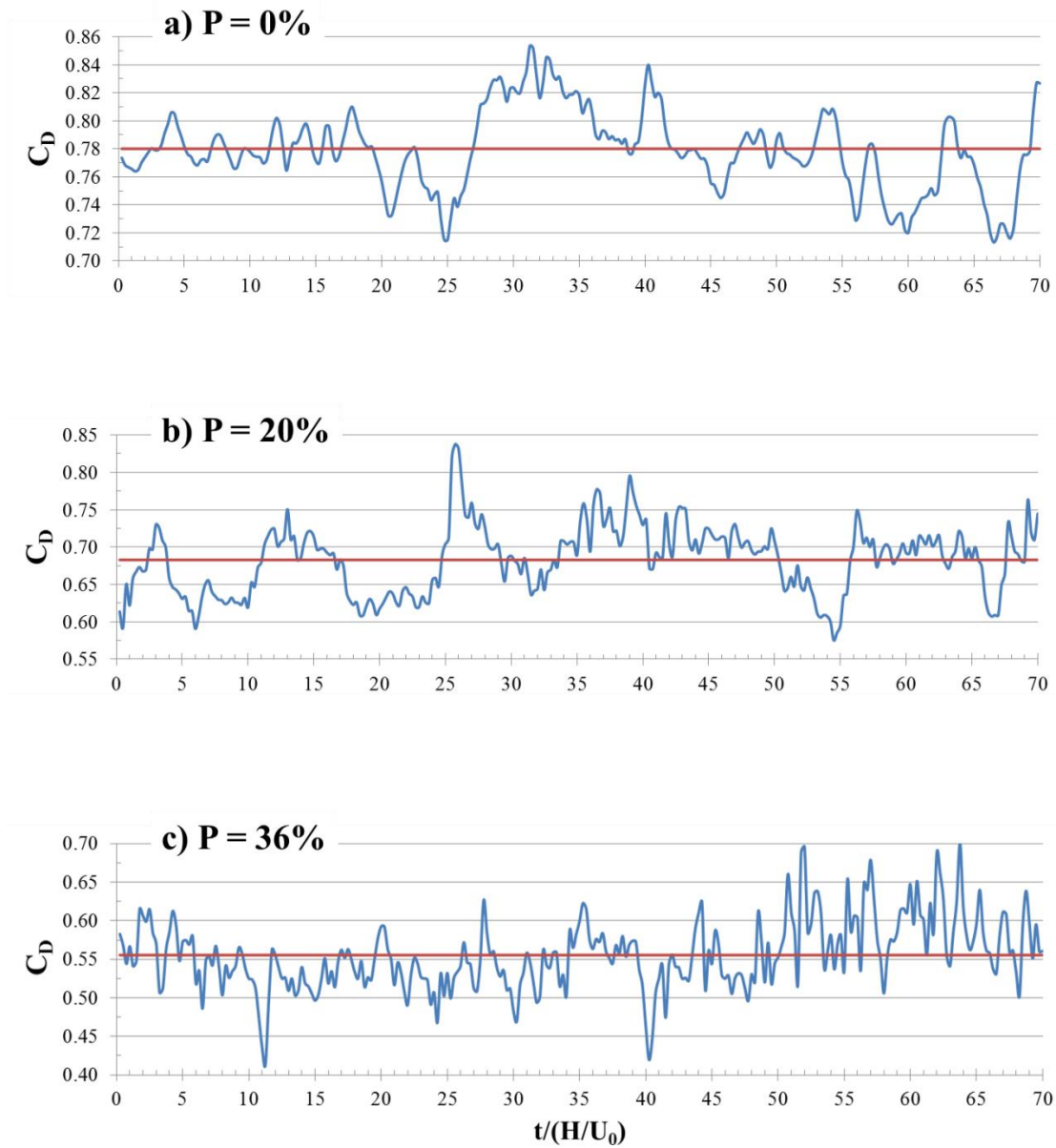
Figure 5.13 Time history of drag coefficient, C_D. The red lines represent the time averaged value of the drag coefficient.
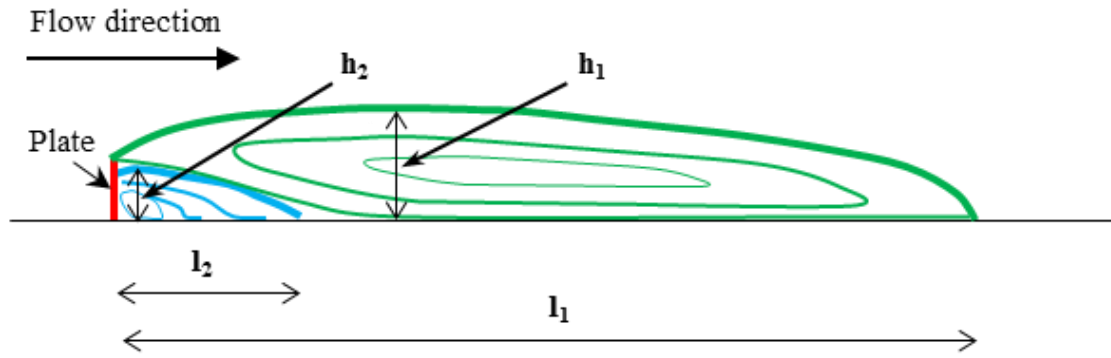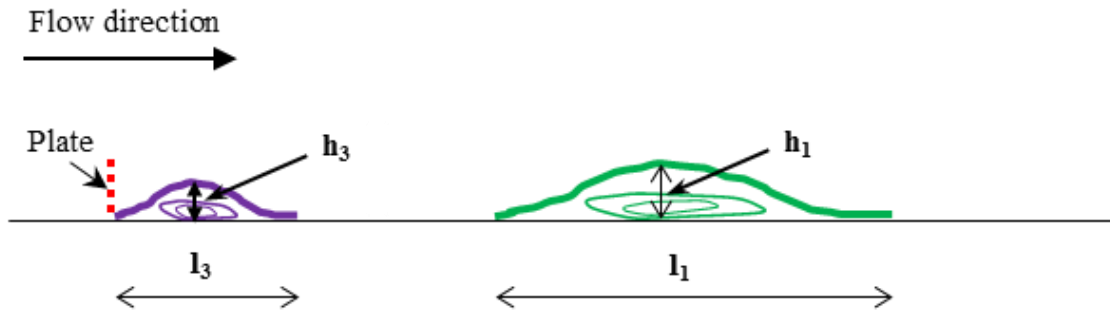
Figure 5.14 Sketch of the mean flow pattern in an x-y plane showing the recirculation bubbles in the flow: a) low plate porosity cases where the main recirculation bubble is in contact with the plate; b) high plate porosity cases where the main recirculation bubble moves away from the plate.
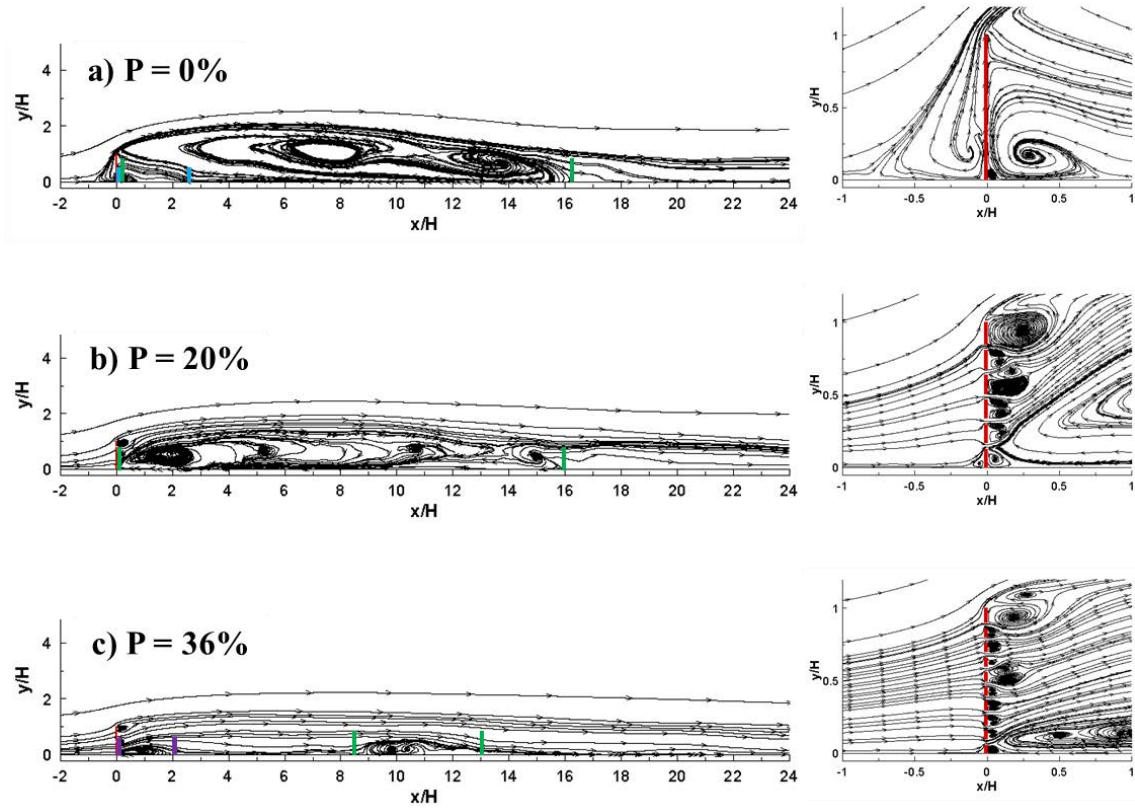
Figure 5.15 Mean flow structure visualized using 2D streamline patterns. Green, blue and purple lines indicate the start and end of the main and secondary recirculation bubble.
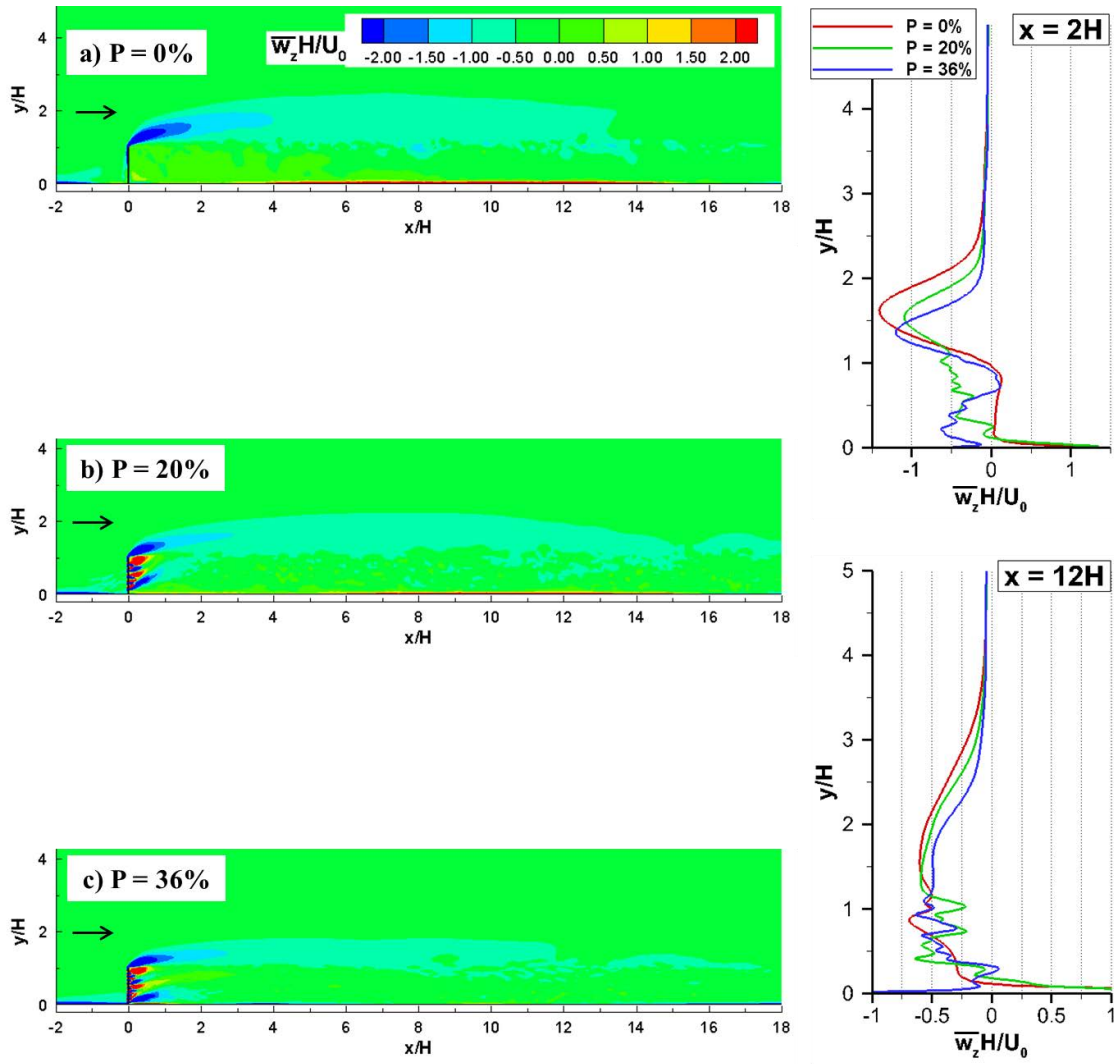
Figure 5.16 Mean spanwise vorticity, $\overline{\omega_z}/(H/U_0)$, in an x-y plane. Also shown are vertical profiles of $\overline{\omega_z}/(H/U_0)$ at x/H=2 and x/H=12.
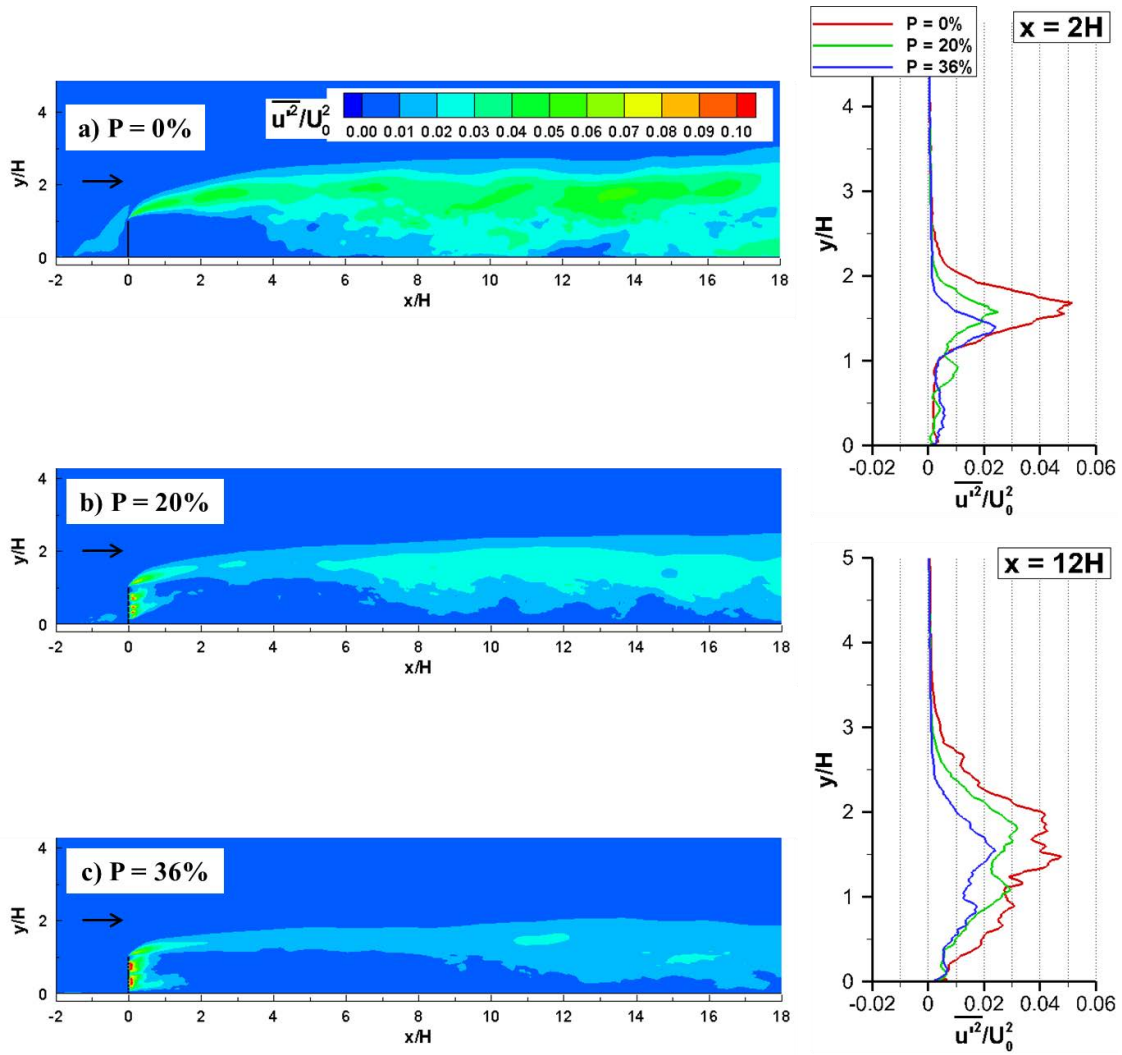
Figure 5.17 Mean streamwise velocity fluctuations, $\overline{u'^2}/U_0^2$, in an x-y plane. Also shown are vertical profiles of $\overline{u'^2}/U_0^2$ at x/H=2 and x/H=12.
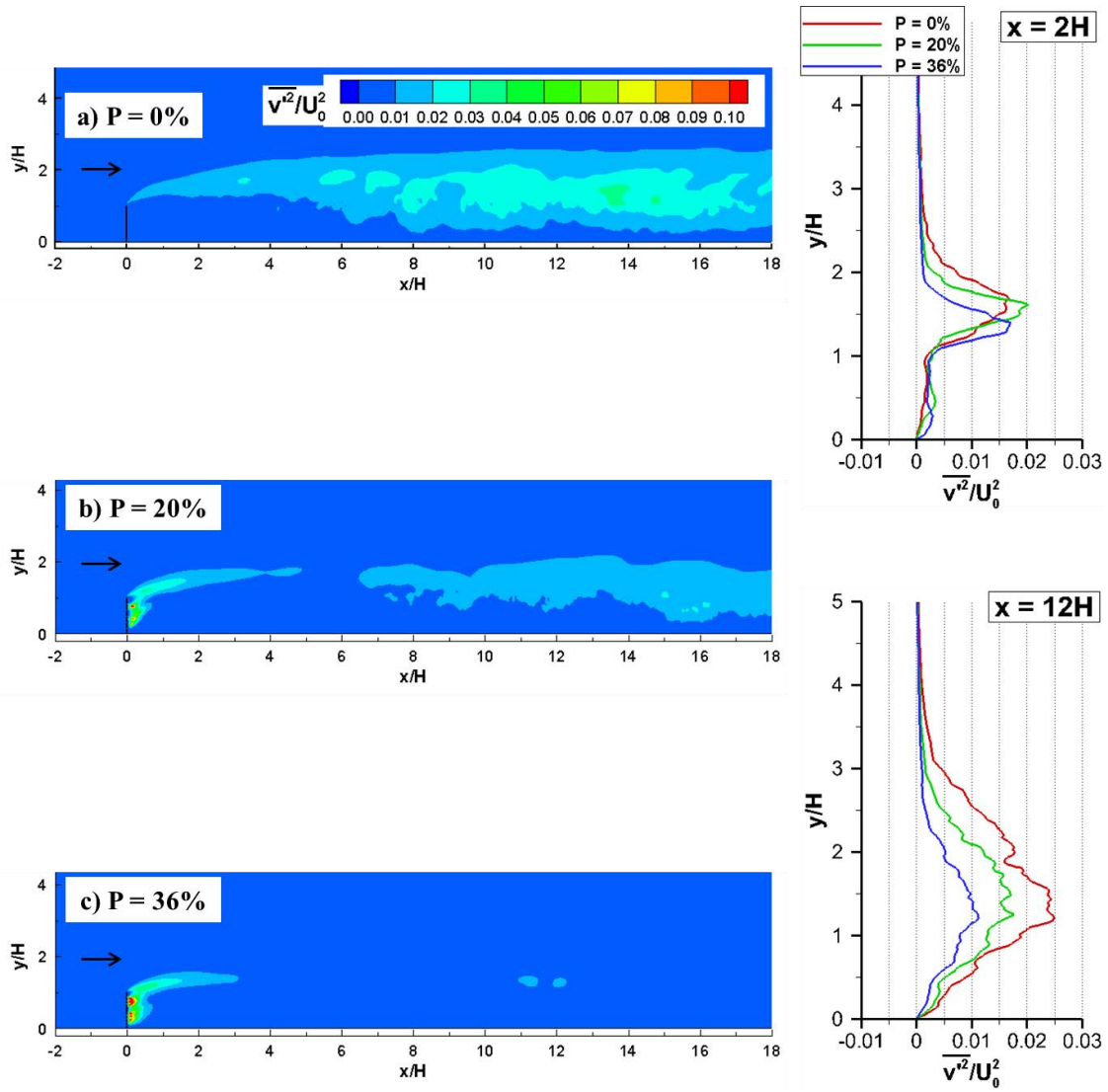
Figure 5.18 Mean vertical velocity fluctuations, $\overline{v'^2}/U_0^2$, in an x-y plane. Also shown are vertical profiles of $\overline{v'^2}/U_0^2$ at x/H=2 and x/H=12.
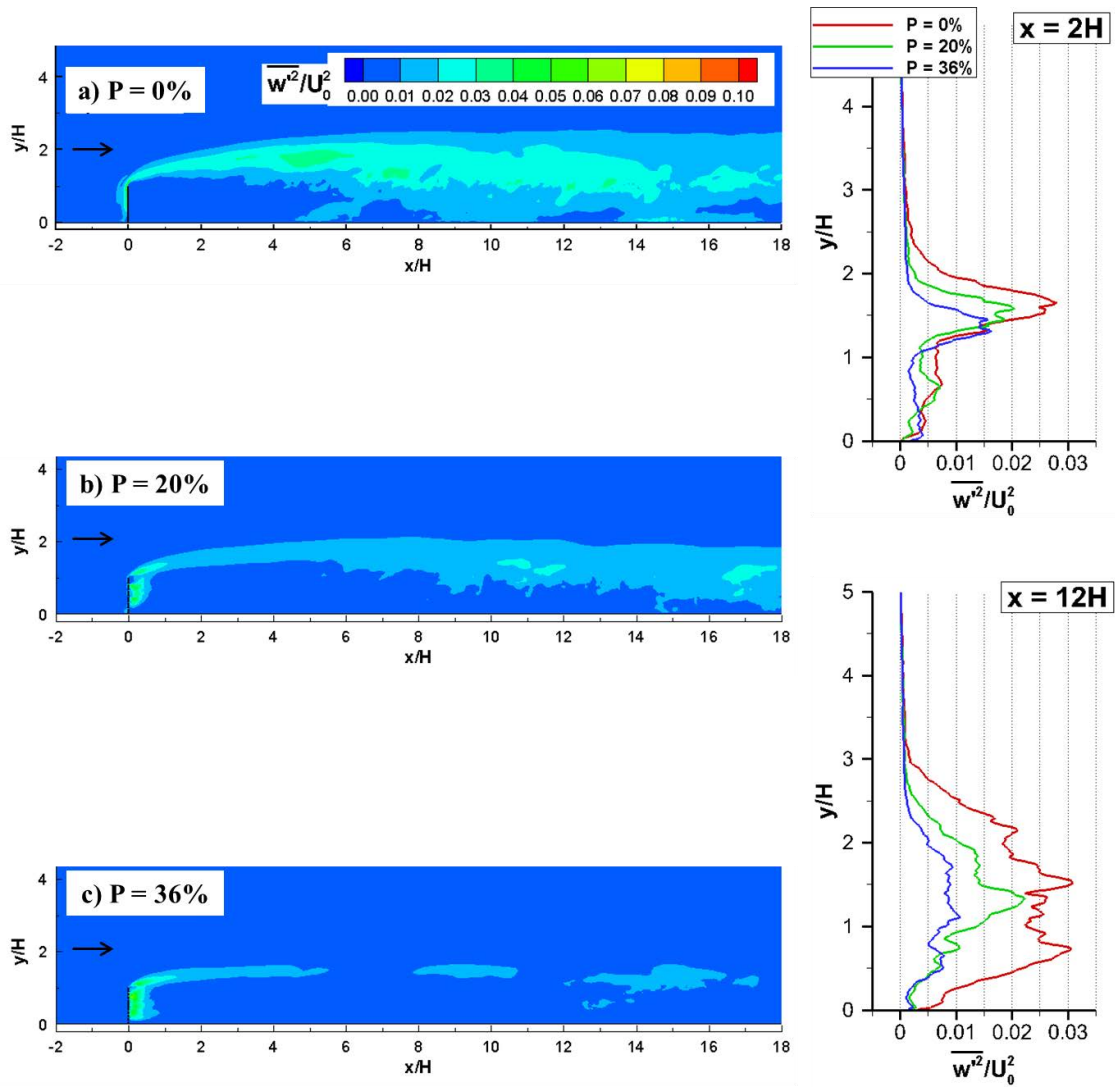
Figure 5.19 Mean spanwise velocity fluctuations, $\overline{w'^2}/U_0^2$, in an x-y plane. Also shown are vertical profiles of $\overline{w'^2}/U_0^2$ at x/H=2 and x/H=12.
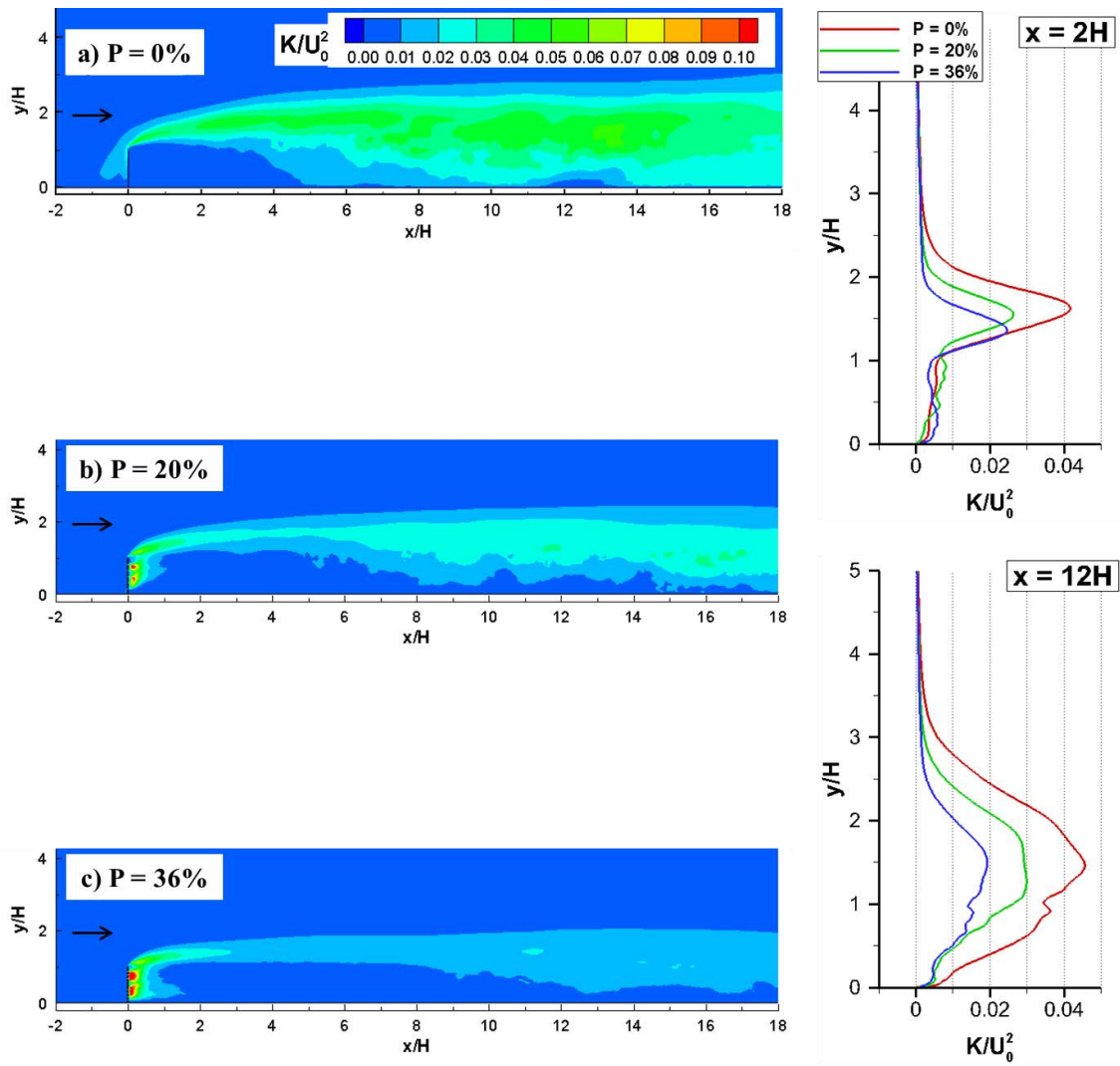
Figure 5.20 Turbulent kinetic energy, K/U_0^2, in an x-y plane. Also shown are vertical profiles of K/U_0^2 at x/H=2 and x/H=12.
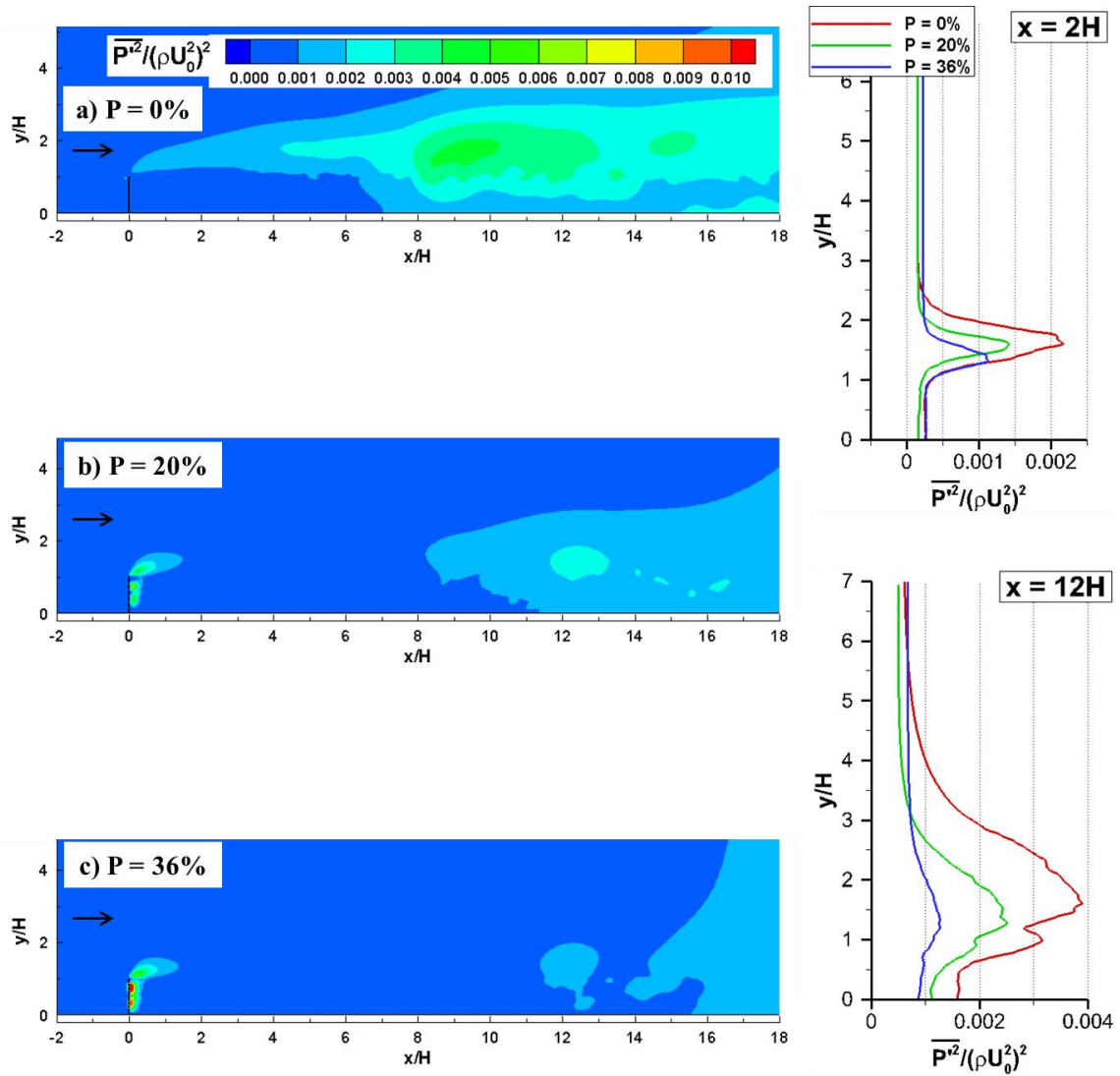
Figure 5.21 Mean pressure fluctuations, $\overline{P'^2}/(\rho U_0^2)^2$, in an x-y plane. Also shown are vertical profiles of $\overline{P'^2}/(\rho U_0^2)^2$ at x/H=2 and x/H=12.
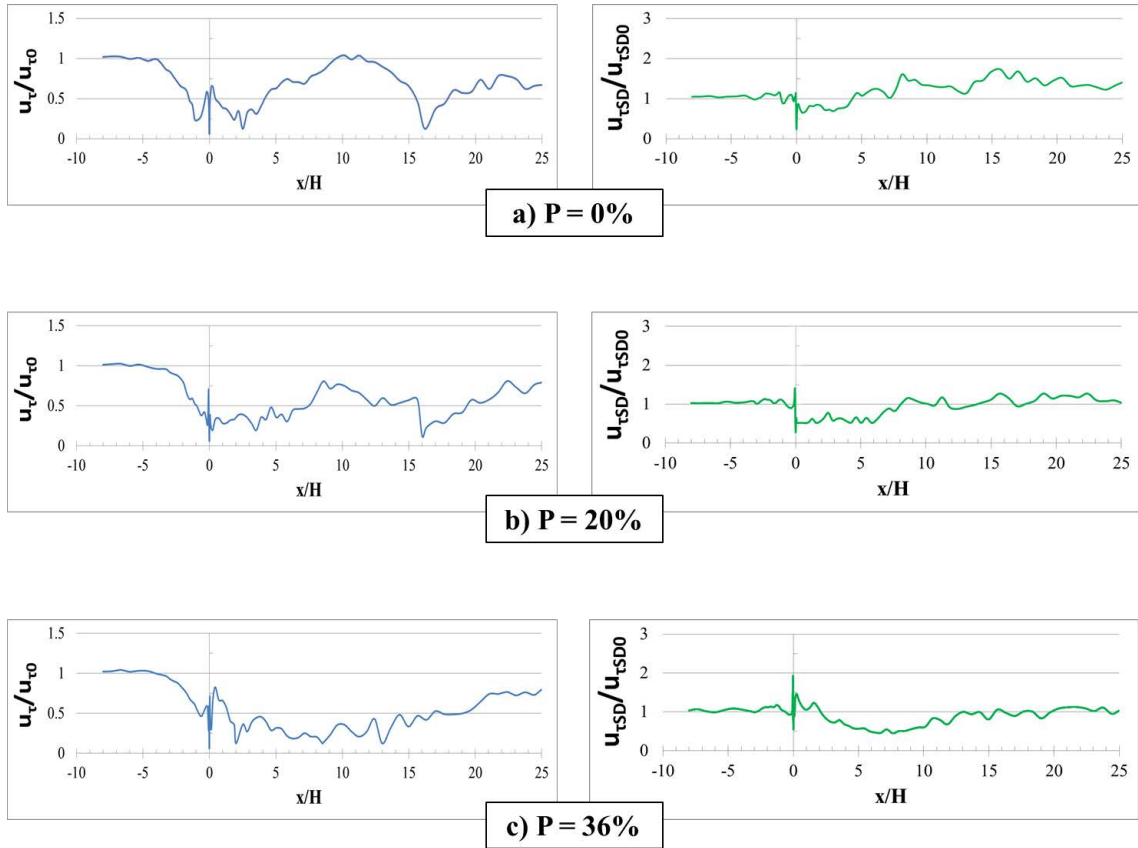
Figure 5.22 Nondimensional spanwise-averaged mean bed friction velocity, $u_\tau/u_{\tau 0}$, where $u_{\tau 0}=0.04U_0$ is the mean bed shear stress in the incoming fully developed turbulent channel flow. Also shown is the nondimensional spanwise-averaged rms of the bed friction velocity fluctuations where $u_{\tau SD0}=0.025U_0$ is the mean rms of the bed shear stress in the incoming fully developed turbulent channel flow.

Table 5.1 Comparison of most energetic nondimensional frequencies (Strouhal numbers) in the SSL and wake regions.

Case	Point	Streamwise distance from the plate	Region	St
P = 0%	10	0.5H	SSL	0.62 and 0.85
	28	18H	SSL/wake	0.08
	43	22.5H	SSL/wake	0.08
P = 20%	10	0.5H	SSL	0.62 and 0.85
	28	18H	SSL/wake	0.065
	43	22.5H	SSL/wake	0.065
P = 36%	10	0.5H	SSL	0.75
	28	18H	SSL/wake	0.095
	43	22.5H	SSL/wake	0.095

Table 5.2 Effect of plate porosity on the variables characterizing the streamwise force acting on the fence and the size of the recirculation bubbles forming behind the fence.

Case	$\overline{C_D}$	$C_D{}^{rms}$	l_1	h_1	l_2	h_2	l_3	h_3	$Q/(\rho U_0 H^2)$
P = 0%	0.78	0.03	16.2H	1.8H	2.5H	0.7H	-	-	-
P = 20%	0.68	0.05	16H	1.3H	-	-	-	-	0.116
P = 36%	0.56	0.06	4.5H	0.5H	-	-	2H	0.3H	0.297

CHAPTER 6 EFFECT OF VARYING BOTTOM GAP ON FLOW PAST A SOLID
VERTICAL PLATE

6.1 Introduction

The main objective of this chapter is to use LES to study the effect of varying bottom gap

on flow past a vertical solid plate placed on a horizontal and smooth channel bottom

surface. Five simulations are performed with relative bottom gaps G=0H, 0.1H, 0.2H, 0.5H

and 1.0H. A sketch of the solid vertical plate used in the five test cases is shown in the

Figure 6.1a. The case with G=0H is the same as the one considered in Chapter 5 (P=0%

case). The flow past a thin plate placed at the centerline of a wide channel can be considered

as a limiting case (very large G/H) for the parametric study discussed in this chapter.

6.2 Simulation Setup

The computational domain, plate height (H), location of the plate (10H from the

inflow section) and the coordinate system are identical to the ones considered in the

simulations discussed in Chapter 5. The only difference is for the G=1H case is which the

length of the computational domain was increased from 35H to 50H to allow the strongly

coherent vortical structures shed in the wake of the plate to exit the domain without

producing unphysical oscillations. The thickness of the solid plate is 0.02H. The

computational domain contains around 19 million (768x384x64) grid points in the G=0H,

0.1H, 0.2H and 0.5H cases and 25 million (1024x384x64) grid points in the G=1H case.

Figures 6.1b and 6.1c show the mesh in a x-y plane around the location of the plate for the

G=1H case.

The x-axis is aligned with the incoming flow direction and the z-axis is aligned

with the vertical direction relative to the horizontal bottom surface of the channel. The plate

height, H, is used as the length scale. The uniform incoming flow velocity, U_0, is used as the velocity scale. The simulations were performed for a Reynolds number of Re=20,000.

Discretization along the x and z directions is the same for all five cases. Only the discretization along the y axis is changed due to the need to resolve the flow near the top and bottom of the plate which is placed at varying distance from the channel bottom. The mesh is uniform along the z direction. Grid points are clustered around the x=constant and y=constant locations corresponding to the solid surfaces of the solid plate (see Figure 6.1c) to resolve the attached boundary layers on these surfaces. When generating the mesh, a minimum grid spacing ($n^+=u_\tau n/\nu$, n is the wall normal direction) of about 2 wall units (assuming u_τ/U_0=0.05) was used in the wall normal direction near the solid surfaces of the vertical plate. This corresponds to a cell size of about 0.002H in the wall normal direction. Away from the plate, the average dimensions of the 3D cells are increased to about 0.07Hx0.06Hx0.05H.

All the boundary conditions are identical to those used in the simulations discussed in Chapter 5. The time step used in simulations was $0.001H/U_0$.

6.3 Flow Structure

6.3.1 Instantaneous Flow Fields

Figure 6.2 and 6.3 compare the nondimensional distributions of the vorticity magnitude and the spanwise velocity for the cases with different values of G/H. In the case the plate is in contact with the channel bottom (G=0H), there is only one SSL forming at the extremity of the plate that is not in contact with the channel bottom. This SSL will be referred as the SSL at the top of the plate. For the other cases, a weaker SSL will form at the bottom extremity of the plate.

Among all 5 cases, the G=0H case is the one for which the mean shear across the SSL at the top of the plate is the highest because all the incoming flow is diverted upwards and then past the top of the plate. This induces a strong flow acceleration on the top side of the SSL. As a result the production of turbulence by mean shear inside the top SSL is the largest in the G=0H case. Merging of the vortex tubes forming over the upstream part of the top SSL results in the formation of larger vortical eddies and the thickening of the SSL. At the end of the recirculation bubble forming behind the plate in the G=0H case, these large vortical eddies start interacting with the channel bed. As described in Chapter 4.2, at times part of the core of these eddies is injected into the recirculation region at the back of the plate. These patches of vorticity are then advected toward the plate and the upstream part of the SSL, where they strongly disturb the eddies advected inside the SSL.

As the plate is moved away from the bottom channel, the main change is the formation of a bottom SSL. The strength of the SSL and its interaction with the top SSL increase monotonically with the increase in G/H. Even for the G/H=0.1 case, the bottom SSL curves toward the top SSL. Similar to the classical mechanism for the formation of wake billow vortices behind isolated bluff bodies (e.g., rectangular cylinders and plates), when the end of the bottom SSL approaches the top SSL, the evolution of co-rotating eddies advected in the stronger top SSL, in between the plate and the location where the bottom SSL reaches the top SSL ($x/H \approx 2$ in Figure 6.2b), is affected. This favors the merging of several of these co-rotating eddies into a larger eddy that resemble a wake billow. Thus, for $x/H > 2$, the top SSL in case G=0.1H contains several of these large billows whose coherence is significantly larger than that of the large scale eddies observed in the G=0H case. The coherence of these billows forming in the top SSL increases with the increase in

G/H because of the increase in the relative strength of the bottom SSL with respect to that of the top SSL. Starting with G/H=0.5, counter-rotating large billows start forming even in the bottom SSL. However, the coherence (e.g., as measured by the circulation) of the billow forming behind the plate from eddies shed in the bottom SSL is significantly less than that of the billows forming in the top SSL. This billow rotates in the opposite sense with respect to the billows forming in the top SSL. Because of the strong streamwise acceleration of the flow through the bottom gap the length of the bottom SSL is larger than the one expected for very large G/H. So the billow corresponding to the bottom SSL forms at a larger distance from plate compared to the case with very large G/H where the presence of the channel bottom has a negligible effect on the flow.

As G/H increases to 1, the intensity of the acceleration of the flow through the gap decreases significantly and the billows originating from the bottom and top SSL form immediately behind the plate, similar to what is observed in cases with very large G/H (see also results in Chapter 4). Though very close to the plate the flow in the G=1H case resembles the one for plates with G/H>>1, this is not the case at larger distances (e.g., for x/H>2 in Figure 6.2e) where the billows shed from the bottom SSL approach the no-slip channel bottom surface. As the billow approaches the channel bed (e.g., around x/H=4 in Figure 6.2e), it slows down and its capacity to rotate around its axis is reduced. As a result the billow starts losing its coherence via vortex stretching. Most of the vortex stretching is induced by the larger billow from the top SSL that extract large patches of vorticity form its core. For the G=1H case the passage of two successive billows from the top SSL is enough to destroy most of the coherence of a bottom SSL billow trapped in the boundary layer forming on the channel bottom. This is why for x/H>8 the wake flow in the G=1H

contains only large billows originating in the top SSL. Finally, for the cases when billows originating in the bottom SSL can form (G/H≥0.5), the coherence of the billows originating in the top SSL increases significantly with respect to cases with smaller G/H, especially at large distances from the plate. This is simply because the larger strength of the bottom SSL favors the merging of a larger number of eddies that are advected in the upstream part of the top SSL into a large billow, before that billow is coherent enough to push away the downstream end of the bottom SSL and to start moving away from the plate.

Given that the mean flow is 2D, the distributions of the spanwise velocity in Figure 6.3 give an indication on the degree of flow three-dimensionality in the SSL and wake. Elongated patches of high positive and negative spanwise velocity are observed in all cases in the wake region. The velocity magnitude inside these patches is of the order of $0.3U_0$, which means that the spanwise transfer of momentum is significant. For the cases with G/H<0.5, a patch of positive spanwise velocity is situated in the immediate vicinity of a patch of negative spanwise velocity, at most locations. Moreover, most of these patches are situated within the region associated with the top SSL. Only in the G=1.0H case, strong patches of high and low spanwise vorticity of magnitude are also observed in the bottom SSL, at least at relatively low distances from the plate (e.g., for x/H<8 in Figure 6.3e). On average, the size of these patches increases sharply between the G=0H and the G=0.1H, then remains fairly constant until the bottom gap is large enough such that the strength of the bottom SSL becomes comparable to that of the top SSL (e.g., case G=1H) and the wake contains large counter-rotating billows, at least close to the plate. Even for G/H=1, at larger distances where the billows shed from the bottom SSL lost their coherence, the distribution of the regions of high spanwise velocity magnitude resembles the one observed for cases

with a lower G/H. Overall, the momentum transport in the spanwise direction increases with increasing G/H, especially close to the plate.

Time series of the velocity and pressure were collected at about 45 points in an x-y plane and at about 210 points in a y-z plane. The positions of the points where time series were collected in an x-y plane for each of three simulations are shown in Figure 6.4. Data were saved over $70H/U_0$ (flow was statistically steady) with a time step of $0.001H/U_0$. The time series of the vertical velocity at point 10 situated inside the SSL, close to the tip of the plate, and at point 35 situated in the top SSL, at about 7H from the plate are compared in Figure 6.5 for some of the cases. For all cases, the time series at point 10 show the presence of high frequency fluctuations associated with the formation of the first vortex tubes in the top SSL. The time series at point 35 show the presence of a range of lower frequencies associated with the advection of large billows in the downstream part of the top SSL. As G/H increases over 0.5, there is a clear dominant frequency associated with the low frequency oscillations in the time series. This is the shedding frequency of large billows behind the plate due to the interaction of the top and bottom SSLs. However, even for cases with a relatively small G/H (e.g., G=0.1H in Figure 6.5), low frequency oscillations are present but there is a range of fairly energetic low frequency oscillations. This is because the interactions of the downstream end of the bottom SSL with the top SSL are not as regular as those observed for cases with a large G/H.

Figures 6.6, 6.8, 6.10, 6.12 and 6.14 show the power spectra of the vertical velocity component at points 10, 28 and 43 for the G=0H, G=0.1H, G=0.2H, G=0.5H and G=1H cases, respectively. Points 28 and 43 are situated inside the top SSL at and 18H and 22.5H,

respectively, behind the plate. Some of the figures also contain the power spectrum for the vertical velocity at point 35 situated at about 7H from the plate

In the G=0H case, the most energetic frequencies in the top SSL, close to the top of the plate, correspond to St=0.62 and 0.85 (see power spectrum at point 10 in Figure 6.6). The range of energetic frequencies is 0.2<St<1.6. The two peak frequencies correspond to the passage frequency of the largest billow vortices within the upstream part of the SSL close to the plate. For example, animations show that the average time interval between the passage of two successive billow vortices at x=3H is close to 1.15H, which corresponds to St=0.85.

As G/H is varied between 0.1 and 0.5, the range of energetic frequencies broadens slightly and the number of peaks of comparable energy within this range increases. This suggests that the size of the largest eddies forming in the top SSL close to the plate decreases with increasing G/H. In the G=1H case where, as opposed to the G=0.5H, the wake billows form immediately behind the plate, the velocity spectrum at point contains one dominant frequency, St=0.14, which is the shedding frequency of the counter-rotating billows. Of course, the spectrum also contains a range of energetic frequencies 0.2<St<2, but most of the energy in the spectrum is contained in the St=0.14 mode (see also time series in Figure 6.5 at Point 10). This is simply because the shedding of the billows induces an up and down movement of the top SSL even very close to the plate. In the G=0.5 case, the top SSL is not subject to these oscillations very close to the plate as the billows form some distance away from the plate (e.g., see time series at Point 10 in Figure 6.5). However, time series of the vertical velocity at more downstream locations (e.g., Point 35 in Figure

6.5) show that the frequency associated with the shedding of billows becomes the dominant starting with the streamwise location where the billows form.

In the G=0H case, the largest vortical eddies in the top SSL continue to grow and eventually start interacting with the bed as the mean flow reattaches around x=16H. Downstream of this location, the dominant frequency in the velocity spectra associated with the passage of the largest eddies is St=0.08 (see spectra at Points 28 and 43 in Figure 6.6). Figure 6.7 illustrates the advection of one of the large eddies through the x=18H location. The time period between the passage of two successive large eddies is $12H/U_0$, which corresponds to St=0.08.

In the G=0.1 case, the dominant frequency in the velocity spectra at locations situated far from the plate is St=0.04, about half the dominant frequency in the G=0H case. The vortical eddy dynamics that induces the dominant frequency in the spectrum is different compared to the G=0H case and is related to the presence of the bottom SSL originating at the lower extremity of the plate and its interaction with eddies shed in the top SSL. The downstream part of the bottom SSL moves regularly toward the top SSL and disturbs the trajectories of the eddies shed in the upstream part of the top SSL. This favors the formation of larger billows in the top SSL via merging of eddies advected in between its origin and the location where eddies from the bottom SSL interact with the top SSL (x≈2.0H). The dominant frequency associated with the interaction between the eddies shed in the two SSLs which results in the formation of strongly coherent billows in the top SSL around x=2.5H is close to 0.08. In between x=2.0H and x≈14H, where the mean flow reattaches, one merging event occurs within the top SSL, such that the dominant frequency associated with the passage of the large billows advected parallel to the channel bed far

from the plate is St=0.08 (see Figure 6.8). The merging occurs between a billow that already reached the channel bed and its downstream movement is slowed down by the interaction with the no-slip surface and the billow behind it that maintains a larger velocity as it is advected toward the billow situated close to the bed. This sequence of events is illustrated in Figure 6.9 that used spanwise vorticity contours to visualize the vortical billows in the flow. The same figure shows that the time interval at which billows pass through the x=18H location is close to 25H/U_0, which corresponds to St=0.04.

The mechanisms are qualitatively similar in the G=0.2H case. The main difference is that the bottom SSL is more energetic and its interaction with the eddies advected in the upstream part of the top SSL happens further downstream, around x=3.5H. The dominant frequency associated with these interactions and formation of strongly coherent billows inside the top SSL is St=0.14 (see spectrum for Point 35 in Figure 6.10), which is close to the shedding frequency of counter-rotating wake billows for plates with a large G/H. Animations show that billows form regularly at the end of the bottom SSL but, once they have formed, their advection velocity is small, as they are trapped inside the recirculation eddy at the back of the plate. Thus, they lose their coherence rapidly via interaction with eddies advected in the top SSL. As for the G=0.1H case, one merging event takes place between successive billows as the front one starts interacting with the channel bed around the location where the mean flow reattaches (x=12.5H). As a result, the dominant frequency in the velocity spectra is St=0.07 for x>12.5H (Figure 6.10). Figure 6.11 confirms that the dominant passage frequency of the large billows at x=18H is St=0.07. The two bottom frames also show two billows from the top SSL in the process of merging around x=11H.

For G/H≥0.5, a separation bubble forms at the back of the plate but no recirculation eddy forms in between the plate and the channel bed (Figure 6.16). The mechanics for the formation of large billows inside the top and bottom SSLs is very similar to that observed for plates with a high G/H ratio for which counter-rotating billows of comparable circulation are shed in the wake of the plate with a frequency close to St=0.14-0.15. For the G=0.5H and G=1H cases, the billow shed from the bottom SSL is of comparable circulation with the billows shed from the top SSL in the formation region. Starting at the back of the recirculation bubble, the dominant shedding frequency of the billows is St=0.12 for the G=0.5H case and St=0.14 for the G=1H case (see spectra at Points 35, 28 and 43 in Figures 6.12 and 6.14). Results in Figure 6.13 and 6.15 show that the time interval associated with the passage of the large billows originating in the top SSL at x=18H is $8H/U_0$ for case G=0.5H and $7H/U_0$ for case G=1H, which corresponds to St=0.12 and St=0.14, respectively. In the G=1H case, the dominant frequency is St=0.14 even in the region where the two SSLs are forming because the billows form just behind the plate (see spectrum at Point 10 in Figure 6.14).

The main difference between the G=0.5H and G=1.0 case and cases with a very large G/H ratio is that the billows shed from the bottom SSL start interacting with the channel bottom. As this happens, the velocity at which they are advected away from the plate and their circulation decays. Severe vortex stretching occurs as the billows shed from the top SSL approaches the slowly moving billow trapped into the boundary layer on the channel bed. Most of the vorticity inside the core of this billow is lost via interactions with the two billows shed from the SSL before and after the shedding of the billow from the bottom SSL. As shown in Figure 6.13, the billow shed from the bottom SSL starts

interacting with the bed around x=2.5H. Most of the core of this billow is then entrained

upwards in between two successively shed billows from the top SSL where its core is

stretched and then splits into two parts that continue to interact with opposite sign vorticity

from the top SSL billows. Eventually, this billow is destroyed. The scenario is similar for

case G=1H (Figure 6.15), except that the billow from the bottom SSL approaches the bed

around x/H=7, such that two billows shed from the bottom SSL are identifiable in most of

the frames of Figure 6.15.

Table 6.2 summarizes the predicted values of the mean drag coefficient, $\overline{C}_D$, and

its root-mean-square fluctuations, $C_D{}^{rms}$, for the five cases. The mean drag coefficient

increases monotonically with the increase in G/H and approaches the value for large G/H

($\overline{C}_D$=2.13-2.17, see Table 4.2). Still, the effect of the bottom wall on $\overline{C}_D$ is not negligible

even for the G=1H case as its value (1.57) is still significantly smaller than the value

predicted for the limiting case of very large G/H (2.13-2.17). This is not surprising given

the significant interactions of the billows shed from the bottom SSL with the channel

bottom in the G=1H case. The other consequence is that the dominant shedding frequency

of the KH billows (St=0.14) in the G=1H case is not the only highly energetic frequency

in the power spectra of C_D, as is the case for very large values of G/H.

Meanwhile, $C_D{}^{rms}$ increases monotonically with the increase in G/H, as the

interactions between the bottom and the top SSLs increase. For G/H>0.5, the rate of

increase of $C_D{}^{rms}$ is sharper because of the observed change in the location where the KH

billows are forming. In the G=1H, the billows form immediately behind the back of the

plate, similar to the limiting case of very large G/H. As a result, larger temporal oscillations

of the streamwise force on the plate are induced as a newly formed billow starts moving

away from the plate. This explains also why the value of $C_D{}^{rms}$ for case G=1H (0.2) is quite close to the predicted value for very large G/H (0.24, see Table 4.2).

6.3.2 Mean Flow and Turbulence Statistics

The 2D mean flow streamline patterns in Figure 6.16 show that a recirculation bubble forms in between the plate and the channel bed for G/H≤0.2 and that a separation bubble forms behind the plate for G/H≥0.5. The length of the main recirculation bubble, l_1, decreases monotonically with the increase in G/H (e.g., from 16H for G=0H to 12.5H for G=0.2H), while its maximum width, h_1, remains close to constant (1.8H). Even for G=0.2H, a separation bubble containing two eddies forms behind the plate and is contained within the recirculation bubble. The length of the separation bubble, l_2, is also given in Table 6.2. The length of the separation bubble decreases monotonically with the increase in G/H. In the G=1H case, its length is very close to the length expected for cases with a large value of G/H. For low G/H values, the size of the lower eddy is larger. The sizes of the two eddies are approximatively equal in the G=1H case.

The mean spanwise vorticity distributions in the 5 cases shown in Figure 6.17 show that the largest amplification of the vorticity in the mean flow occurs over the upstream part of the SSLs. The penetration length of the region of high spanwise vorticity magnitude associated with the top increases monotonically with G/H until G/H=0.2 and then starts decreasing with increasing G/H. The same is true for the bottom SSL. Moreover, due to the flow acceleration occurring in the gap between the plate and the channel bottom, the lower SSL is stronger than the top SSL for G/H≥0.5 (see Figure 6.17). For cases where the bottom SSL sheds wake billows, the largest amplification of the vorticity within the top

SSL occurs around G/H=0.5 at large distances from the plate, where the billows shed from the bottom SSL do not penetrate (e.g., see line plots at x/H=8 in Figure 6.18).

The distributions of the mean flow fluctuations of the velocity components in all three directions in Figures 6.19, 6.20 and 6.21 show an amplification of the turbulence inside the region where billows are shed from the top and bottom SSLs. The contribution to the TKE associated with the spanwise velocity component is less but still comparable to that of the streamwise and vertical components, which indicates a strong three-dimensionality of the flow in the wake of the plate despite the mean flow being two dimensional. For cases where alternate vortex shedding of billows occurs behind the plate, the largest amplification of the mean vertical velocity fluctuations occurs in the region where the interaction of the top and bottom SSLs result in the formation of the wake billows (see Figures 6.19d and 6.19e). For G/H≥0.2, the amplification of the mean velocity fluctuations and TKE in the bottom SSL is similar to that observed in the top SSL, at least until the two SSL start interacting or the billows shed from the bottom SSL start interacting with the channel bed. Close to the channel bed, the mean velocity fluctuations and the TKE decay fast downstream of the location where the billows shed from the bottom SSL lose their coherence (e.g., x/H=6 for G=0.5H, see Figures 6.22d and x/H=8 for G=1H, see Figure 6.22e). Downstream of the region where the bottom SSL or billows shed from the bottom SSL penetrate, the TKE increases with increasing G/H, as also observed from the TKE profiles at x/H=8 in Figure 6.22. As expected, for relatively large G/H, the region of peak TKE correlates with the one in which the interaction between the SSLs results in the formation of counter-rotating wake billows.

The spanwise-averaged distributions of the bed friction velocity in Figure 6.23 allow estimating the spatial extent of the region where u_τ/U_0 is amplified with respect to the mean value in the incoming fully developed flow, which is close to 0.04. The flow advected through the bottom gap leads to a significant amplification of u_τ/U_0 over some distance from the plate. For G/H$\geq$0.1, the peak value within this decreases monotonically with increasing G/H (e.g., from about 0.15 for G=0.1H case to about 0.08 for G=1H case). The length of the region where $u_\tau/U_0\geq$0.04 peaks around G/H=0.3. For the G/H=1 case there is a second region where $u_\tau/U_0\geq$0.04 centered around the location where the billows shed from the bottom SSL start interacting with the channel bottom. As expected, $u_\tau/U_0<$0.04 in the wake of the plate for the G=0H case. Still, u_τ/U_0 approaches this value close to the center of the main recirculation bubble. The bed friction velocity reduces to zero around the location where the flow attaches or detaches from the channel bottom. Though not shown, it is important to mention that the presence of the plate also induces regions characterized by large mean bed friction velocity fluctuations. These fluctuations is associated with the passage of large scale eddies in the vicinity of the bed and can substantially amplify the capacity of the flow to entrain sediment in the case of a loose bed with respect to the sediment entrainment capacity estimated based on the mean flow distributions of u_τ/U_0. The length of the region situated downstream of the plate where the rms of the bed friction velocity is larger than the value associated with the fully developed incoming turbulent flow is larger than the one where $u_\tau/U_0>$0.04. For example the length of this region is 4.5H in the G=0.1H case, 7H in the G=0.5H case and 10H in the G=1H case. For G/H>0.1, the peak value of the rms of the bed friction velocity within this regain decays monotonically with increasing G/H.

6.4 Conclusions

LES of flow past a 2D solid plate with varying bottom gap ($0 \leq G/H \leq 1$) have been performed at a moderate cylinder Reynolds number (Re=20,000) to investigate the effects of bottom gap on flow and turbulence structure. The plate height was kept constant. Results were also compared with the limiting case of a plate with a very large G/H where the effect of the channel bottom is negligible (see results reported in Chapter 4).

Results show that for cases with $G/H \leq 0.2$, a recirculation region forms in between the plate and the channel bottom, while for $G/H \geq 0.5$, a recirculation bubble containing two eddies forms behind the plate, similar to cases with a large G/H. Even for cases with relatively small G/H values, the bottom SSL has a strong effect on the coherence of the eddies forming in the top SSL. The interactions are similar to those that result in the formation of wake billows behind bluff bodies situated far from other boundaries. In cases when a recirculation region forms and $G/H>0$, a merging event occurs between successively shed billows inside the top SSL, as the front eddy slows down as it reaches the bed close to the region where the mean flow reattaches. Thus the dominant frequency in the wake past the reattachment location is two times lower than the frequency of the large eddies forming in the upstream part of the top SSL as a result of the interaction with eddies advected in the bottom SSL. In cases where only a recirculation bubble forms at the back of the plate, the coherence of billows shed from the top and bottom SSLs is initially comparable. However, once the billows originating in the bottom SSL start interacting with the channel bed, they lose rapidly their coherence due to interactions with the large billows advected in the top SSL. Moreover, as G/H increases, the shedding frequency approaches monotonically the shedding frequency observed for cases with a large G/H ratio (St=0.14-0.15).

The mean drag coefficient and its rms fluctuations increases monotonically with increasing G/H. The length of the main recirculation region decreases monotonically with increasing G/H. The same is true for the length of the separation bubble observed for G/H>0.2. The flow advected through the gap between the plate and the channel bottom induces a strong increase of the bed friction velocity and its rms values beneath and downstream of the plate, which can result in scour developing around the plate position. Simulation results shows that for G/H>0.1, the maximum value of the bed friction velocity decreases with increasing G/H while the length of the region characterized by large rms values of the bed friction velocity increases monotonically with G/H. Overall, the sediment entrainment capacity of the flow peaks around G/H=0.2.

The parametric study conducted in this chapter allowed understanding how the flow, vertical dynamics and turbulence structure change with the increase in G/H between the limiting cases of a solid plate attached to a horizontal bottom and a solid plate situated in the middle of a very wide channel (large G/H) and revealed the critical role played by the bottom SSL in controlling the flow dynamics.
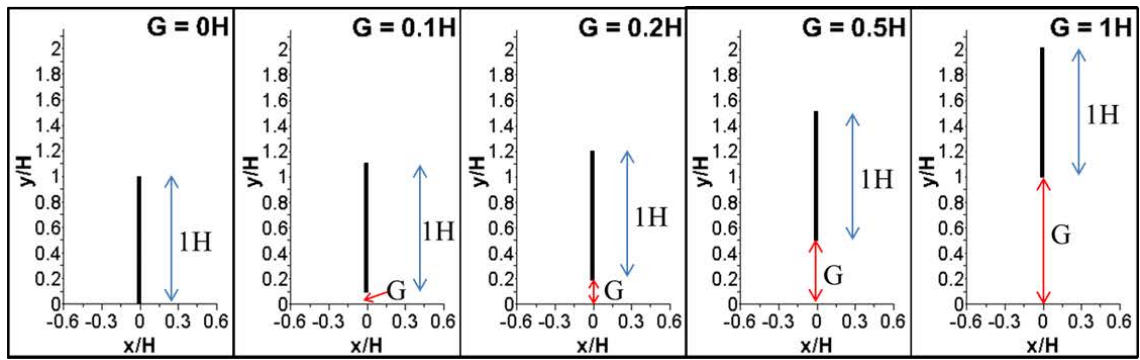
a)
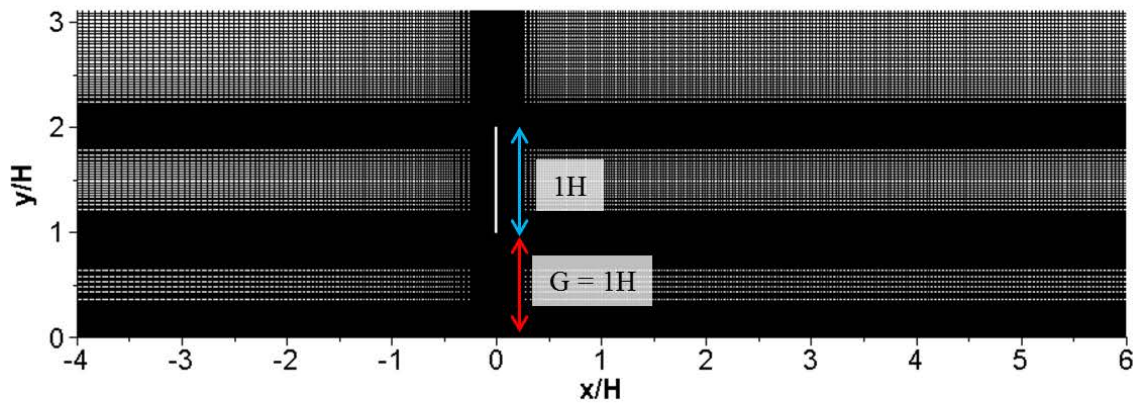
b)
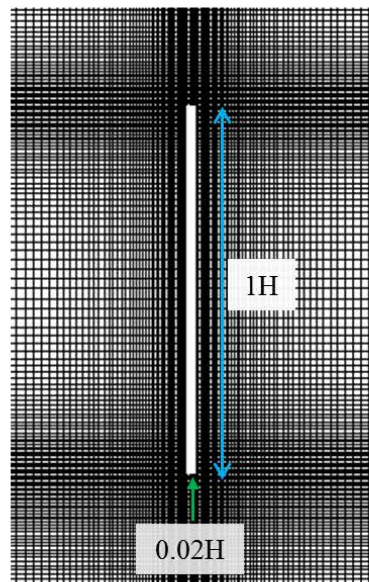
c)

Figure 6.1 Sketch showing relative position of the vertical plate relative to the channel bottom in the five cases (a) and sample computational mesh around the plate (b, c).
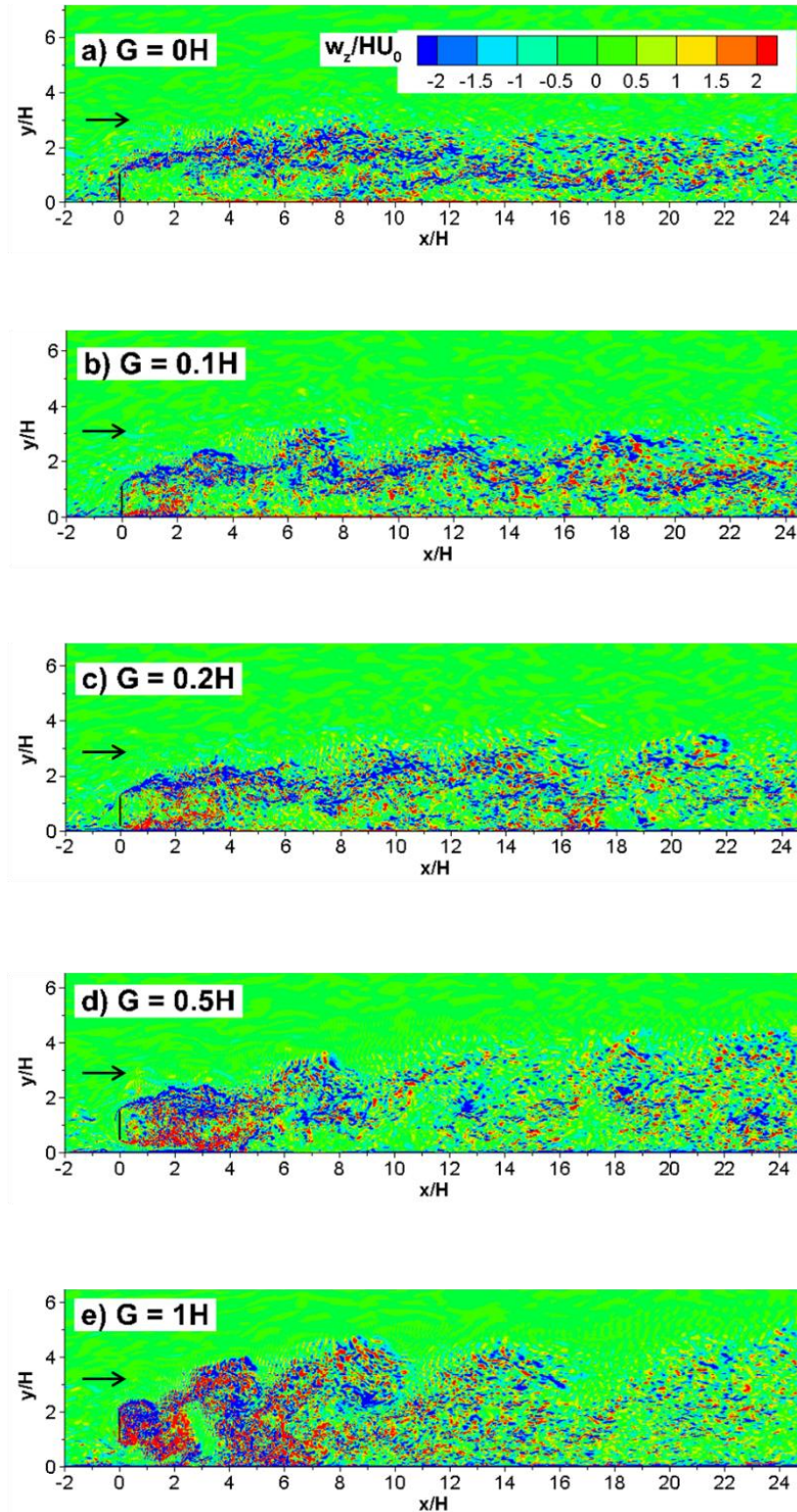
Figure 6.2 Instantaneous spanwise vorticity, $\omega_z/(H/U_0)$, in an x-y plane.
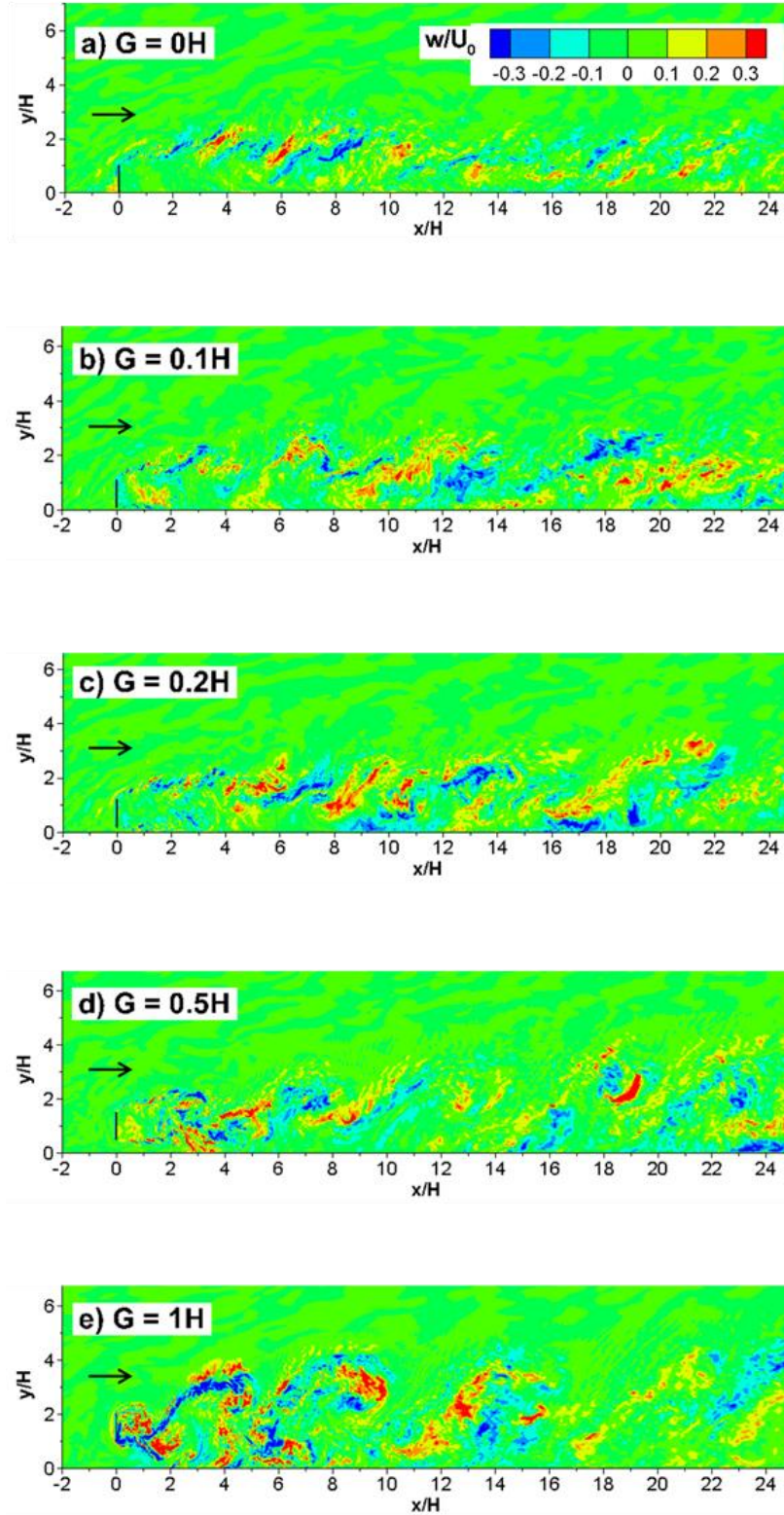
Figure 6.3 Instantaneous spanwise velocity, w/U_0, in an x-y plane.
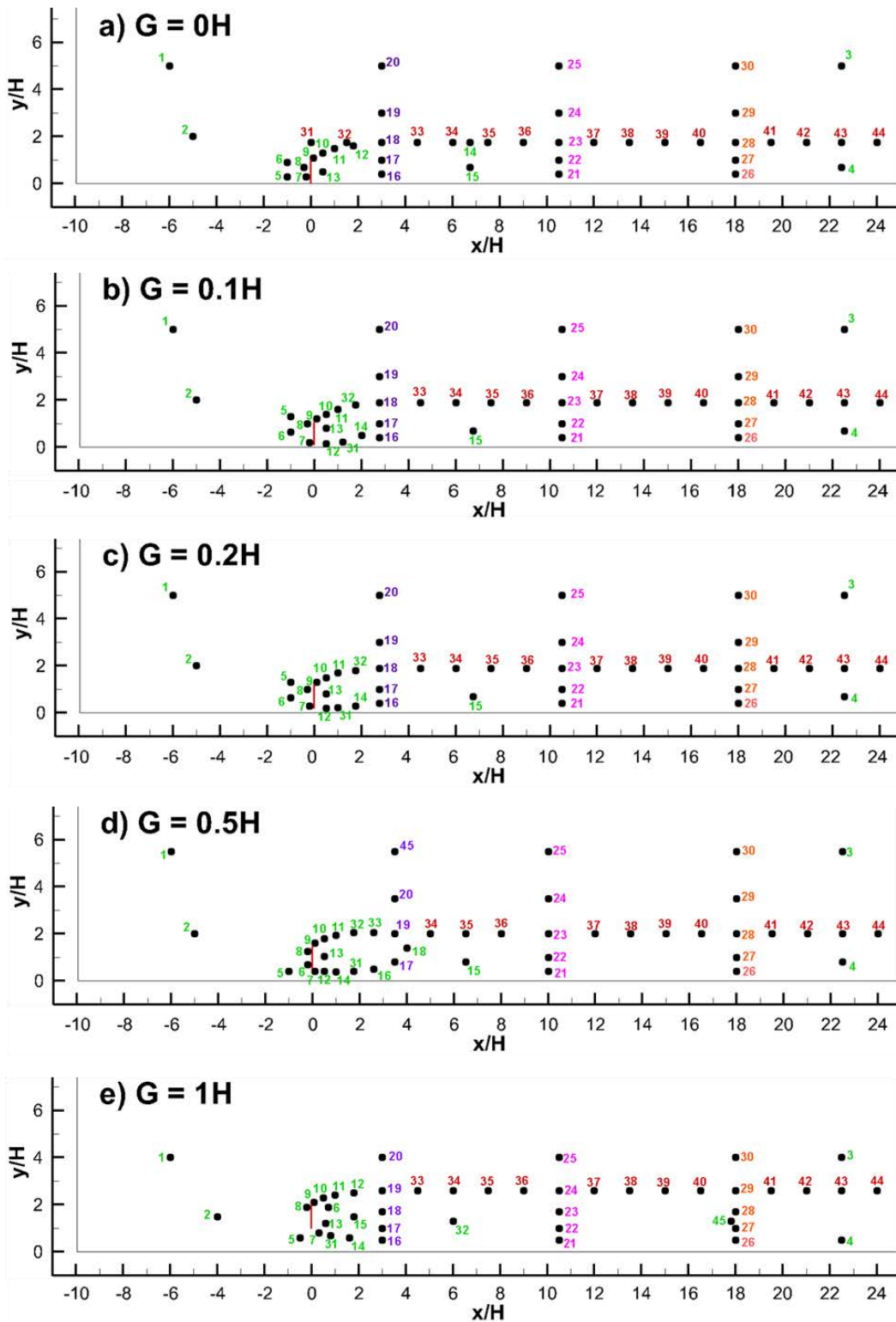
Figure 6.4 Location of points where time series were collected to analyze spectral content of the flow.
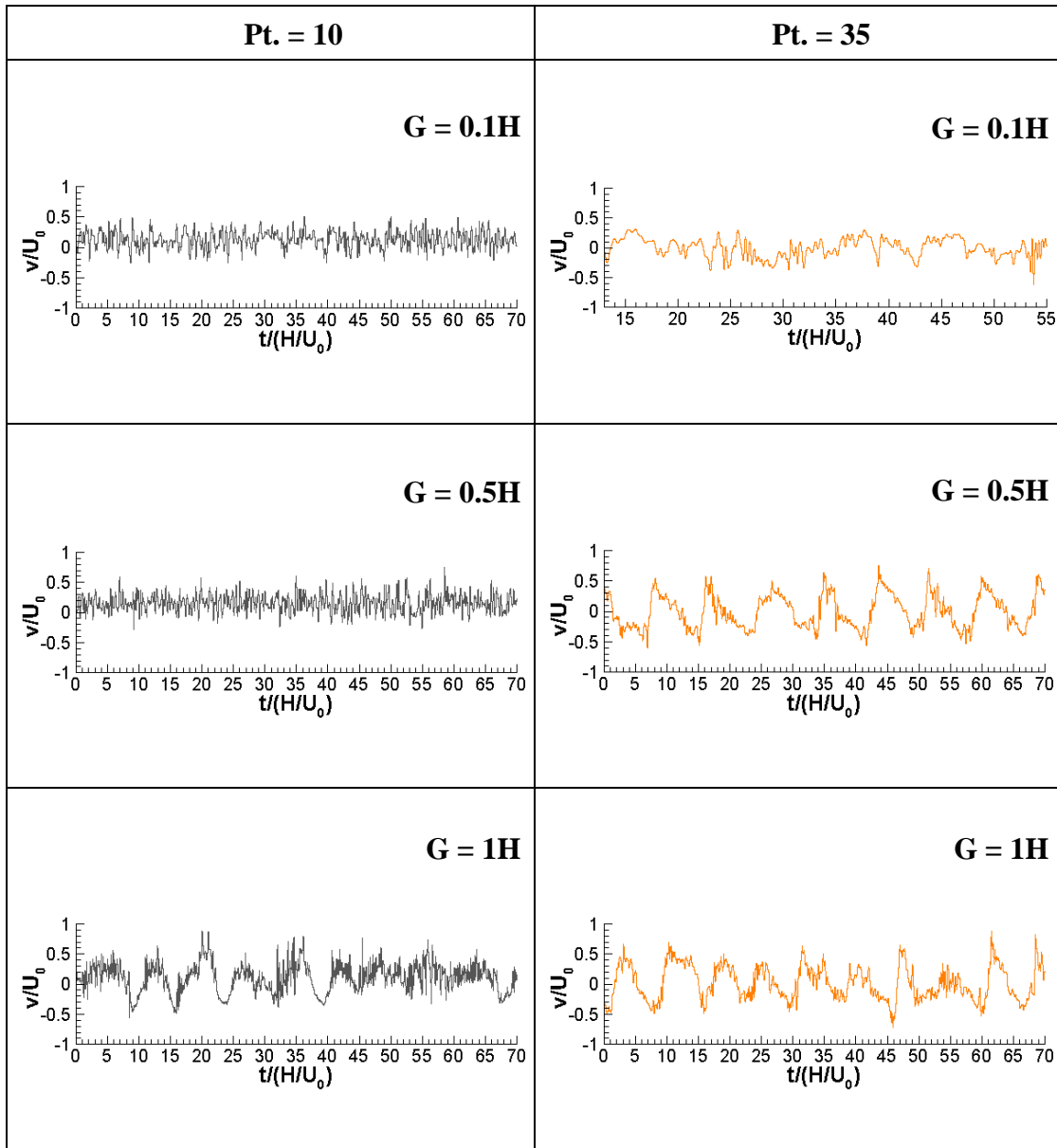
Figure 6.5 Time series of vertical velocity at point 10 (x=0.5H) and point 35 (x=7.5H) for cases G=0.1H, G=0.5H and G=1H. Location of points is shown in Figure 6.13. The spanwise coordinate is z=1.75H (mid length).
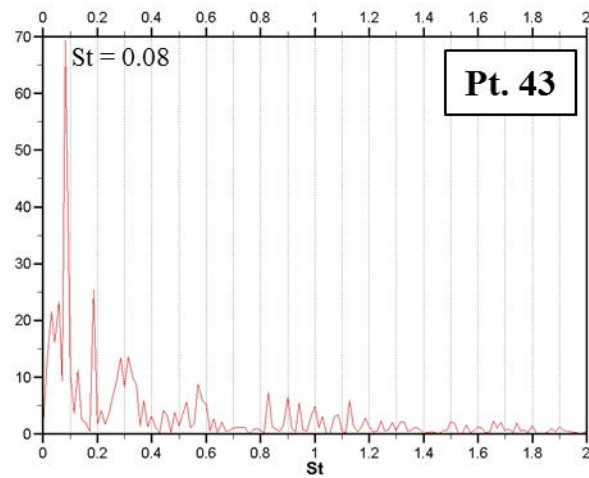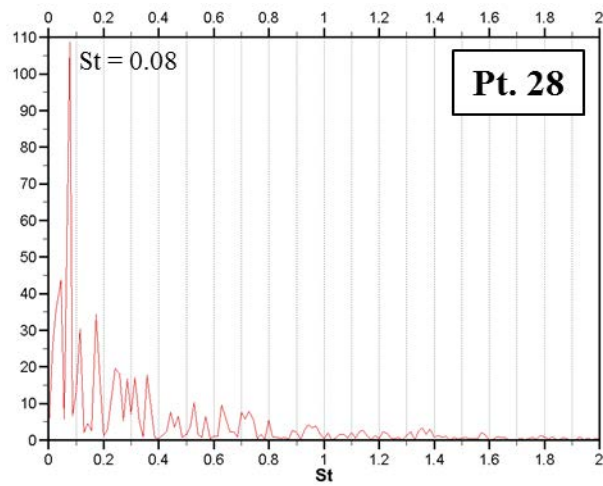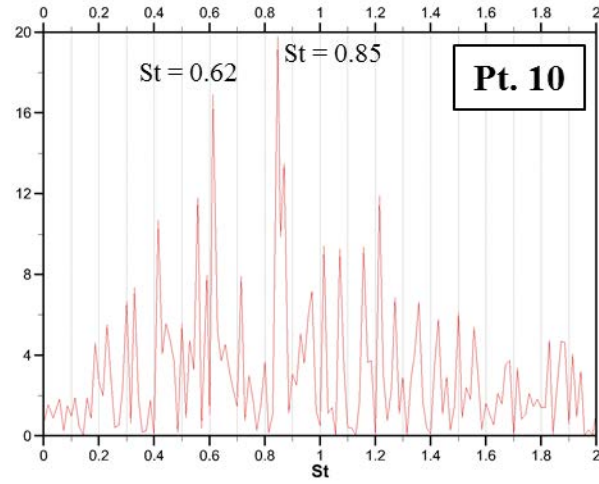
Figure 6.6 Power spectra of vertical velocity for G=0H case at: point 10 (x=0.5H, y=1.3H), point 28 (x=18H, y=1.76H) and point 43 (x=22.5H, y=1.76H). Location of points is shown in Figure 6.13a.

176
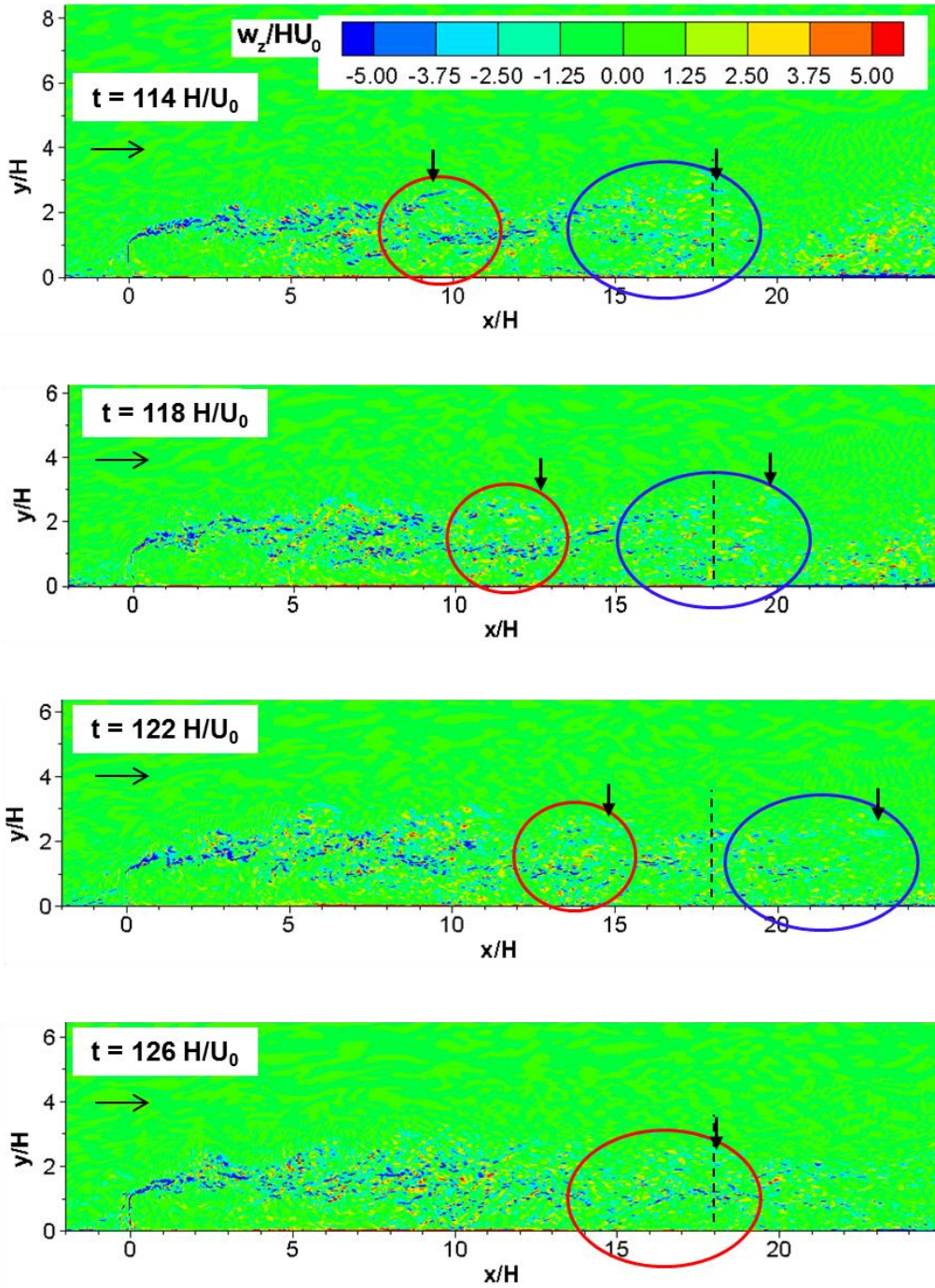
Figure 6.7 Temporal evolution of the spanwise vorticity field in the G=0H case, showing advection of large-scale eddies into the upstream part of the SSL, around x=18H. The two successive eddies are identified using a red and a blue circle. The period of passage of such an eddy is $12H/U_0$ corresponding to St=0.08.

177
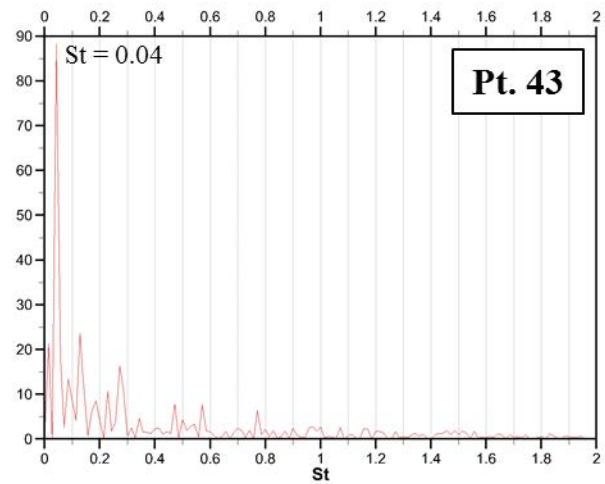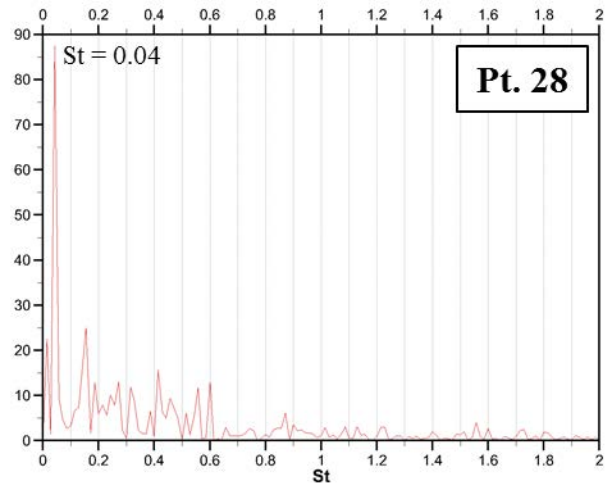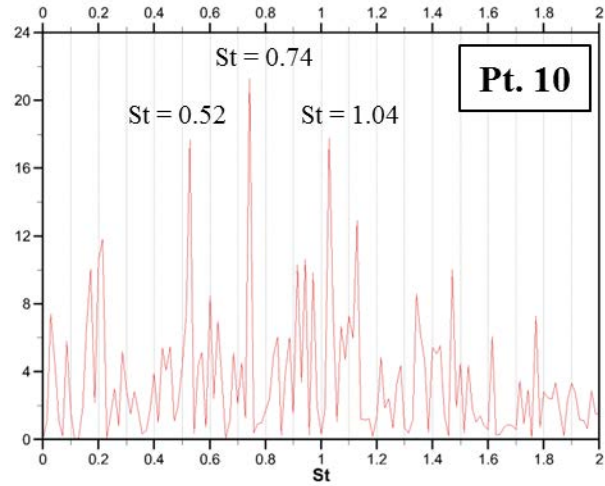
Figure 6.8 Power spectra of vertical velocity for G=0.1H case at: point 10 (x=0.5H, y=1.3H), point 28 (x=18H, y=1.76H) and point 43 (x=22.5H, y=1.76H). Location of points is shown in Figure 6.13b.

178
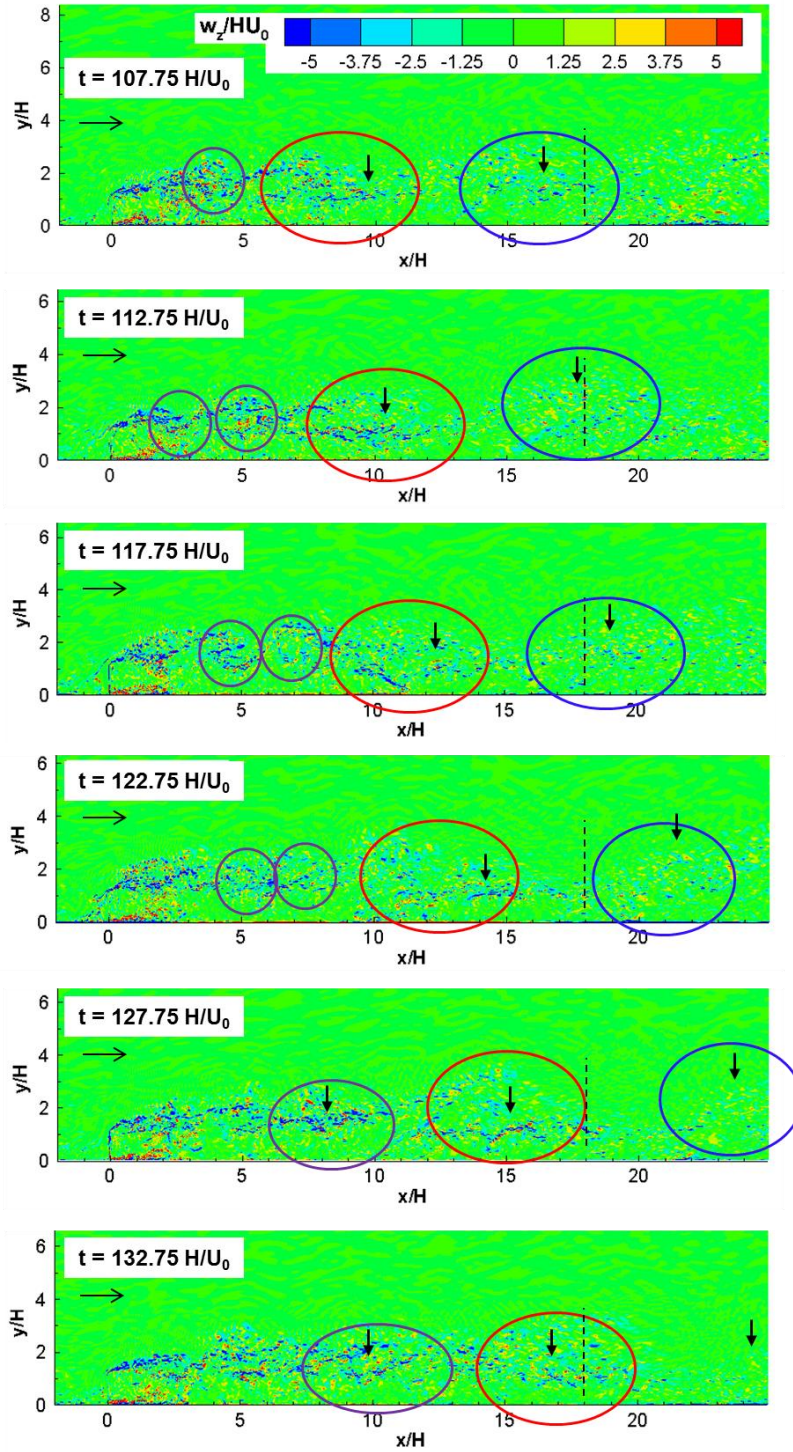
Figure 6.9 Temporal evolution of the spanwise vorticity field in the G=0.1H case, showing advection of large-scale eddies into the upstream part of the SSL, around x=18H. The two successive eddies are identified using a red and a blue circle. The period of passage of such an eddy is $25H/U_0$ corresponding to St=0.04. Also shown is the merging between two billows shed in the top SSL close to the region where the mean flow reattaches.
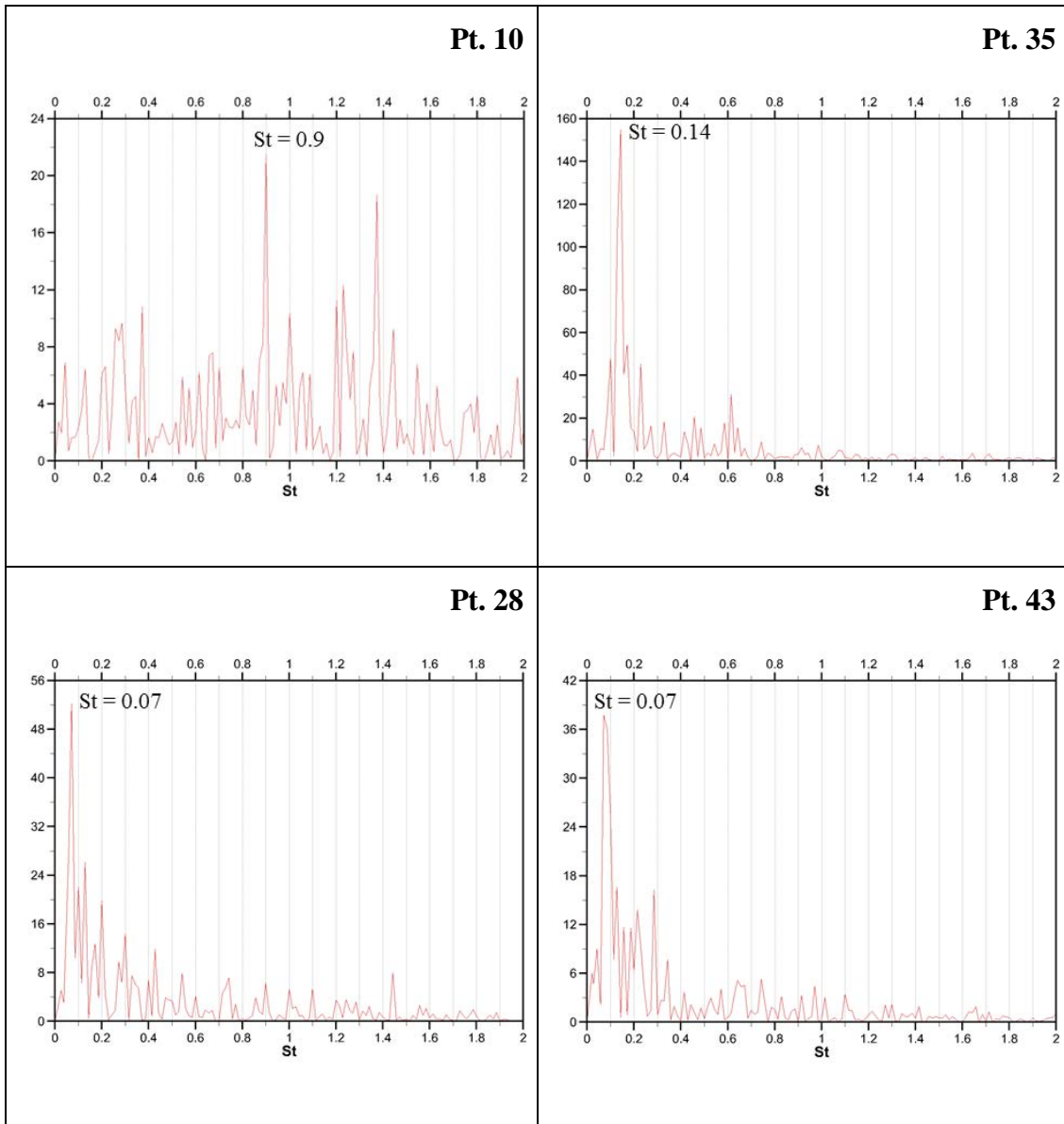
Figure 6.10 Power spectra of vertical velocity for G=0.2H case at: point 10 (x=0.5H, y=1.3H), point 35 (x=7.5H, y=1.9H), point 28 (x=18H, y=1.76H) and point 43 (x=22.5H, y=1.76H). Location of points is shown in Figure 6.13c.
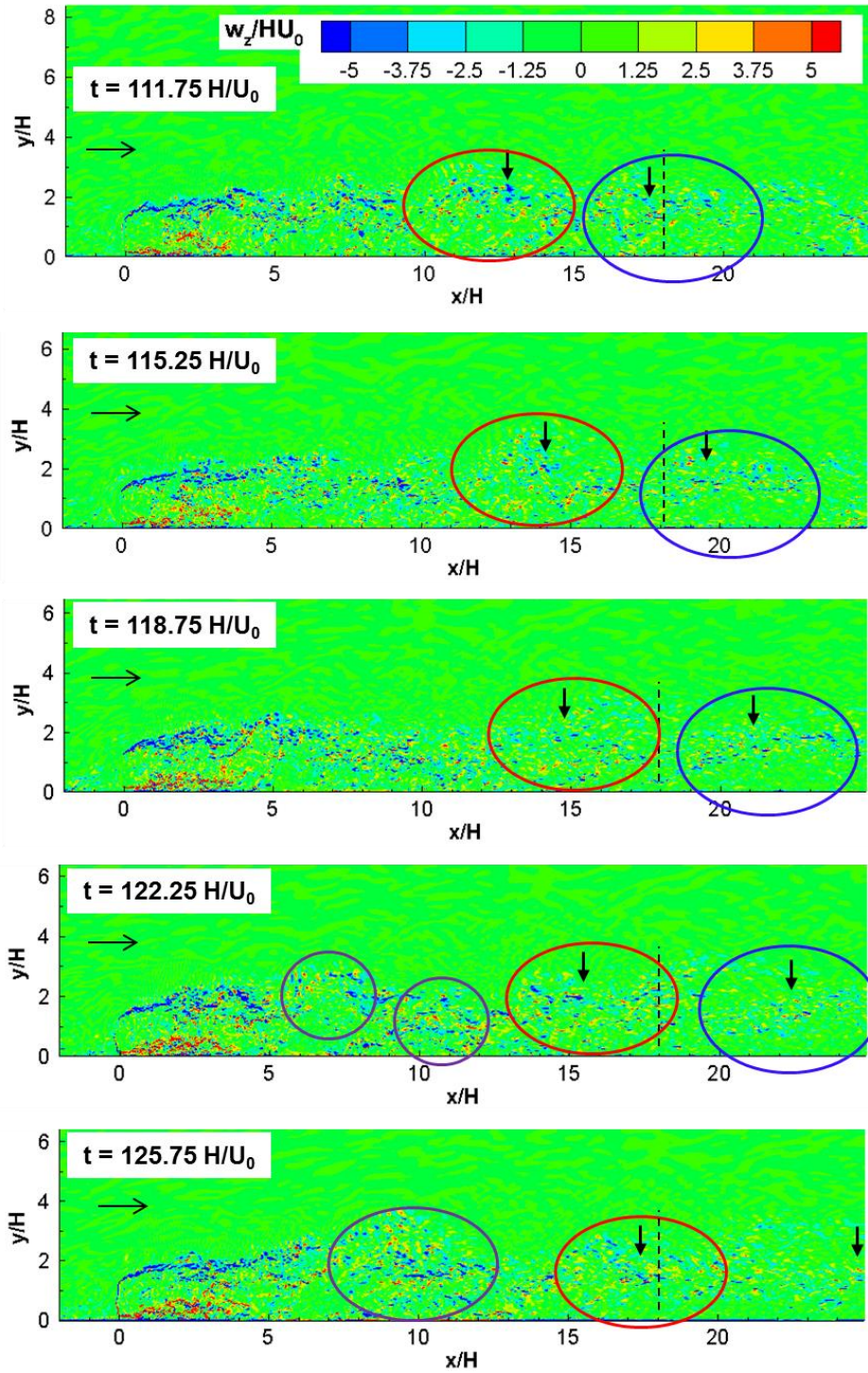
Figure 6.11 Temporal evolution of the spanwise vorticity field in the G=0.2H case, showing advection of large-scale eddies into the upstream part of the SSL, around x=18H. The two successive eddies are identified using a red and a blue circle. The period of passage of such an eddy is $14H/U_0$ corresponding to St=0.07. Also shown is the two bottom frames is the merging between two billows shed in the top SSL close to the region where the mean flow reattaches.
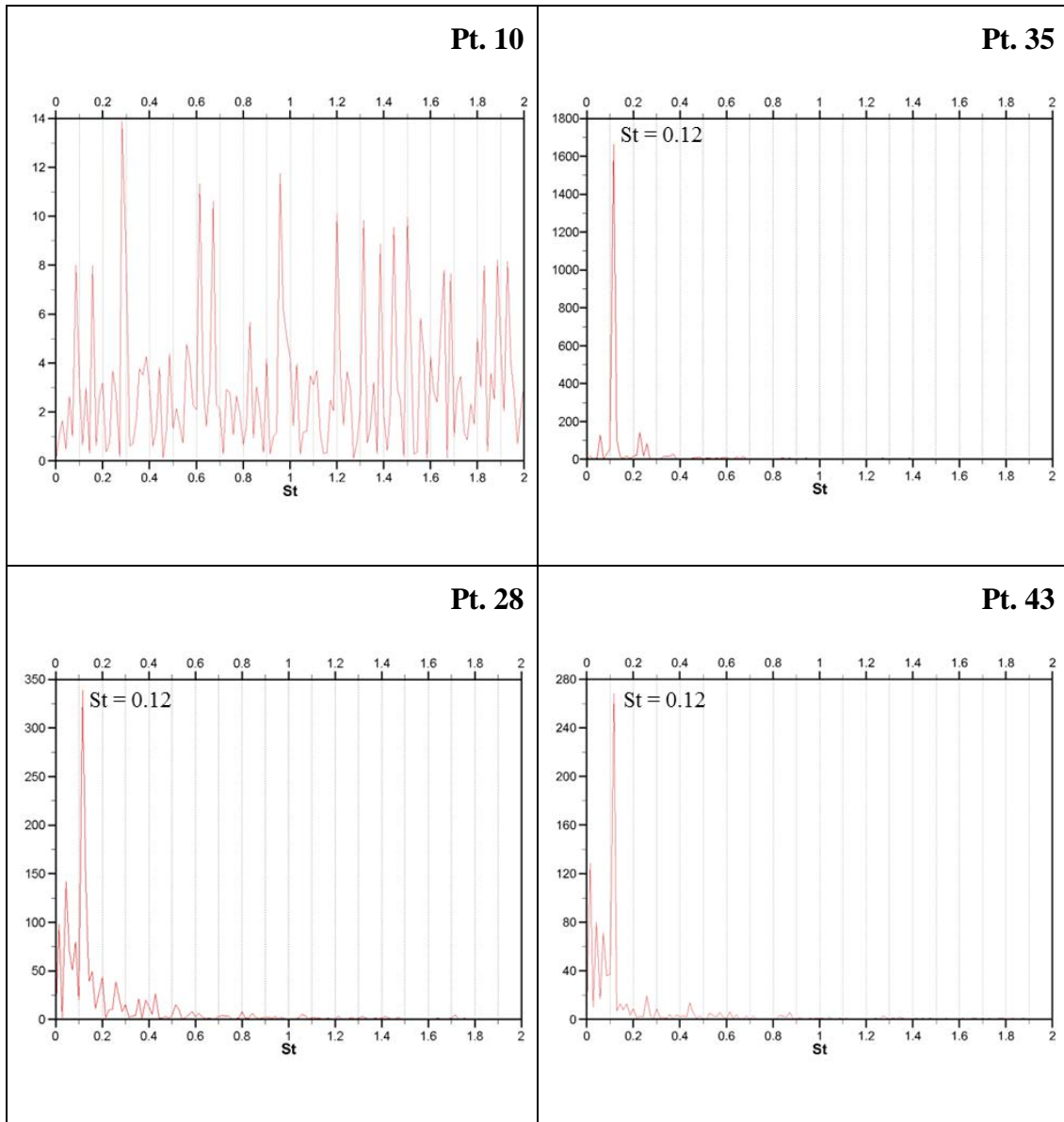
Figure 6.12 Power spectra of vertical velocity for G=0.5H case at: point 10 (x=0.5H, y=1.3H), point 35 (x=7.5H, y=1.9H), point 28 (x=18H, y=1.76H) and point 43 (x=22.5H, y=1.76H). Location of points is shown in Figure 6.13d.
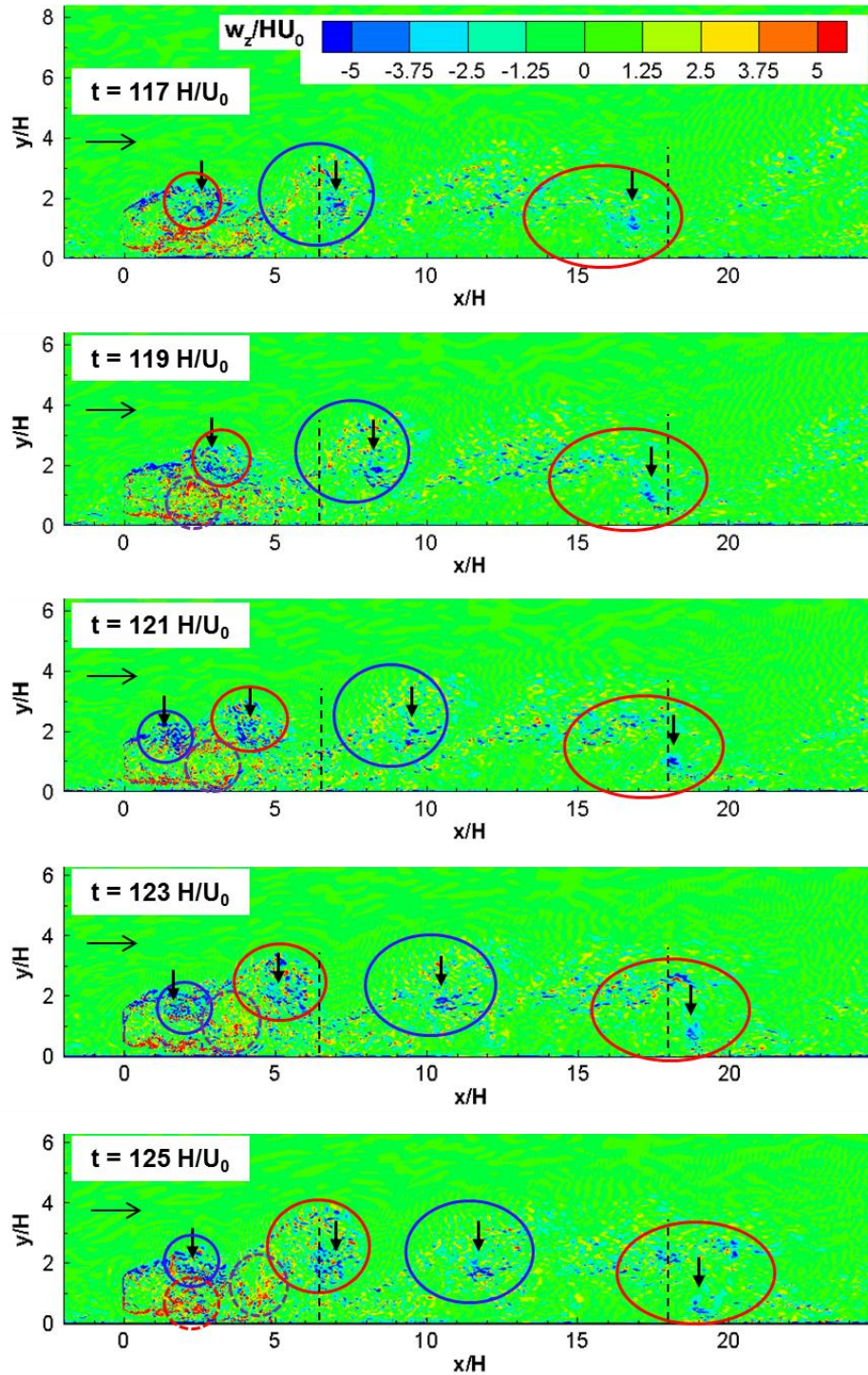
Figure 6.13 Temporal evolution of the spanwise vorticity field in the G=0.5H case, showing advection of large-scale eddies into the upstream part of the SSL, around x=6.5H and 18H. The two successive eddies are identified using a red and a blue circle. The period of passage of such an eddy is $8H/U_0$ corresponding to St=0.12. Also shown are the billows shed from the bottom SSL and their entrainment by the billows advected in the top SSL.
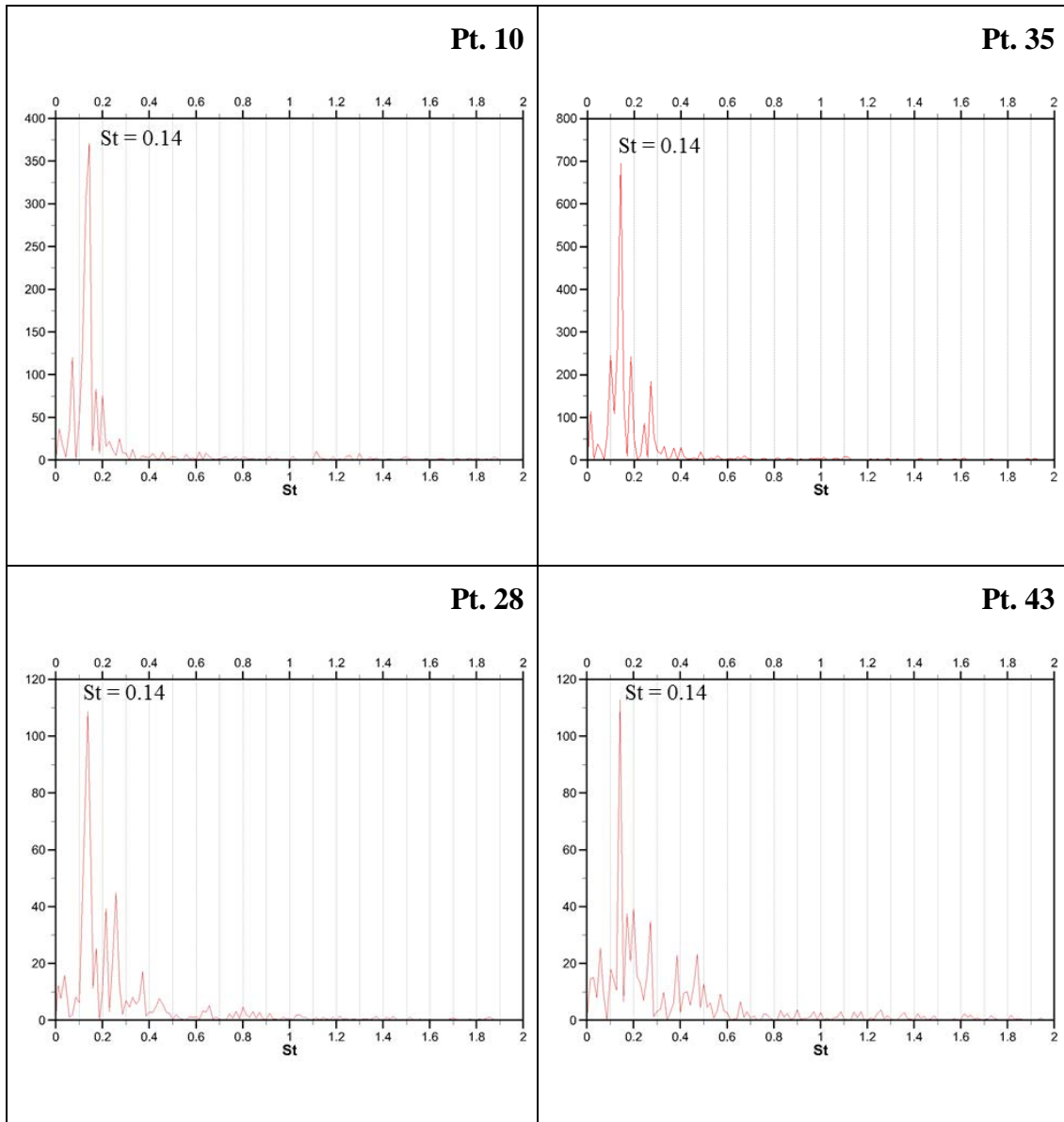
Figure 6.14 Power spectra of vertical velocity for G=1.0H case at: point 10 (x=0.5H, y=1.3H), point 35 (x=7.5H, y=1.9H), point 28 (x=18H, y=1.76H) and point 43 (x=22.5H, y=1.76H). Location of points is shown in Figure 6.13c.
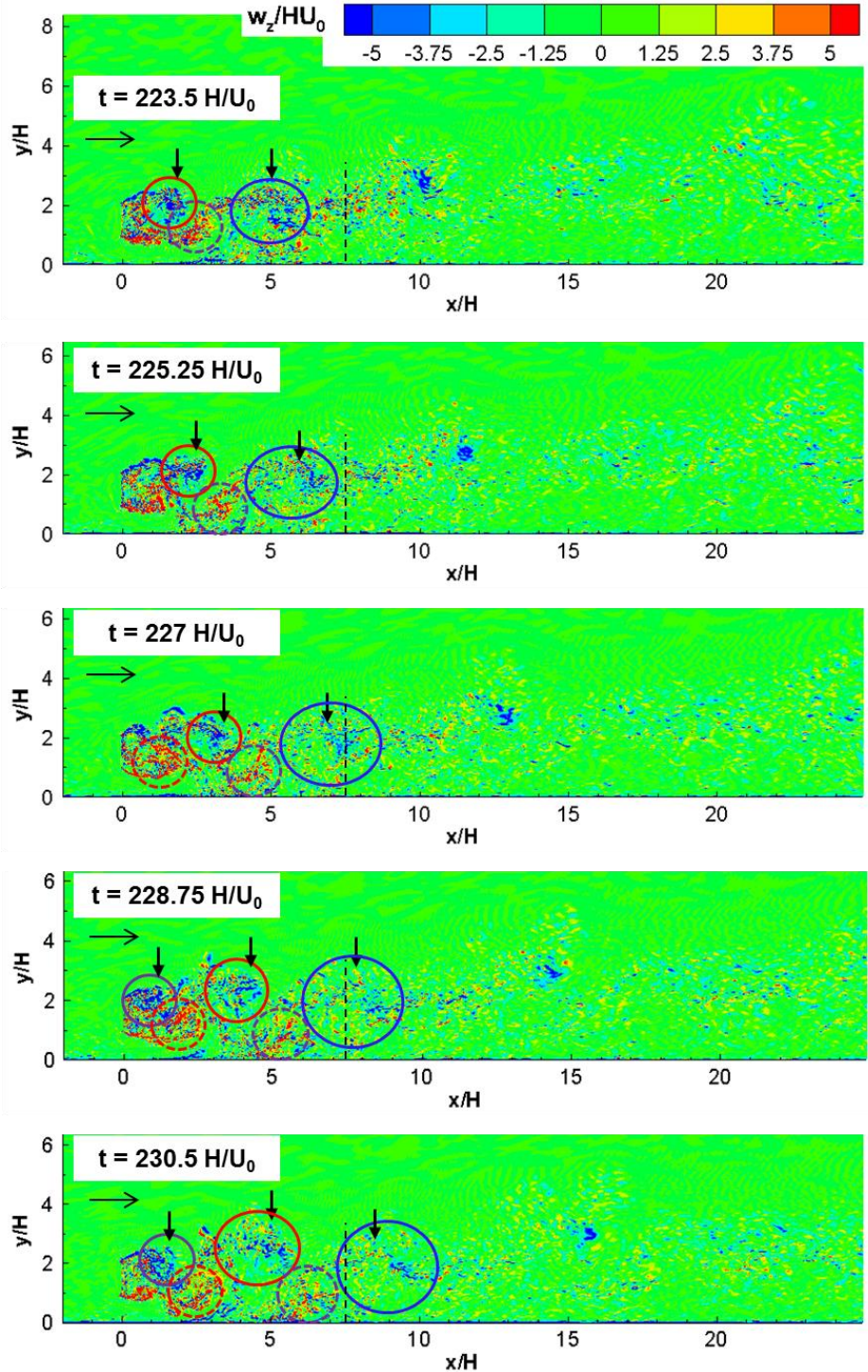
Figure 6.15 Temporal evolution of the spanwise vorticity field in the G=1.0H case, showing advection of large-scale eddies into the upstream part of the SSL, around x=7.5H. The two successive eddies are identified using a red and a blue circle. The period of passage of such an eddy is $7H/U_0$ corresponding to St=0.14. Also shown are the billows shed from the bottom SSL, their interaction with the channel bed and their entrainment by the billows advected in the top SSL.

185
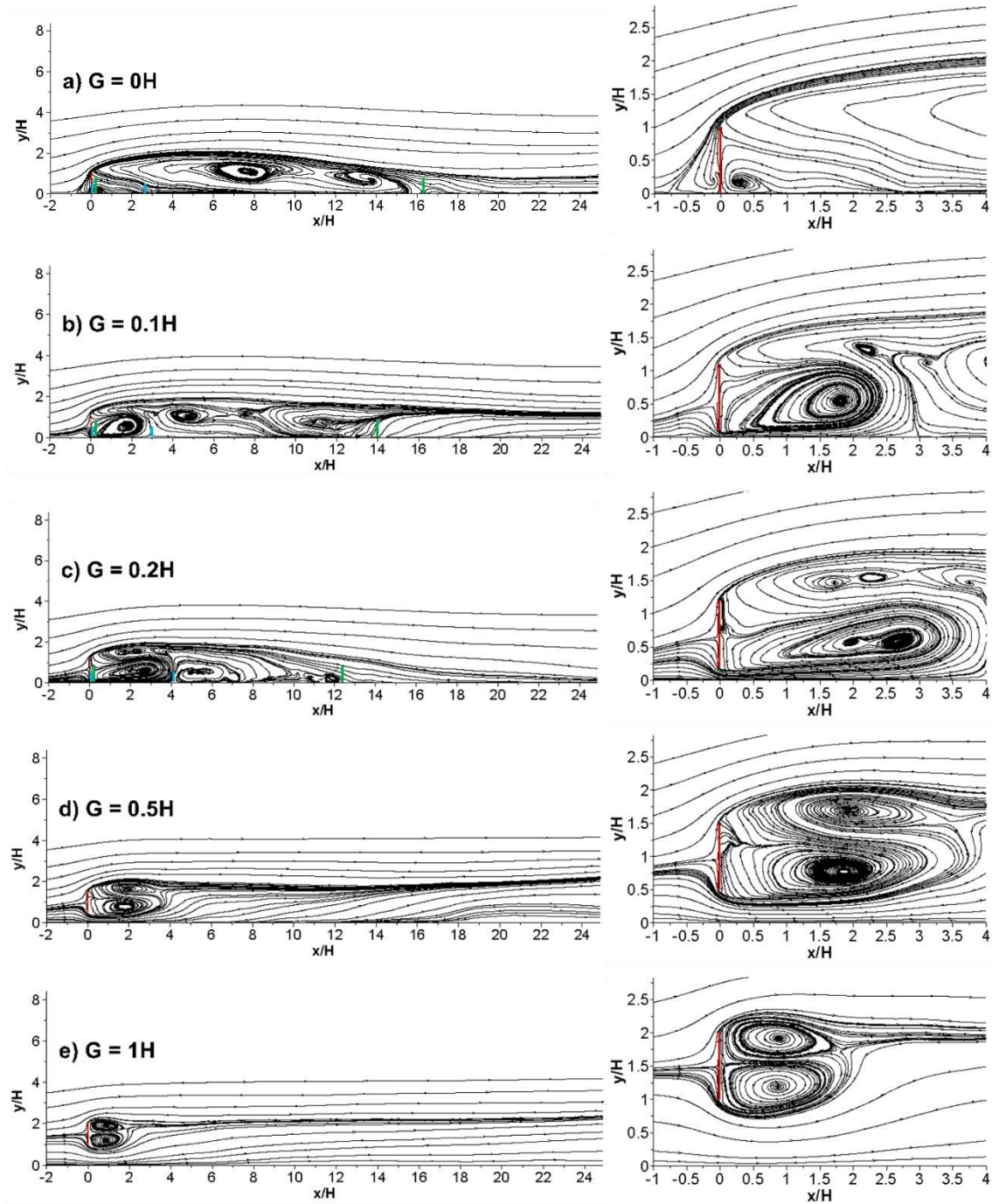
Figure 6.16 Mean flow structure visualized using 2D streamline patterns.
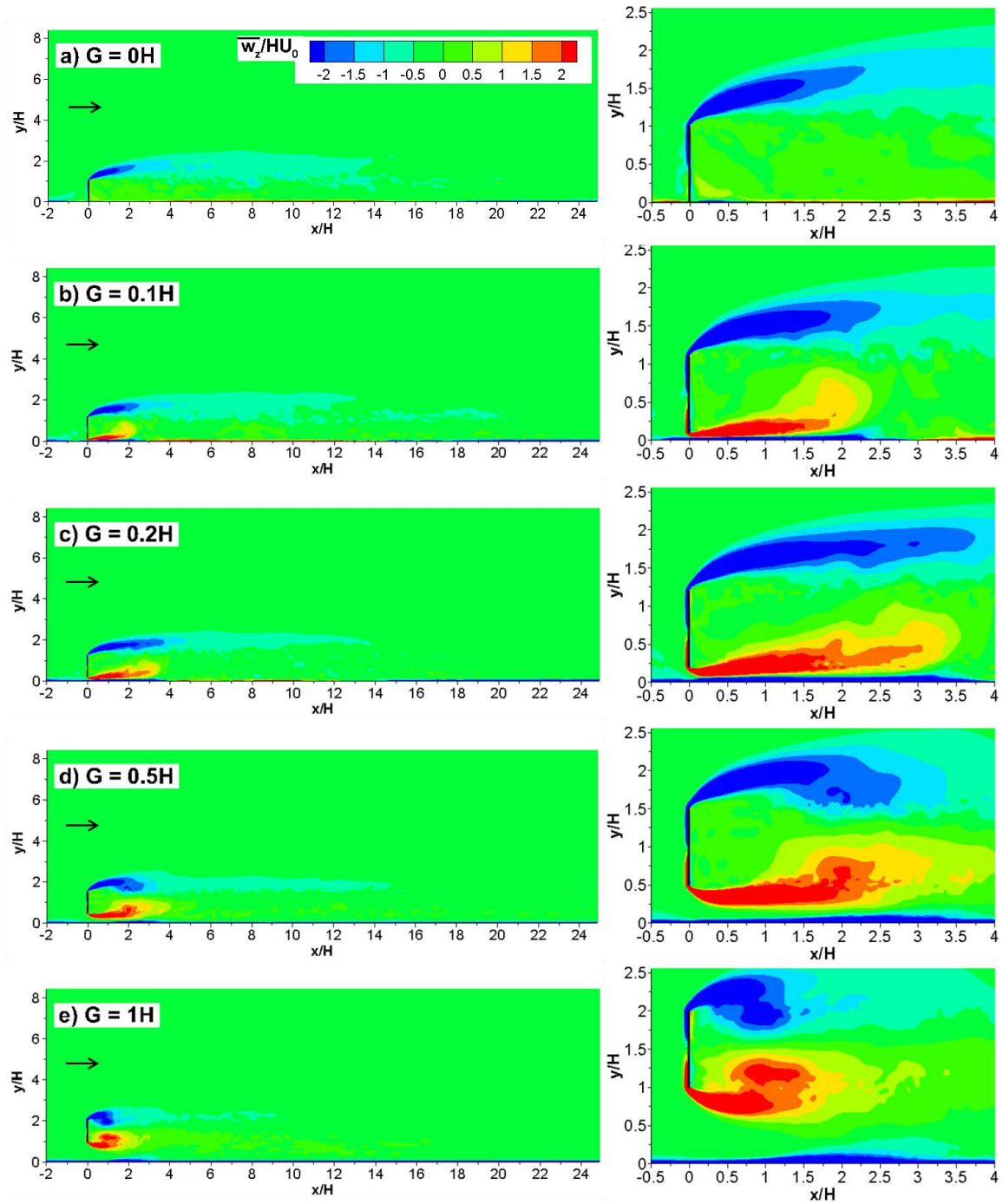
Figure 6.17 Mean spanwise vorticity magnitude, $\overline{\omega_z}/(H/U_0)$, in an x-y plane.
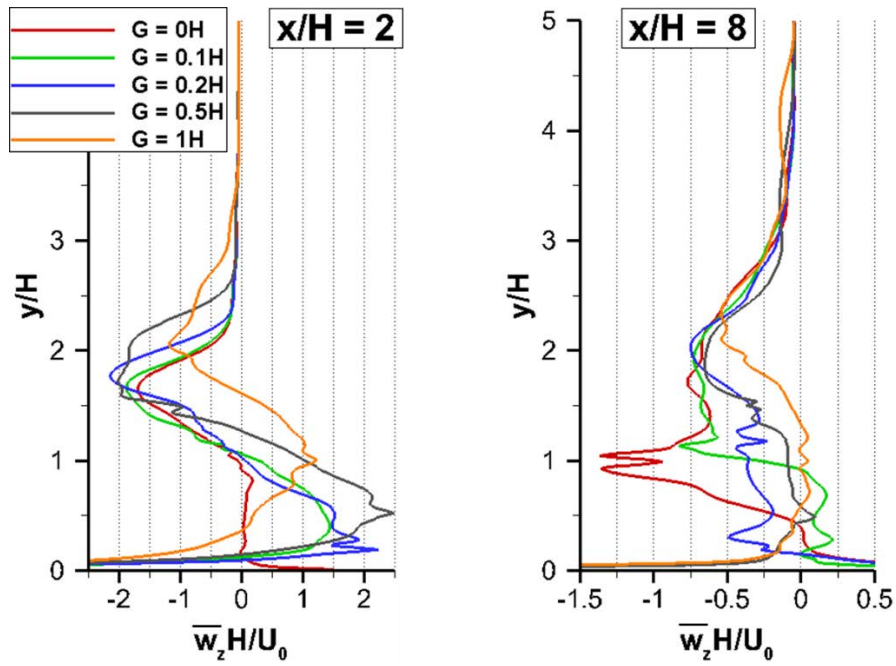
Figure 6.18 Vertical profiles of mean spanwise vorticity magnitude, $\overline{\omega_z}/(H/U_0)$, at x/H=2 and x/H=8.
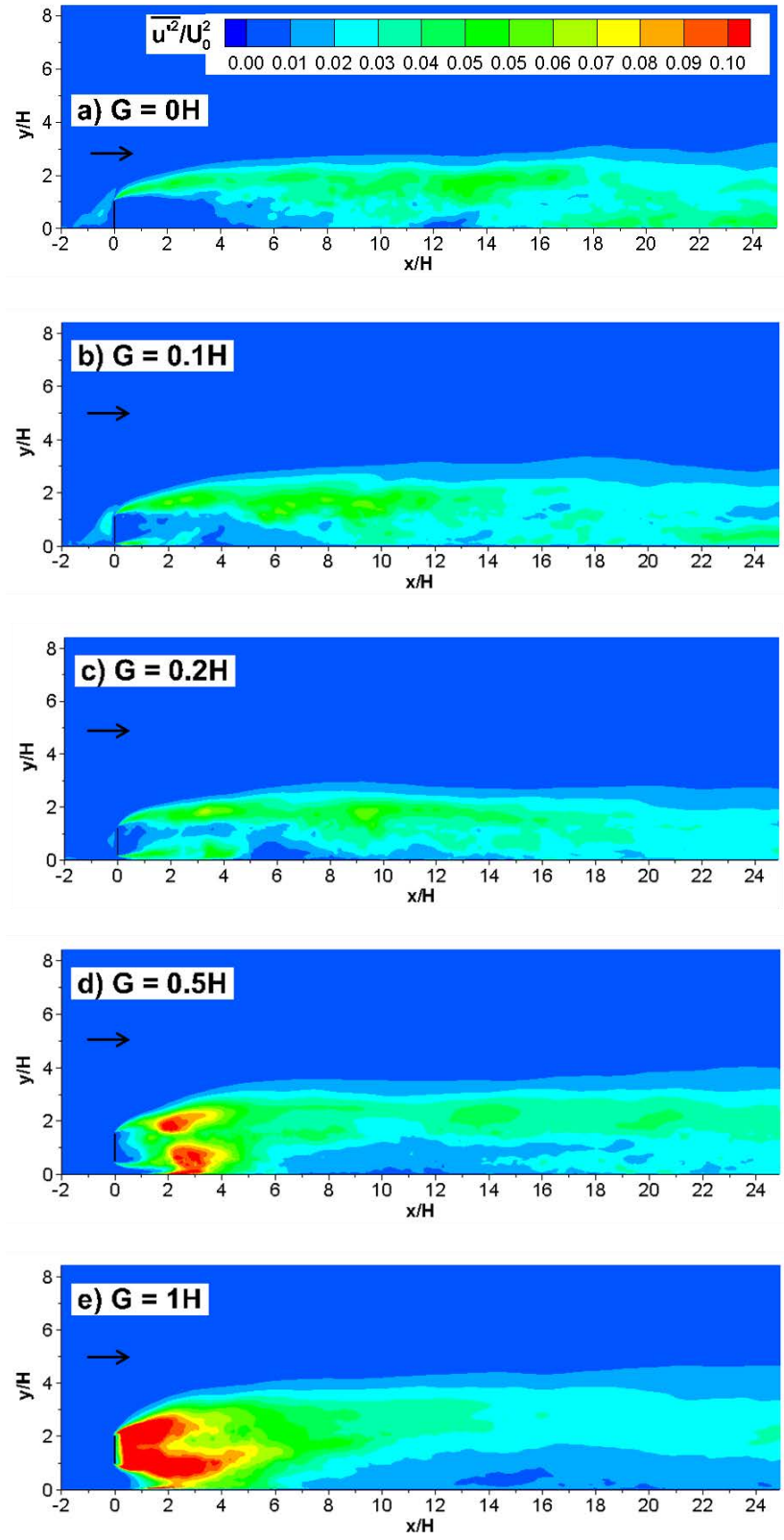
Figure 6.19 Mean streamwise velocity fluctuations, $\overline{u'^2}/U_0^2$, in an x-y plane.
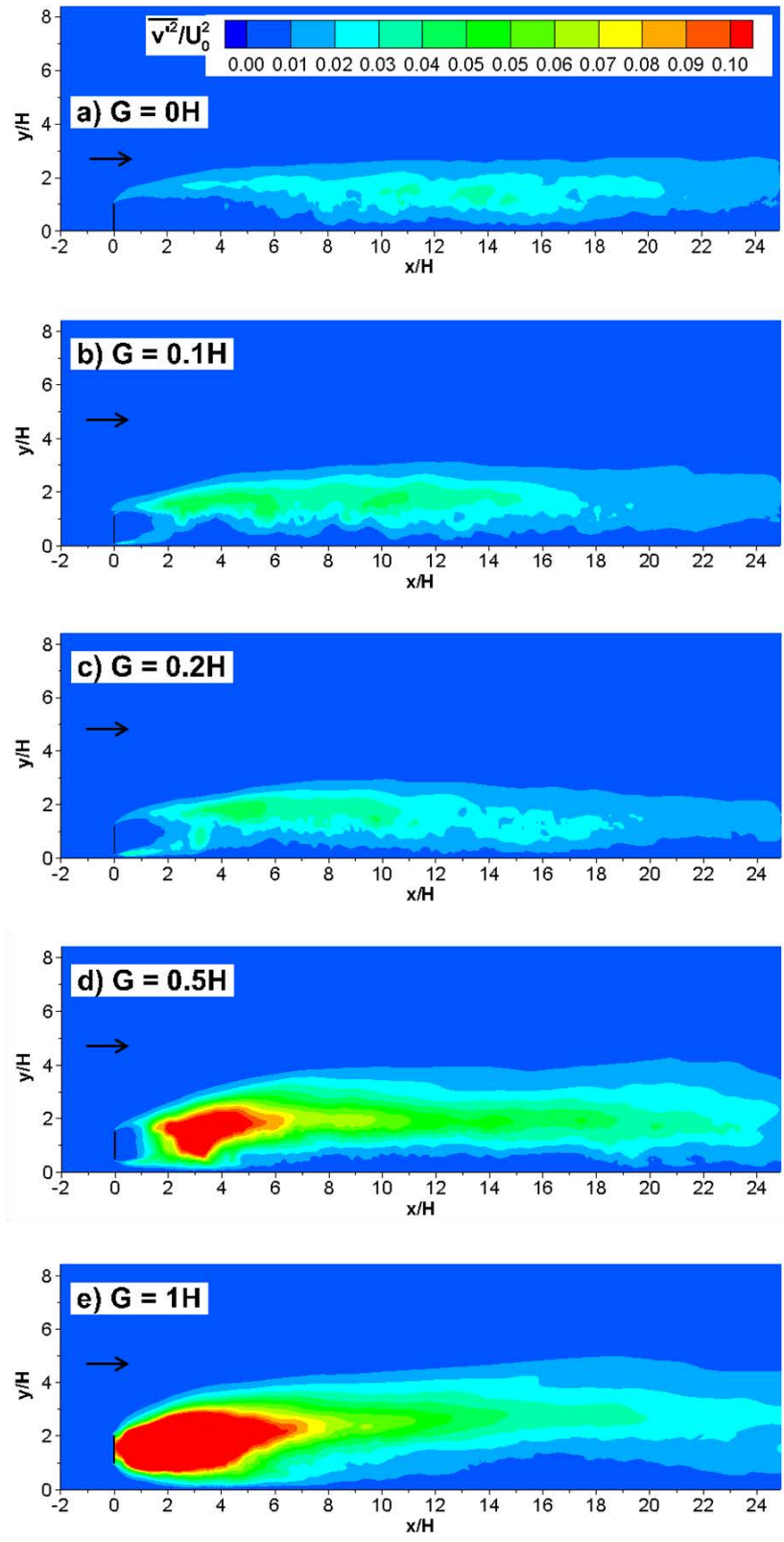
Figure 6.20 Mean vertical velocity fluctuations, $\overline{v'^2}/U_0^2$, in an x-y plane.
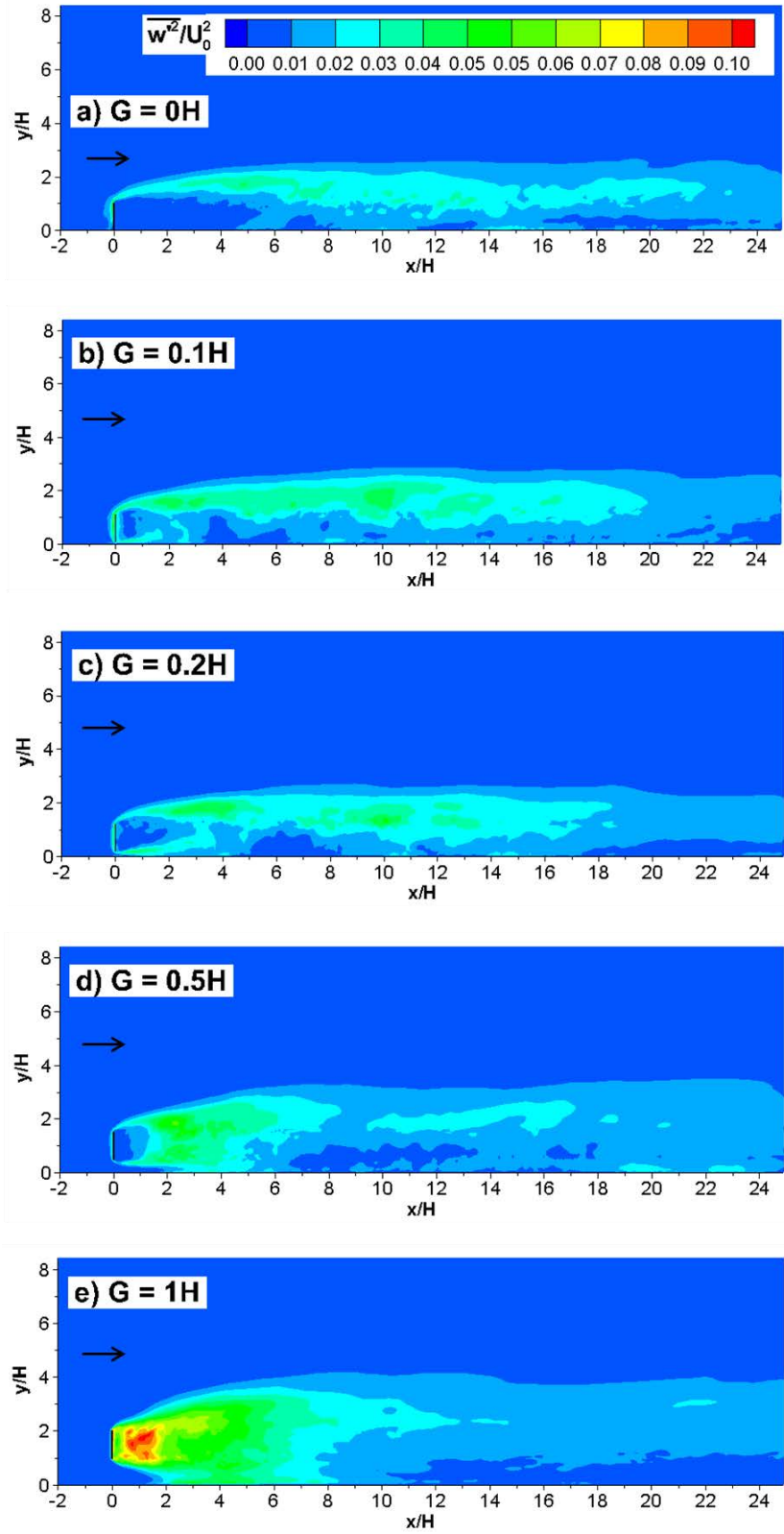
Figure 6.21 Mean spanwise velocity fluctuations, $\overline{w'^2}/U_0^2$, in an x-y plane.
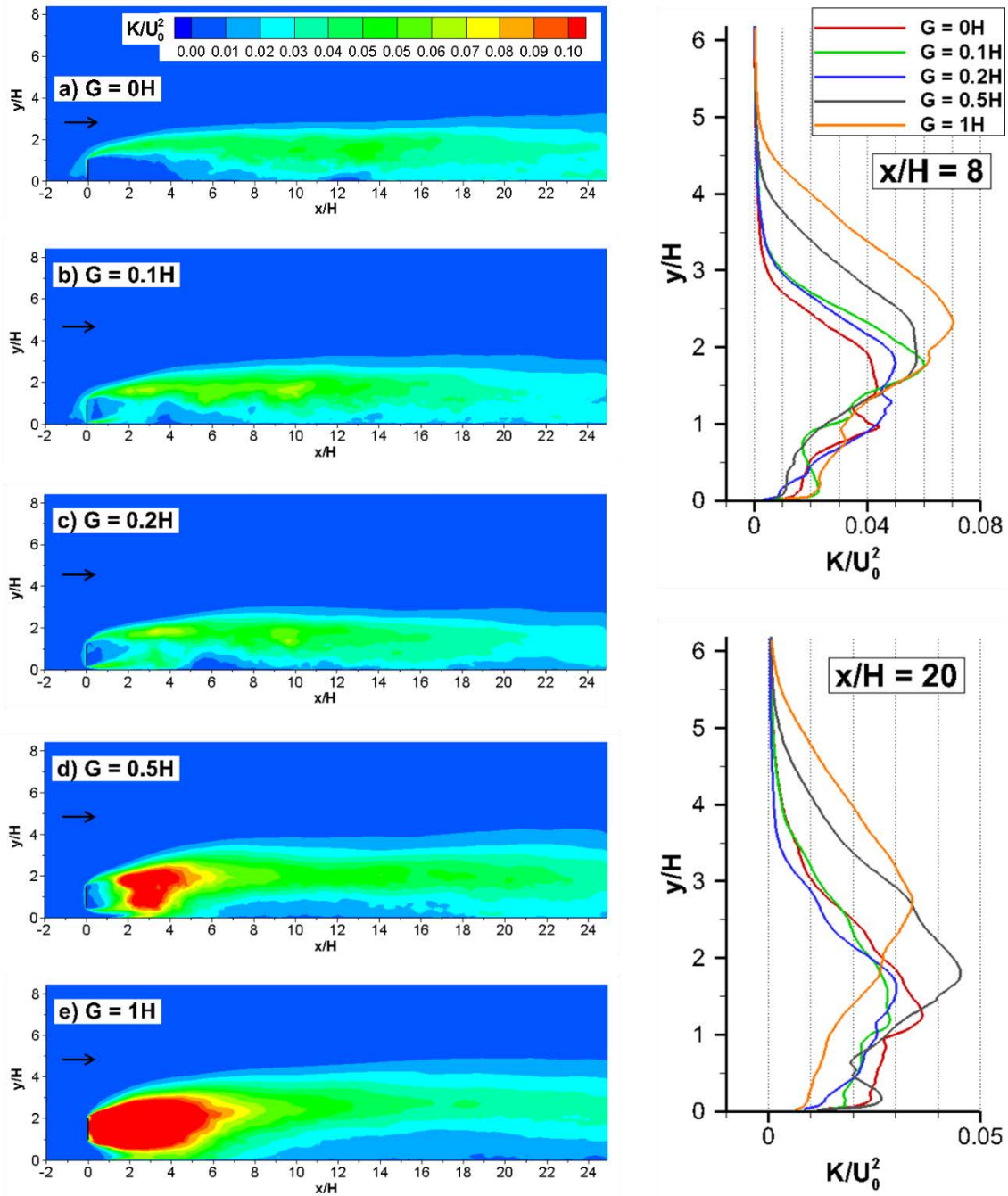
Figure 6.22 Turbulent kinetic energy, K/U_0^2, in an x-y plane. Also shown are vertical profiles of K/U_0^2 at x/H=8 and x/H=20.
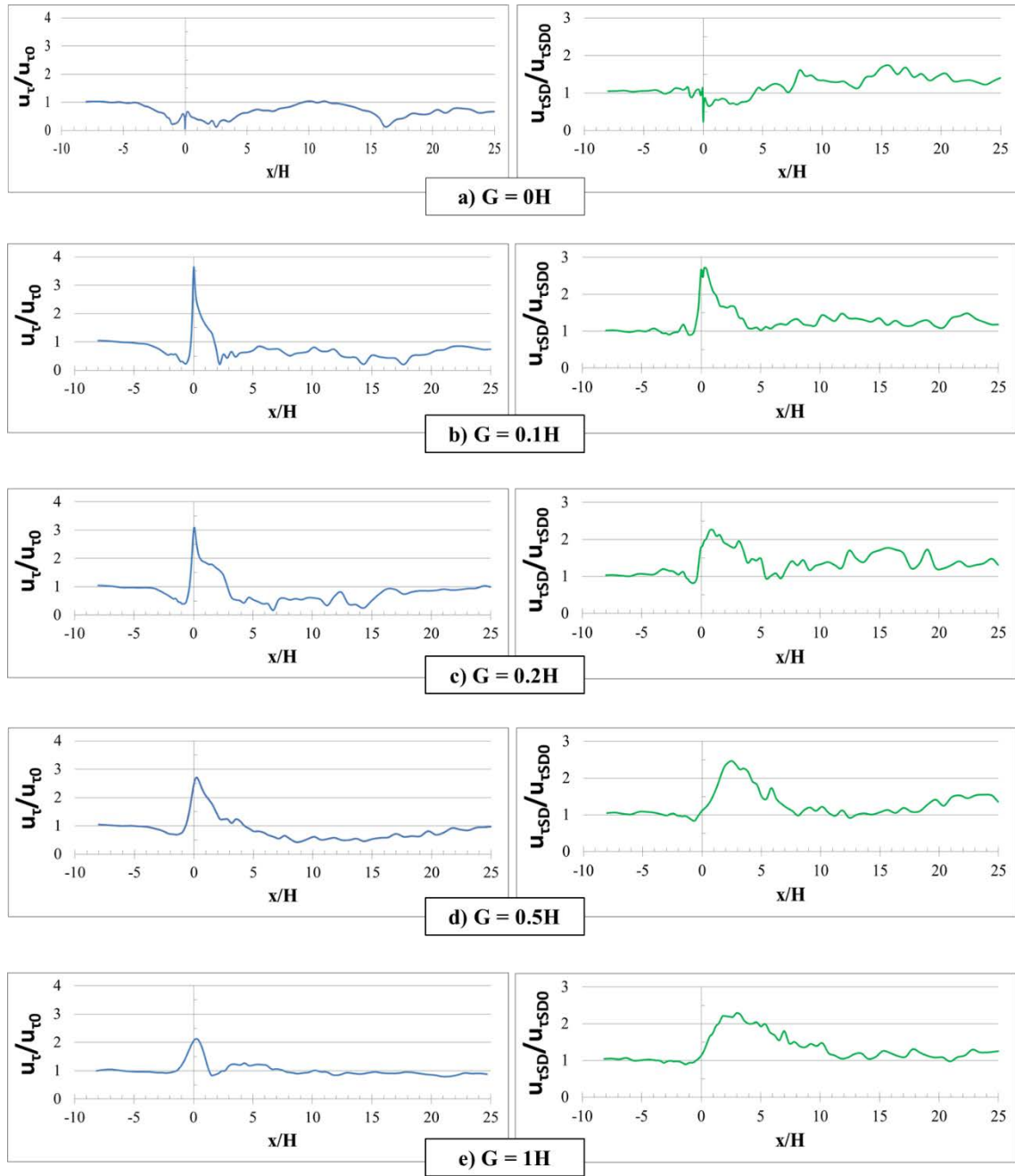
Figure 6.23 Nondimensional spanwise-averaged mean bed friction velocity, $u_\tau / u_{\tau 0}$, where $u_{\tau 0}=0.04U_0$ is the mean bed shear stress in the incoming fully developed turbulent channel flow. Also shown is the nondimensional spanwise-averaged rms of the bed friction velocity fluctuations where $u_{\tau SD0}=0.025U_0$ is the mean rms of the bed shear stress in the incoming fully developed turbulent channel flow.

Table 6.1 Comparison of Strouhal numbers associated with advection of billows in the top SSL.

Case	Point	Streamwise downstream distance from the plate	Region in the wake	St
G=0H	10	0.5H	Top SSL	Energetic range 0.2-1.6
	28	18H	Top SSL/wake	0.08
	43	22.5H	Top SSL/wake	0.08
G=0.1H	10	0.5H	Top SSL	Energetic range 0.1-2.0
	35	7.5H	Top SSL	0.08
	28	18H	Top SSL/wake	0.04
	43	22.5H	Top SSL/wake	0.04
G=0.2H	10	0.5H	Top SSL	Energetic range 0.1-2.0
	35	7.5H	Top SSL	0.14
	28	18H	Top SSL/wake	0.07
	43	22.5H	Top SSL/wake	0.07
G=0.5H	10	0.5H	Top SSL	Energetic range 0.1-2.0
	35	6.5H	Top SSL	0.12
	28	18H	Top SSL/wake	0.12
	43	22.5H	Top SSL/wake	0.12
G=1H	10	0.5H	Top SSL	Energetic range 0.02-2.0
	35	7.5H	Top SSL	0.14
	28	18H	Top SSL/wake	0.14
	43	22.5H	Top SSL/wake	0.14

Table 6.2 Comparison of integral parameters.

Case	$\overline{C_D}$	C_D^{rms}	l_1	h_1	l_2
G = 0H	0.78	0.03	16.2H	1.8H	-
G = 0.1H	0.89	0.04	14.0H	1.8H	-
G = 0.2H	0.93	0.045	12.5H	1.8H	4.2H
G = 0.5H	1.11	0.06	-	-	3.8H
G = 1H	1.57	0.2	-	-	2.0H

CHAPTER 7 EFFECT OF VARYING BOTTOM GAP ON FLOW PAST A POROUS VERTICAL PLATE

7.1 Introduction

The main objective of this chapter is to use LES to study the effect of varying bottom gap on flow past a vertical porous plate placed on a horizontal and smooth channel bottom surface. The presence of a bottom gap has two main effects on the plate. As the incoming flow is fully developed, the average velocity of the incoming flow between the bottom and top of the plate varies with G/H. Moreover, the flow through the bottom gap is strongly accelerated, which also reduces the pressure. As a result, a vertical force acts of the plate. However, for the thin plates considered in this study, the lift force is small. Finally, a bottom separated shear layer forms at the bottom extremity of the plate. This bottom SSL can be subject to strong interactions with the top SSL and also with the channel bottom. Five simulations are performed with relative bottom gaps G=0H, 0.1H, 0.2H, 0.5H and 1.0H, same as the ones considered in the parametric study performed in Chapter 6 for solid plates (P=0%). The plate porosity was kept constant (P=36%) in the simulations discussed in the present chapter. A sketch of the porous vertical plate used in the five test cases is shown in the Figure 7.1a. The case with G=0H is the same as the one considered in Chapter 5 (P=36% case).

7.2 Simulation Setup

The computational domain, plate height (H), location of the plate (10H from the inflow section) and the coordinate system are identical to the ones considered in the simulations discussed in Chapters 5 and 6. The thickness of the solid plate is 0.02H and the length of the computational domain is 35H. The computational domain contains around 25 million (768x512x64) grid points in the G=0H, 0.1H and 0.2H cases and 28 million

(728x576x64) grid points in the G=0.5H and G=1H cases. Figures 7.1b and 7.1c show the mesh in a x-y plane around the location of the porous plate, for the G=1H case.

The x-axis is aligned with the incoming flow direction and the z-axis is aligned with the vertical direction relative to the horizontal bottom surface of the channel. The plate height, H, is used as the length scale. The uniform incoming flow velocity, U_0, is used as the velocity scale. The simulations were performed for a Reynolds number of Re=20,000.

Discretization along the x and z directions is the same for all five cases. Only the discretization along the y axis is changed with G/H due to the need to resolve the flow near the solid elements of the porous plate and over the gap region. The mesh is uniform along the z direction. Grid points are clustered around the x=constant and y=constant locations corresponding to the solid surfaces of the solid plate (see Figure 7.1c) to resolve the attached boundary layers on these surfaces. When generating the mesh, a minimum grid spacing ($n^+=u_\tau n/\nu$, n is the wall normal direction) of about 2 wall units (assuming u_τ/U_0=0.05) was used in the wall-normal direction near the solid surfaces of the porous plate. This corresponds to a cell size of about 0.002H in the wall normal direction. Away from the plate, the average dimensions of the 3D cells are increased to about 0.07Hx0.06Hx0.05H.

All the boundary conditions are identical to those used in the simulations discussed in Chapter 5. The time step used in simulations was $0.001H/U_0$. Statistics were then collected over $70H/U_0$.

7.3 Flow Structure

7.3.1 Instantaneous Flow Fields

Similar to the case of a solid plate discussed in Chapter 6, the upstream part of the top SSL is the most coherent (e.g., in terms of the circulation and size of the eddies advected) in the G=0H case, in which the deflection of the flow past the top of the plate and thus the turbulence production by mean shear are the largest among the five cases. Still, even for the G=0H case, only a fraction of the incoming flow is deflected around the plate, the other part is advected through the plate and forms the bleeding flow. This is why for same G/H the top SSL is always weaker for a porous plate compared to a solid plate. As opposed to the solid plate case, where a large recirculation bubble forms behind the plate, only two small recirculation bubbles are observed in the corresponding porous plate case with G/H=0 (see also Figure 7.13a). Still, the eddy structure of the top SSL in the G=0H case (Figure 7.2a) looks qualitatively similar to the one observed for a solid plate (Figure 6.2a), with large billows forming downstream of the end of the separation bubble (x/H>13) that interact with the channel bed as they are advected downstream. The bleeding flow acquires large-scale turbulence generated by the jets forming in between the solid elements of the porous plate. The streamwise momentum of the bleeding flow decays with the distance from the plate. Its main role is to impede the reattachment of the top SSL to the bed surface.

For G/H>0 (Figures 7.2b and 7.2c), a second SSL forms at the bottom of the plate and part of the incoming flow is diverted into the bottom gap, where the flow acceleration is very large, especially for relatively large bottom gaps (e.g., for G/H=1). Though the bottom SSL curves toward the top SSL, as also observed for solid plates, its effect in terms of influencing the dynamics of the large eddies advected into the top SSL and favoring

merging of successively shed co-rotating eddies in the top SSL is not significant, as long as G/H<0.3. This is an important difference with the case of solid plates with small bottom gaps, where the bottom SSL induced strong disturbances of the top SSL that resulted in the formation of larger, more coherent eddies in the top SSL than those observed in the G=0H case. The reason for this difference is the presence of a relatively strong the bleeding flow in between the two SSLs that delays the interaction between the SSLs in the porous plate case. Moreover, the small, but highly-3D, eddies generated by the porous plate elements stretch the eddies adevected in the lower SSL, such that for G/H<0.3 no strongly-coherent eddies from the bottom SSL approach the top SSL, even at large distance from the porous plate.

The vortical flow structure changes qualitatively in the G=0.5H case, where the upstream part of the bottom SSL is not anymore in contact with the channel bottom. Though no clearly defined wake billows form at the end of the bottom SSL, the top and bottom SSLs are interacting around x=8H. The wake flow behind the plate starts resembling that of the flow past a porous plate with a very large G/H, in which the lengths of the two SSLs are increasing monotonically with the plate porosity. The main difference is that counter-rotating wake billows are not shed in the wake for G=0.5H. The main reason is that the SSL is oriented slightly away from the plate centerline, such that strong interactions of the eddies advected in the bottom SSL with the channel bed are observed for x/H>4. This slows down these eddies and weakens their rotational movement. As a result they lose fairly rapidly their coherence via vortex stretching induced by the eddies in the bottom boundary layer and also by the highly 3D eddies transported by the bleeding flow.

For even larger bottom gaps (G=1H case in Figure 7.2), counter-rotating billows start forming in the wake of the porous plate, similar to the case of flow past porous plates with a very large G/H. These wake billows form around x=5H. By comparison, the billows formed around x=1.5H in the corresponding solid plate case (Figure 6.2e). This is simply an effect of the bleeding flow. However, similar to the solid plate case, the evolution of the billows originating from eddies advected in the bottom SSL is very different than those of the billows originating in the top SSL. This is mainly due to the no-slip bed surface. Once they form, the wake billows originating in the bottom SSL are slightly deflected laterally and increase their size via diffusion. As a result, similar to the G=0.5H case, these eddies start interacting with the bed for x/H>7. This results in a fairly sharp decrease of their coherence as they are advected downstream. These wake billow lose most of the coherence before reaching x=16H. As opposed to the G=0.5H case, the main mechanism that results in the loss of the coherence of these billows is the passage of the larger counter-rotating billows originating from the top SSL that, once the bottom eddies are slowed down by their interaction with the bed, move at a faster speed. As they overpass a bottom eddy, they extract vorticity from the core of that eddy.   This is again similar to what was observed for the solid plate with G=1H (see discussion in Chapter 6). For x/H>18, the wake contains only billows originating from the top SSL.

The distributions of the spanwise velocity in Figure 7.3 give an indication on the degree of three dimensionality of the wake flow. For cases with G/H<0.3, elongated patches of positive and negative spanwise velocity generated by the passage of the large eddies in the top SSL are present in the instantaneous velocity fields. Compared to the corresponding solid plate cases in Figures 6.3a-c, the magnitude of the spanwise velocity

inside these patches is smaller by about 30% and these patches of high spanwise velocity magnitude form at a larger distance from the plate in the porous plate simulations with small G/H (e.g., for x/H>8 in Figures 7.3a-c). Interestingly, for cases with G/H>0.3 (Figures 7.3d-e), the average velocity magnitude inside these patches does not increase, most of the patches do not assume an elongated shape and, at most times, no patches of high spanwise velocity magnitude are generated in the bottom SSL, as was the case in the corresponding solid plate simulations (see Figures 7.3d-e). These changes are an obvious consequence of the bleeding flow that contains highly energetic and relatively small eddies that stretch the larger eddies and tend to make the flow more homogeneous. This is the main reason why, in the case of a porous plate, the momentum transport in the spanwise direction does not increase with increasing G/H. Results in Figure 7.3 suggest that the momentum transport in the spanwise direction peaks around G/H=0.1.

Figure 7.4 shows the distribution of the points where velocity time series were collected to analyze the spectral content of the flow. Similar to the solid plate cases, time series were collected at 45 points in an x-y plane and at 210 points in a y-z plane. The time series of the vertical velocity at point 10 situated inside the SSL, close to the tip of the plate, and at point 35 situated in the top SSL, at about 7H from the plate are compared in Figure 7.5 for the G=0H and G=1H cases. For all cases, the time series at point 10 show the presence of high frequency fluctuations associated with the formation of the first vortex tubes in the top SSL. The dominant frequency associated with the passage of the vortex tubes varies little between G=0H (St=0.75, see also Figure 7.6a) and G=1H (St=0.81, see also Figure 7.11a) but the energy associated with these fluctuations increases with increasing G/H. The vertical velocity power spectra in Figures 7.6, 7.8, 7.9 confirm that

the dominant frequency component associated with the formation of vortex tubes is close to 0.6-0.7 and the energy associated with this component varies little with G/H until counter-rotating billows start forming in the wake of the porous plate. Once that happens, (e.g., see case G=1H), there is a significant increase (e.g., by more than 100%, compare Figures 7.9a and 7.11a) in the energy of the component associated with the passage of vortex tubes in the upstream part of the top SSL.

For the G=0H case, the time series at point 35 show the presence of a range of lower frequencies associated with the advection of large billows in the downstream part of the top SSL. No dominant frequency can be clearly identified based only on the time series. By contrast, in the G=1H case, the time series contain a dominant frequency with a period $T \sim 6H/U_0$, which correspond to $St \sim 0.16$. This is the shedding frequency of the large billows behind the porous plate. Even for this case, the signal is not exactly quasi-periodic, as expected for a plate with a very large G/H, mainly because of the less regular dynamics of the eddies shed in the bottom SSL and the presence of the bottom boundary layer, which results in less regular interactions between the two SSLs.

Figures 7.6, 7.8, 7.9 and 7.11 also show vertical velocity power spectra at points 28 and 43 situated, respectively, at 18H and 22.5H behind the plate and inside the top SSL. The main frequency component in the velocity spectra at these two points are associated with the passage of large eddies inside the top SSL. For G/H<0.3, there is little variation in the value of the Strouhal number associated with this frequency (St=0.095-0.1). Then, similar to what was observed for solid plates (see Table 6.1), the Strouhal number associated with the shedding of billows in the wake of the porous plate increases with increasing G/H. Its value is 0.13 for G=0.5H and 0.16 for G=1.0H. The later value is

slightly larger than the value observed in the corresponding solid plate case (St=0.14 for G=1H) and for solid plates with very large G/H (St=0.14-0.15). This shows that the plate porosity does not affect significantly the main shedding frequency of wake billows, while influencing the wake structure (e.g., by increasing the length of the SSL and the distance from the plate where billows form). In terms of the energy associated with the dominant component, a sharp increase (by about 4 times, e.g., compare spectra at points 28 and 43 in Figures 7.8 and 7.9) takes place as one moves from a regime where the lower SSL does not interact with the top SSL (G/H<0.3) to a regime where such interactions are significant and result in the formation of counter-rotating wake billows (G/H>0.5). For all cases, the velocity power spectra at points 28 and 43 contain a range of fairly energetic frequencies until St~1.6.

Figure 7.7 illustrates the advection and growth of large-scale eddies forming in the top SSL after the last merging event that takes place around x/H=10-12 for the G=0H case. This location also corresponds to the position of the small bottom-attached recirculation bubble present in the mean flow velocity fields (Figure 7.13a). No merging events are observed downstream of this location. As shown in Figure 7.7, the average time interval between two successive eddies passing through the x=18H location is close to $10.5H/U_0$, which corresponds to the dominant frequency St=0.095 observed in the velocity spectra in Figure 7.6.

The dynamics of the large-scale eddies forming inside the top SSL is similar for the G=0.1H and G=0.2H cases. As opposed to the solid plate case, no significant change is observed in the dominant passage frequency in the G=0.1H case (St decays from 0.08 to 0.04 as G/H is increased from 0 to 0.1) compared to the G=0H case. This is because the

bleeding flow does not allow significant interactions between the bottom SSL and the top SSL in the case of a porous plate with a relatively high porosity (P=36% in the present cases) and small G/H.

Figure 7.10 illustrates the dynamics of the main eddies in the top and bottom SSLs for the G=0.5H case. Animations show that larger patches of vorticity originating in the bottom SSL form close to x=10H and interact with the eddies advected in the top SSL. However, the coherence of these patches of vorticity, of opposite sign to that of eddies in the top SSL, is lost quickly for the reasons already explained. As a result, the wake does not contain counter-rotating billows for x/H>12. However, the formation of these patches of vorticity affects the dynamics of the large eddies advected in the top SSL. The average passage time interval of these eddies decreases from about $10H/U_0$ (cases with G/H<0.3) to $8H/U_0$ (St=0.13, Figure 7.9) in the G=0.5H case. Also no merging event between eddies advected in the top SSL downstream of x/H=10 is observed.

The wake structure becomes much more different in the G=1H case (Figure 7.12), where the interaction of the ends of the two SSLs results in the formation of counter-rotating billows. The mechanism is very similar to that observed in the corresponding solid plate case. The main difference is the larger distance from the plate where the billows form in the case of a porous plate (e.g., around x=5H for P=36%). As already discussed, the shedding frequency is close to St=0.16 and this frequency is the most energetic starting around the location where the billows form. Similar to the classical case of flow past a solid plate with large G/H, no merging between co-rotating wake billows is observed. Figure 7.12 shows that the circulation/coherence of the billows originating in the two SSLs is comparable. This is because the interactions of the bottom SSL with the channel bottom

are not important until x=4-5H. The average time period associated with the passage of the billows from the bottom SSL through the x=7H location is $6H/U_0$. Further downstream, the billows originating in the bottom SSL start interacting with the channel bed and their streamwise advection is slowed down by x=7H. Figure 7.12 illustrates how the coherence of a billow from the bottom SSL situated at x=9H in the top frame is gradually lost by the interaction with the counter-rotating billow passing over it. The billows originating from the bottom SSL never penetrate downstream of x=13H. As also illustrated in Figure 7.12, the average time period associated with the passage of the billows from the top SSL through the x=13H location is also $6H/U_0$ (St=0.16). One should also note that the billows originating in the top SSL remain fairly far from the channel bottom as they are advected downstream.

Table 7.1 summarizes the predicted values of the mean drag coefficient, $\overline{C}_D$, and its root-mean-square fluctuations, $C_D{}^{rms}$, for the five porous plate cases. Similar to the solid plate cases (Table 6.2), $\overline{C}_D$ and $C_D{}^{rms}$ increase monotonically with the increase in G/H. These variations are due to the presence of the channel bottom and the increase of the interactions between the top and bottom SSLs with increasing G/H. Due to the bleeding flow, for same G/H, the values of the mean drag coefficient are smaller in the case of a porous plate. For low G/H, the values of $C_D{}^{rms}$ are larger in the case of a porous plate due to the turbulence generated by the jets forming in between the solid elements of the porous plate. For large G/H, where vortex shedding takes place in the wake of the plate, $C_D{}^{rms}$ is larger in the case of a solid plate. This is because the main contributor to the oscillations of the drag coefficient is due to the advection of billow vortices away from their formation

region. As already discussed, the billow vortices form at a smaller distance from the plate in the case of a solid plate.

7.3.2 Mean Flow and Turbulence Statistics

The 2D mean flow streamline patterns in Figure 7.13 show recirculation regions are present only for the G=0.0H. The main recirculation bubble extends from x=8.5H to x=13H and its maximum height is 0.5H. For all the other cases, flow separation is absent at the channel bed. In all cases, a small fence-attached recirculation bubble forms behind the top solid element of the porous fence. A second fence-attached recirculation bubble forms at a lower height, where the bleeding force through the fence divides into a component that is advected toward the top SSL and a component that is advected toward the bottom SSL. While for small G/H most of the bleeding flow is advected toward the top SSL, the ratio will approach one for very large G/H. For G=0.1H to G=1H the percentage of the discharge advected toward the lower SSL with respect to the total bleeding flow discharge is close to 31% even though there is a monotonic increase of the bleeding flow discharge with G/H (see Table 7.1). The size of this second bubble that contains two eddies of unequal size increases monotonically with G/H (e.g., its streamwise length increases from 0.25H for G/H=0.1 to 2.3H for G/H=1). A third, much smaller, bubble forms behind the bottom element of the porous fence. Though the size of this bubble increases with increasing G/H, its length remains smaller than that of the corresponding bubble at the top of the fence in all 5 simulations. It is expected that for cases with very large G/H, the sizes of the first and third bubbles will become equal, and the second bubble will be situated at the middle of the porous fence.

The distributions of the spanwise vorticity in the mean flow allow comparing the variation in the relative strength of the top and bottom SSLs with increasing G/H. The top SSL is stronger (e.g., in terms of vorticity magnitude values) than the bottom SSL until G/H~0.3. This is because, for small G/H, only a small part of the incoming flow toward the porous plate is diverted through the bottom gap. As G/H increases, not only that a larger amount of the incoming flow penetrates through the bottom gap, but the presence of the channel bottom helps maintaining a region of relatively large streamwise velocities close to the channel bottom for large distances from the porous plate. This is the main reason why the bottom SSL becomes stronger than the top SSL. The maximum difference is recorded around G/H=0.5. Then, as G/H is further increased, the penetration length of the bottom SSL decreases such that the strength of the two SSLs will become equal for very large G/H.

Compared to the corresponding results for solid plates in Figure 6.17, some interesting differences are observed. While in the porous plate cases, the penetration length of the top SSL is close to constant until G/H=0.2 and then increases monotonically with G/H, in the solid plate cases, the length of the top SSL increases with G/H until G/H=0.3 and then decreases. The decrease is induced by the start of the shedding regime and the fact that the billows are shed just behind the solid plate for cases with a large G/H. While, billow vortices also form in the porous plate cases for G/H>0.5, the wake of a porous plate is characterized by the formation of wake billows at relatively large distances from the plate. In fact, the distance at which the wake billows form increases monotonically with the plate porosity (e.g., from x/H=1 for P=0% to x/H=2.5 for P=36%). For the same reason, the penetration length of the bottom SSL is much larger for the porous plate case compared

to the corresponding solid plate case, once that G/H is sufficiently large such that wake billows start forming. Another observation is that only for relatively small G/H are the strength and penetration length of the top SSL larger in the case of a solid plate. This is because the mean shear across the top SSL is larger compared to the corresponding porous plate case, where part of the incoming flow enters the wake region through the plate surface.

Similar to the solid plate results in Chapter 6, the distributions of the mean fluctuations of the velocity components in the horizontal and vertical directions (Figures 7.16 and 7.17) and of the TKE (Figure 7.18) show an amplification of the turbulence inside the region where billows are shed from the top and bottom SSLs. Still, for all cases the values of the mean velocity fluctuations and of the TKE in the regions of strong turbulence amplification are, in average, about twice smaller compared to the corresponding solid plate results. Similar to the solid plate results, the contribution to the TKE associated with the spanwise velocity component (not shown) is less, but still comparable to that of the streamwise and vertical components. This indicates a fairly strong three-dimensionality of the flow in the wake of the porous plate.

Also similar to the solid plate results, for cases where alternate vortex shedding of wake billows occurs behind the plate (case G=1H for the porous plate), the largest amplification of the mean vertical velocity fluctuations occurs in the region where the interaction of the top and bottom SSLs results in the formation of the wake billows (see Figure 7.17e). For the same reasons, the TKE is strongly amplified in the same region. For $G/H \geq 0.5$, the amplification of the mean velocity fluctuations and TKE in the bottom SSL is similar to that observed in the top SSL. In fact, once vortex shedding occurs, the TKE is

slightly higher in the bottom SSL because of the flow constriction imposed by the channel

bottom. That induces the shedding of stronger eddies within the bottom SSL.

Meanwhile, the TKE amplification in the lower part of the wake decreases faster

after the billow forms. As shown in Figure 7.18e for the G=1H case, the mean streamwise

velocity fluctuations and the TKE amplification are larger within the upper half of the wake

past x=12H, once the billows originating in the bottom SSL are slowed down by the

boundary layer on the channel bottom and lose their coherence. The position of the region

of high TKE amplification corresponds to the one in which the interaction between the

SSLs results in the formation of these billows.

The spanwise-averaged distributions of the bed friction velocity in Figure 7.19

allow estimating the spatial extent of the region where u_τ/U_0 is amplified with respect to

the mean value in the incoming fully developed flow, which is close to 0.04. As for the

solid plate cases, the flow advected through the bottom gap leads to a significant

amplification of u_τ/U_0 beneath the porous plate and over some distance from it. However,

for all cases with G/H>0, the peak levels observed beneath the gate in the porous case are

30-60% lower than the values predicted for solid plates. This is because part of the

incoming flow toward the plate moves through the plate. So, the proportion of the incoming

flow diverted beneath the bottom of the fence is always smaller in the case of a porous

plate compared to that of a solid plate.

In the cases with G/H>0, the bed friction velocity decays sharply past the solid

plate. This is then followed by a region of mild decay toward a minimum value that is less

the bed friction velocity value in the incoming flow. Then, as the streamwise velocity in

the wake recovers toward the free stream values and the flow becomes more uniform in the

vertical direction, the bed friction velocity increases gradually back to the value in the incoming flow. Downstream of the plate, the lowest value of u_τ/U_0 are observed in the G=1H case. Even if the acceleration of the flow past the bottom edge of the plate and the size of the region of high streamwise velocity increase with G/H, the lateral extent of this region of high streamwise velocity grows less than G/H. This is the reason why the u_τ/U_0 levels are lower in case G=1H compared to case G=0.5H in Figures 7.19d and 7.19e.

Figure 7.19 also offers information of the rms of the bed friction velocity fluctuations. These fluctuations are mainly induced by the passage of large scale eddies originating in the bottom SSL in the bed vicinity. Qualitatively, the distribution of the rms of the bed friction velocity is similar in the porous plate and solid plate cases. As G/H increases, the peak in the rms fluctuations moves away from the plate. The peak values are recorded at the streamwise location where the bottom SSL containing strongly coherent eddies is situated the closest to the channel bed (e.g., around x/H=4 for the G=0.5H and G=1H case). Downstream of this location, the rms bed friction velocity fluctuations start decaying slowly and approach the value associated with the incoming fully developed flow around the location where the eddies advected in the bottom SSL or the wake billows originating from the bottom SSL lose their coherence (e.g., around x/H=14 for the G=1H case). One exception is the G=0.1H case, where the bottom SSL is oriented away from the channel bed and the bed friction velocity fluctuations decay quickly below the value in the incoming flow before starting recovering slowly toward this value.

7.4 Conclusions

LES of flow past a 2D porous plate (P=36%) with varying bottom gap (0≤G/H≤1) have been performed at a moderate cylinder Reynolds number (Re=20,000) to investigate

the effects of bottom gap on flow and turbulence structure. The plate height was kept constant. Results were also compared with the corresponding cases of a solid plate with varying bottom gap discussed in Chapter 6.

Results show that, except for the limiting case of no bottom gap, no recirculation regions attached to the channel bed are present for flow past porous plates with P=36%. Rather, several smaller recirculation regions form just behind the porous plate. One of this eddies is situated at the location where the bleeding flow splits into two components that are advected toward the top and bottom SSLs, respectively.

Similar to the solid plate cases, for sufficiently larger G/H values, counter-rotating billow vortices form as a result of the interactions between the top and bottom SSLs. However, the G/H values at which the vortex shedding starts is larger in the case of a porous plate. The same is true for the distance at which wake billows are shed (e.g., for G/H=1, billows form at x/H=6 in the case of a porous plate and at x/H=1.5 in the case of a solid plate). The Strouhal number corresponding to the main shedding frequency was slightly higher in the porous plate cases with relatively large G/H. Still, this frequency was close to the one associated with vortex shedding past solid plates with a very large G/H (St=0.14-0.15). Due to the bleeding flow, the natural interaction of the two SSLs is impeded close to the plate. This explains the much larger length of the SSLs for large G/H in the porous plate cases compared to the corresponding solid plate cases. Similar to the solid plate cases, the large eddies advected in the bottom SSL, or the billows generated from the bottom SSL for cases with a relatively large G/H, started interacted with the bottom channel. These interactions resulted in a reduction of the advective velocity of these

eddies and a loss of their coherence due to the passage of the larger, more coherent, eddies from the top SSL.

For all cases, the values of the mean drag and its rms fluctuations were smaller in the case of a porous plate compared to the corresponding case of a solid plate. This was due to the fact that part of the incoming flow toward the porous plate is advected through the plate and forms the bleeding flow. As already commented, the bleeding flow delays the interaction of the SSLs. Thus, the wake billows form at a larger distance from the porous plate, which explains the smaller temporal oscillations of the drag coefficient. The values of the mean bed friction velocity and its rms fluctuations downstream of the plate were smaller in the case of a porous plate compared to the corresponding solid plate case.
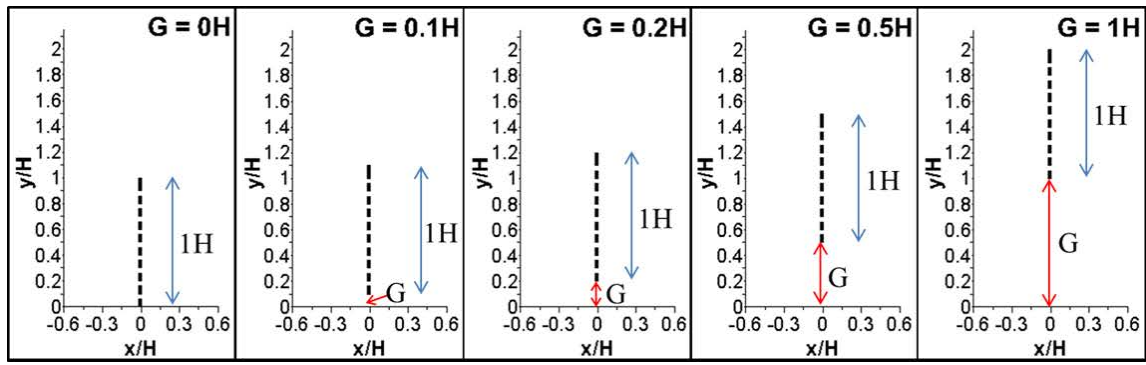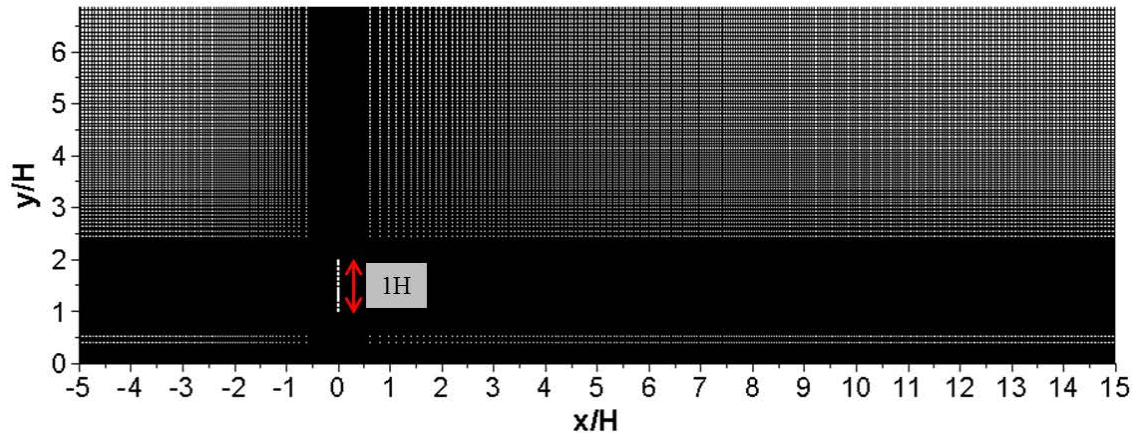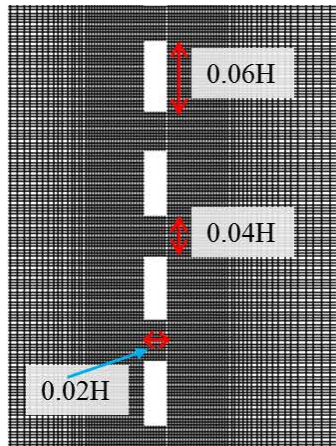
Figure 7.1 Sketch showing relative position of the vertical plate relative to the channel bottom in the five cases (a) and sample computational mesh around the plate (b, c).
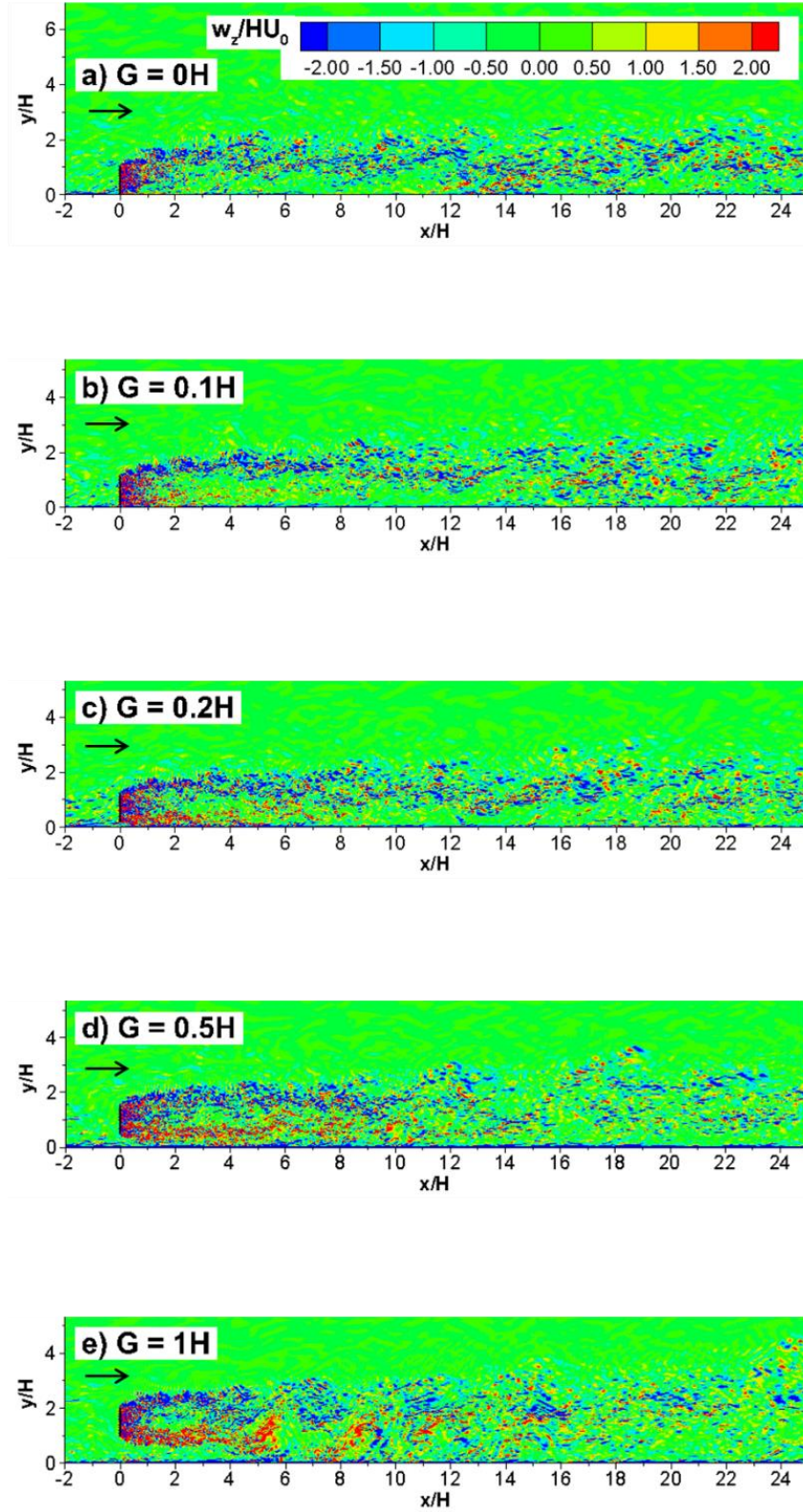
Figure 7.2 Instantaneous spanwise vorticity, $\omega_z/(H/U_0)$, in an x-y plane.

Figure 7.3 Instantaneous spanwise velocity, w/U_0, in an x-y plane.
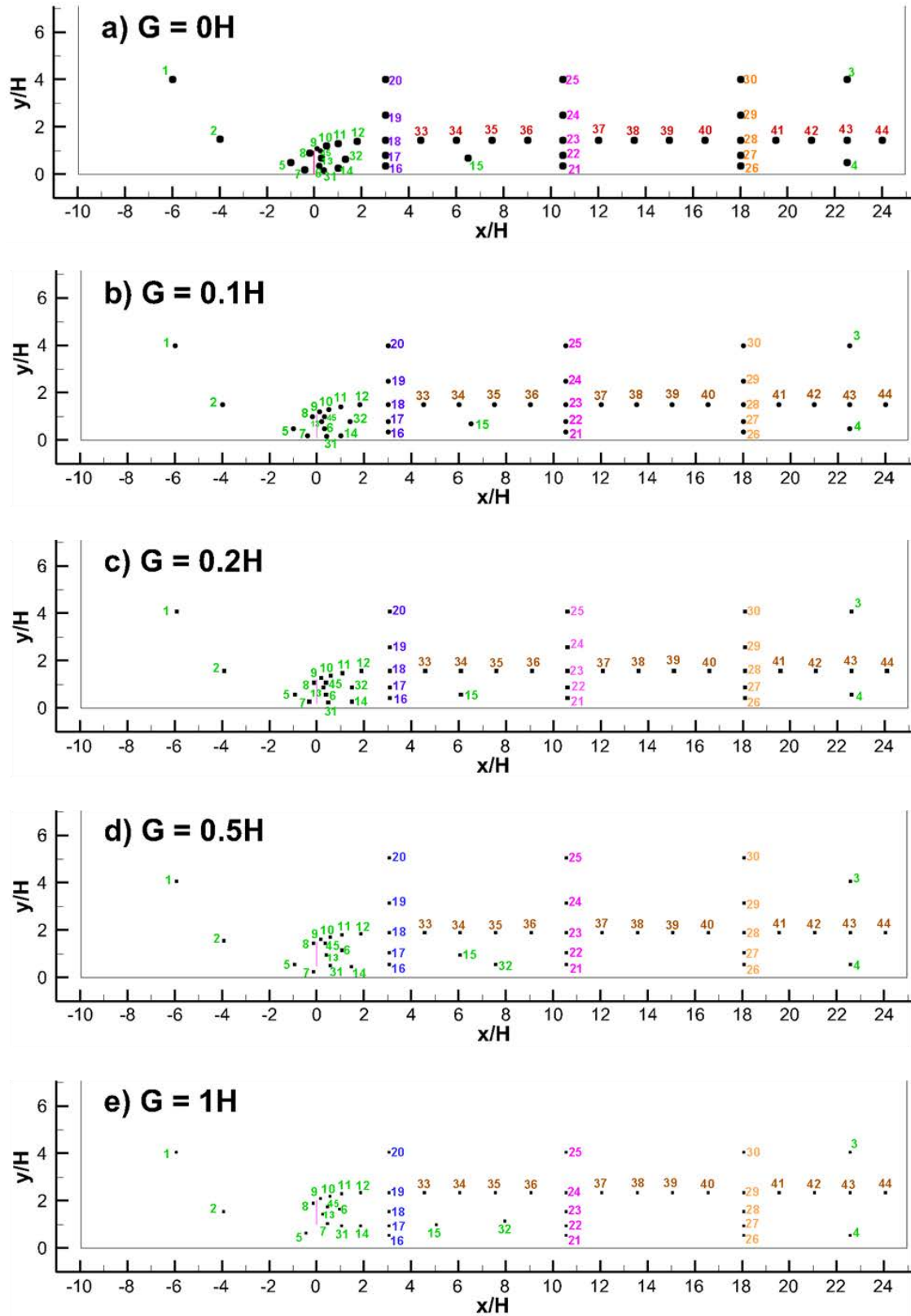
Figure 7.4 Location of points where time series were collected to analyze spectral content of the flow.

216

Figure 7.5 Time series of vertical velocity at two different locations: point 10 (x=0.5H), and point 35 (x=7.5H) for cases G=0H and G=1H. Location of points is shown in Figure 7.4. The spanwise coordinate is z=1.75H (mid length).
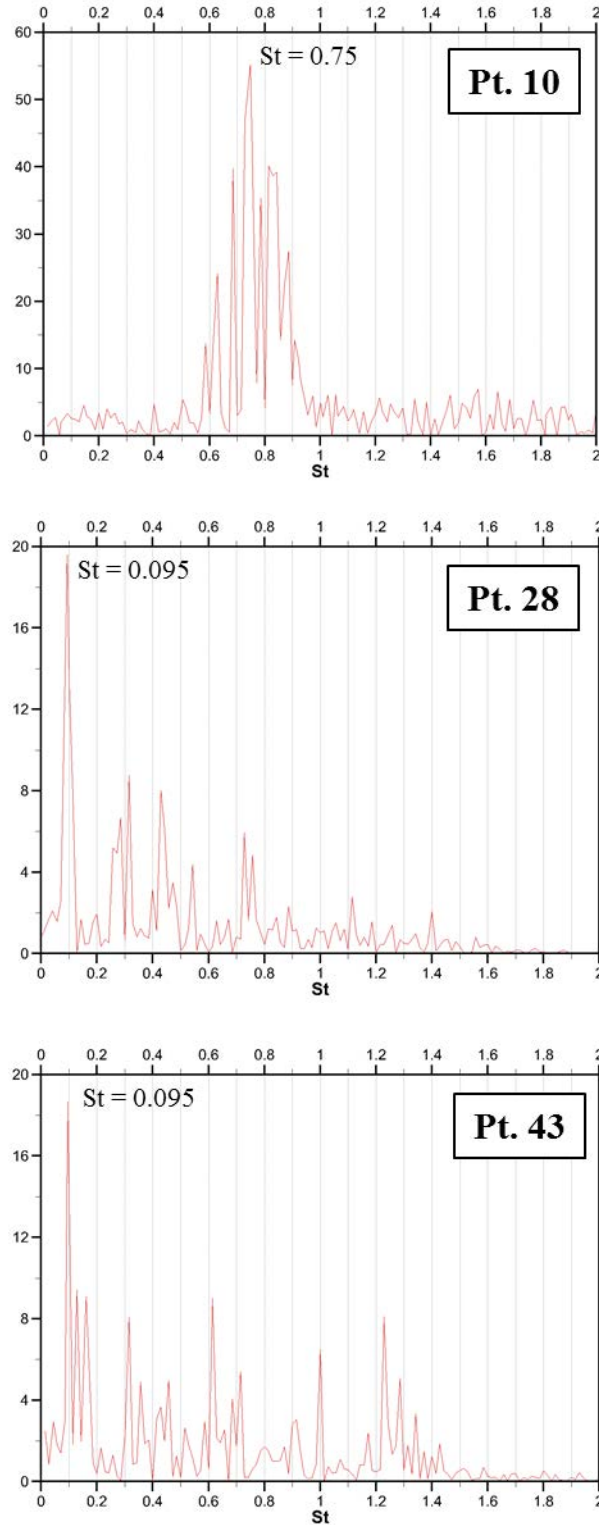
Figure 7.6 Power spectra of vertical velocity for G=0H case at: point 10 (x=0.5H, y=1.3H), point 28 (x=18H, y=1.76H) and point 43 (x=22.5H, y=1.76H). Location of points is shown in Figure 7.4a.
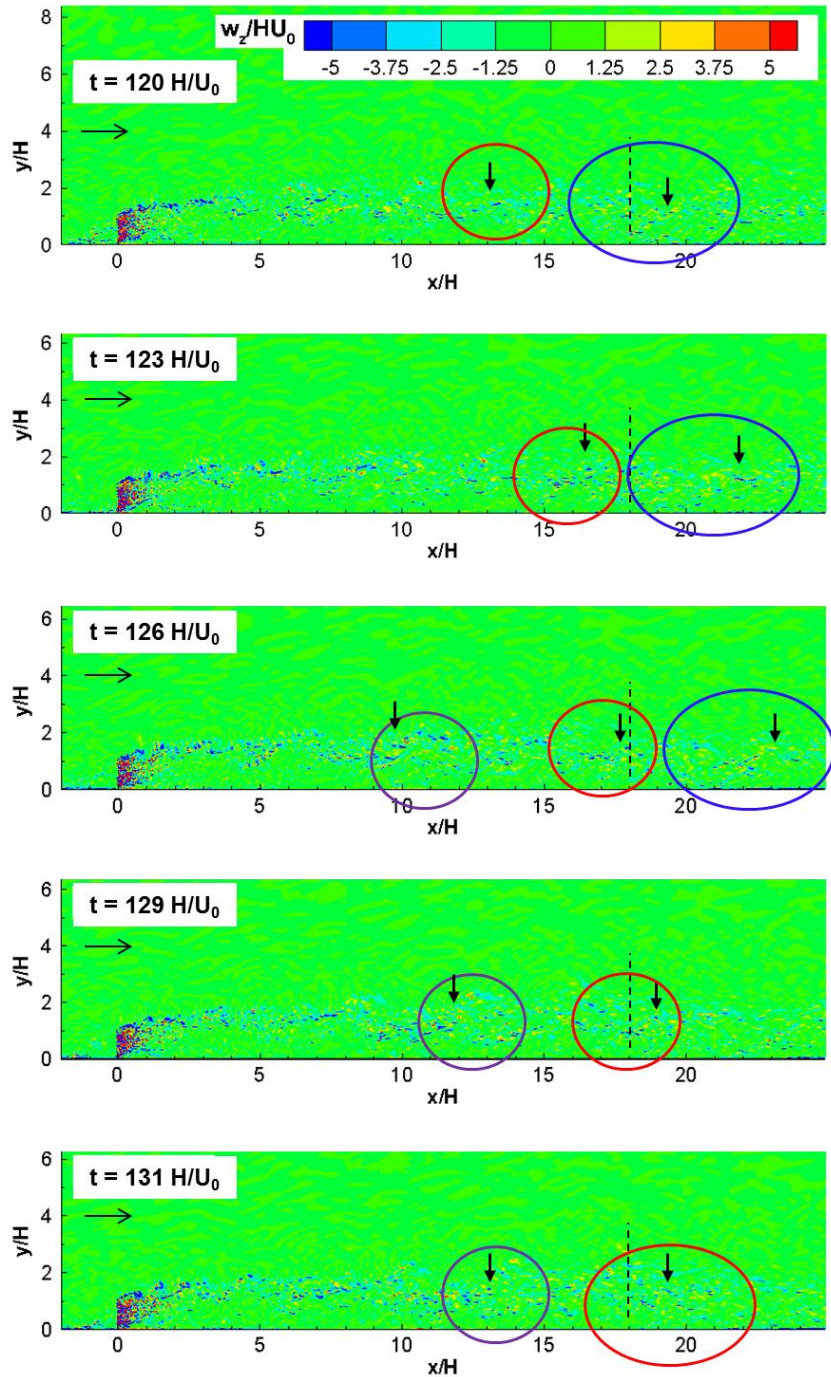
Figure 7.7 Temporal evolution of the spanwise vorticity field in the G=0H case, showing advection of large-scale eddies into the upstream part of the SSL, around x=18H. The two successive eddies are identified using a red and a blue circle. The period of passage of such an eddy is $11H/U_0$ corresponding to St=0.095 (see also power spectra in Figure 7.6).
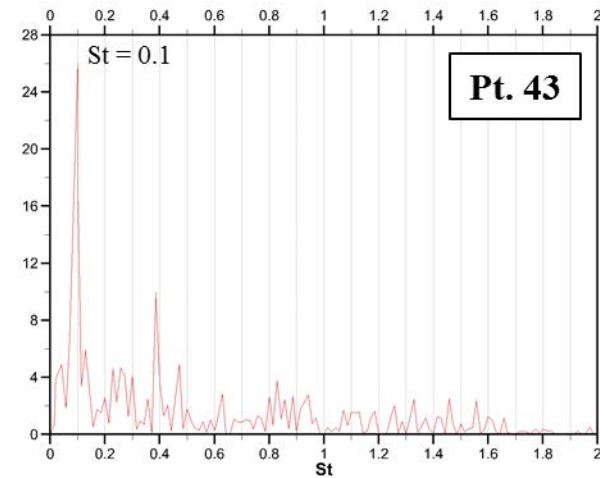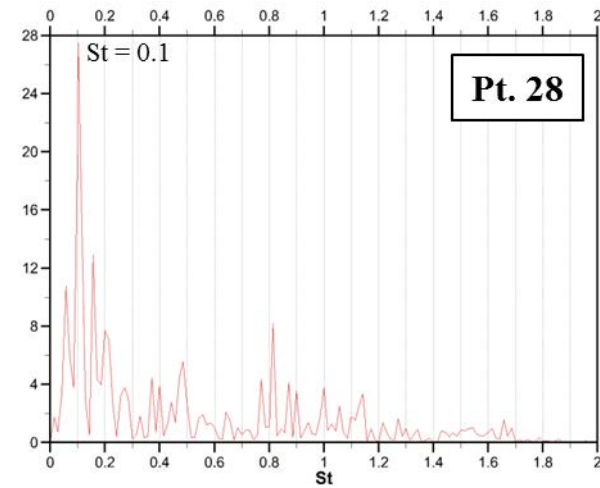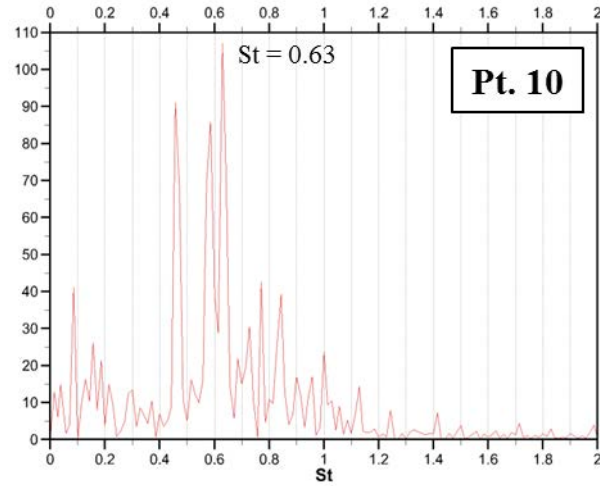
Figure 7.8 Power spectra of vertical velocity for G=0.2H case at: point 10 (x=0.5H, y=1.3H), point 28 (x=18H, y=1.76H) and point 43 (x=22.5H, y=1.76H). Location of points is shown in Figure 7.4c.
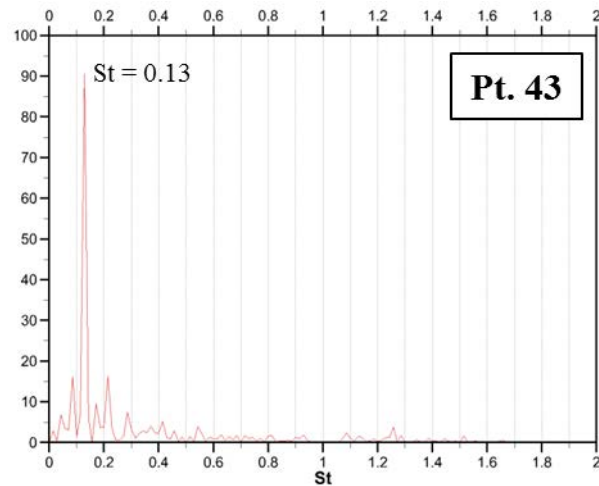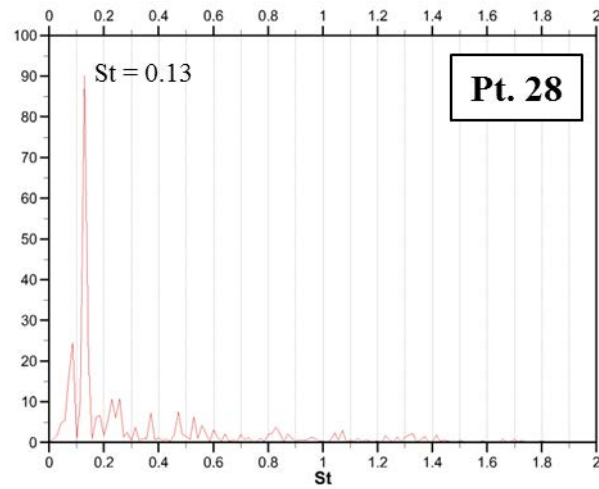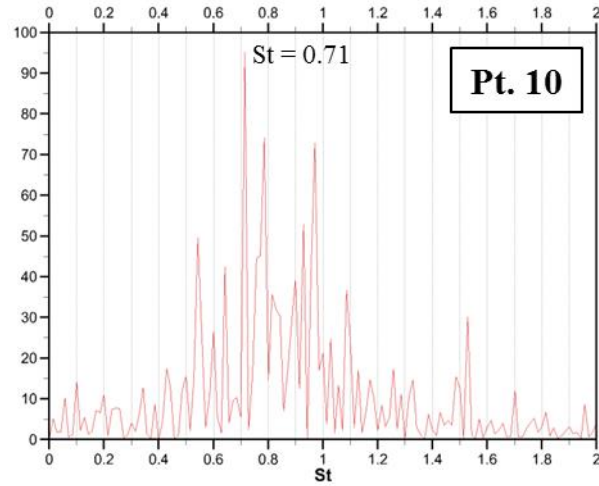
Figure 7.9 Power spectra of vertical velocity for G=0.5H case at: point 10 (x=0.5H, y=1.3H), point 28 (x=18H, y=1.76H) and point 43 (x=22.5H, y=1.76H). Location of points is shown in Figure 7.4d.

221
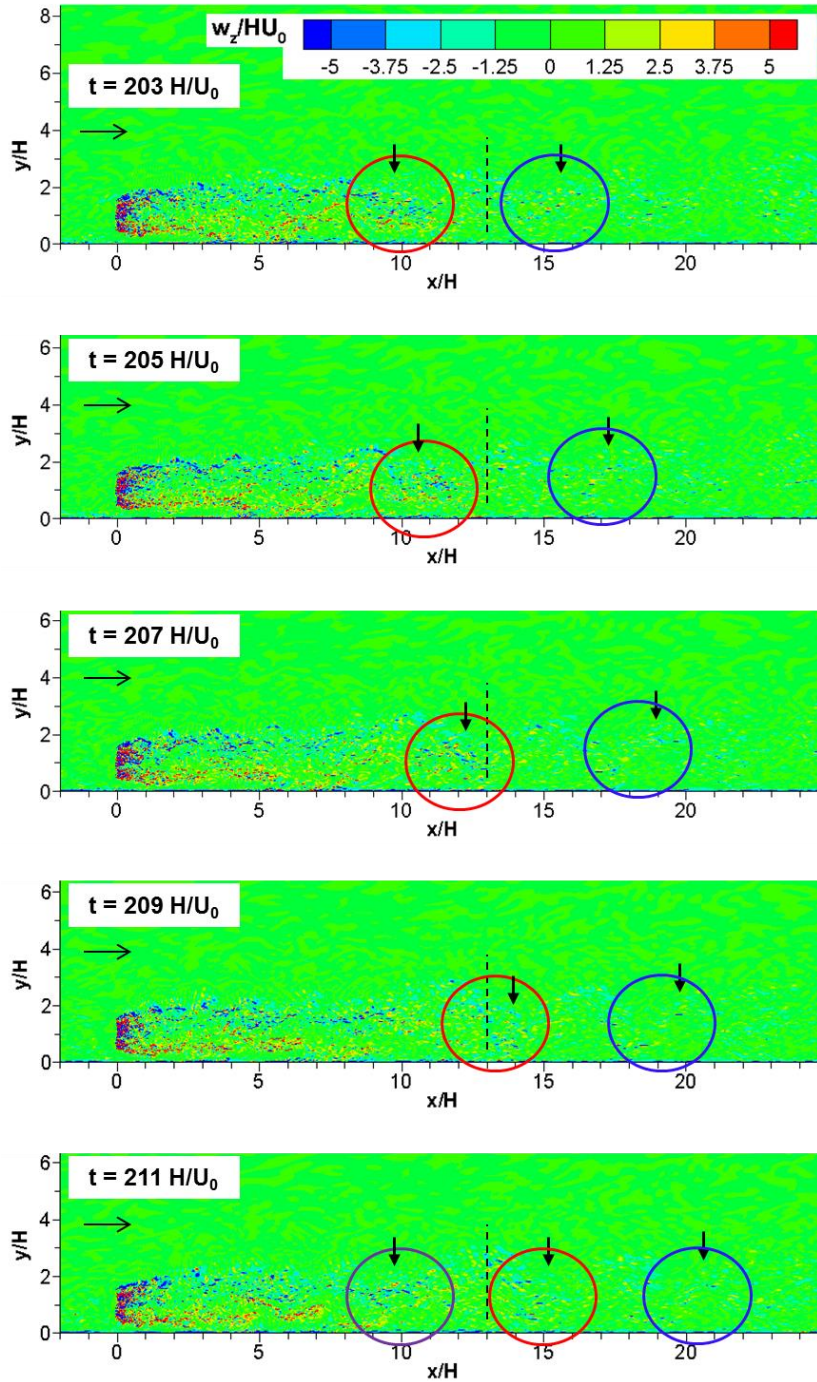
Figure 7.10 Temporal evolution of the spanwise vorticity field in the G=0.5H case, showing advection of large-scale eddies into the upstream part of the SSL. The two successive eddies are identified using a red and a blue circle. The period of passage of such an eddy is $8H/U_0$ corresponding to St=0.13 (see also power spectra in Figure 7.9).
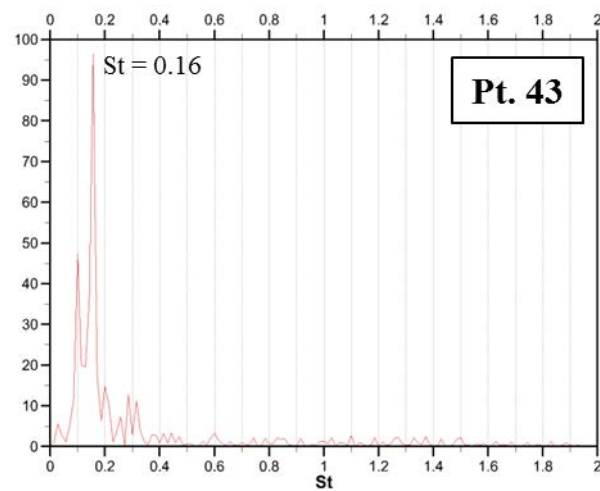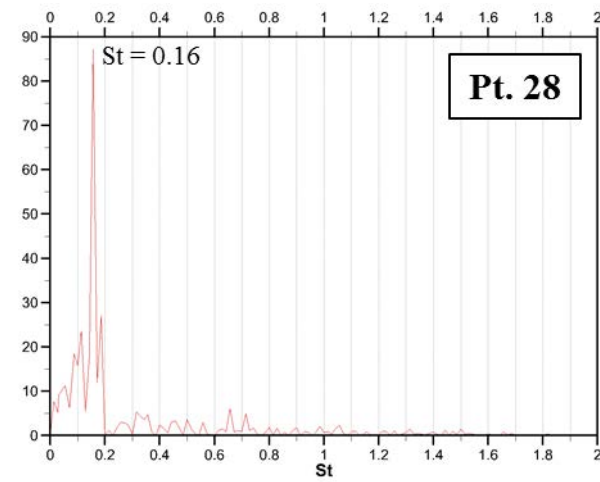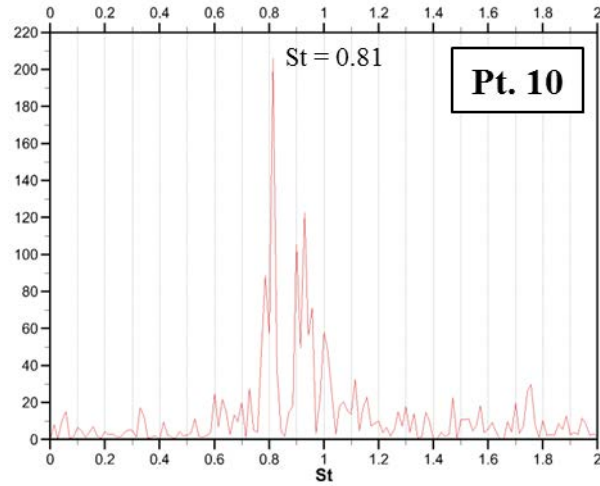
Figure 7.11 Power spectra of vertical velocity for G=1.0H case at: point 10 (x=0.5H, y=1.3H), point 28 (x=18H, y=1.76H) and point 43 (x=22.5H, y=1.76H). Location of points is shown in Figure 7.4e.
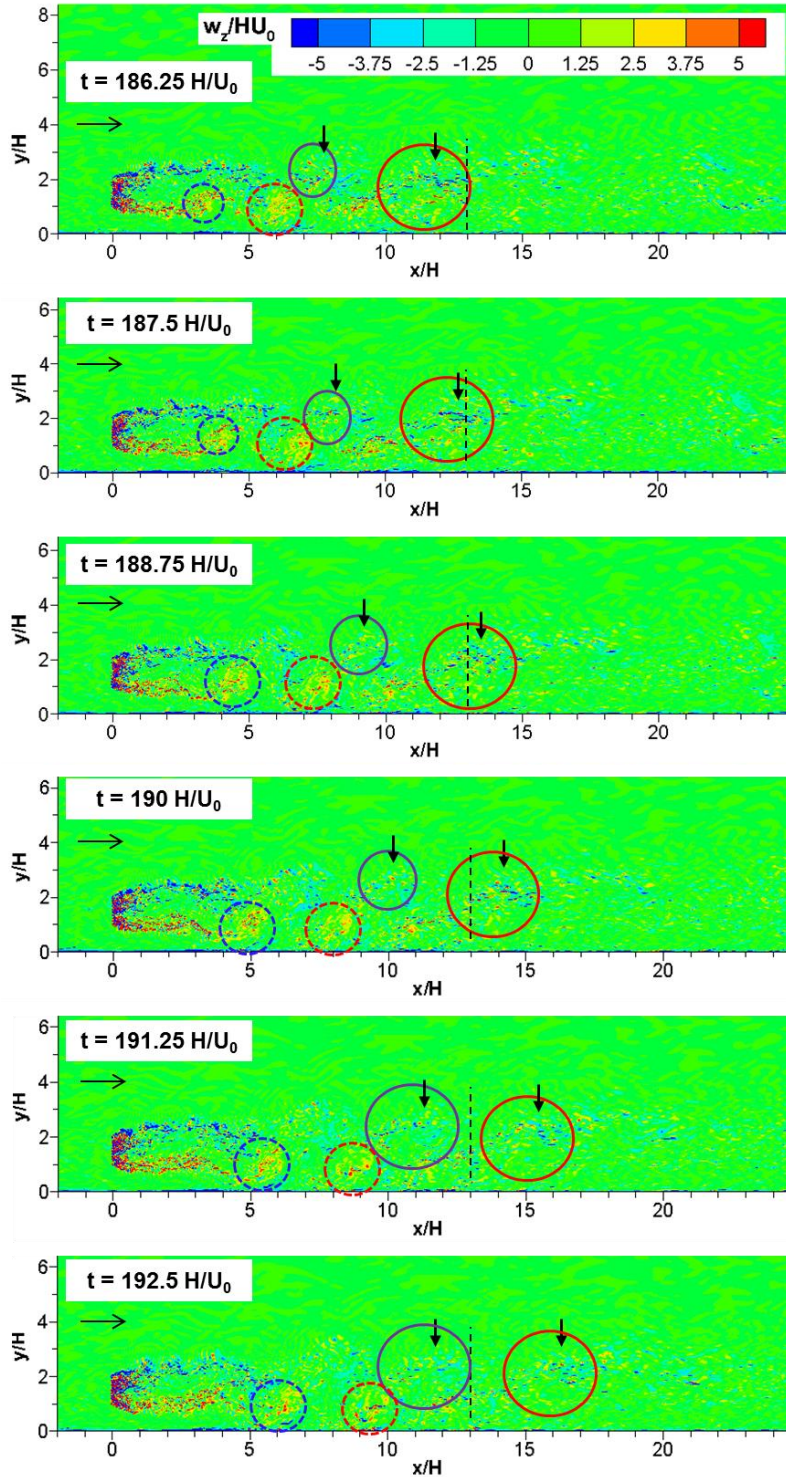
Figure 7.12 Temporal evolution of the spanwise vorticity field in the G=1.0H case, showing advection of large-scale eddies into the upstream part of the SSL, around x=13H. The two successive eddies are identified using a red and a blue circle. The period of passage of such an eddy is $6H/U_0$ corresponding to St=0.16 (see also power spectra in Figure 7.11). Also shown is the trajectory of billows forming in the bottom SSL.
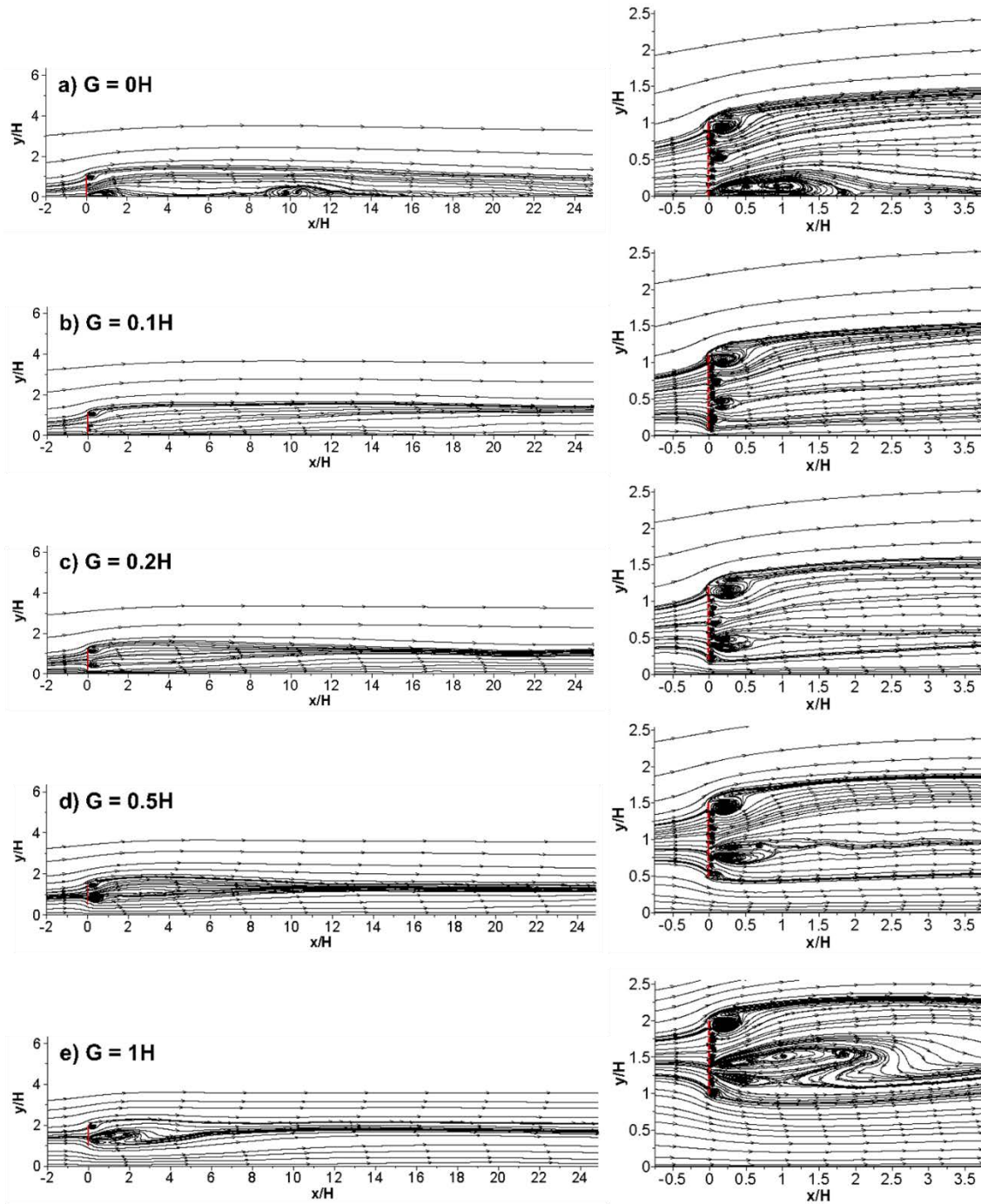
Figure 7.13 Mean flow structure visualized using 2D streamline patterns.
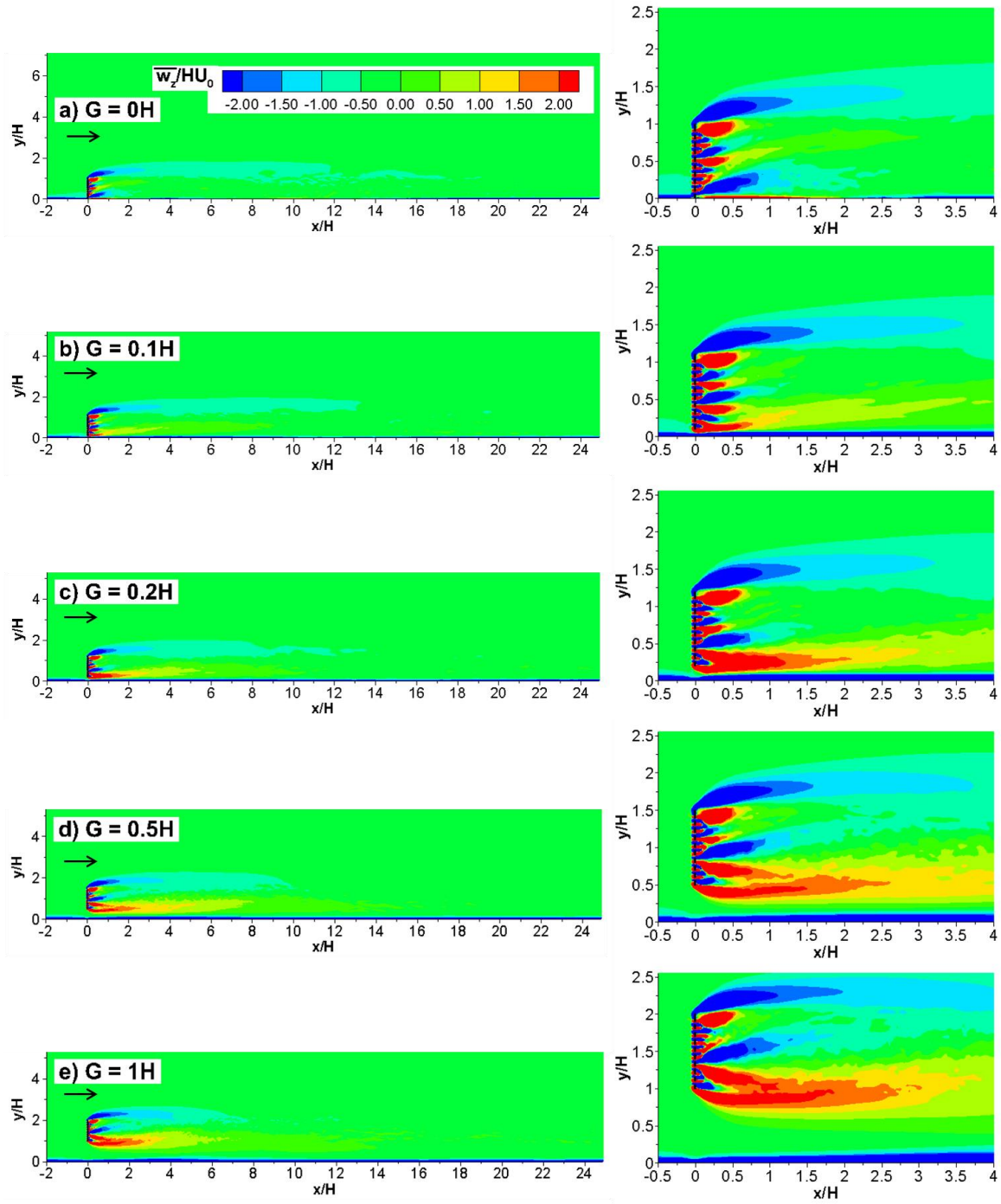
Figure 7.14 Mean spanwise vorticity magnitude, $\overline{\omega_z}/(H/U_0)$, in an x-y plane.
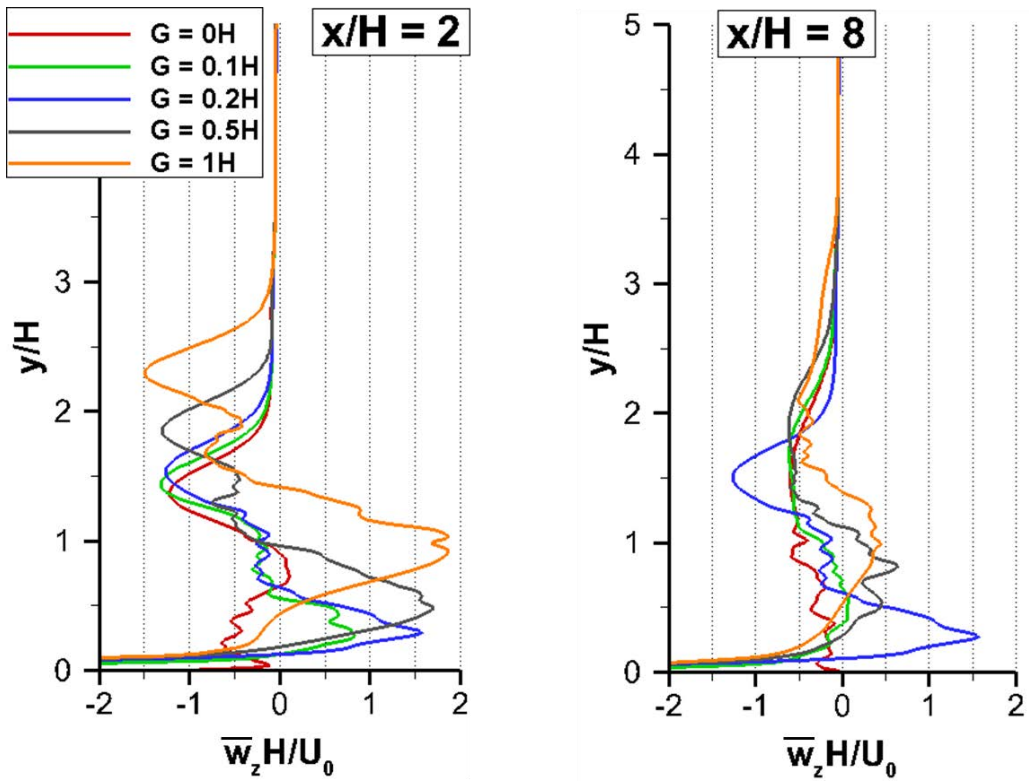
Figure 7.15 Vertical profiles of mean spanwise vorticity magnitude, $\overline{\omega_z}/(H/U_0)$, at x/H=2 and x/H=8.
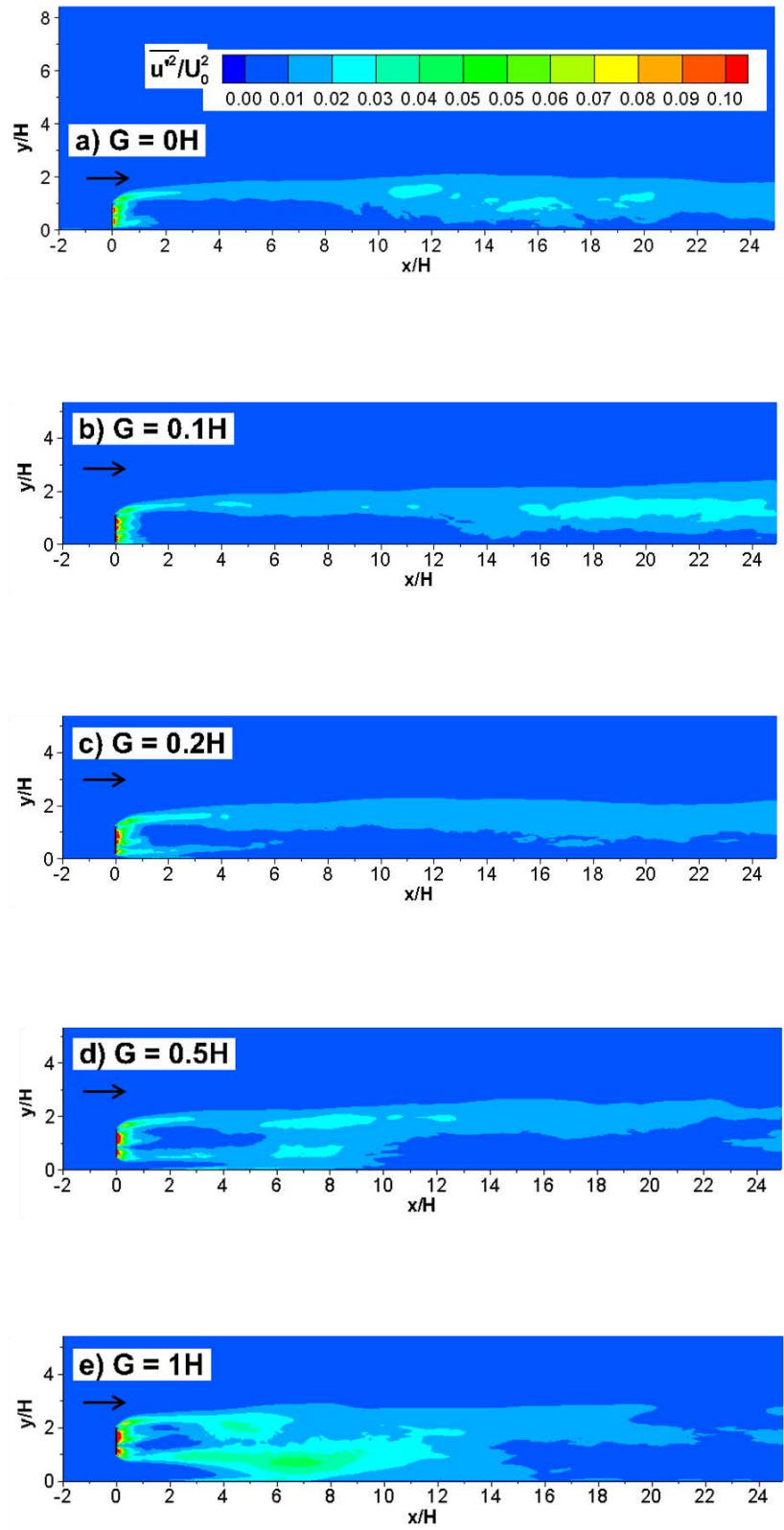
Figure 7.16 Mean streamwise velocity fluctuations, $\overline{u'^2}/U_0^2$, in an x-y plane.
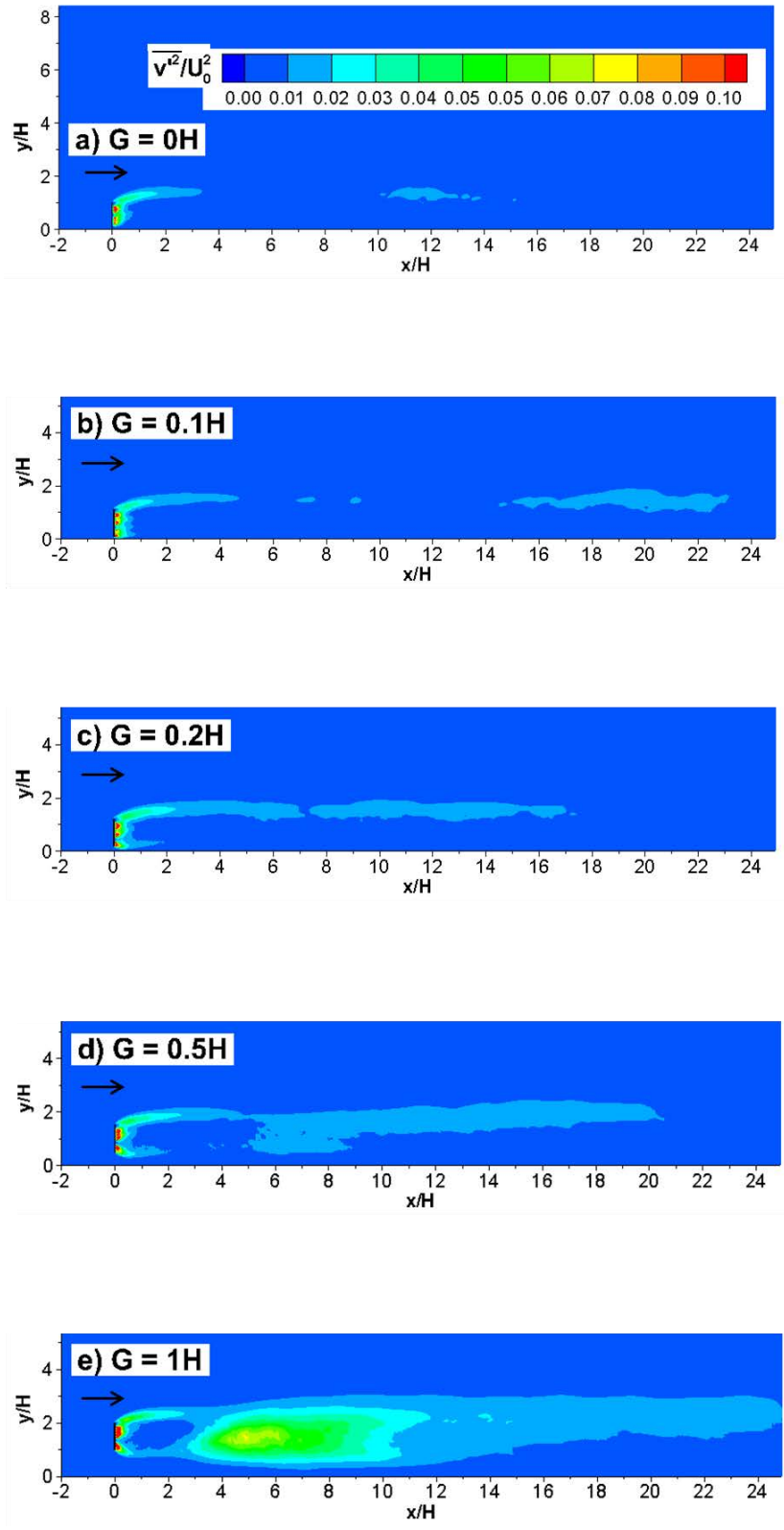
Figure 7.17 Mean vertical velocity fluctuations, $\overline{v'^2}/U_0^2$, in an x-y plane.
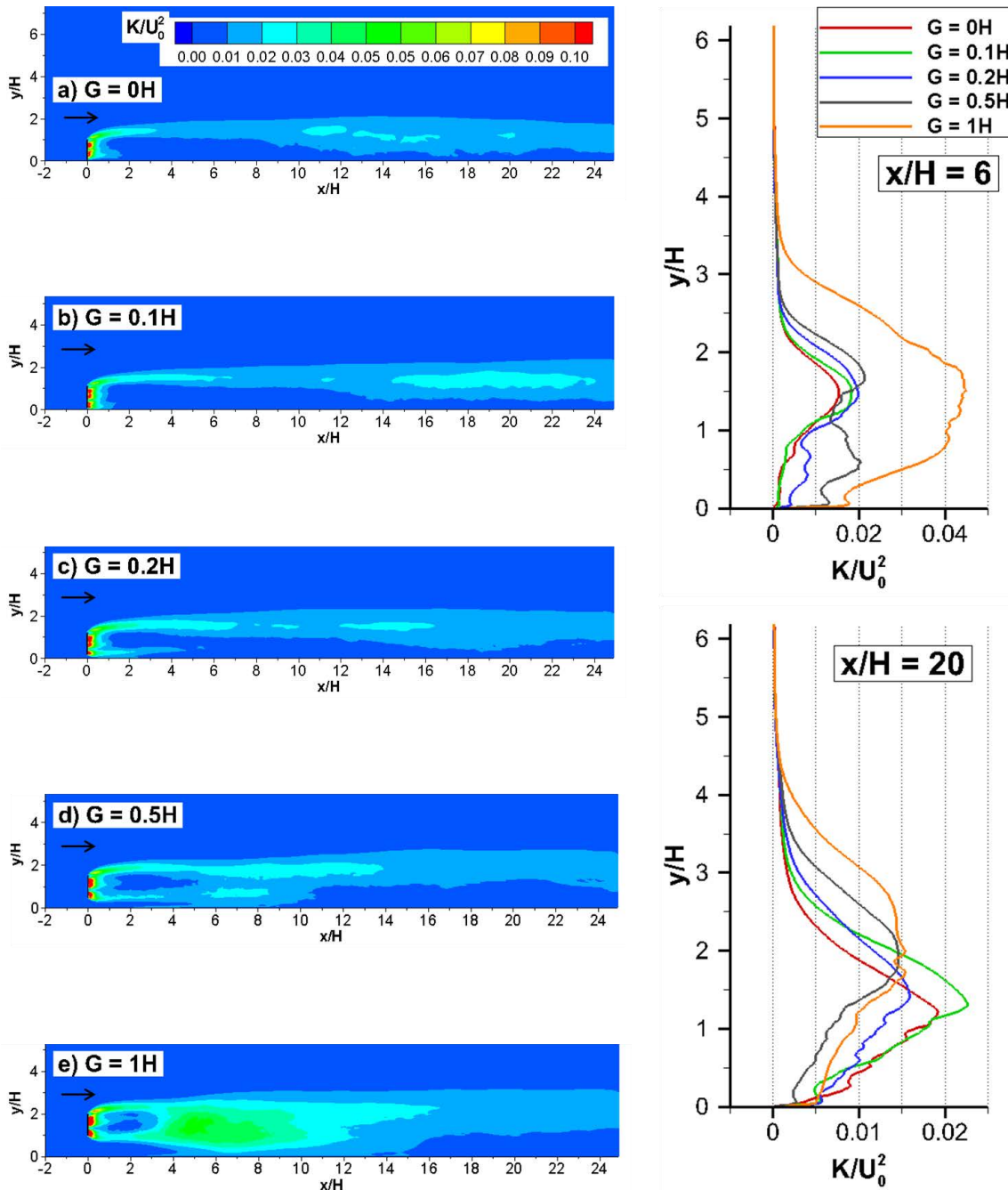
Figure 7.18 Turbulent kinetic energy, K/U_0^2, in an x-y plane. Also shown are vertical profiles of K/U_0^2 at x/H=6 and x/H=20.
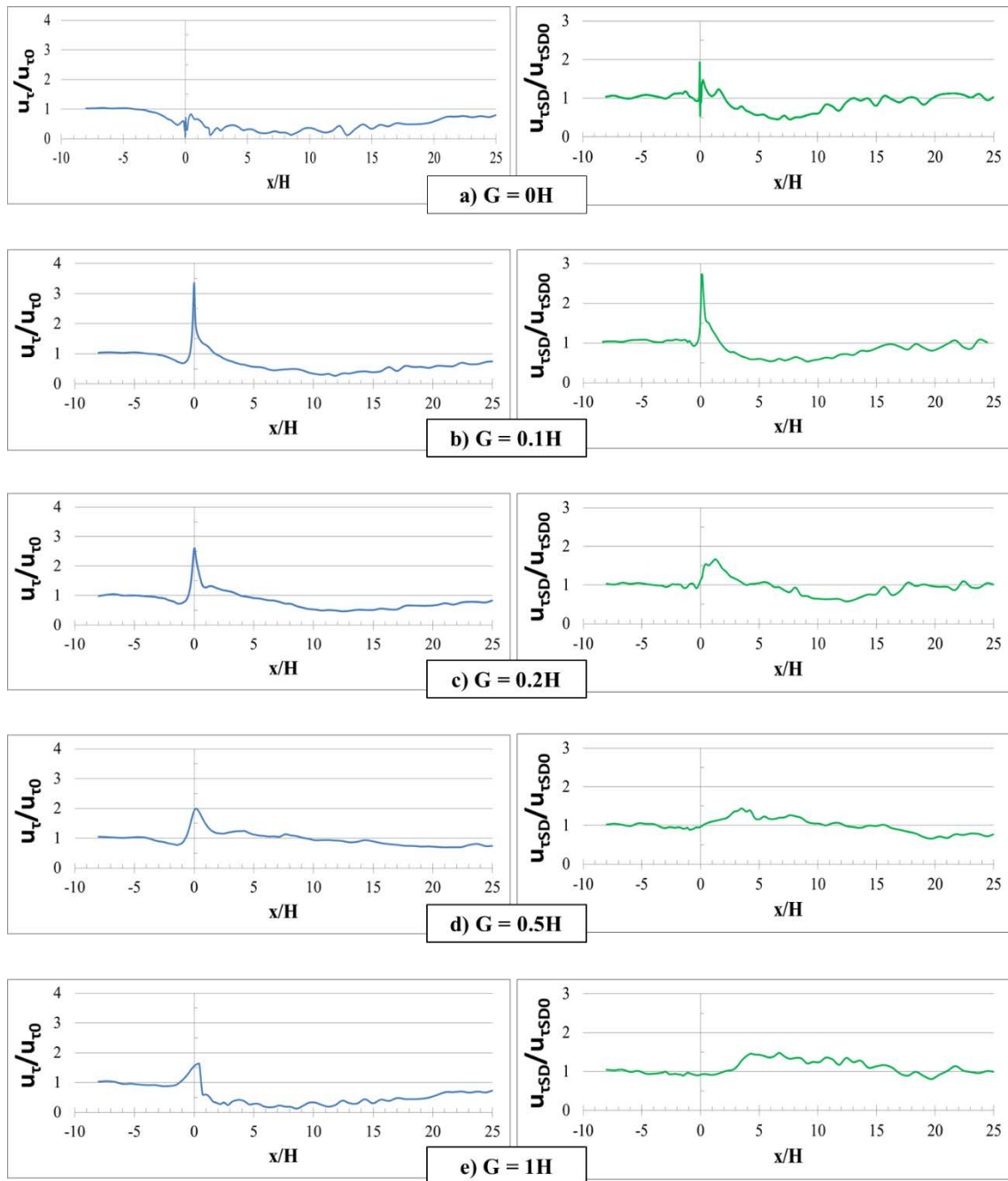
Figure 7.19 Nondimensional spanwise-averaged mean bed friction velocity, $u_\tau/u_{\tau 0}$, where $u_{\tau 0}=0.04U_0$ is the mean bed shear stress in the incoming fully developed turbulent channel flow. Also shown is the nondimensional spanwise-averaged rms of the bed friction velocity fluctuations where $u_{\tau SD0}=0.025U_0$ is the mean rms of the bed shear stress in the incoming fully developed turbulent channel flow.

Table 7.1 Comparison of integral parameters.

Case	$\overline{C_D}$	$C_D{}^{rms}$	St	$Q/(\rho U_0 H^2)$	$Q_L\%$
G = 0H	0.56	0.06	0.095	0.297	-
G = 0.1H	0.62	0.06	0.1	0.310	30.9
G = 0.2H	0.65	0.07	0.1	0.312	30.9
G = 0.5H	0.78	0.08	0.13	0.323	31.3
G = 1H	0.88	0.09	0.16	0.339	31.4

CHAPTER 8 EFFECT OF HOLE SIZE ON FLOW PAST A POROUS VERTICAL PLATE

8.1 Introduction

The main objective of this chapter is to use LES to study the effect of varying distance between the solid elements of the porous fence (this geometrical parameter, d, is referred as the hole size by analogy to porous fences containing circular openings of constant diameter) on flow past a vertical porous plate placed on a horizontal and smooth channel bottom surface with no bottom gap (G/H=0). Three simulations are performed with d=0.02H, 0.04H and 0.09H, respectively. The plate porosity is kept constant (P=36%) in the simulations discussed in the present chapter. A sketch of the porous vertical plate used in the three test cases is shown in the Figure 8.1. The case with d=0.04H is the same as the one considered in Chapter 6 (P=36% case, G/H=0).

8.2 Simulation Setup

The computational domain, plate height (H), location of the plate (10H from the inflow section) and the coordinate system are identical to the ones considered in the simulations discussed in Chapters 5, 6 and 7. The thickness of the solid plate is 0.02H and the length of the computational domain is 35H. The computational domain contains around 25 million (768x512x64) grid points in each of the three cases. Figure 8.2 shows the mesh in a x-y plane around the location of the porous plate.

The x-axis is aligned with the incoming flow direction and the z-axis is aligned with the vertical direction relative to the horizontal bottom surface of the channel. The plate height, H, is used as the length scale. The uniform incoming flow velocity, U_0, is used as the velocity scale. The simulations were performed for a Reynolds number of Re=20,000.

Discretization along the x and z directions is the same for all three cases. Only the discretization along the y axis is changed due to the need to resolve the flow near the solid elements of the porous plate. The mesh is uniform along the z direction. The cell size in the wall normal direction was close to 0.002H for all solid surfaces. This distance corresponds to close to 2 nondimensional wall units. Away from the plate, the average dimensions of the 3D cells are increased to about 0.07Hx0.06Hx0.05H.

All the boundary conditions are identical to those used in the simulations discussed in Chapters 5, 6 and 7. The time step used in simulations was $0.001H/U_0$. Statistics were then collected over $70H/U_0$.

<center>8.3 Flow Structure</center>

<center>*8.3.1 Instantaneous Flow Fields*</center>

The vortical structure of the top SSL, as visualized by the instantaneous spanwise vorticity in Figure 8.2, looks qualitatively similar in all three simulations. The main difference is the length of the region over which the bleeding flow contains large-scale eddies. This length increases from about 1.8H in the d=0.02H case to 2.5H in the d=0.04H case to 3.2H in the d=0.09H case. This is due to the increase of the average size of the eddies generated by the jets forming in between the solid elements of the porous plate with the hole size. As some of these eddies interact with the larger eddies advected in the top SSL, the effect of increasing d/H is to decrease slightly the coherence of the largest eddies advected in the top SSL due to the higher capacity of the eddies carried by the bleeding flow to stretch the eddies advected in the top SSL. As the large-scale turbulence generated by the jets is highly 3D, the increase of d/H also induces an increase in the spanwise velocity magnitude in the region where the bleeding flow contains highly energetic eddies

<center>234</center>

(see Figure 8.4). The aforementioned reduction in the coherence of the largest eddies advected in the top SSL with increasing d/H also explain the slight decrease of the instantaneous spanwise velocity magnitude with increasing d/H in the downstream part of the top SSL in Figure 8.4.

Figure 8.5 shows the distribution of the points where velocity time series were collected to analyze the spectral content of the flow in the three simulations. Figures 8.6, 8.7 and 8.8 show the power spectra of the vertical velocity at point 10 situated inside the top SSL, close to the tip of the plate, and at point 43 situated in the top SSL, at about 22.5H from the plate, for the three cases. Comparison of the power spectra at point 10 suggest that for relatively small hole sizes, the dominant passage frequency of the vortex tubes is slightly larger than for relatively large hole sizes (e.g., the Strouhal number associated with the dominant frequency decays from 0.94 in the d=0.02H case to 0.75 in the d=0.04 and d=0.09 cases). However, the energy associated with the dominant frequency component increases monotonically with increasing d/H. All three simulations predict broad power spectra at point 10 with energetic frequencies for 0.4<St<2.

Analysis of the velocity power spectra at point 43 show that the effect of the hole size on the dominant passage frequency of the largest eddies forming in the top SSL is very small. The Strouhal number associated with this frequency is close to 0.095 in the d=0.02H and d=0.04H cases and decreases slightly to St=0.09 in the d=0.09H case. One can speculate this is due to the increasing interactions between the energetic eddies in the bleeding flow and the vortex tubes shed in the upstream part of the top SSL with increasing d/H.

Table 8.1 summarizes the predicted values of the mean drag coefficient, $\overline{C}_D$, and its root-mean-square fluctuations, C_D^{rms}, for the three cases. The values of $\overline{C}_D$ increase monotonically with increasing d/H though the rate of increase is very weak for d/H>0.04. This is probably due to the slight decrease of the bleeding flow discharge with increasing

d/H. The values of C_D^{rms} are also increasing monotonically with increasing d/H. The main reason for this are the larger size and increased coherence of the eddies shed in the SSLs of the jets forming in between the solid elements of the porous plate as the distance between these elements increases.

8.3.2 Mean Flow and Turbulence Statistics

The effect of increasing d/D is larger in terms of the size of the recirculation eddies forming at the channel bed downstream of the porous plate. As shown by the 2D mean flow streamlines in Figure 8.9, the length of the main recirculation region, l_1, is decreasing with increasing d/H, while its height, h_1, is remaining approximatively constant (Table 8.1). The separation point associated with this recirculation eddy moves slightly downstream with increasing d/H (e.g., from x=7H in case d=0.02H to x=8.5H in cases d=0.04H and d=0.09H). A second recirculation eddy starting at the plate is present in the cases with a relatively large d/H. It is induced by the suction effect associated with the top SSL that entrains some of the bleeding flow. The dimensions of this second eddy, l_3 and h_3, are also given in Table 8.1.

The distributions of the mean spanwise vorticity magnitude in Figure 8.10 show that the effect of increasing the hole size is to decrease the vorticity magnitude within the top SSL. Meanwhile, there is an increase in the vorticity magnitude levels behind the porous plate with d/H due to the increase in the penetration distance of the SSLs generated by the jets forming in between the solid elements of the porous fence with increasing d/H.

The TKE contours in Figure 8.11 show that the main effect of increasing the hole size is to increase the turbulence behind the porous plate in the region where the bleeding flow contains energetic eddies generated by the advection of part of the incoming flow through the fence. The TKE distribution within the upstream part of the top SSL is very

much unaffected by the variation of d/D. The only noticeable effect is that the region of high TKE penetrates faster close to the bed in the simulations with a relatively large d/D (e.g., the core of high TKE gets close to the bed starting at x/H=16 in the d=0.02H case and starting at x/H=12 in the d=0.04 and d=0.09H cases).

The spanwise-averaged distributions of the bed friction velocity in Figure 8.12 show a very slight increase of $u_\tau/u_{\tau 0}$ and the rms of the bed friction velocity fluctuations with increasing d/H beneath the plate. Past the plate, the bed friction velocity decays due to the fact that the mean streamwise velocity of the bleeding flow is less than that of the incoming flow. While the bed friction velocity takes a long distance to recover toward the values in the incoming fully turbulent channel flow, the rms of the bed friction velocity recovers to the incoming flow values around x/H=17 in the d=0.02H case and around x/H=12 in the d=0.04H and d=0.09H cases. Lower levels of the bed friction velocity fluctuations are observed in between the end of the region containing eddies generated by the openings between the solid elements of the porous plate and the region where the bottom part of the top SSL approaches the channel bed.

8.4 Conclusions

LES of flow past a 2D porous plate (P=36%) with no bottom gap (G/H=0) have been performed at a moderate cylinder Reynolds number (Re=20,000) to investigate the effects of varying the hole size (distance between the solid elements of the porous plate) on flow and turbulence structure.

Overall results showed that the effect of varying d/D on the flow is fairly mild. This included the position and streamwise extent of the separated flow regions forming in the wake of the porous plate and the dominant frequency associated with the passage of the

largest eddies in the top SSL at various distances from the plate. The main effect of increasing d/D was to increase the streamwise length of the region of high turbulence generated by the eddies originating in the jets forming in between the solid elements of the porous plate and to induce earlier contact between the bottom of the top SSL with the channel bed. Another effect was the mild increase of the mean drag coefficient and its rms fluctuations with increasing d/D.
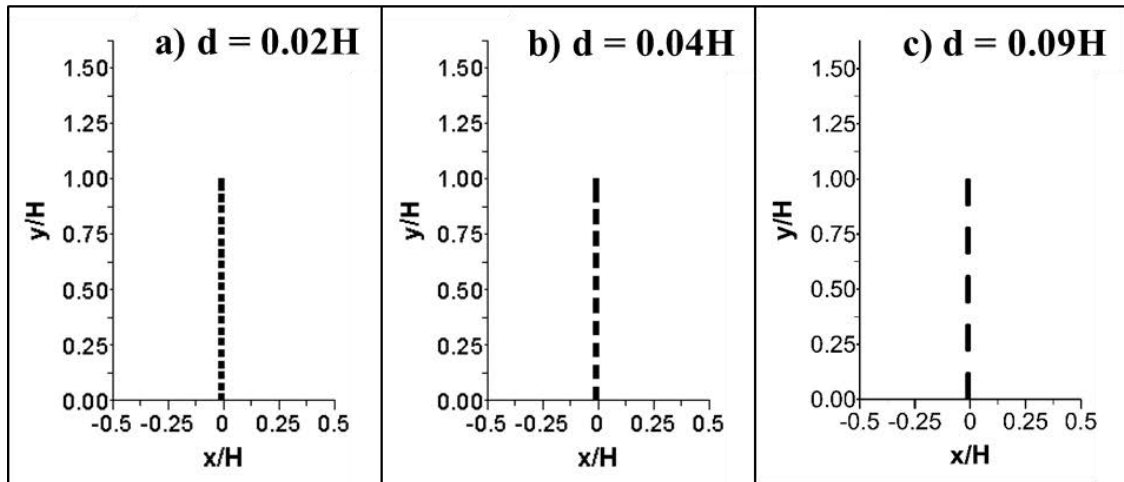
Figure 8.1 Sketch showing position of the vertical plate relative to the channel bottom in the three cases with varying d/H (G/H=0).
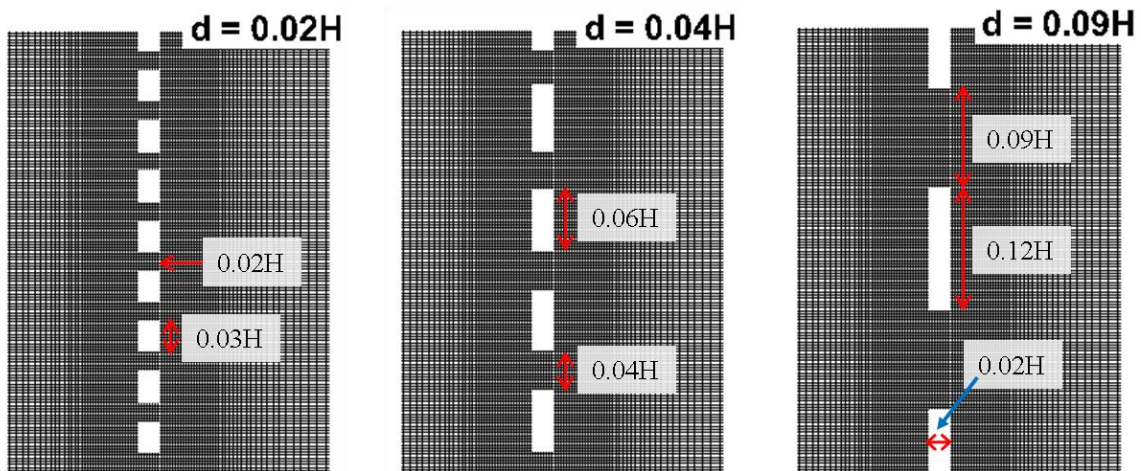
Figure 8.2 Sample computational mesh around the plate bottom in the three cases with varying d/H (G/H=0).
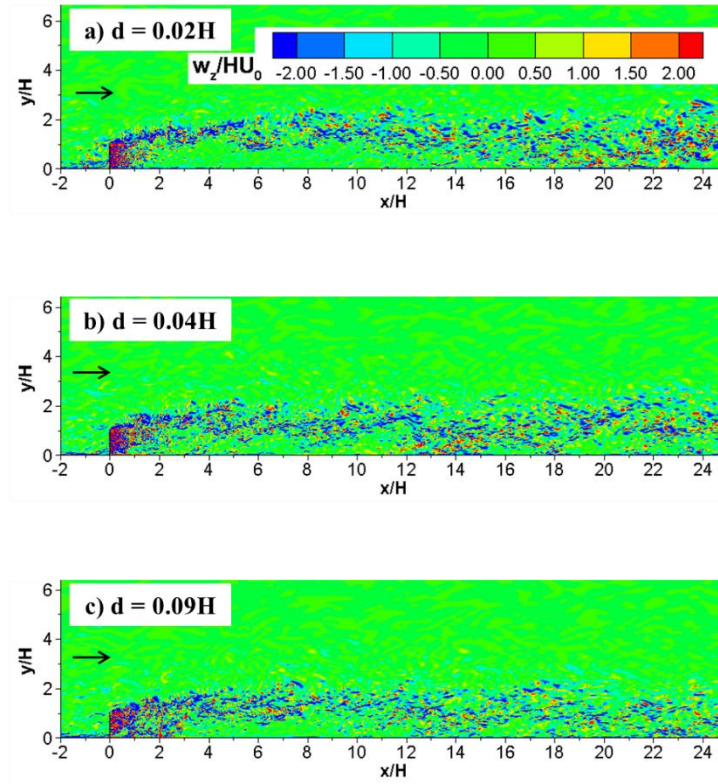
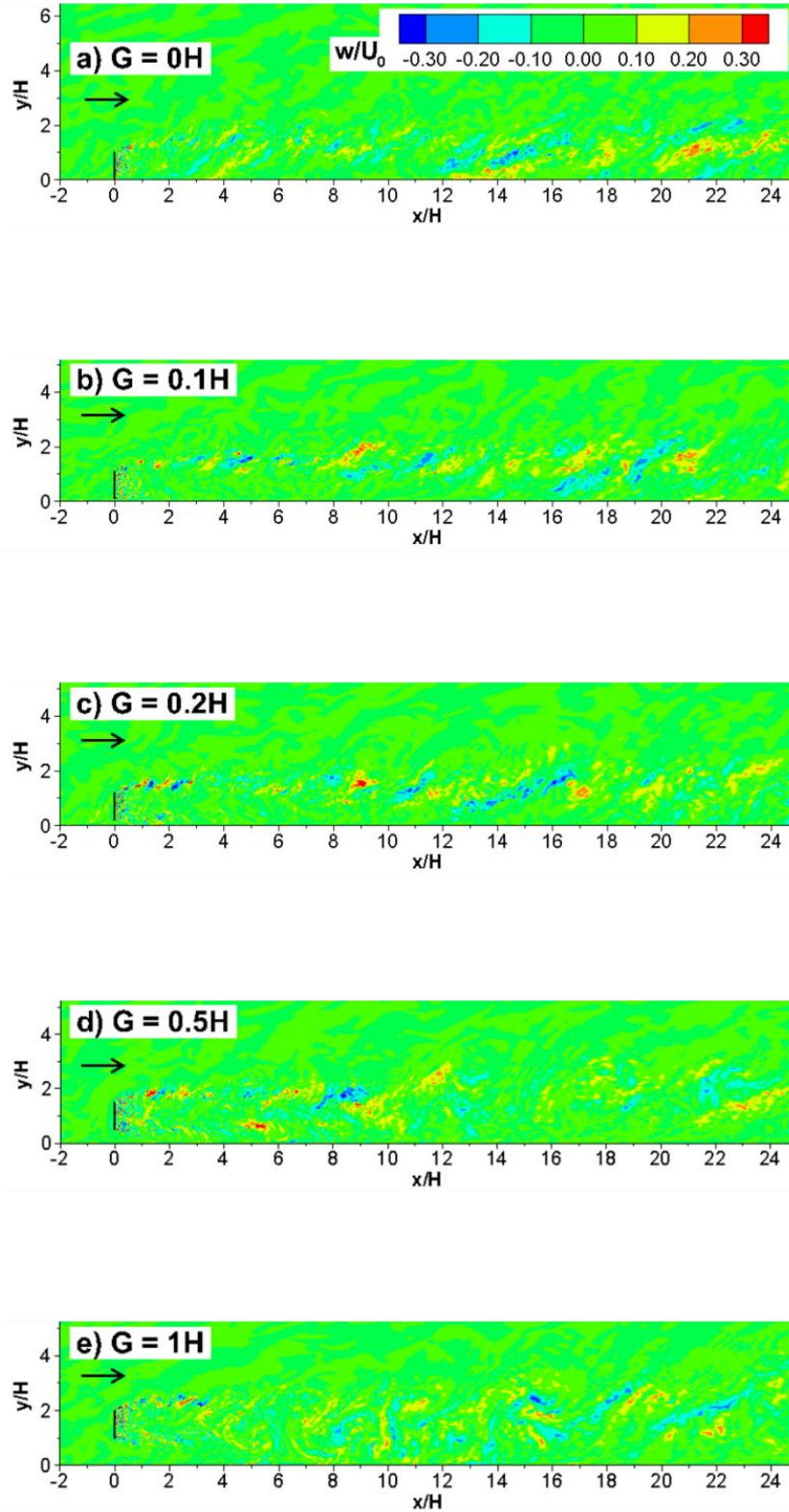Figure 8.3 Instantaneous spanwise vorticity, $\omega_z/(H/U_0)$, in an x-y plane.
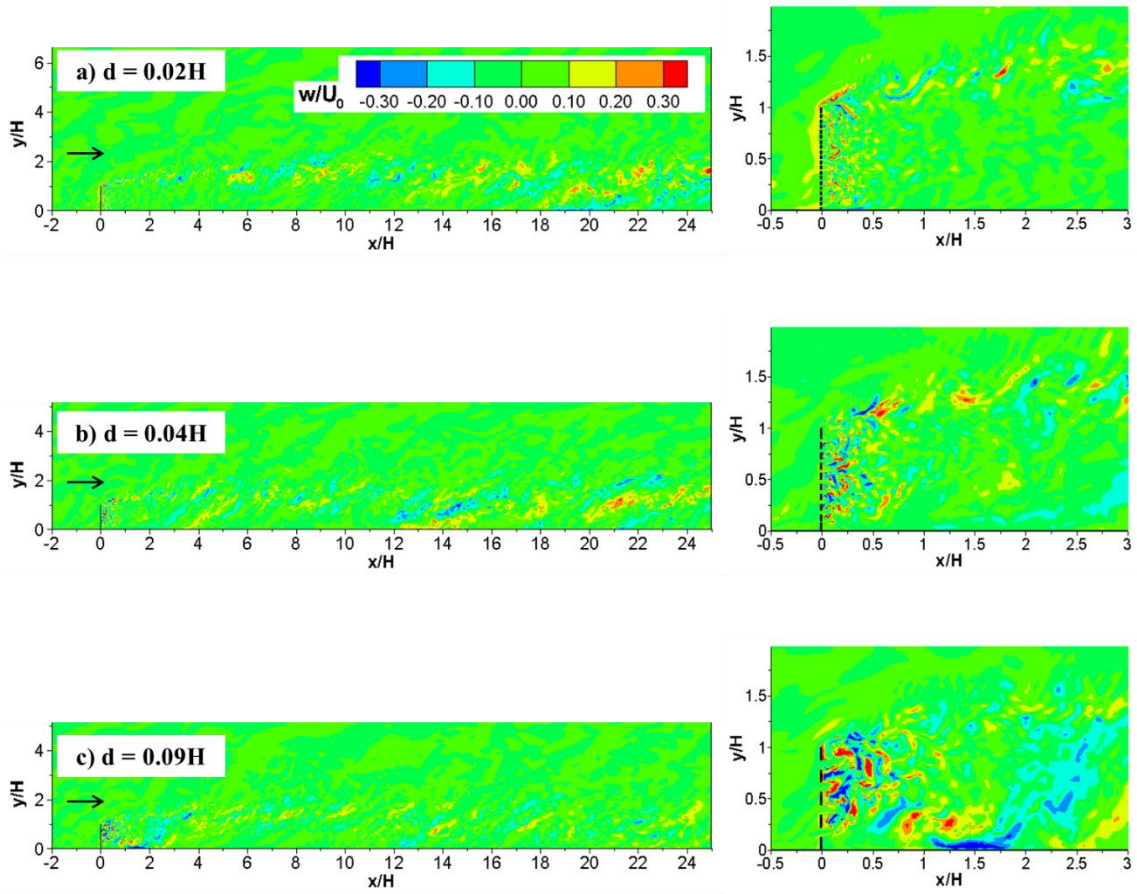
Figure 8.4 Instantaneous spanwise velocity, w/U_0, in an x-y plane.
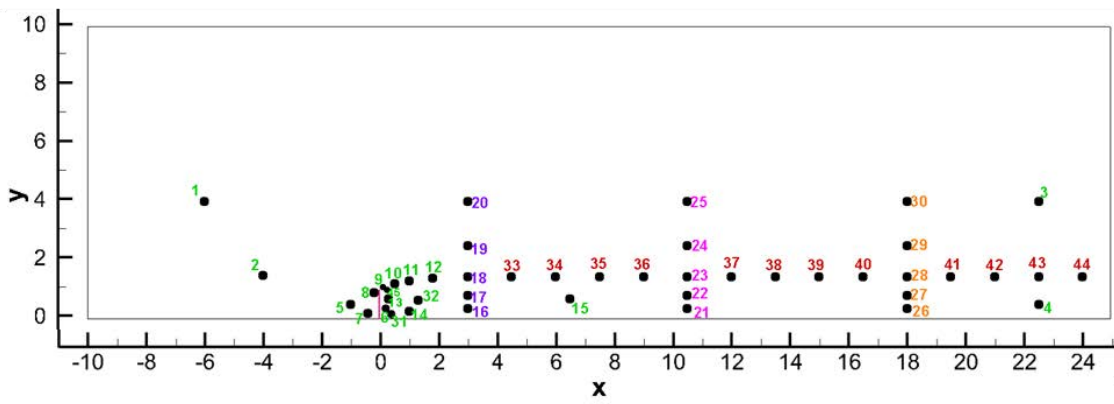
Figure 8.5 Location of points where time series were collected to analyze spectral content of the flow for the three cases with varying d/H.
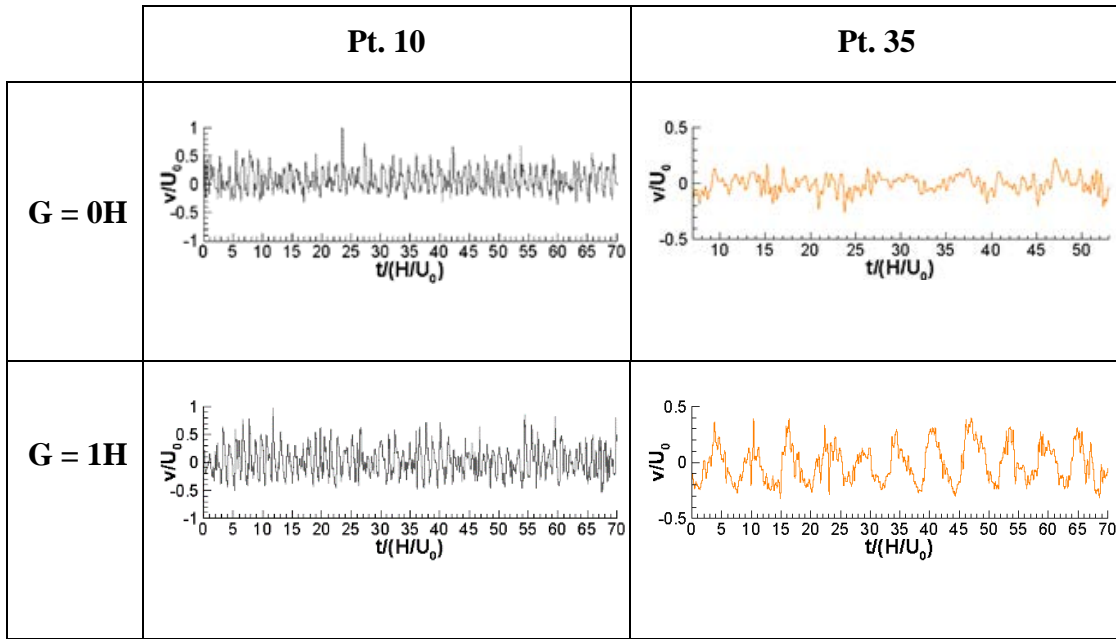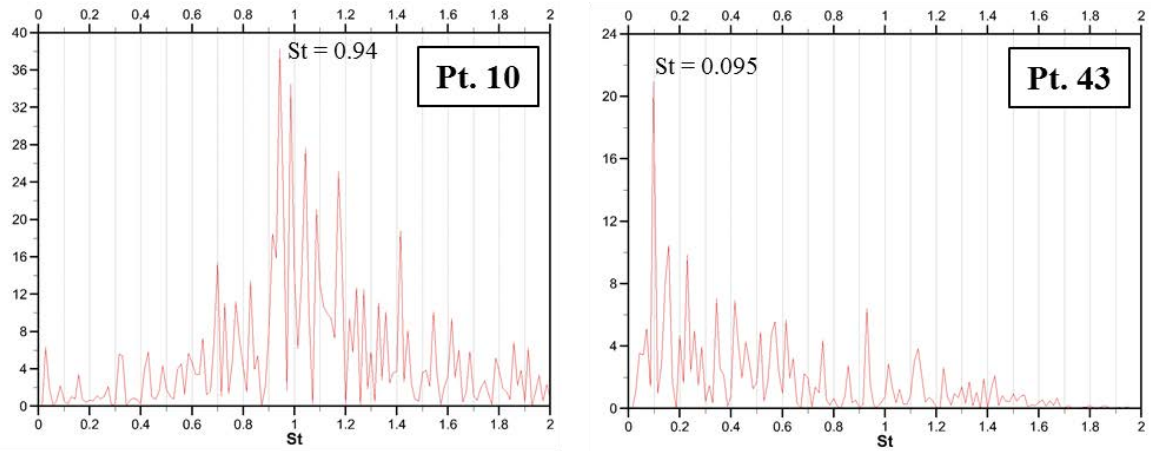
Figure 8.6 Power spectra of vertical velocity for d=0.02H case at: point 10 (x=0.5H, y=1.3H) and point 43 (x=22.5H, y=1.76H). Location of points is shown in Figure 8.5.
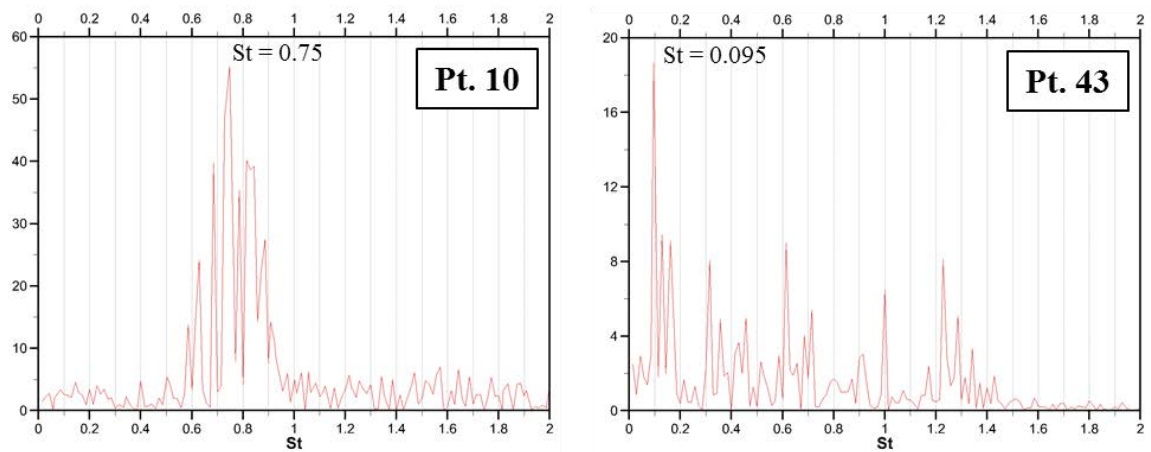
Figure 8.7 Power spectra of vertical velocity for d=0.04H case at: point 10 (x=0.5H, y=1.3H) and point 43 (x=22.5H, y=1.76H). Location of points is shown in Figure 8.5.
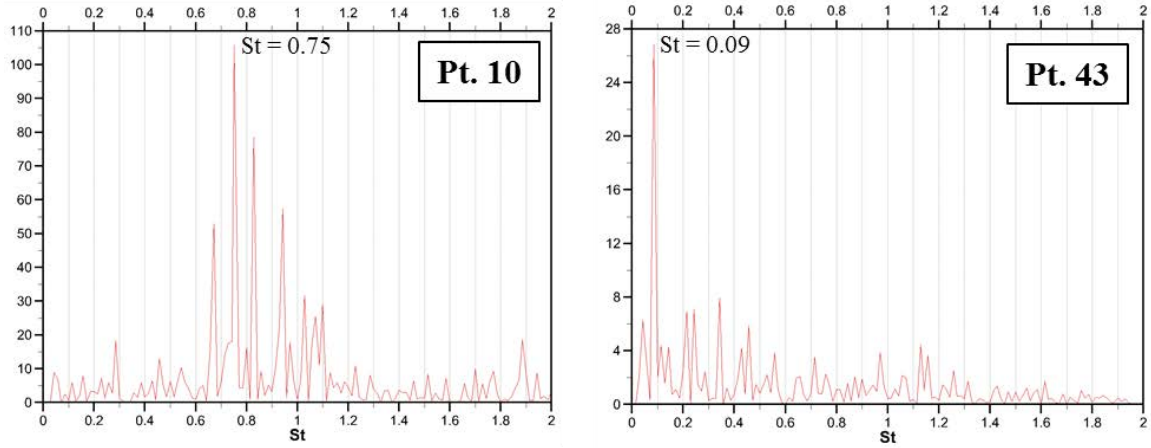
Figure 8.8 Power spectra of vertical velocity for d=0.09H case at: point 10 (x=0.5H, y=1.3H) and point 43 (x=22.5H, y=1.76H). Location of points is shown in Figure 8.5.
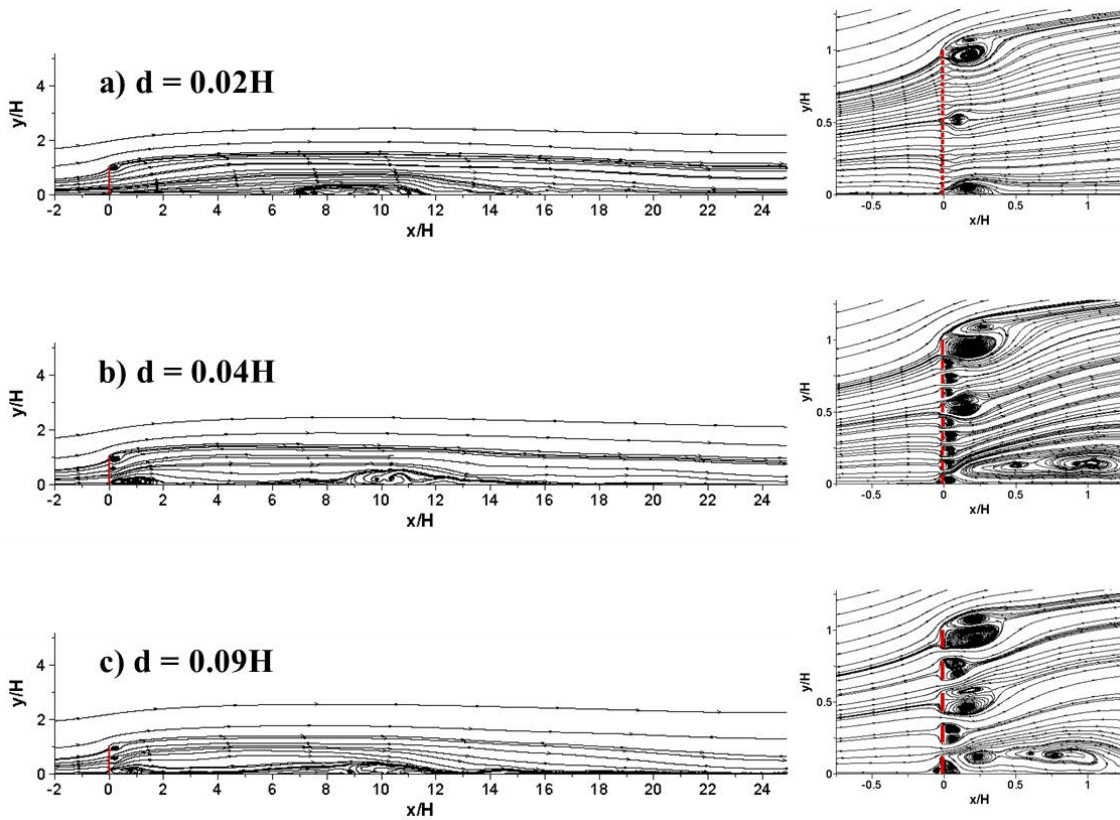
Figure 8.9 Mean flow structure visualized using 2D streamline patterns.
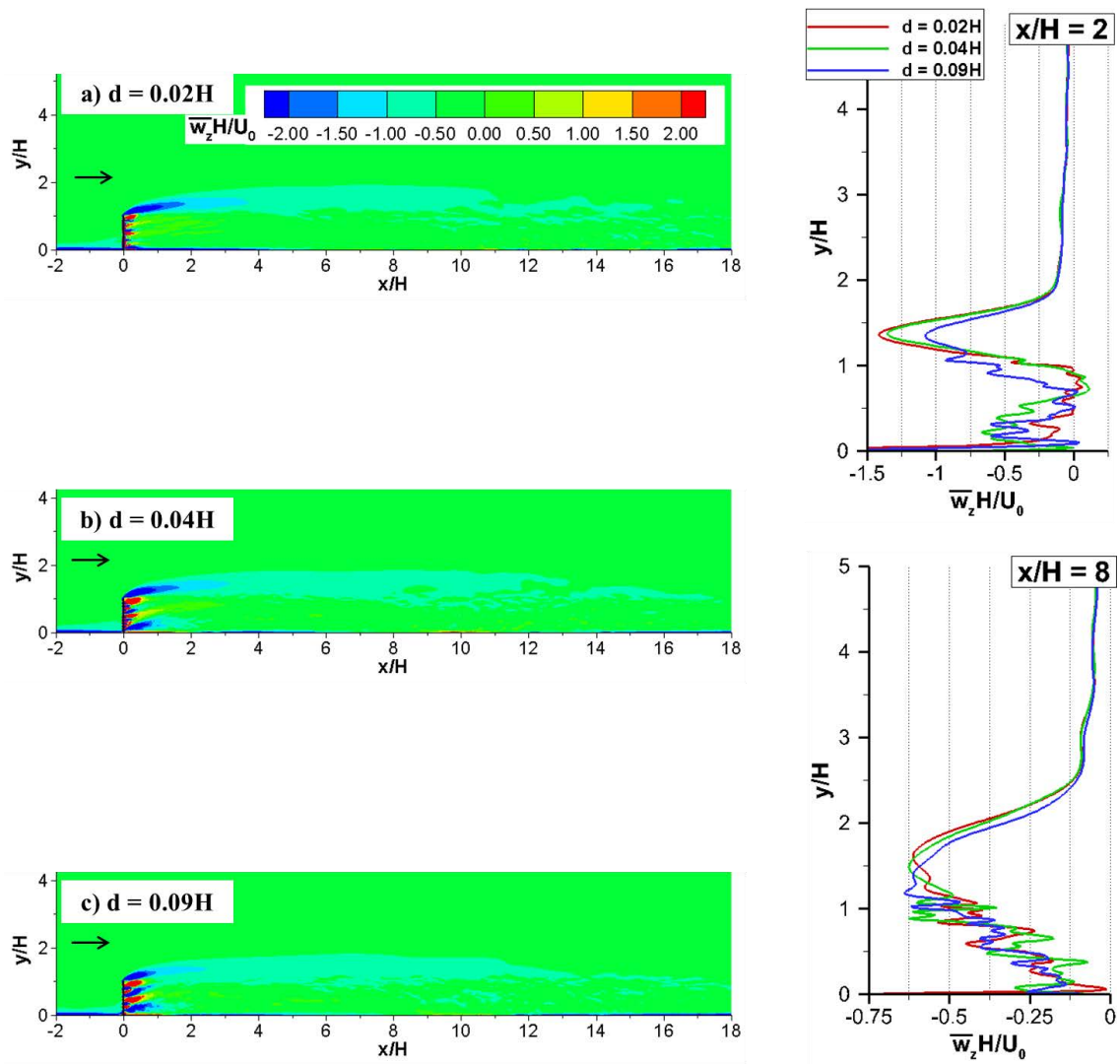
Figure 8.10 Mean spanwise vorticity magnitude, $\overline{\omega_z}/(H/U_0)$, in an x-y plane and vertical profiles at x/H=2 and x/H=8.
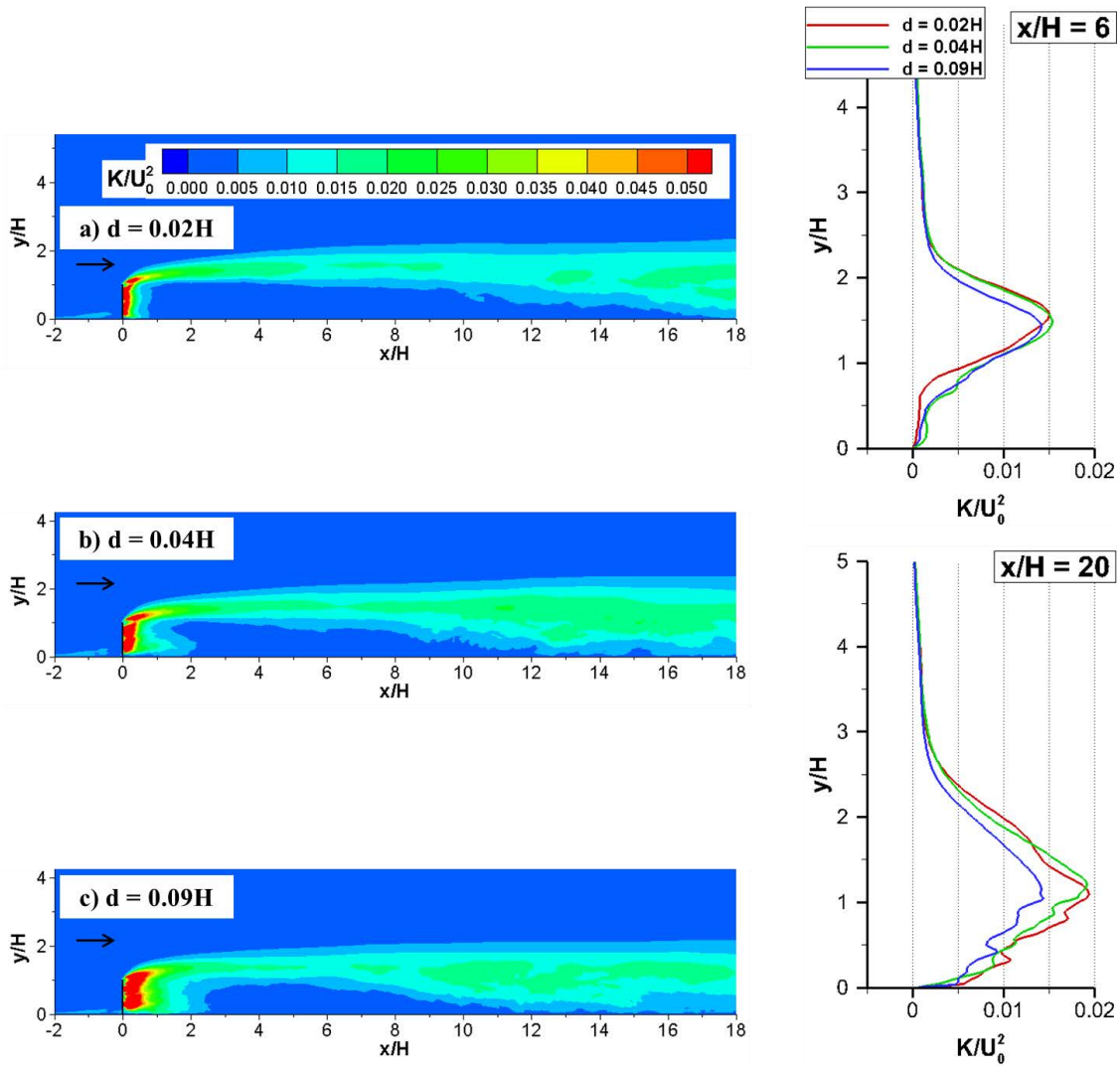
Figure 8.11 Turbulent kinetic energy, K/U_0^2, in an x-y plane. Also shown are vertical profiles of K/U_0^2 at x/H=6 and x/H=20.
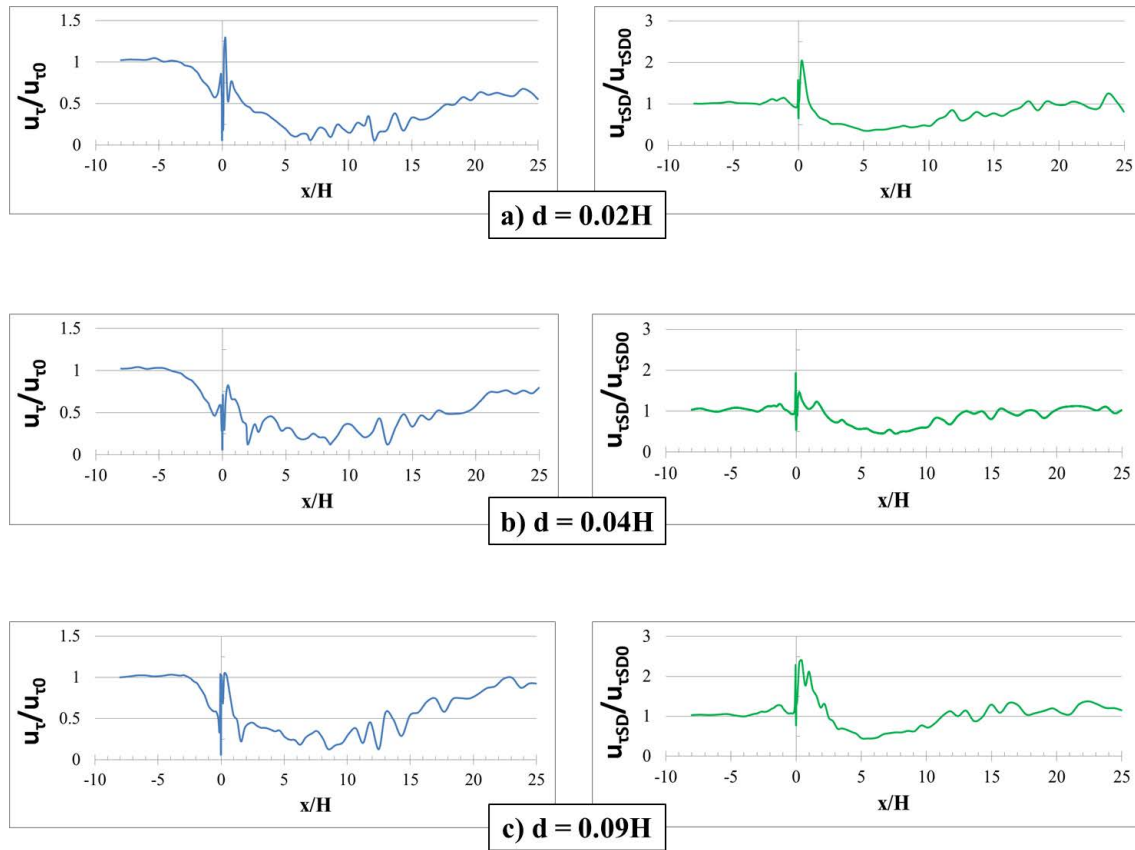
Figure 8.12 Nondimensional spanwise-averaged mean bed friction velocity, $u_\tau / u_{\tau0}$, where $u_{\tau0}=0.04U_0$ is the mean bed shear stress in the incoming fully developed turbulent channel flow. Also shown is the nondimensional spanwise-averaged rms of the bed friction velocity fluctuations where $u_{\tau SD0}=0.025U_0$ is the mean rms of the bed shear stress in the incoming fully developed turbulent channel flow.

Table 8.1 Effect of plate porosity on the variables characterizing the streamwise force acting on the fence and the size of the recirculation bubbles forming behind the fence.

Case	$\overline{C_D}$	$C_D{}^{rms}$	l_1	h_1	l_3	h_3	St	$Q/(\rho U_0 H^2)$
d = 0.02H	0.52	0.06	5H	0.5H	-	-	0.095	0.301
d = 0.04H	0.56	0.06	4.5H	0.5H	2H	0.3H	0.095	0.297
d = 0.09H	0.57	0.07	4H	0.5H	1.8H	0.3H	0.09	0.277

CHAPTER 9 EFFECT OF BED ROUGHNESS ON FLOW PAST A VERTICAL PLATE

9.1 Introduction

In this chapter the effects of the bed roughness on the flow past vertical plates with a porosity of 0% and 36% are investigated by comparing cases in which the bed is smooth with the corresponding cases in which an array of identical square ribs is present at the bed. The investigation is limited to plates in contact with the bottom surface (G/H=0). A sketch of the vertical plate with P=0% and P=36% used in the four cases investigated in this chapter is shown in the Figure 9.1. The smooth bottom surface cases with P=0% and P=36% are the same as the ones considered in Chapter 5 (P=0%, G/H=0) and Chapter 6 (P=36%, G/H=0), respectively.

9.2 Simulation Setup

The computational domain, plate height (H), location of the plate (10H from the inflow section) and the coordinate system are identical to the ones considered in the simulations discussed in Chapters 5 and 6. The thickness of the solid plate is 0.02H and the length of the computational domain is 35H. The computational domain contains about 19 million (768x384x64) grid points in P=0% smooth-bed case and about 25 million (768x512x64) grid points in the P=36% smooth-bed case. For the simulations with a rough bed, the number of mesh cells was increased to about 38 million (1536x384x64) grid points in P=0% case and to about 50 million (1536x512x64) in P=36% case. Figure 9.2 shows the position of the square ribs. The ribs' height is k=0.15H and their streamwise spacing is λ=1.2H.

The x-axis is aligned with the incoming flow direction and the z-axis is aligned with the vertical direction relative to the horizontal bottom surface of the channel. The plate

height, H, is used as the length scale. To resolve the flow near the surface of the ribs, the discretization along the x axis was changed in the simulations with ribs compared to the simulations conducted with a smooth bed (no ribs). Grid points were clustered around the x=constant and y=constant locations corresponding to the solid surfaces of the solid plate and square ribs (see Figure 9.2) to resolve the attached boundary layers on these surfaces. The mesh was uniform along the z direction. The cell size in the wall normal direction was close to 0.002H for all solid surfaces. This distance corresponds to close to 2 nondimensional wall units. Away from the plate, the average dimensions of the 3D cells were increased to about 0.07Hx0.06Hx0.05H.

The simulations were performed for a Reynolds number of Re=20,000. All the boundary conditions are identical to those used in the simulations discussed in Chapters 5 and 6. The time step used in simulations was $0.001H/U_0$.

The simulations were performed for a Reynolds number of Re=20,000. All the boundary conditions are identical to those used in the simulations discussed in Chapters 5 and 6. The time step used in simulations was $0.001H/U_0$.

9.3 Flow Structure

9.3.1 Instantaneous Flow Field

In the solid plate case (P=0%), the effect of the presence of ribs at the bottom surface is to increase the range of energetic eddies approaching the plate (Figures 9.3a-b). The main reason for that are the eddies detaching from the SSLs of the individual ribs that are then advected toward the plate and act as a main source of disturbance for the vortex tubes forming in the upstream part of the top SSL. Close to the plate, these eddies occupy a region whose height is close to the plate height, H. As these eddies are characterized by

a large degree of randomness, one expects the formation of vortex tubes will be much more irregular in the top SSL. The other main effect is that the interactions between the large billows forming in the top SSL and the bottom surface occur much earlier in the rough-bed case. Highly-3D energetic eddies are shed from the SSLs of the ribs situated within the main recirculation region and interact with the large eddies advected in the top SSL. These interactions are noticeable starting at x/D=4. By contrast, in the smooth bed case, interactions between the large SSL eddies and the bottom surface occur only for x/D>10, toward the end of the main recirculation region in the mean wake flow.

Similar effects are also observed in the P=36% case (Figures 9.3c-d). In particular, strong interactions between the large eddies advected in the top SSL and the bottom surface are observed starting at x/H=12 in the smooth-bed case, where the flow reattaches at the end of the recirculation bubble (Figure 9.10c), and at x/H=7 in the rough-bed case. Another effect due to bed roughness is the slight reduction in the length over which the bleeding flow contains highly-energetic 3D eddies downstream of the porous plate.

Due to the additional disturbances induced by the eddies generated by the ribs upstream of the solid plate, the elongated streaks of positive and negative values of the instantaneous spanwise velocity inside the upstream part of the top SSL are less regular and smaller in the rough-bed case compared to the smooth-bed case (see Figures 9.4a-b). The effects on the dynamics and regularity of the regions of high and low spanwise velocity magnitude are less obvious for the porous case (see Figures 9.4c-d). In the P=36% case, the effect of the bed roughness is to increase the level of the spanwise velocity fluctuations over both the upstream (x/H<12, see also Figures 9.10c-d) and the downstream parts of the

top SSL. This is also confirmed by the examination of the mean spanwise velocity fluctuations in an x-y plane for the two cases (not shown).

Figure 9.5 shows the distribution of the points where velocity time series were collected to analyze the spectral content of the flow in the four simulations. Figures 9.6 to 9.9 show the power spectra of the vertical velocity at point 10 situated inside the top SSL, close to the tip of the plate, and at point 28 situated in the top SSL, at about 18H from the plate. In some cases the power spectrum at point 35 situated at x=7.5H from the plate is also included. Comparison of the power spectra at point 10 show no significant effect of the bed roughness on the dominant frequency of the vortex tubes in the upstream part of the SSL and the overall range of energetic frequencies within the top SSL close to the plate.

Larger differences are observed for the P=0% case in the downstream part of the top SSL, where the dominant frequency changes from St=0.08 for the smooth-bed case (Figure 9.6) to St=0.06 for the rough-bed case (Figure 9.7). Animations show that in the rough-bed case some of the large SSL eddies start interacting with the bottom roughness elements between x/H=4 and x/H=8. As an eddy is slowed down, it starts merging with the eddy advected behind it to form a larger eddy. Thus, the effect of the roughness elements present behind the plate is to favor vortex pairing within the top SSL. This also explains why the dominant frequency in the top SSL is St~0.12 at x=7.5H (point 35 in Figure 9.7), which is about twice the dominant frequency at x=18H (point 28).

In the case with P=36%, the effect of the bed roughness elements on the dominant frequencies present in the wake flow is fairly small. The dominant passage frequency varies from St=0.095 in the smooth-bed case (Figure 9.8) to St=0.1 in the rough-bed case (Figure 9.9). The presence of a relatively strong bleeding flow in between the rough bed and the

top SSL, reduces the effect of the roughness elements on the dynamics of the large eddies advected in the top SSL.

Table 9.1 summarizes the predicted values of the mean drag coefficient, $\overline{C_D}$, and its root-mean-square fluctuations, C_D^{rms}, for the four cases. For both cases (P=0% and P=36%), $\overline{C_D}$ decreases significantly (e.g., by 20-30%) due to the presence of roughness elements at the bottom surface. Most of this reduction is due to the roughness elements present upstream of the plate. The near-bed incoming flow loses energy as it is advected over these roughness elements and starts to decelerate at a larger distance from the plate. As a result, the pressure forces and the adverse pressure gradients are milder in the case of a rough bed. This explains the observed decay in the mean drag coefficient for the rough bed cases. The effect of the roughness elements situated upstream of the plate is to increase the higher frequency oscillation of the pressure drag force due to the eddies generated by the ribs that approach the upstream face of the plate. Meanwhile, by disturbing the vortex tubes forming in the upstream part of the top SSL, there is a decrease in the energy of the lower frequency oscillations induced by the large SSL eddies advected away from the plate. The end effect is that the values of C_D^{rms} are fairly insensitive to the level of bed roughness.

9.3.2 Mean Flow and Turbulence Statistics

In the P=0% case (Figures 9.10a-b), a main effect of the roughness elements on the wake flow is to reduce the maximum width of the main recirculation bubble in the mean flow from 1.8H to 1.5H and its length from 16.2H to 9.6H with respect to the smooth bed case, if one ignores the local recirculation regions induced by the roughness elements. In the P=36% case (Figures 9.10c-d), the effect of increasing the bed roughness is to move closer to the plate the start of the main recirculation bubble attached to the bed (e.g., from

x/H=8.5 to x/H=4.7) and to increase the length of the same bubble (e.g., from 4.5H to about 6H). This is one of the reasons why the effect of the roughness elements on the large eddies advected in the top SSL is relatively small in the P=36% case. A secondary effect is the increase of the length of the upstream secondary bubble starting close to the porous plate (e.g., from 2H in the smooth-bed case to about 3.5H in the rough-bed case). One should also notice that despite the differences observed in the position and size of the main recirculation bubbles, the SSL attaches to the bed in the mean flow around x/H=14-15 in both cases.

The effect of the bed roughness on the vorticity amplification inside the top SSL is very small for both P=0% and 36% cases (Figure 9.11). The only noticeable change is that the upstream part of the top SSL reduces its inclination with respect to the streamwise direction as the bed roughness is increased, which is consistent with the change in the shape of the main recirculation bubble in Figure 9.10. The increase in the turbulence levels of the incoming flow approaching the porous plate also induces a decay of the penetration length of the tongues of vorticity associated with the jets forming in between the solid elements of the porous plate (Figures 9.11c-d).

In both cases, the effect of the roughness elements present upstream of the plate is to increase the turbulent kinetic energy in the vicinity of the bed surface (Figure 9.12). The height of the layer where the TKE is amplified is increasing monotonically as the plate is approached. This is due to the production of small-scale energetic eddies in the SSLs of the roughness elements situated upstream of the plate.

Consistent with the distributions of the vorticity in the instantaneous flow that showed that the length over which highly 3D eddies are present in the bleeding flow

252

decreases with the increase in the bed roughness in the P=36% case, the streamwise decay of the TKE away from the face of the porous plate is faster in the rough-bed case (Figures 9.12c-d). In both cases (P=0% and P=36%), the effect of the ribs placed downstream of the plate is to reduce the streamwise distance at which the region of high TKE penetrates up to the bottom surface. Additionally, the TKE levels within the region where the SSL is situated in the immediate vicinity the bottom surface are increasing with the bed roughness in the P=36% case. This is due to the 3D energetic eddies generated by the flow within the top SSL moving over the roughness elements. The effect is much less noticeable in the P=0% case.

9.4 Conclusions

The effect of bed roughness on flow past solid (P=0%) and porous (P=36%) vertical plates mounted on a flat horizontal surface (G/H=0) was studied by comparing simulations conducted with a smooth bed with simulations in which an array of identical square ribs was placed at the bed. The height of the ribs was 0.15H.

Simulation results showed that the effect of the ribs situated upstream of the obstacles was to generate a layer containing highly energetic eddies in the vicinity of the bed and to decrease the kinetic energy of the flow approaching the plate. As a result, the mean drag coefficient was lower in the simulations with ribs. These highly energetic eddies induced strong disturbances in the upstream part of the top SSL. For the case of a porous plate, the downstream length over which the bleeding flow contained highly energetic eddies originating in the jets forming in between the solid elements of the porous fence decayed with the increase in the bed roughness. This effect is also related to the presence

of small-scale turbulence in the flow penetrating through the openings of the porous fence in the case ribs were present upstream of the fence.

The presence of the ribs downstream of the fence affected the position and length of the main recirculating regions forming downstream of the solid and porous plates. In particular, the energetic eddies generated by the ribs were able to interact with the larger eddies advected in the top SSL starting at a smaller distance from the plate. For the solid plate case, where there is no bleeding flow, these interactions resulted in the merging of successively shed eddies around $x/H=7$ and the decrease by a factor of two of the dominant frequency associated with the advection of large eddies inside the downstream part of the top SSL. The dominant passage frequency of the large eddies inside the downstream part of the top SSL was much less affected in the porous plate case, where the bleeding flow diminishes the strength of the interactions between the eddies advected in the top SSL and the turbulence generated by the roughness elements. Compared with the smooth bed case, the interactions between the turbulence generated by the ribs with the eddies advected in the top SSL forming past the porous plate resulted in a noticeable amplification of the turbulence within the top SSL downstream of the location where the SSL approached the bed.
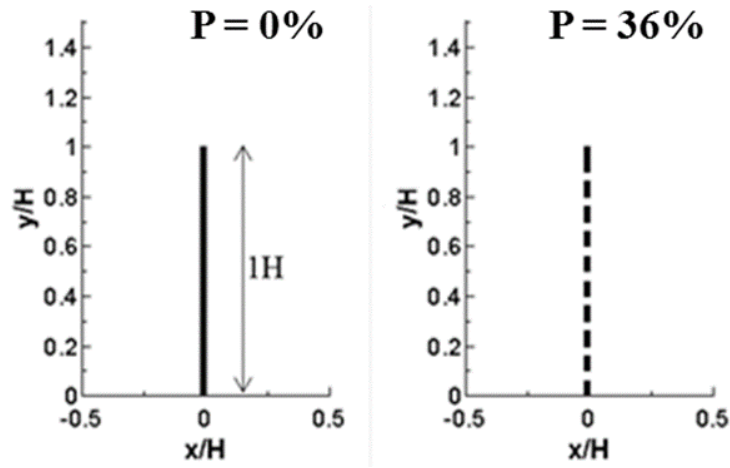
Figure 9.1 Sketch showing geometrical characteristics of the vertical solid and porous plates.
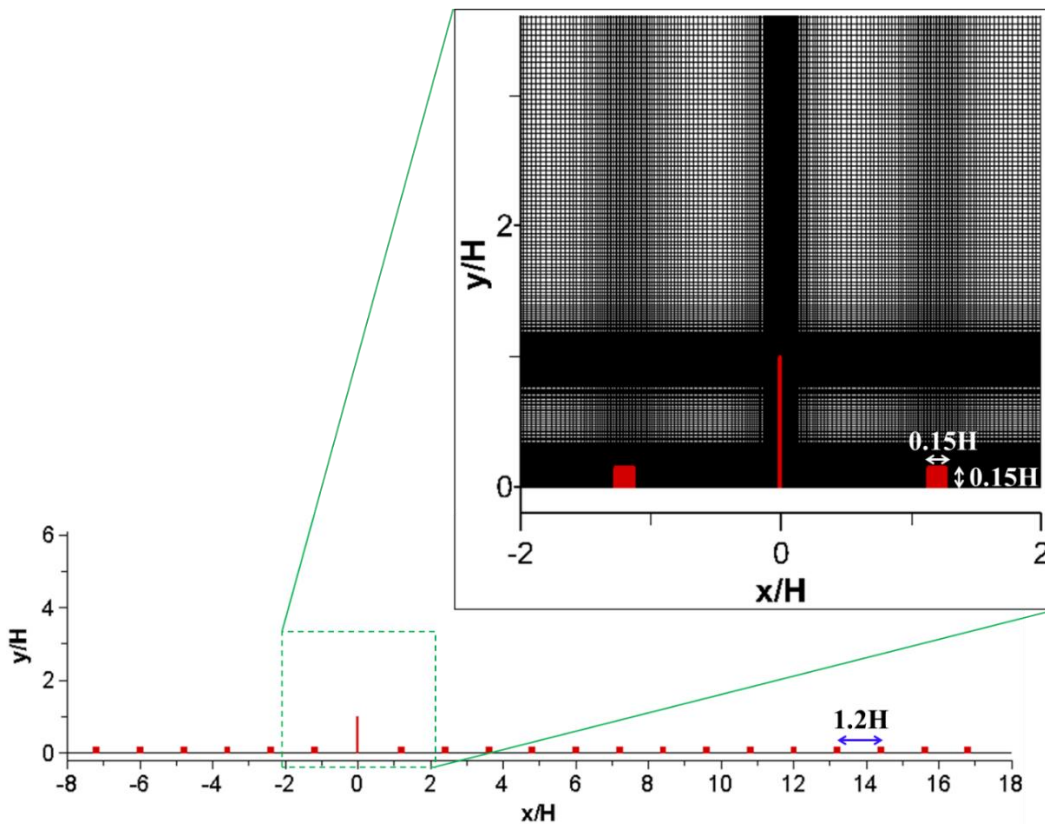
Figure 9.2 Sketch showing computational domain used in the simulation with ribs. Also indicated is the position of the plate (x/H=0). The height of the square ribs is k=0.15H ribs. The distance between consecutive ribs is λ=1.2H. Also shown is the mesh around the ribs and the plate for P=0% case.

255
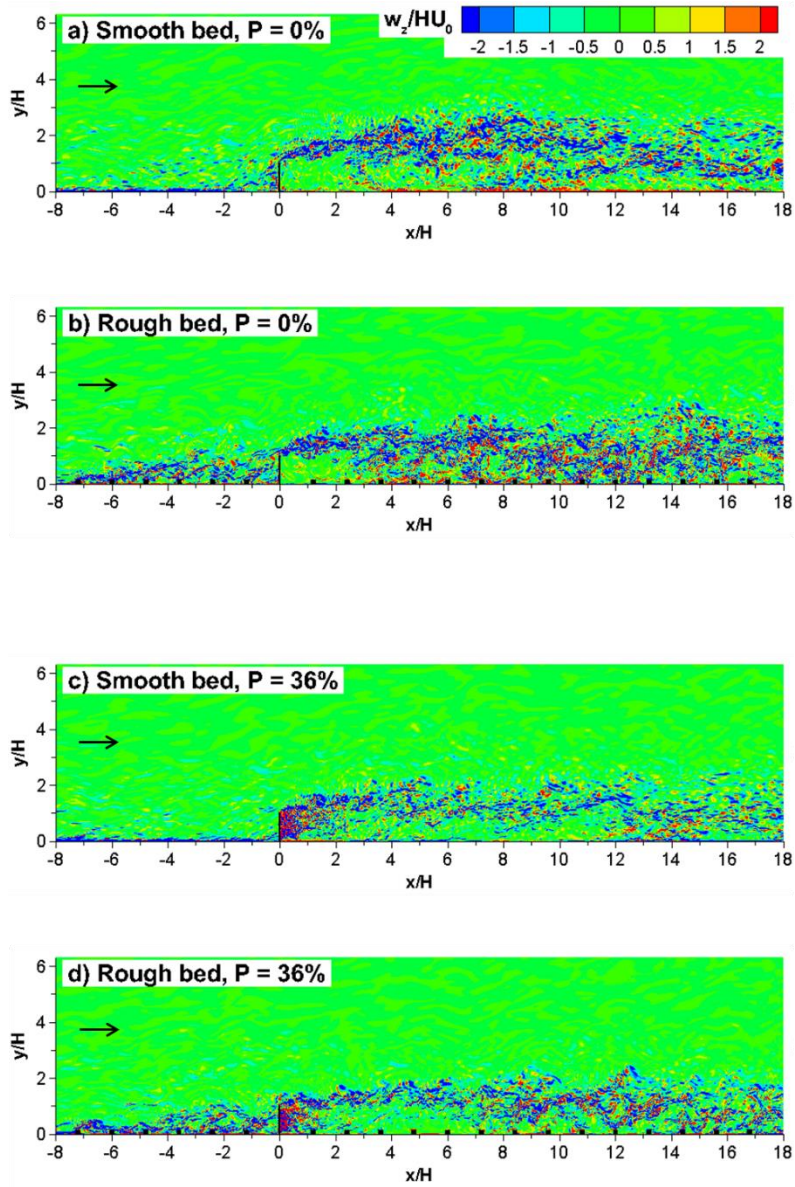
Figure 9.3 Instantaneous spanwise vorticity, $\omega_z/(H/U_0)$, in an x-y plane.
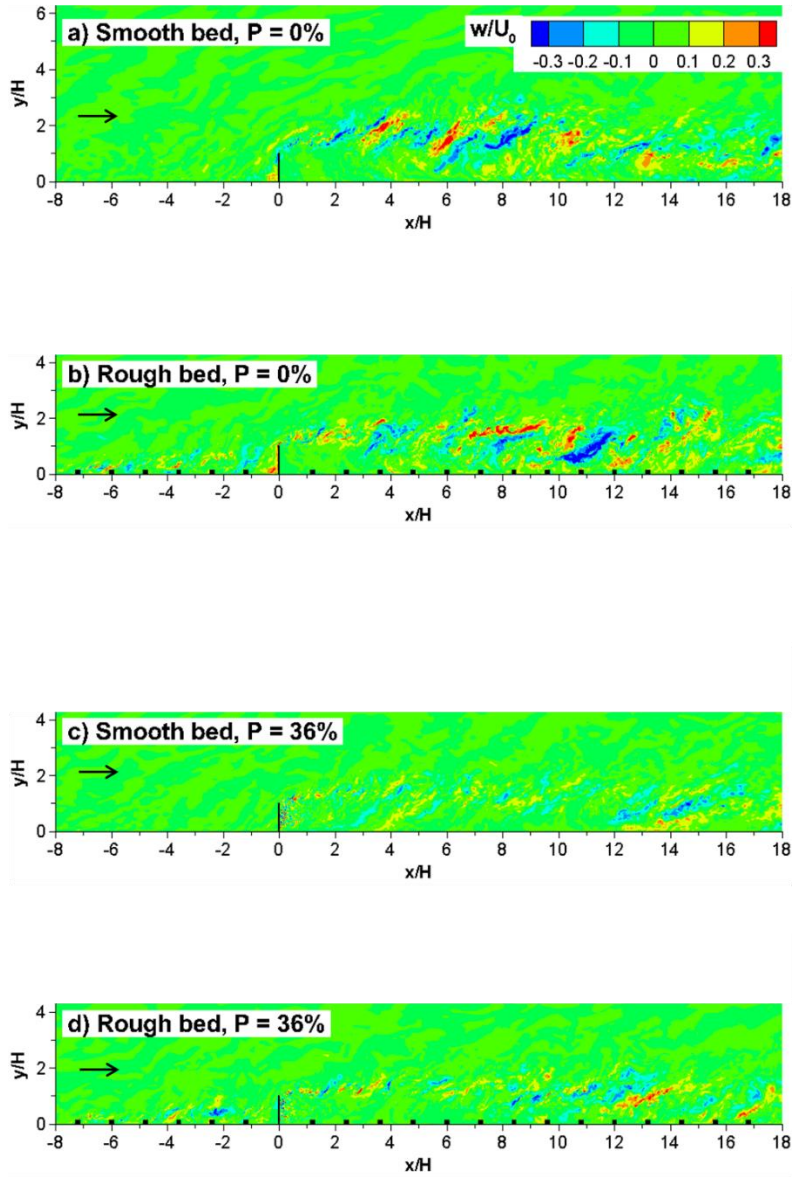
Figure 9.4 Instantaneous spanwise velocity, w/U_0, in an x-y plane.
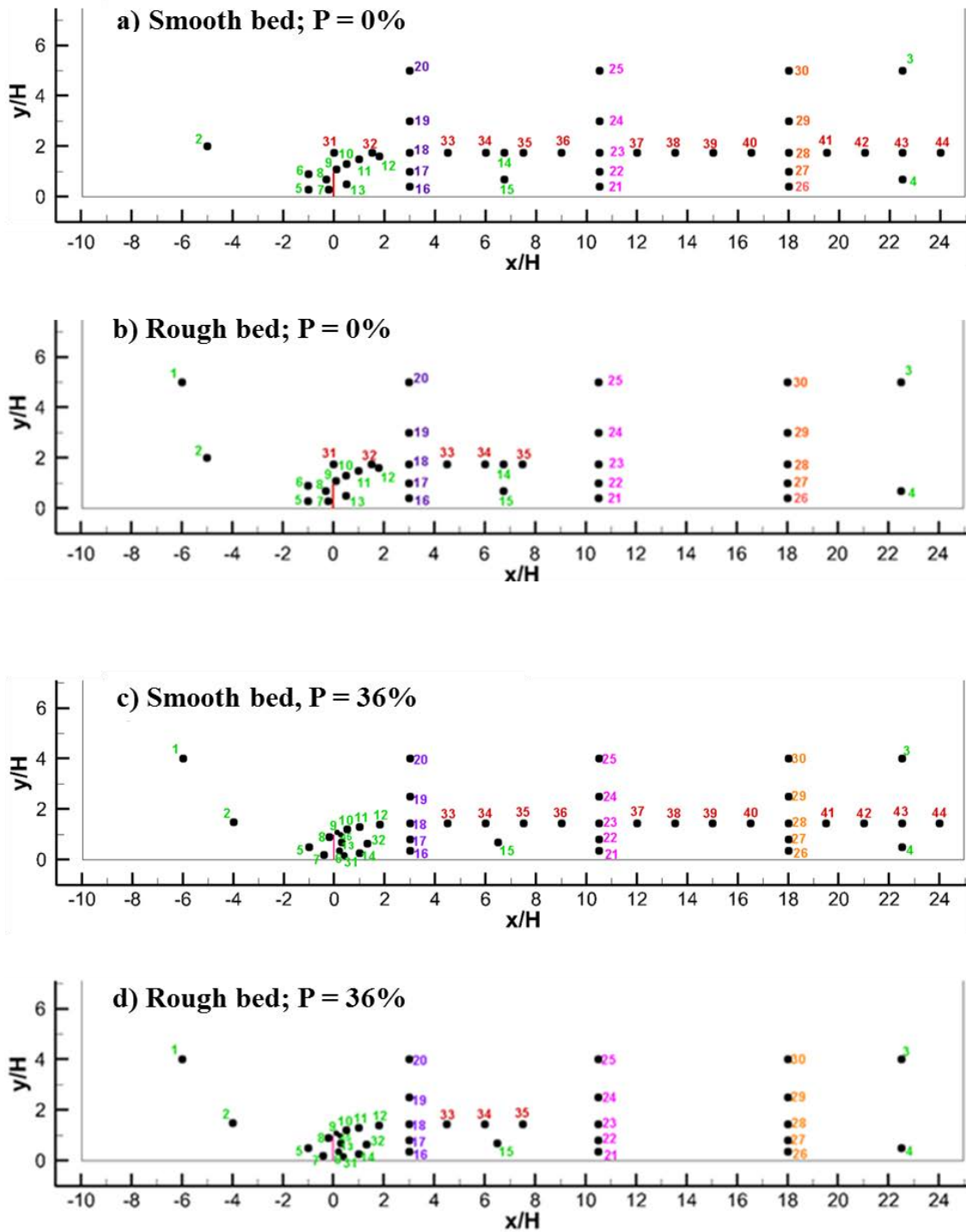
Figure 9.5 Location of points where time series were collected to analyze spectral content of the flow.
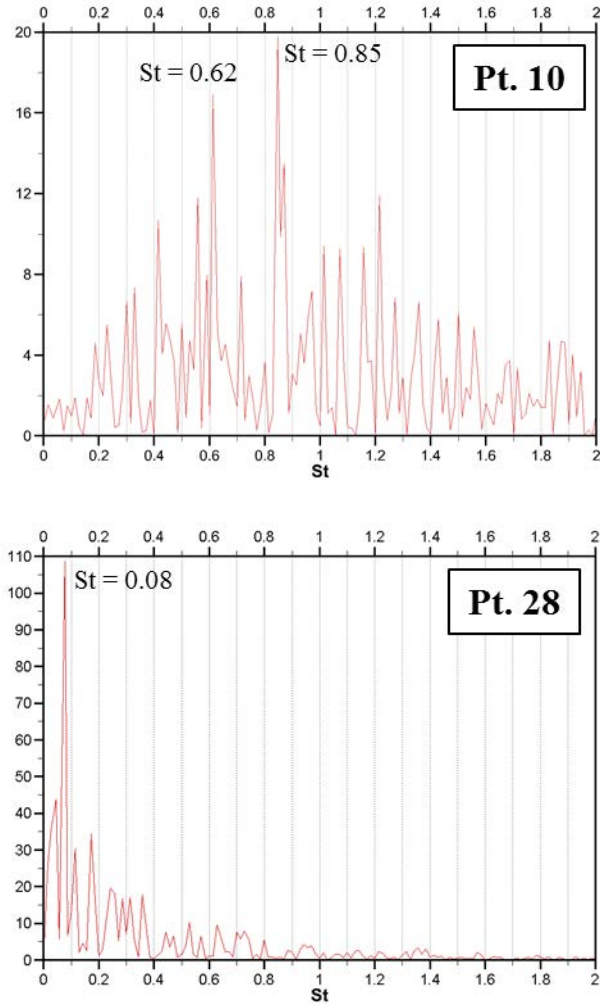
Figure 9.6 Power spectra of vertical velocity for the P=0% smooth-bed case at: point 10 (x=0.5H, y=1.3H) and point 28 (x=18H, y=1.76H). Location of points is shown in Figure 9.5a.
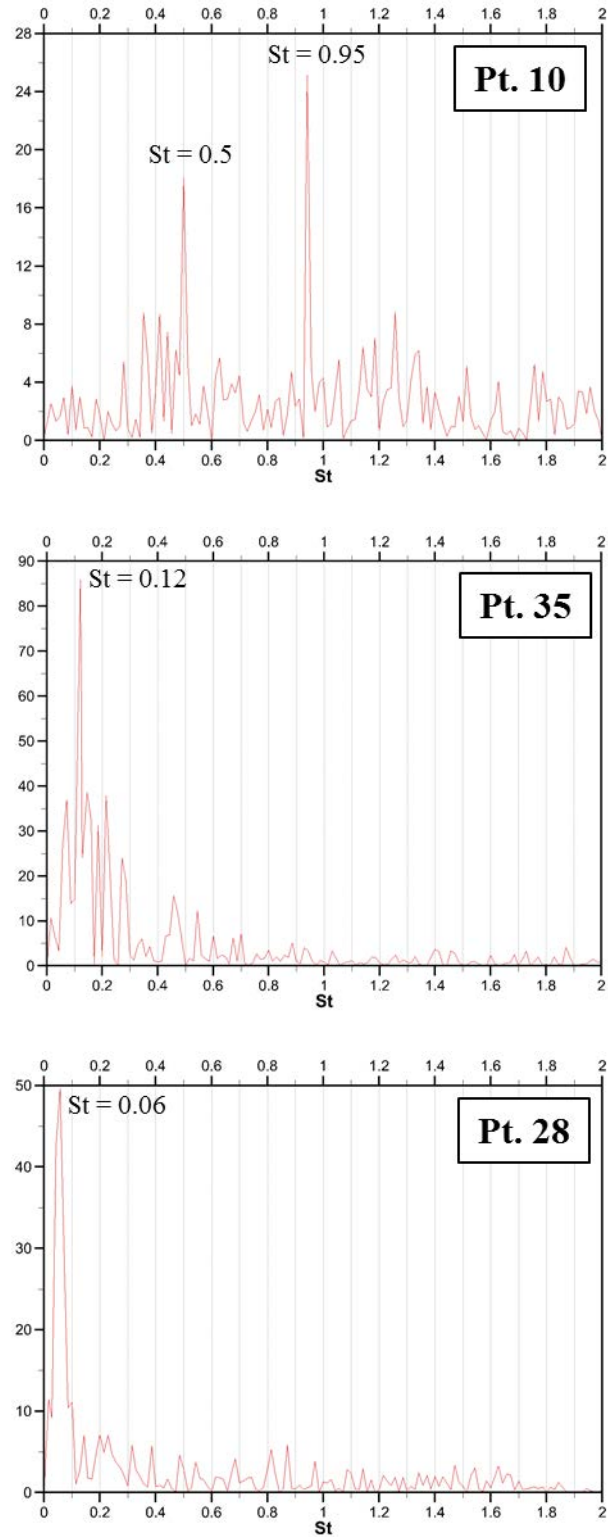
Figure 9.7 Power spectra of vertical velocity for the P=0% rough-bed case at: point 10 (x=0.5H, y=1.3H), point 35 (x=7.5H, y=1.76H) and point 28 (x=18H, y=1.76H). Location of points is shown in Figure 9.5b.
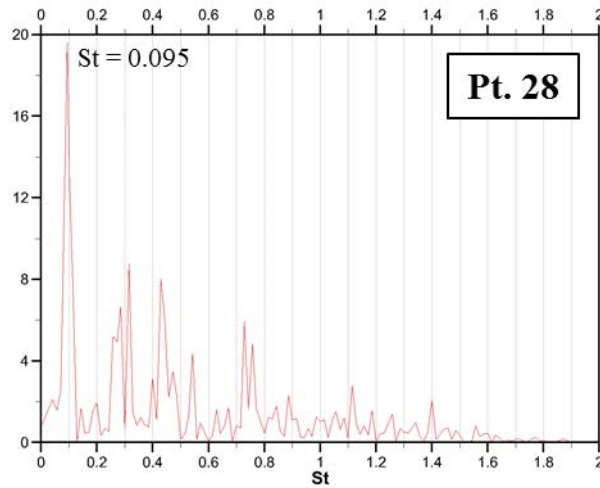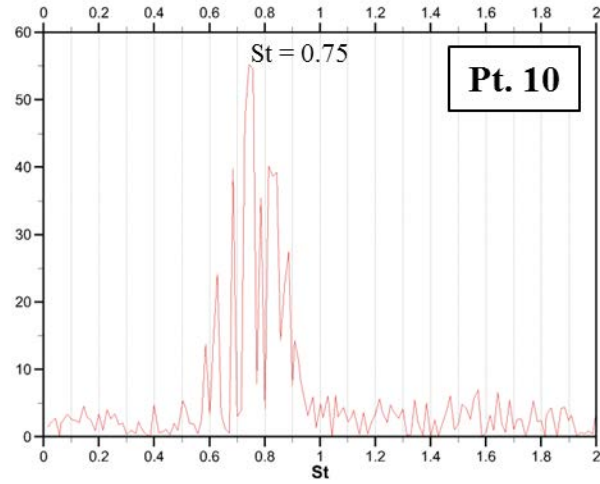
Figure 9.8 Power spectra of vertical velocity for the P=36% smooth-bed case at: point 10 (x=0.5H, y=1.3H) and point 28 (x=18H, y=1.76H). Location of points is shown in Figure 9.5c.
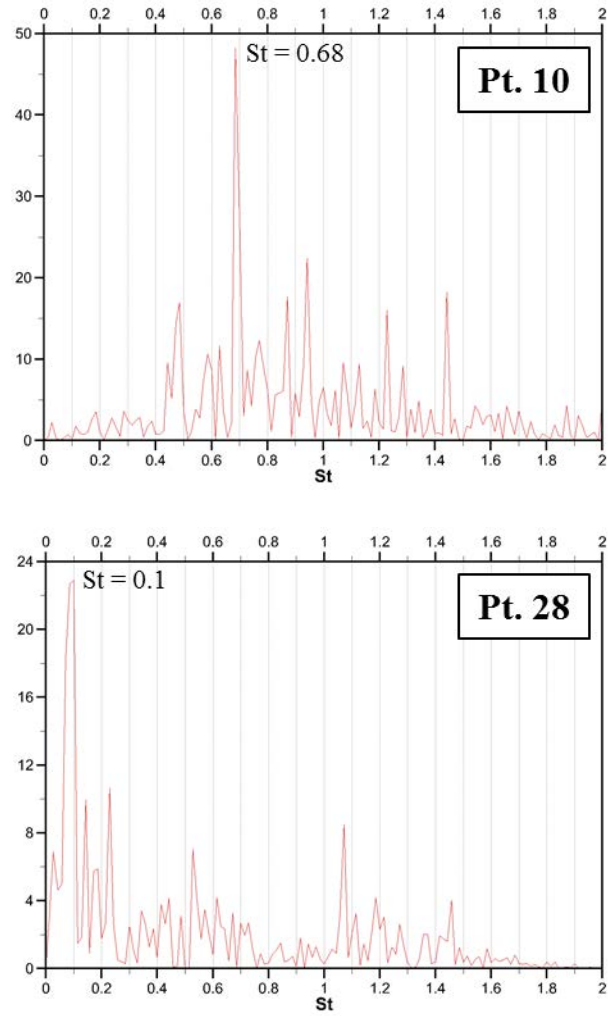
Figure 9.9 Power spectra of vertical velocity for the P=36% rough-bed case at: point 10 (x=0.5H, y=1.3H) and point 28 (x=18H, y=1.76H). Location of points is shown in Figure 9.5d.
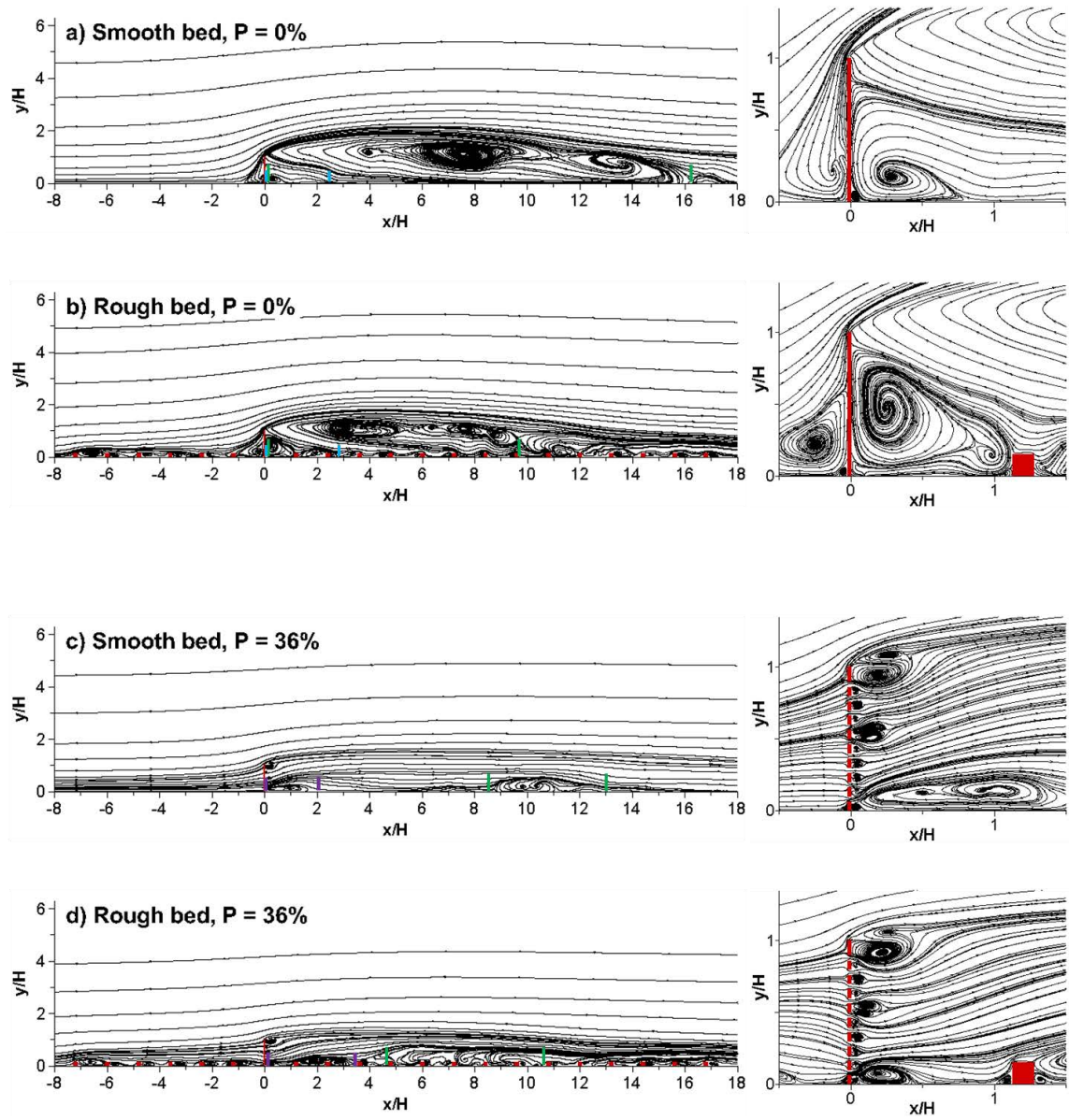
Figure 9.10 Mean flow structure visualized using 2D streamline patterns. The vertical thick lines denote the start and end of the bottom attached recirculation bubbles.
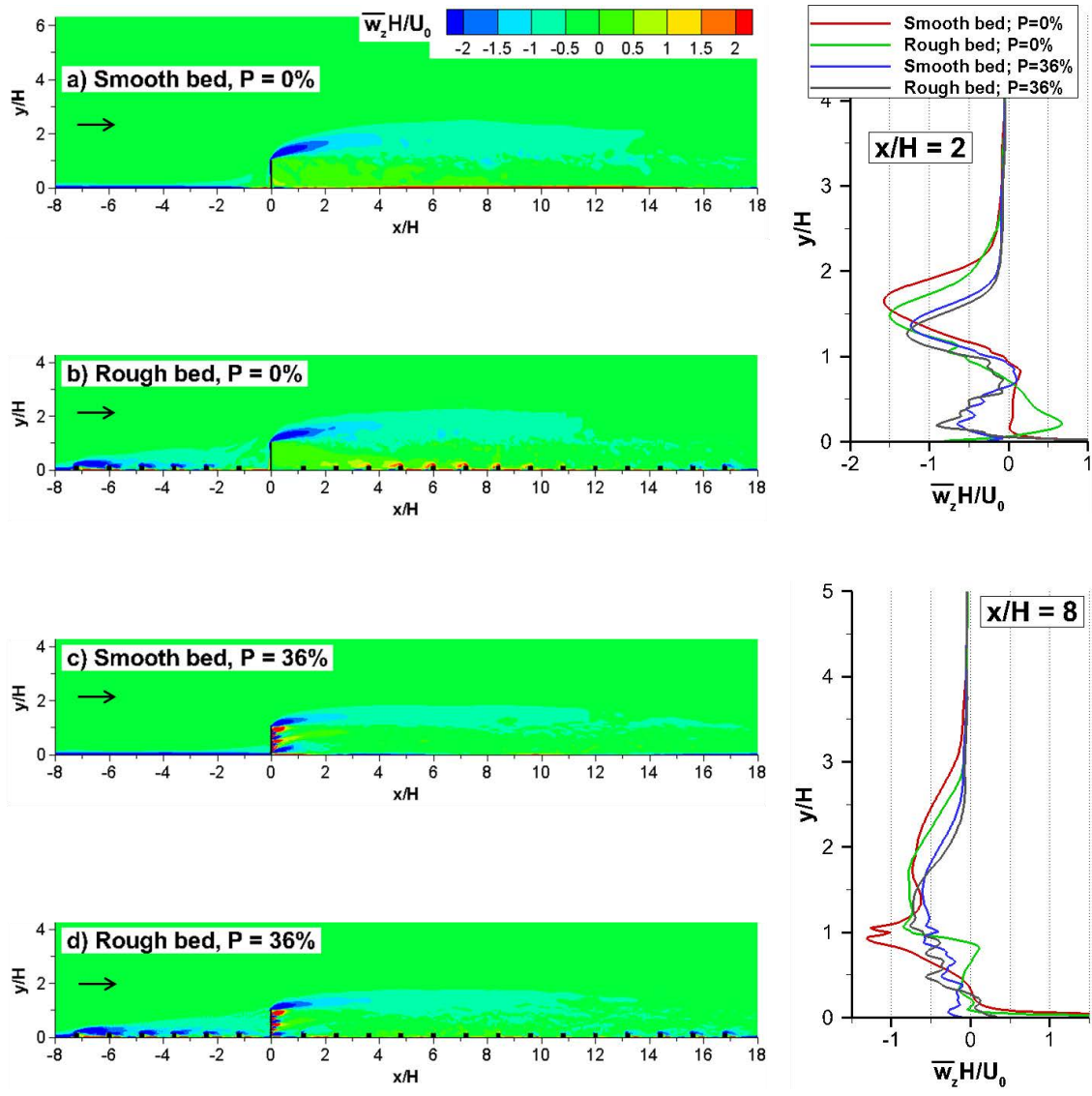
Figure 9.11 Mean spanwise vorticity, $\overline{\omega_z}/(H/U_0)$, in an x-y plane and vertical profiles at x/H=2 and x/H=8.
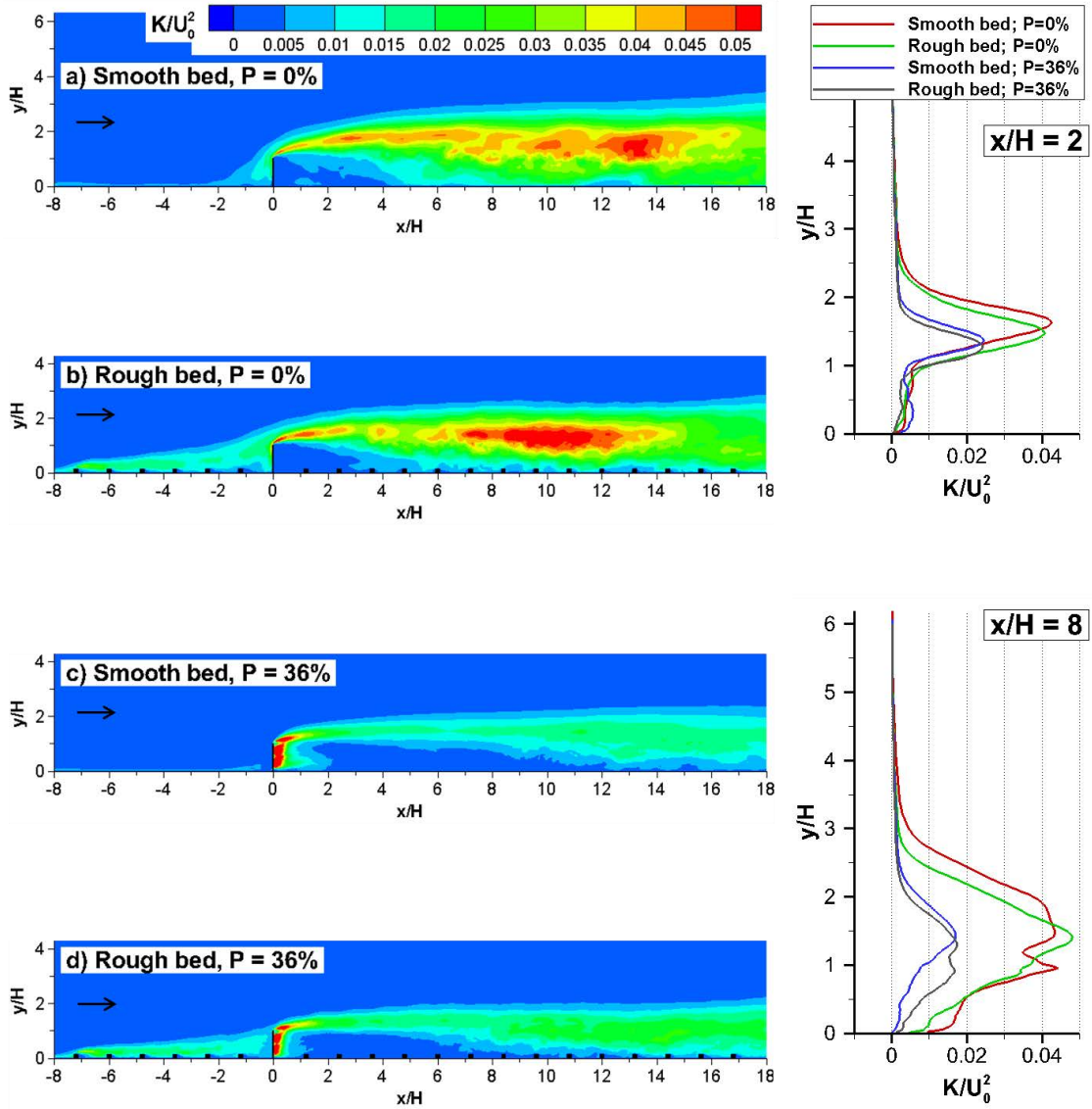
Figure 9.12 Turbulent kinetic energy, K/U_0^2, in an x-y plane. Also shown are vertical profiles of K/U_0^2 at x/H=2 and x/H=8.

Table 9.1 Effect of bed roughness on the variables characterizing the streamwise force acting on the fence and the size of the recirculation bubbles forming behind the fence.

Case	$\overline{C_D}$	C_D^{rms}	l_1	h_1	l_2	h_2	l_3	h_3	St	$Q/(\rho U_0 H^2)$
Smooth bed; P=0%	0.78	0.03	16.2H	1.8H	2.5H	0.7H	-	-	0.08	-
Rough bed; P=0%	0.63	0.04	9.6H	1.5H	2.7H	0.8H	-	-	0.06	-
Smooth bed; P=36%	0.56	0.06	4.5H	0.5H	-	-	2H	0.3H	0.095	0.297
Rough bed; P=36%	0.39	0.04	6H	0.7H	-	-	3.5H	0.4H	0.1	0.239

CHAPTER 10 A METHOD TO ASSESS EFFICIENCY AND IMPROVE DESIGN OF
SNOW FENCES

10.1 Introduction

The main objective of this chapter is to propose a joint experimental and numerical
approach to monitor snow deposits around snow fences, quantitatively estimate snow
deposits in the field, assess the efficiency and improve the design of snow fences. As
opposed to the more complex numerical approach adopted in the first part of this study to
understand fundamental physics of flow past solid and porous obstacles, in this chapter
computationally less expensive 2D RANS simulations (see section 3.3) are used to estimate
main features of the mean flow patterns around snow fences of different designs in a more
realistic set up. The approach described in the present chapter was tested and validated for
lightweight plastic snow fences that are commonly used to protect roads in the US Midwest
against the snow drifting. Of particular interest was to assess the performance of
lightweight plastic snow fences with a lower porosity than the typical 50% porosity used
in standard designs of such fences. The proposed design solution can be used for protection
against snow drifting in regions with narrow rights of way, where standard fences cannot
be deployed at the recommended distance from the road. The novel methodology described
in this chapter can be extended to improve the design of other types of snow fences.

10.2 Problem Statement

Ideally, roads are designed to facilitate accumulation of snow in road ditches, while
the snow moving over the road should be prevented from starting to accumulate on the
road. Designing roads such that snow drifts never accumulate on the roadways is not
always possible. Snow fences are generally installed perpendicular to the prevailing wind
direction and along the roadway. Snow particles are prone to deposit on the downwind side

267

of the snow fence, where the velocity magnitude is small. The amount of snow that a fence can retain on its downwind side is mainly a function of the fence porosity and the size of the bottom gap. Snow fences can be constructed from several materials (Sañudo-Fontaned et al., 2011) and are called structural snow fences (e.g., wooden fence and plastic fence). Another alternative is the use of living snow fences which consist of trees and/or local grasses hedge planted along the roads (see Nixon et al., 2006). Both structural and living snow fences have advantages and disadvantages, as described in Tabler (1991).

Moreover, snow fences make the roads safer by improving the visibility for drivers. Several states in U.S. (e.g., Minnesota, Wyoming and Utah) have established a clear link between the deployment of snow fences in critical areas of highways and a significant reduction (by about 50%) of the number of serious vehicle accidents associated with snow drifting and blowing. This was accompanied by a major cut in winter maintenance costs, as snow fences lower the cost of snow removal and decreases freezing effects on the roadway (Tabler, 1991).

Snow Fence Guides (e.g., Tabler, 1991 and 2003; Iowa DOT: Iowa's Cooperative Snow Fence Program, 2005) provide design recommendation regarding the setback distance from roads, the porosity and the bottom gap. For structural snow fences, the snow drift extends downwind generally up to 25 to 35 times the fence height, while the height of the drift is comparable to that of the fence (Tabler, 2003). As already discussed in the literature review chapter, most conventional snow fence designs recommend the use of structural snow fences with porosity close to 50%. To maximize the snow storage capacity of such fences, it is generally recommended the bottom gap under the fence is equal to 10% of the total fence height, H=h+G. A main design challenge occurs when the right of way

of the road to be protected is too narrow to allow placing the snow fence at the distance from the edge of the roadway recommended by the guidelines. There are two main ways to address this problem.

The first option is to install fences of complex design. For example, one solution is to use the so-called 'blower' snow fences that have lateral fins attached obliquely to the vertical support (Haniu et al., 2009). The fins play the role of wind straightening vanes. Another design approach involves the use of metallic snow fences with airfoil snow plates placed close to the roadway (García Nieto et al., 2010). Though such designs were successfully tested in field conditions, they were never deployed on a large scale. The main reasons are that manufacturing them is fairly expensive compared to conventional designs (e.g., plastic snow fences in most U.S. states). In some countries the deployment of heavy and rigid structures very close to the road is considered unsafe.

The second option is to modify the porosity, bottom gap and height of conventional snow fences (e.g., inexpensive wood lath fences or lightweight plastic snow fences mounted on a welded fence) such that they lead to more efficient snow trapping in road areas with narrow right of way. Fences with a lower porosity induce a larger downwind wake region where the smaller velocity magnitude favors snow deposition compared to higher-porosity fences. The capacity of the fence to retain snow also scales with the fence height. Meanwhile, it is highly likely that, to work efficiently, these lower-porosity fences should be designed with a larger bottom gap than that of standard higher-porosity fences. This is needed because once the bottom gap becomes filled with snow during a large snow event the snow retention capacity of the fence diminishes drastically. So, the two main variables based on which a design will be assessed as being superior compared to another

one is the length from the fence over which significant snow deposits occur and the amount of snow deposited within the gap. An improved design will reduce the length of the snow deposit and maintain a free, or close to free, bottom gap after major snow events such that the fence continues to work well if another major snow event follows at a short time interval.

For the present study the focus was on the second option which, if proven successful, is a more economical and general solution to protect regions with narrow rights of ways against adverse effects associated with snow drifting. This is also justified by the fact that lightweight plastic snow fences are among the most inexpensive and common types of snow fences. The optimization strategy is to reduce fence porosity while, at the same time, increasing the bottom gap such that to augment the snow retention capacity of the fence and diminish the distance away from the fence over which snow deposition is significant. This will allow using lower-porosity fences in regions with narrower straight of ways. This solution is adopted in many regions of U.S. because such fences can be easily and rapidly deployed or removed from the field.

10.3 Methodology

10.3.1 Field Testing Site and Snow Fence Deployment

To assess the performance of a snow fence design one needs field observations at a testing site where the flow and topography can be considered to be close to two-dimensional. Moreover, the site should be long enough such that several designs can be tested at once under close to identical conditions in terms of incoming wind direction and magnitude, temperature and snow precipitation during a snow event. For the present study, a field testing site fulfilling the aforementioned requirements and known for severe snow

drift problems was identified on Highway 20 near Williams, Iowa, U.S. (Figure 10.1). Field monitoring at the site was performed over a two-year period (two winter seasons). Figure 10.2 shows a picture of one of the lightweight plastic snow fences installed at the site. The lightweight plastic snow fences considered in the present study were mounted on a 2mm diameter welded wire mesh (see also Figure 10.2b). The height, porosity and bottom gap of the plastic snow fence were varied among the different designs tested at the site.

During each winter season, three different snow fence designs were tested at the site. Figure 10.3 shows the general layout of the field testing site. Same layout was used for each of the three snow fence designs tested concomitantly at the site.

10.3.2 General Approach to Monitor Performance of Snow Fences and Improve their Design

A joint approach based on multi-year monitoring of snow deposition and performance of several snow fence designs at the field site and numerical simulations was adopted to assess the efficiency and improve snow fence design. The standard design of lightweight plastic snow fences assumes the porosity is close to 50%. As already mentioned in the literature review chapter, previous studies have shown that the major change in wake structure (recirculation region similar to wake past solid fences vs. no recirculation region) occurs for fences with a porosity close to 30% and that for constant fence height, h, fences with a lower porosity may retain more snow and the region of significant snow deposition may be extending less away from the fence compared to fences with a higher porosity. Based on these observations, the present study focuses on identifying optimum designs for plastic snow fences with porosity, P, of 30% and 50%. A two-year monitoring campaign was undertaken.

During the first year of monitoring, the goal was to identify the snow fence with the best performance among several snow fence designs with P=50%. Three different designs (A1, A2 and A3) of fences with P=50% and varying relative bottom gap G/H were tested in the field. The design that showed minimal snow deposition within the bottom gap, minimum length of the snow drift deposit and maximum volume of snow drift during the large snow events occurring during the first winter was identified as best design. Snow profile measurements were conducted after one of the most severe snow storms during the first winter for which the duration of snow fall was about 12 hours with the peak snowfall about 4 cm/day and the dominant wind speed of 9 m/s with the direction NW 330^0.

In parallel, 2-D Reynolds-Averaged Numerical Simulations (RANS) were conducted using the geometry of the three snow fences monitored in-situ. A commercial CFD software STAR CCM+ (see section 3.3 for a description of the numerical method and boundary conditions) was used to perform steady state simulations of the air-flow around the snow fence for a given topography and fence design. It was found that the best design was the one for which the streamwise extent and width of the region of small velocity magnitude situated close to the bare ground were the largest. This region corresponded approximately to the one where significant snow deposit occurred during the large snow events. Based on this criterion, several other designs for fences with P=50% were tested based only on numerical simulations. None of the new designs appeared to perform significantly better than the one identified as best design among the three designs tested in the field. In fact, many of the new designs performed visibly worse. Then, more than 10 designs of fences with P=30% were tested. In particular, in two series of simulations, the height of the bottom gap, G, was varied while maintaining the fence height h and,

respectively, the total fence height, H=h+G, constant. Based on analysis of the velocity magnitude fields, two candidates for best design of fences with P=30% were identified. These designs are denoted B1 and B2.

During the second year, the performances of the best fence design with P=50% and the two candidates for best design for fences with P=30% were monitored in the field using the same criteria as those described for the monitoring campaign undertaken during the first year. Snow profile measurements were conducted after one of the most severe snow storms that occurred during the second winter season. For this snow storm, the duration of snow fall was about 24 hours with a peak snowfall rate of about 4.5 cm/day and a dominant wind speed of 12 m/s in the direction NW 315^0. As the discussion of the results will show, the overall performance of both proposed designs with P=30% was better than that of the best design identified for fences with P=50%.

10.3.3 Real Time Monitoring System and Field Measurements

The field monitoring entailed two sets of observations. The first consisted of a real time observing system aimed to determine if snow deposition accumulated during storms was significant enough to visit the site and conduct detailed measurements of the snow profiles in situ. For this purpose a Moultrie i65 GAME Spy camera and the Moultrie Game Management System were used for continuous imaging of the field test site during the winter seasons (see Figures 10.3 and 10.4). The Moultrie camera is equipped with a GPS connect system that sends the images taken in the field over a wireless cellular network to the Moultrie Game Management System website. Pictures can be downloaded online at any time to monitor conditions at the site (see Figure 10.4). Additionally, the system allows controlling remotely the camera settings via the internet. The system allows both photo

273

mode and video mode and choosing the time interval at which pictures are stored on the website.

Marker poles arranged as shown in Figure 10.3 were installed at each observation site. The marker poles were needed to assist the topographic surveys. The marker poles were set perpendicular to the road in between the snow fence and the road shoulder. The marker poles were surveyed before the winter season at the ground level. After each storm, the snow deposits were mapped over the imaged area to capture the 3-D topology of the snow deposit produced by the snow fence.

Three Moultrie i65 GAME Spy cameras were used to record images every hour around the region where the marker poles were installed for each of the fence designs tested concomitantly at the site. They provided additional information on the temporal evolution of the snow deposits. However, this information is accessible only after pictures are downloaded during site visits by the monitoring team.

A GPS based real-time kinematic (RTK) survey was conducted at the start of the first winter season to obtain the bare ground profile in the direction defined by the marker poles installed at each of the three fence designs tested in the field. This first RTK survey provided the coordinates [x,y,z] of the contact points between the marker poles and the bare ground (Figure 10.9). The bare ground profiles at the three locations where marker poles were present were quite close. Thus, when comparing the data (snow deposition), the represented bare ground profile corresponds to the mean of the bare ground profiles determined at the three locations. During both winters, RTK surveys were conducted after the end of each significant snow event at the three locations to obtain the coordinates [x,y,z] of the intersection points between the marker poles and the top of the snow deposit (Figure

274

10.9). Equally important, the position and height of each marker pole were known such that the height of the snow blanket at the pole location could be obtained from analysis of the images. This protocol ensured that the cameras did not move under the actions of strong winds during storms so that the images can be used further to perform close range photogrammetry (e.g., to determine the volume of snow retained by the snow fence).

10.3.4 Numerical Simulations

2-D RANS numerical simulations were performed to calculate the flow field around the porous snow fences. The bare ground profile was obtained from the RTK survey. The height of the computational domain was 10m, which is much larger than the height of the largest snow fence simulated (H<2.5m). In the computational domain, the axis of the fence is situated at x=0m (Figure 10.8a). The inlet and outlet boundaries are located at 50m upwind and 157m downwind of the fence, respectively. The inlet is situated far enough from the region where the presence of the snow fence disturbs the incoming flow field that was assumed to be fully turbulent. The distributions of the mean velocity and turbulent quantities in the inflow section were obtained from a preliminary simulation of the flow in a straight channel of identical height with periodic conditions in the streamwise direction. This is standard treatment for this type of problems (e.g., see Kirkil and Constantinescu, 2009; Constantinescu et al., 2011).

The simulations were performed at a sufficiently high Reynolds number (Re=1.53x10^6, where Re is defined with the mean incoming wind velocity in the direction perpendicular to the road, U=12m/s, and a length scale H=2m corresponding to the average fence height) for the solution to be only weakly dependent on the Reynolds number. A parametric study in which the Reynolds number was varied between Re=1x10^6 and

Re=3x10^7 confirmed the distributions of the nondimensional mean velocity components and turbulent kinetic energy were close to independent of the value of Re. This is fully expected for these high values of the physical Reynolds number (Re>10^5, see also Constantinescu et al., 2008; Sinha et al., 2012).

As discussed in section 3.3, an important feature of the present numerical simulations is that the solid elements defining the fence porosity are resolved by the mesh (Figure 10.8c). In this regard, the use of the local mesh refinement procedure (quadtree-mesh based) available in the grid generator integrated with STAR CCM+ was critical to successfully generate a high quality mesh. The thickness of the solid elements was identical to that of the plastic snow fence (2mm). The distance between two solid elements was close to the mean height of the openings in the plastic snow fence tested in the field. Close to 20 grid points were used to resolve the flow through each of the fence openings. The minimum size of the smallest grid cells was about 1mm. This small size was needed to resolve the flow around the upwind and downwind faces of the thin fence elements. The minimum grid spacing in the wall normal direction was around 1-2mm. In the regions situated away from the fence and the bare ground, the mean size of the grid cells was increased to about 40cm. The increase was gradual to maintain a high mesh quality and low stretching ratios (e.g., see Figure 10.8b).

10.3.5 Validation of RANS model for relevant configurations

Before discussing results of RANS simulations performed for the porous fences that were tested in the field as part of the present study, it is important to assess the capabilities of such simulations to predict the mean flow field around porous fences installed in the vicinity of a ground surface. One of the test cases studied experimentally

by Huang et al. (2012) is chosen for testing the performance of 2D RANS simulations performed using STAR-CCM+. Besides wind tunnel experiments, Huang et al. (2012) also reported results of a 2D Large Eddy Simulation (LES) performed using a dynamic Smagorinsky model on a relatively coarse mesh containing close to 18,000 grid points. Because the mesh was coarse, wall functions were used in LES. In the present 2D RANS simulations, the viscous sublayer is resolved (no wall functions are used) and the mesh is much finer (400,000 grid points).

The computational domain and the porous fence are shown in Figure 10.6. The design of the nonuniform porous fence was identical to that used in experiment and the 2D LES of Huang et al. (2012). The incoming flow velocity was U_0=10.6m/s and the total fence height was H=h=0.06m. As shown in Figure 10.6, a nonuniform porous fence was tested. The upper half of the fence was solid, while the lower half of the fence had a porosity P=30%. The height of the fence elements was 0.116H and the opening between two elements was 0.05H. The bottom gap was equal to zero (G=0) and the fence width was 0.02H. The Reynolds number defined with the mean incoming wind velocity, U_0, and the fence height, H, was 41,000. The inflow conditions corresponded to fully developed turbulent channel flow at Re=41,000. The height of the domain was 10H. The nondimensional velocity magnitude flow field, V/U_0, is shown in Figure 10.6. As expected, a region of low velocity magnitude is generated some distance behind the porous fence, close to the bottom boundary. The flow is deflected upwards and downwards by the upper solid part of the fence.

The vertical variation of the nondimensional streamwise velocity, u/U_0, is compared in Figure 10.7 with experimental hot-wire anemometer measurements and

results of 2D LES. The comparison is shown at four streamwise locations situated between 1H and 12H downstream of the fence. As expected, the velocity behind the fence is larger in the region with y<0.5H than in the region defined by 0.5H<y<1.5H. This happens because the upper half of the fence is solid while a bleeding flow is present for y<0.5H. Overall, 2D RANS captures fairly well the main features of the measured profiles of the streamwise velocity at all four locations shown in Figure 10.7. Moreover, the predictive capabilities of 2D RANS are superior to the ones shown by the 2D LES. There is little doubt that 3D LES performed on sufficiently fine meshes will give mean flow predictions similar or better than 2D RANS. However, for the purpose of the present study that uses the velocity magnitude flow field around the fence to guide selection of candidates for best design for a certain type of snow fence, the level of accuracy of 2D RANS performed using the two-layer k- model is sufficient.

10.4 Results of the Field Monitoring Study and RANS Simulations

All three fence designs tested during the first winter had a fence porosity of 50%. One of them (A3) had a total height $H \cong 1.9$ and a relative bottom gap G/H=0.08. This is the conventional design used by the Iowa Department of Transportation for plastic snow fences. As the main goal of the present project is to study the performance of lower porosity fences with P=30% which need larger relative bottom gaps, it is interesting to first understand what is the effect of G/H on the amount of snow retained by the fence and on the shape of the snow deposit for fences with P=50%. As the fence porosity decreases, the potential for the snow deposit to advance toward the fence, fill the bottom gap and eventually touch the downwind side of the fence increases. Once that happens, the snow

fence capacity to further reduce snow drift is negligible. To understand this effect, the relative bottom gap was increased to 0.2 for design A2 and 0.34 for design A1.

The other goal of the field testing conducted during the first year was to understand how the snow retaining capacity and performance of fences with P=50% changes with the relative bottom gap for a constant snow fence height h and for a constant total fence height, H. This is why the fence height was kept the same (h ≅ 1.25) for fence designs A1 and A2, while the total fence height was kept the same (H ≅ 1.9) for fence designs A1 and A3.

The nondimensional snow deposition profiles after the most severe snow event recorded during the first winter are compared in Figure 10.9. As expected, fence design A3 performs the best in terms of the total volume of snow deposit per unit length (direction parallel to the road and fence) and the streamwise extent of the region of high snow deposition relative to the fence. Comparison of snow profiles for cases A1 and A3 shows that maintaining the same total fence height while increasing substantially the bottom gap greatly reduces snow deposition in the immediate vicinity of the fence and pushes the region of high snow deposition away from the fence. In fact, the relative bottom gap for design A1 is sufficiently high such that the snow deposit within the bottom gap is negligible. However, the total volume of snow deposited behind the fence is much smaller compared to that observed for design A3. Though part of the difference is due to the larger fence height (by 40%) of design A3, clearly the performance of design A1 is poorer than that of design A3.

If the fence height, h, is kept constant (designs A1 and A2), results in Figure 10.9 show that the shape of the snow deposition profile changes qualitatively past a threshold value of G/H. The snow deposition profile for design A2 is qualitatively very similar to

that observed for design A3, which is not the case for design A1. For fences with P=50%, design A1 has clearly a too large G/H. The ratio of the volume of snow deposit for designs A3 and A2 is about 2.5, which is significantly larger than the ratio of the fence height (1.5) for the two designs. This suggests that the relative bottom gap for design A2 (G/H=0.2) is too high. It is very likely the ratio will be closer if the fence would have been built with the same height as for design A2, but with G/H close to the value used for design A3 (G/H $\cong$ 0.1).

Figure 10.10 compares the nondimensional velocity magnitude distributions for designs A1, A2 and A3. The plot in Figure 10.10c contains a long and relatively thick region of reduced velocity magnitude downwind of the fence and close to the ground. The results for design A2 (Figure 10.10b) are qualitatively similar, though the streamwise extent of this region is significantly lower than that observed for design A3 and the average velocity magnitude within this region is somewhat higher. The strong horizontal momentum of the jet-like flow originating within the bottom gap region of design A1 is the main reason why no significant snow deposition is observed for design A1 close to the fence.

Based on these results, a number of simulations for fences with P=30% were performed. In these simulations G/H was varied between 0.1H and 0.4H by keeping either h or H constant. Two of the designs that appeared to be the most promising based on the fact that the velocity magnitude field predicted by the simulation contained a long and relatively thick bottom region of reduced velocity magnitude (see Figures 10.11 and 10.10c) were selected to be tested in the field during the next winter together with the design A3 that worked the best for fences with P=50%. The fence height, h, in the cases

with P=30% (design B1 has G/H=0.25 while design B2 has G/H=0.2) was about the same as that of design A3.

Figure 10.12 compares the nondimensional snow deposition profiles measured after the most severe snow event recorded during the second winter. The total volume of snow deposit per unit length for designs B1 and B2 are by about 12% lower and 7% larger, respectively, than that for design A3. So, one can argue that all three designs retain a comparable amount of snow. However, there is an important difference in the snow deposition patterns. The length of the region where significant snow deposition occurs extends up to 10-13H from the fence for the two designs with P=30% while the same region extends up to 15-17H from the fence for design A3. For a snow event of slightly larger magnitude than the one analyzed in Figure 10.12, the region of snow deposition induced by the A3 fence design will reach the road.

Figure 10.13 compare the snow depths at each marker pole position along the marker poles line behind the three fences. The other problem with design A3 when compared to B2 and especially to B1 is the large snow height at the fence location (x=0H in Figure 10.13). The snow level for design A3 is 0.28H, which means all the bottom gap region is filled with snow. The snow level within the bottom gap is about 0.5G for design B2 and is insignificant for design B1 (see Figure 10.14). This means that both designs with P=30% will continue reducing snow drifting on the road in the case of a larger snow event or if a subsequent snow event will occur a short time after the one analyzed in Figure 10.13. In conclusion, design B2 retains more snow but also has a smaller future capacity to continue accumulating snow compared to design B1. So, it appears the optimum G/H value

for fences with porosity P=30% is situated somewhere in between 0.2 and 0.25 and the overall performance of these lower-porosity fences is better than that of design A3.

10.5 Changes in the flow patterns around the fence during a snow event

One relevant question is how do the flow patterns (e.g., velocity magnitude distribution) change during a major snow event? To answer this, several numerical simulations were run corresponding to a major snow storm occurring at the site during the second winter season. Results are presented in Figure 10.15 for the B1 fence (P=30% and G/H=0.25). Measurements were available only before the snow storm and at the end of the snow storm (Figure 10.15d). As there was no snow deposition before the snow storm, the bareground profile was used to determine the flow pattern past the snow fence at the start of the snow storm in Figure 10.15a. Two other simulations were performed with snow deposition profiles corresponding to 33% and 66% of the total snow deposition observed at the end of the storm event. Results are shown in Figures 10.15b and 10.15c, respectively.

Results in Figure 10.15 show that as the snow profile raises, the total length of the region of low velocity magnitude on the downwind side of the fence remains close to constant. Meanwhile, the size and streamwise length of the core of very small velocity magnitude decrease monotonically as the snow profile raises. As the presence of regions of very low velocity magnitude in the vicinity of the snow surface is expected to favor snow deposition, this results suggests that the capacity of the snow fence to retain snow decreased as the snow profile raises. One important factor not accounted in the numerical simulations is that as the snow profile raises, snow starts accumulating within the fence bottom gap, which further reduces the efficiency of the snow fence.

10.6 Conclusions

A methodology based on field monitoring of snow fences, field measurements of snow deposit profiles and numerical simulations was developed to help improve the design of snow fences. Of critical importance for successfully applying the proposed methodology is that a sufficiently long field test side is available, where several fence designs can be tested under close to identical conditions, and that accurate methods are used to determine the snow deposition profiles after major snow events at the site.

The methodology was applied for lightweight snow fences which are inexpensive to deploy and a very common type of snow fences, especially in the U.S. Midwest. The standard design for this type of fences recommends fence porosity close to 50% and that the bottom gap is about 10% of the fence height.

The study investigated the effectiveness of similar fences with a lower porosity because of the possibility that such fences retain more snow and/or the length of the region of significant snow deposit on the downwind side of the fence is reduced. If that is indeed the case, then lower porosity fences can be used for effective protection against snow drifting in regions with narrower rights of way. As previous studies have shown that the air flow fields past snow fences do not contain a recirculation region for fences with a porosity larger than 30%, the goal of the design methodology was to identify an optimum design for fences with P=30%. Obviously, the optimum design for fences of lower porosity should involve using a large bottom gap relative to the fence height. This is because as the fence porosity decreases, the conditions for snow deposition immediately downwind of the fence increase. This leads to a rapid filling with snow of the bottom gap and eventually to a loss in the capacity of the snow fence to protect the road against snow drifting.

The field monitoring program conducted over the first year confirmed that the optimum design of plastic snow fences with a porosity of 50% has a fence bottom gap which is about 10% of the fence height. It also allowed understanding how the shape of the snow deposit changes as the ratio G/H increases. Numerical simulations were then used to understand the main characteristics of the mean flow past the fence and how these characteristics vary with the fence height, fence porosity and bottom gap. It was found that the fence with P=50% and G/H=0.08 induced the formation of an elongated and fairly thick region of small velocity magnitude close to the ground, which favors snow deposition. For the other two designs with P=50%, the streamwise extent and shape of this region were different. Similar simulations were undertaken for snow fences with P=30%. Two of the designs that were found to be good candidates for optimum design based on the distribution of the mean velocity magnitude were tested during the next winter along with the optimum design for fences with P=50%. To make easier to estimate the efficiency of the different designs, all three designs tested in the field during the second winter had the same height but different bottom gaps.

While the volume of the snow deposit retained by the three designs was found to be comparable, the length of the snow deposit was reduced by about 30% for the two fence designs with P=30% compared to the optimum fence design with P=50%. Moreover, the snow level at the location of the fence never exceeded the height of the bottom gap, which means the fences with P=30% will continue to work well even under more severe snow events than the peak snow event recorded during the second winter. By contrast, the bottom gap was all filled with snow for the optimum design for fences with P=50%. The optimum ratio between the bottom gap and total fence height for fences with P=30% was found to

be 0.2-0.25. As expected, this value is significantly larger than the one recommended to maximize efficiency of fences with P=50%.

Besides formulating design recommendations for plastic snow fences with P=30%, a main finding is that properly designed fences with P=30% can be as efficient as fences with P=50% of same height, but they can be placed closer to the road. This means such lower-porosity fences are a better option to protect roadways against snow drifting in regions with narrow right of ways.

In the present implementation of the proposed methodology to monitor performance of snow fences, the measurements of the snow deposit were conducted using a GPS-based real-time kinematic survey. However, other imaging techniques based on Large-Scale Particle Image Velocimetry concepts (Fujita and Kunita, 2011; Hauet et al., 2008 and 2009; Muste et al., 2009 and 2011; Basnet and Ettema, 2011) can be used to determine the snow deposition profiles. In fact, such techniques were tested as part of the field monitoring campaign but because the GPS-based real-time kinematic surveys were as accurate and faster to perform, the protocols developed to apply LSPIV to measure the snow deposition profiles were not described in this chapter. However, the next chapter will discuss the use of a novel technique based on 3-D close range photogrammetry (e.g., Yakar et al., 2010) to monitor the evolution of the snow deposit in time. Finally, the approach developed to test and improve the design of snow fences described in this chapter can be applied to other types of structural snow fences and can be extended for living snow fences.

(a)

(b)
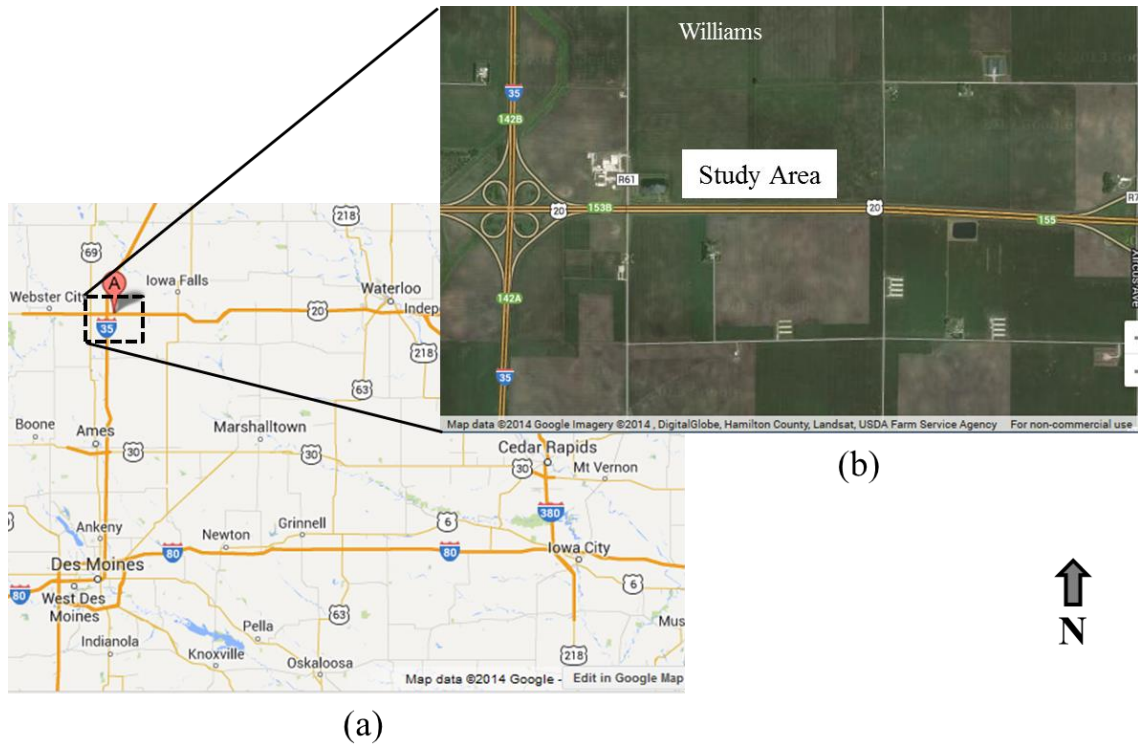
Figure 10.1 Field testing site located on Highway 20, Williams, Iowa, U.S.

a)   b)

Figure 10.2: a) View of one of the lightweight plastic snow fences tested at the field site (A1 fence: P=50%, G/H=0.34, H$\cong$1.9); b) Close view showing the 2 mm diameter welded wire frame used to support the plastic fence.
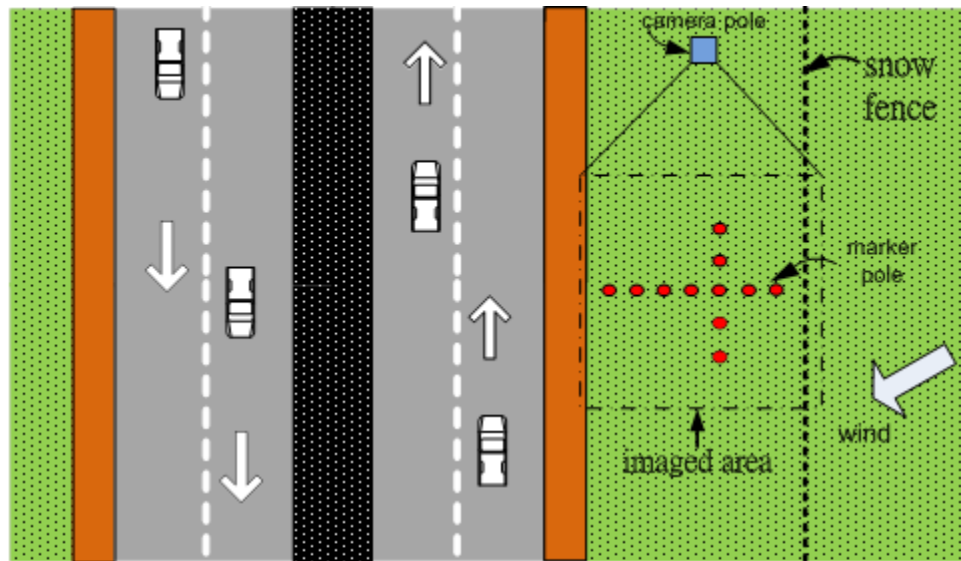
Plan view
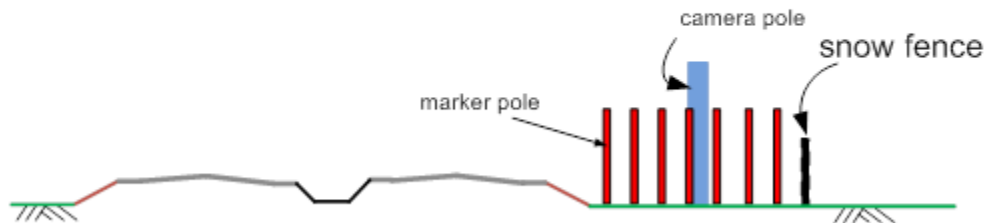
Side view

Figure 10.3 Sketch of the field testing site showing the position of the road, the snow fence, the marker poles and the camera pole used to support the video camera employed for monitoring snow deposits at the site. Drawing is not at scale.
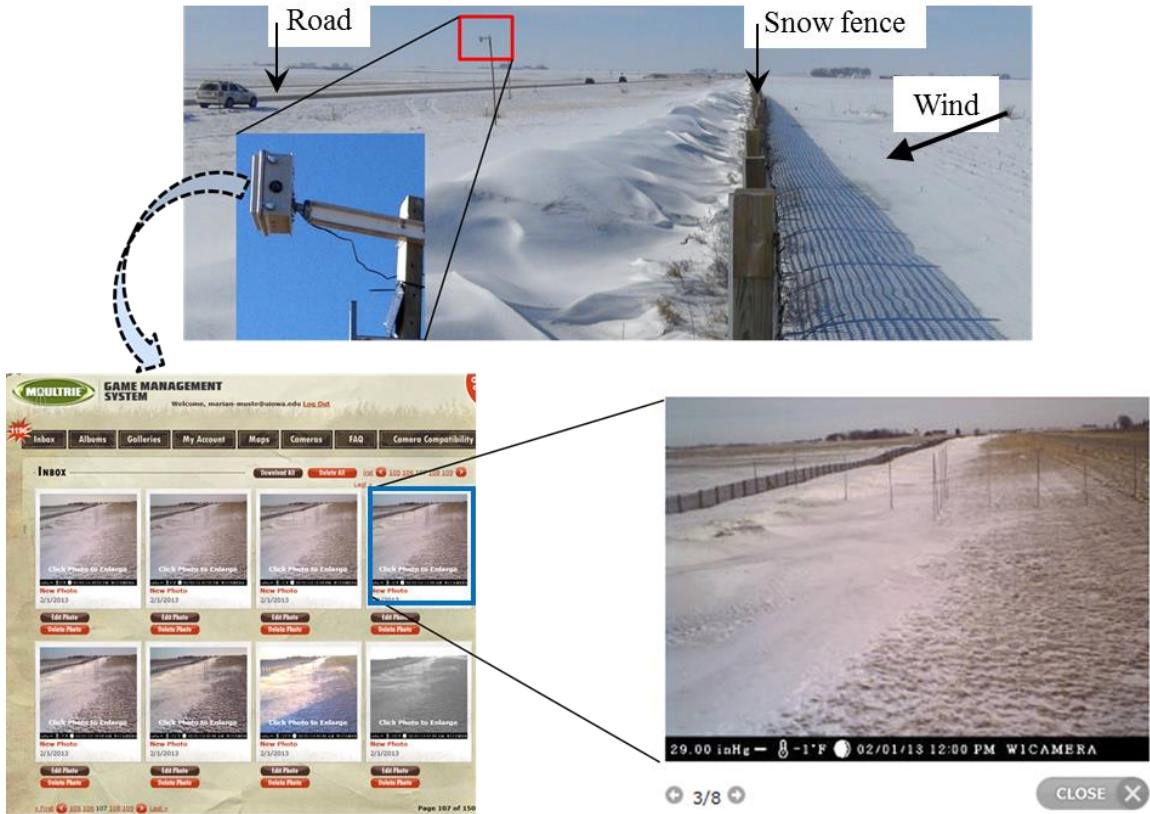
Figure 10.4 Field set-up and information provided by the real-time monitoring system.
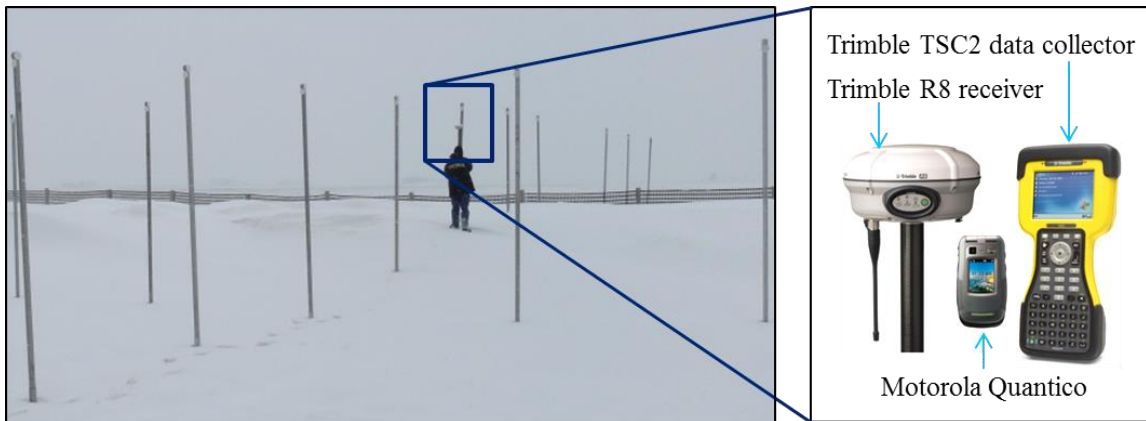
Figure 10.5 RTK survey conducted along the marker poles. Also shown are the main devices used during the data collection.
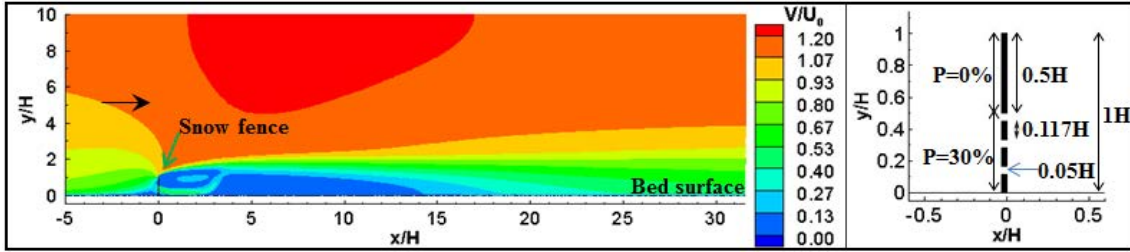
Figure 10.6 Distribution of velocity magnitude around and downstream of the nonuniform porous fence predicted by a 2D RANS simulation. The simulation corresponds to the experimental set up of Huang et al. (2012). Also shown is a close up view of the porous fence.
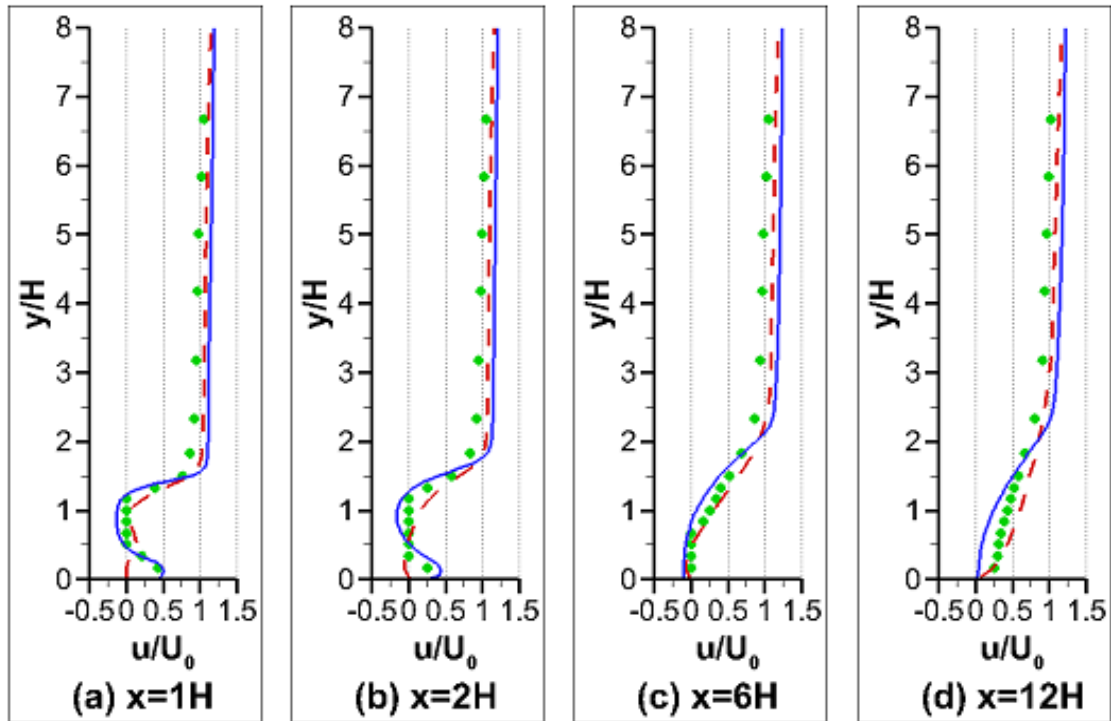
Figure 10.7 Comparison between mean streamwise velocity profiles predicted by numerical simulations with measured data. a) x=1H; b) x=2H; c) x=6H; d) x=12H. The green symbols correspond to the experimental results of Huang et al. (2012). The solid blue line corresponds to the present 2D RANS results. Also shown with a dashed red line are the results of a 2D LES performed by Huang et al. (2012).
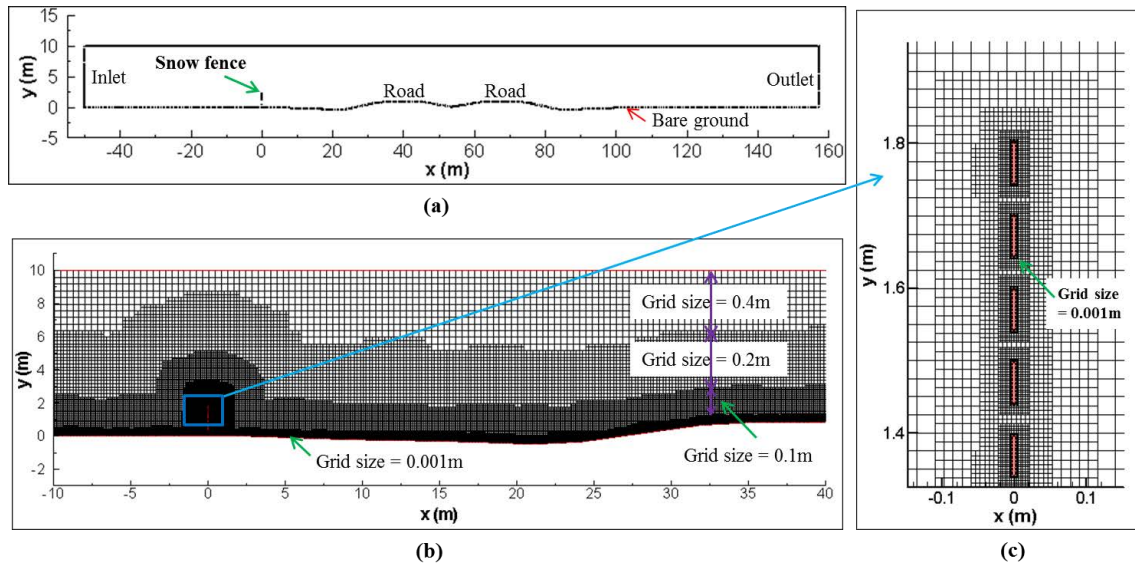
Figure 10.8 Computational domain and mesh: a) Sketch of the computational domain; b) view of the mesh in the region situated in between the fence and the extremity of the road; c) detail view showing the local mesh refinement around the fence elements for a fence with a porosity of 30%.
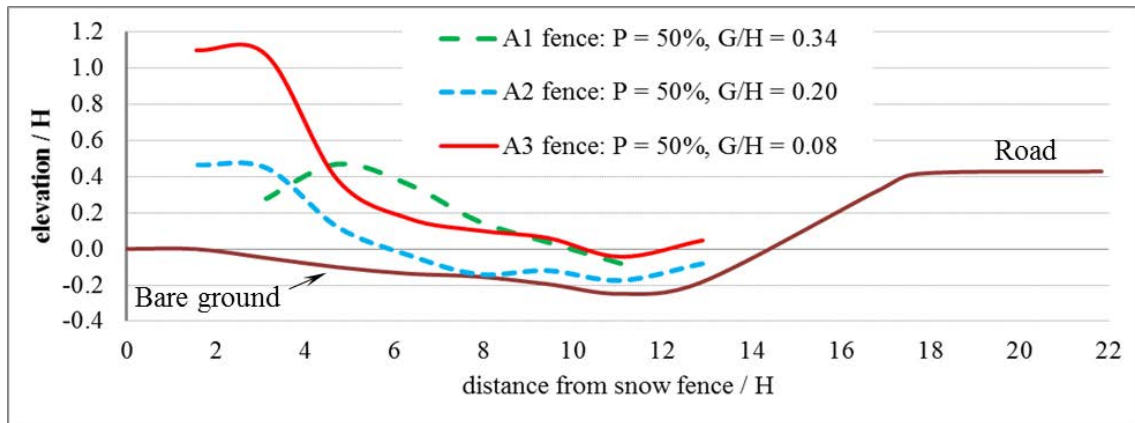
Figure 10.9 Snow deposition profiles behind the fence designs tested during the first winter (A1, A2, and A3). H (= 2m) is the length scale characterized by average fence height. The fence is located at distance from snow fence = 0H.
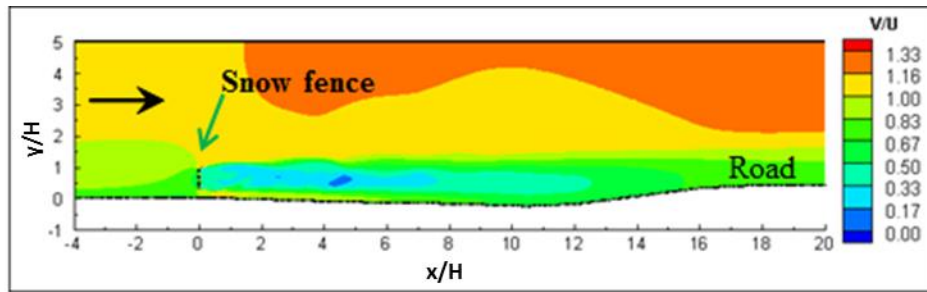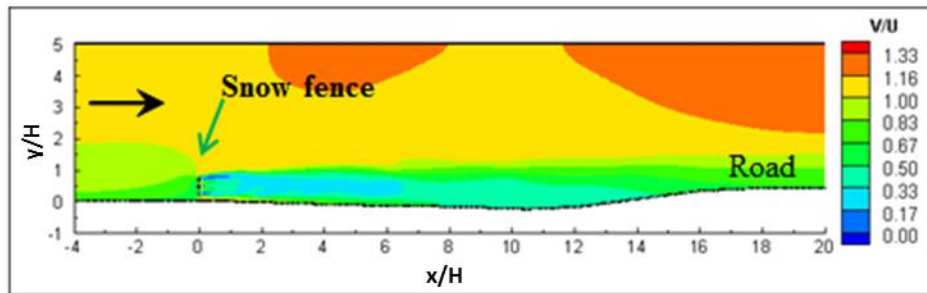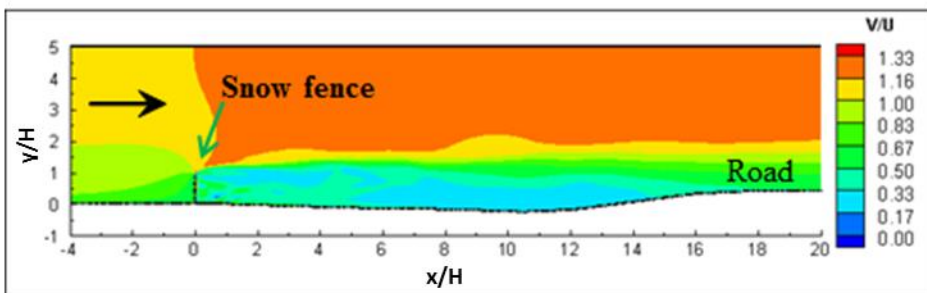
Figure 10.10 Distribution of velocity magnitude around and downstream of the fence designs with a porosity of 50% tested during the first winter (A1, A2, and A3): a) A1 fence: P=50%, G/H=0.34; b) A2 fence: P=50%, G/H=0.20; c) A3 fence: P=50%, G/H=0.08. H (= 2m) is the length scale characterized by average fence height and U (= 12m/s) is the mean incoming wind velocity. The fence is located at x = 0H.

291
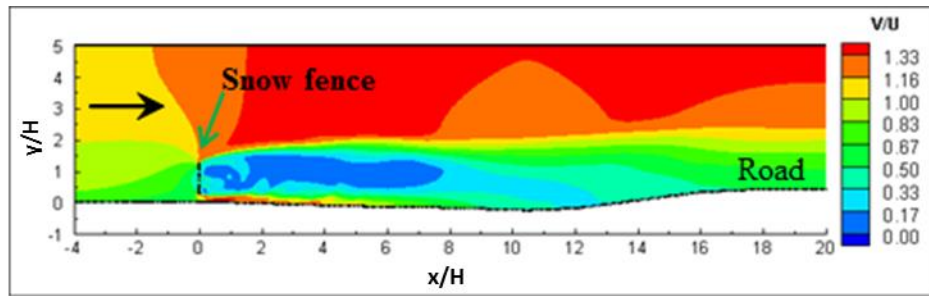
(a)
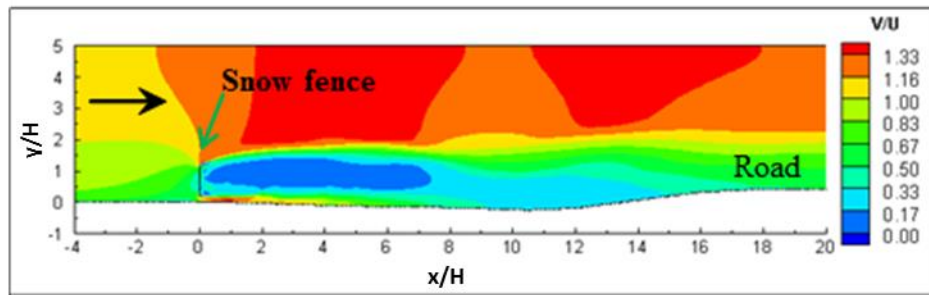
(b)

Figure 10.11 Distribution of velocity magnitude around and downstream of the fence designs with a porosity of 30% tested during the second winter (B1 and B2): a) B1 fence: P=30%, G/H=0.25; b) B2 fence: P=30%, G/H=0.20. H (= 2m) is the length scale characterized by average fence height and U (= 12m/s) is the mean incoming wind velocity. The fence is located at x = 0H.
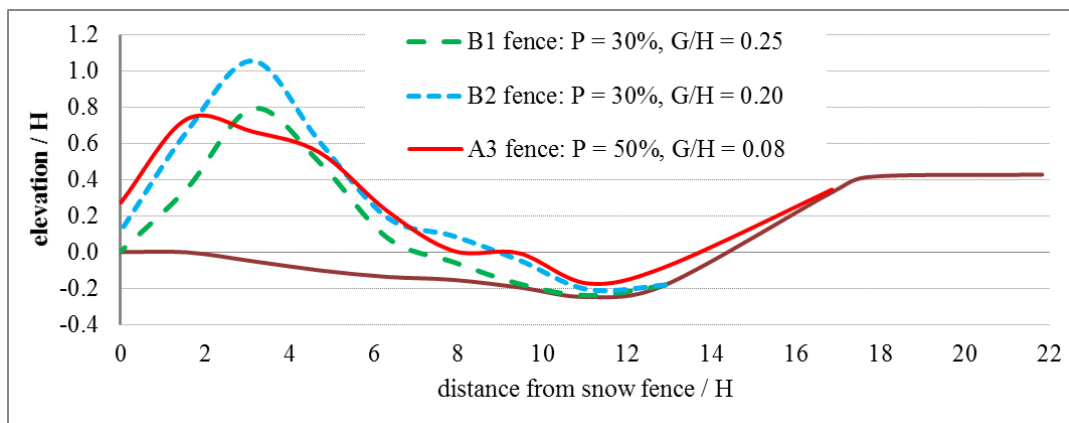
Figure 10.12 Snow deposition profiles behind the fence designs tested during the second winter (B1, B2, and A3). H (= 2m) is the length scale corresponding to the average fence height. The fence is located at x= 0H.
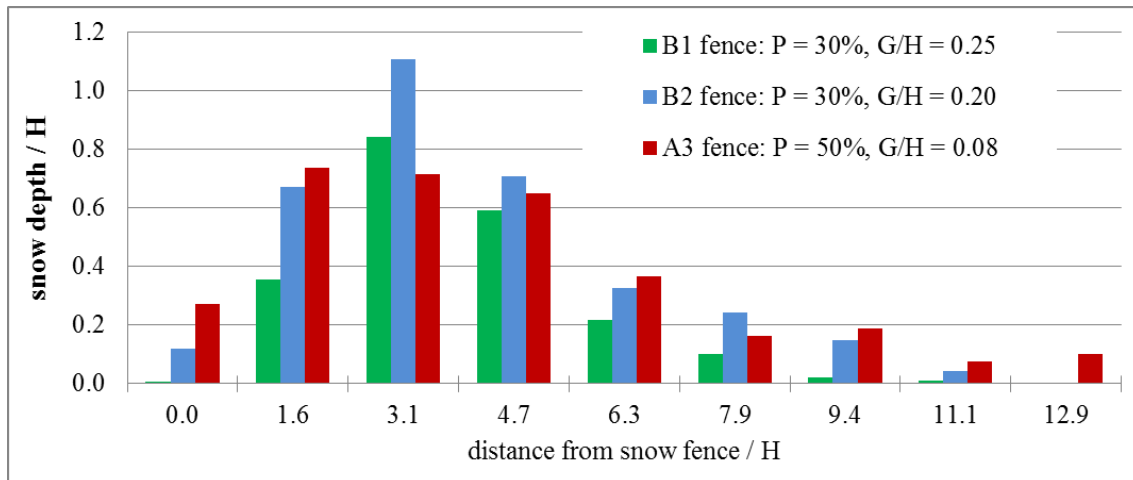
Figure 10.13 Comparison of snow depths deposited at 9 different downwind distances from the fence location for the three fence designs tested during the second winter (B1, B2, and A3). H (= 2m) is the length scale corresponding to the average fence height.
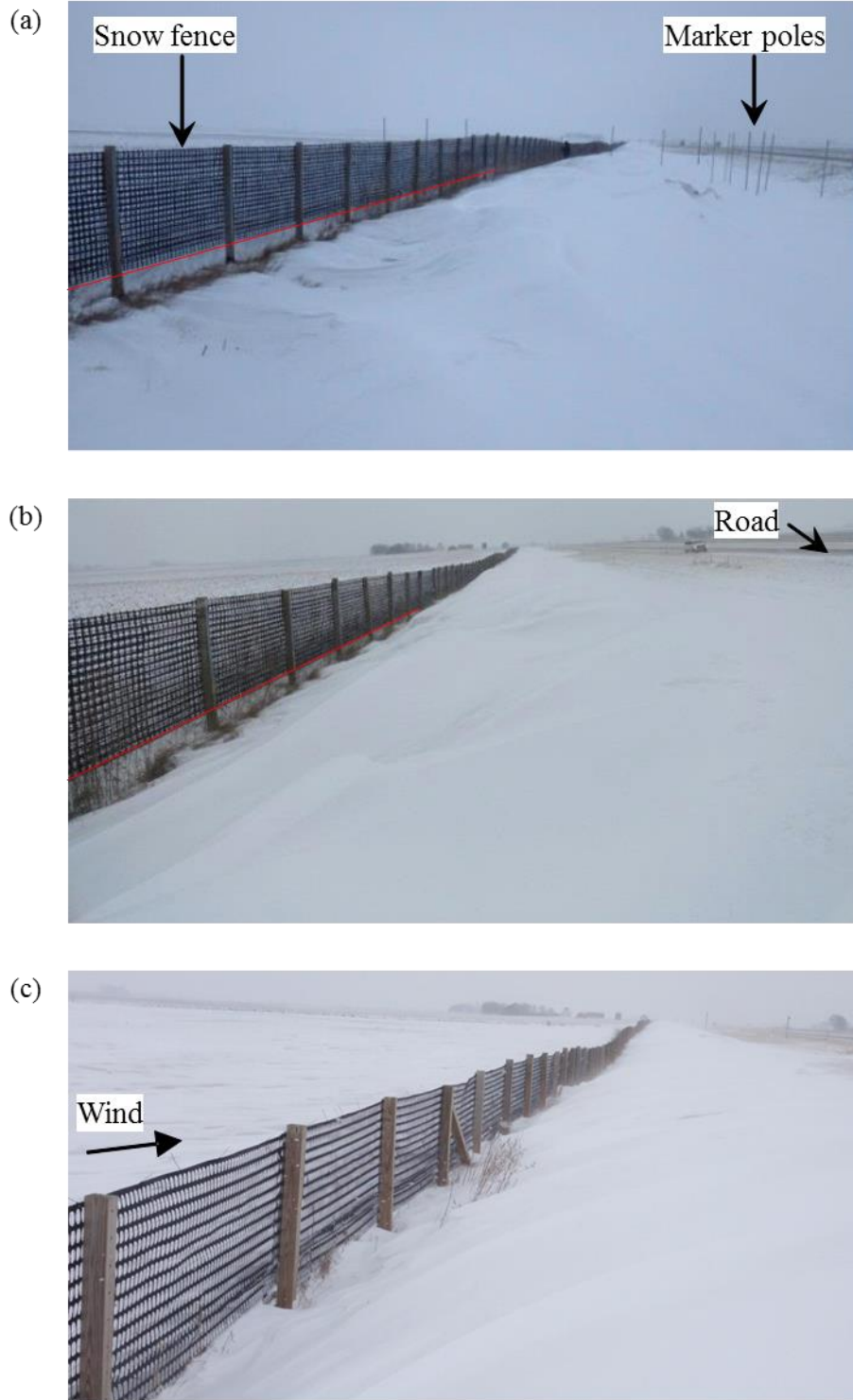
Figure 10.14 Views showing snow deposition close to the fence immediately after the end of the largest snow event during the second winter: a) B1 fence (P=30%, G/H=0.25; b) B2 fence (P=30%, G/H=0.2); c) A3 fence (P=50% and G/H=0.08). The red lines indicate bottom of the fence.
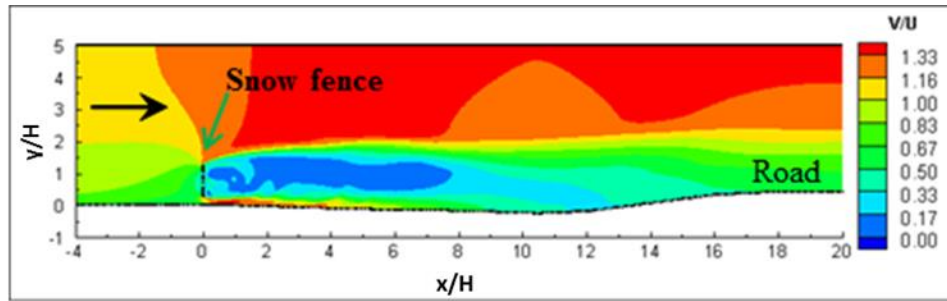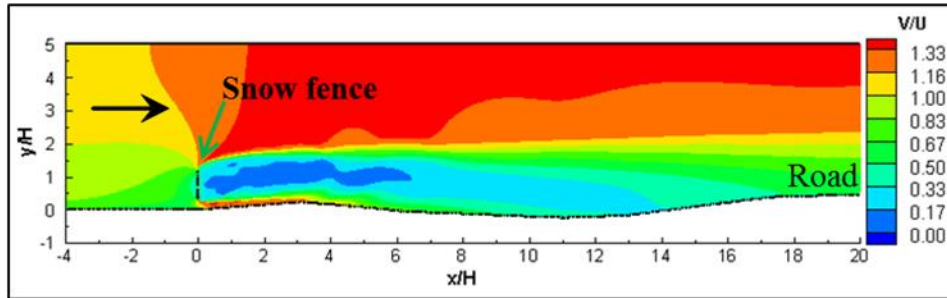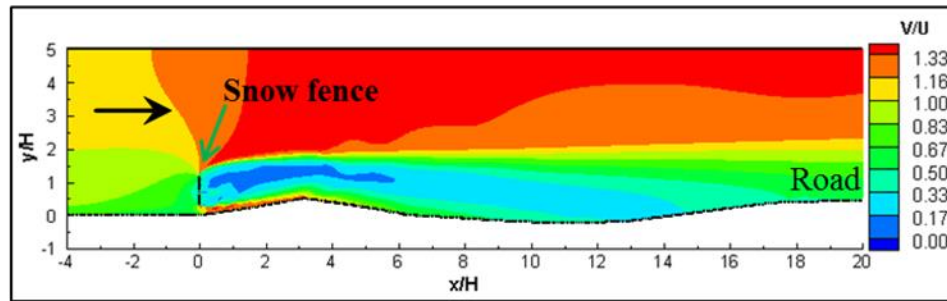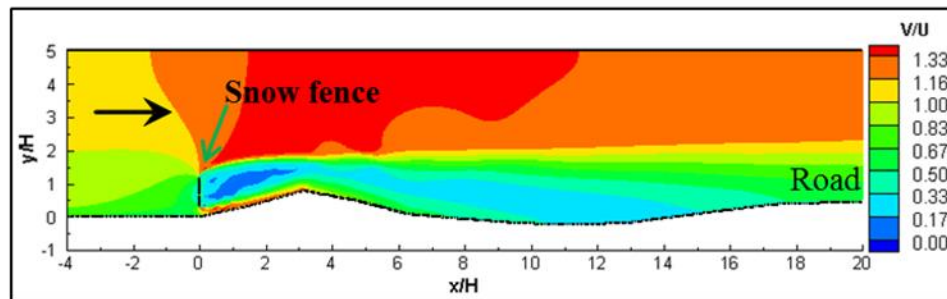
Figure 10.15 Distribution of velocity magnitude around and downstream of the B1 fence
(P=30% and G/H=0.25) for four different snow profiles: a) 0% snow deposition (the bare
ground profile is used); b) 33% snow deposition; c) 66% snow deposition; d) 100% snow
deposition corresponding to snow profile measured at the end of the snow event. The
fence is located at x=0H.

CHAPTER 11 CLOSE RANGE PHOTOGRAMMETRY FOR DYNAMICALLY TRACKING DRIFTED SNOW DEPOSITION

11.1 Introduction

As discussed in Chapters 1 and 2, designing snow fences requires sound engineering judgment and a thorough evaluation of the potential for snow blowing and drifting at the construction site. Among the critical parameters involved in fence design and assessment of the post-construction efficiency of a snow fence is the quantification of snow accumulation at the fence site. Conventional methods for quantification of snow accumulation (e.g., the GPS based real time kinematic surveys used to obtain snow deposit profiles after major snow storms, see Chapter 11) are accurate but tedious and, given the harsh winter weather environment when some of these surveys have to be performed, may lead to human accidents. In this chapter, a novel method for non-intrusive remote estimation of the snow deposit volume is proposed and tested. The novel method to determine the volume of accumulated snow at a fence site is based on close range photogrammetry (CRP) and has the capability to determine the continuous evolution of the snow deposition profiles over large periods of time. Such information is very useful for the overall assessment of the performance of a snow fence design. Mapping of snow deposits using CRP entail several complexities that are not typically present in conventional CRP applications. Most of these complexities stem from the lack of texture and of control points over the snow surface whose topography is measured. Besides presenting the general methodology, this chapter discusses the challenges of using CRP to determine the evolution of the volume of snow deposited at the fence site and proposes solutions for the practical implementation of the method in the field.

11.2 Background

Designing snow fences requires sound engineering judgment and a thorough evaluation of the potential for snow blowing and drifting at the snow fence construction site. Conventional protocols for designing snow fences such as the WYDOT Snow Drift Profiler software (Wyoming DOT Report, 2007) requires site-specific design parameters typically obtained with semi-empirical relations characterizing local snow transport conditions. A critical role in establishing some of the parameters (e.g., the snow relocation coefficient) is the estimation of the snow volume accumulating on the downwind side of the fence. The assessment of the efficiency of the built snow fence at a site also requires accurate information on the snow volumes deposited in the wake of the snow fence. The mapping of the snow volumes using conventional tools (e.g., total station or Global Positioning System-based techniques) is a difficult and tedious process mostly due to the adversity of the measurement environment during winter season.

The conventional measurement technology used to estimate the volume of materials dislocated in natural environments has been the theodolite. This instrument combines optical and mechanical components assembled with high precision (Gannett, 1906). Currently, this approach is increasingly replaced by non-intrusive survey methods based on electromagnetic, optical, and acoustic-based principles. Contemporary alternatives for representation of terrain topography include modern versions of the theodolite (a.k.a. total station), real-time kinematic (RTK) and terrestrial light detection and ranging (LIDAR) based measurement technologies (Kizil and Tisor, 2011). Neither of these instruments can provide simultaneous measurements at multiple points over the volume surface. Moreover, a physical presence is required at the location where the measurement is performed.

The initial configurations of the total stations require an operator and an auxiliary person carrying a graduate rod or a reflector. Currently, such systems have the option of a scanning mode that measures reflectorless, including for snow surfaces (Prokop et al., 2008). For RTK measurements, the instrument is sequentially placed at each surveying point; therefore the survey can be conducted by a single person. Terrestrial (ground-based) LIDAR is a laser-based remote sensing technology that is capable of producing cloud of points over the surveyed volume without the need of an operator or sensor positioning at the measurement points (Prokop, 2008; Gatziolis et al., 2010; Moskal and Zheng, 2012). Limitations of this technique are related to their high cost and with the signal return from rough surfaces (with increased multi-directional scattering). Overall, the above listed techniques require physical presence in the field for quantification of snow accumulation that, most often, is difficult, given the harsh winter weather environment and can even be risky, at times.

The brief review of the above technologies indicates that while each of them has uniquely strong capabilities (theodolite – high accuracy; RTK – improved operational aspects; LIDAR - measurements at multiple points can be remotely acquired), they are expensive in terms of equipment or personnel involved in the measurement operations, especially in areas where the access is risky or difficult. Consequently, the quest for novel accurate, cost- and operationally-effective means for conducting terrestrial surveys is on-going. A strong candidate among this latter category of techniques is Close-range Photogrammetry (CRP), a method that currently receives lots of attention due to its efficiency and relatively low cost.

The CRP technique stems since the pre-digital era of the mid-nineteenth century (Lenzano et al., 2014). By early 1930s, most of the topographic and thematic maps produced in the United States have been generated using aerial photography and photogrammetric methods (Matthews, 2008). Today, CRP surveys are routinely executed for civil and industrial projects where during various phases of their construction, volumes of cutting and filling materials need to be estimated for planning and management of the construction phases (e.g., Matthews, 2008). Similar surveys are conducted for evaluation of the volumes dislocated by natural hazards such as landslides and snow avalanches (Baldi et al., 2008). In general, the CRP implementation is based on a tradeoff between intensity of the field work and the desired accuracy for the volume estimation, as the latter is a function of the number and the spatial distribution of in-situ observations (control points) covering the surface of the volume to be mapped (Soole and Poropat, 2000, Yakar and Yilmaz, 2008).

Implementation of CRP for mapping of snow deposits has been already tested for applications related to avalanches. This implementation is still in its infancy (Prokop et al, 2015), as most surveys are generally performed using terrestrial lidar scanning (Prokop and Delaney, 2012; Deems et al., 2013). The emergence of such image-based techniques provides an alternative way to obtain information on topography at sites where direct access of personnel during some critical periods is not easy or can be subject to a high hazard risk (see Muste et al., 2009 and 2011; Basnet and Ettema, 2011). This study contributes toward the development of methods to implement photogrammetry based techniques for mapping snow volumes.

This chapter reports on the capability and limitations of CRP to map snow accumulations produced by snow fences installed to mitigate adverse effects of drifting snow at roadways. While the study does not target scientific research or fundamental aspects of photogrammetry, it reports an engineering approach to implement a contemporary technique to an application that it is otherwise difficult, expensive and challenging to document with alternative survey techniques. The study is exploratory in its nature as it aims to establish a convenient and efficient way of dynamically tracking in real-time accumulations of snow deposits over small-scale areas such as the snow piles retained by snow fences placed on roads' right-of- ways. This chapter describes the stages that we developed for using a photogrammetry-centric system to perform this tasks. However, as will be subsequently discussed and illustrated, the limitations of the technique cannot be easily overcome without additional provisions. These provisions increase the cost of the measurement approach implementation, almost on par with other available alternatives such as terrestrial lidars (e.g., Deems et al., 2013; Hood and Hayashi, 2010; Prokop et al., 2008; Prokop and Delaney, 2012; Prokop et al., 2015). To the knowledge of these authors, the mapping of snow volumes and their change over the duration of the storm for relatively small area sites is a new engineering application for CRP, hence valuable for demonstrating its effectiveness compared to other survey alternatives.

11.3 Study Site and Experimental Needs

The field measurements discussed in the present study were taken at a fenced portion of Highway 20 near Williams (in Iowa, U.S.A.), where snow drifting problems occur regularly (Figure 11.1). The site was monitored over two winter seasons using various experimental methods to support calibration and validation of a methodology for

improving design of snow fences (Basnet et al., 2014). Taking advantage of the existence of several alternative snow volume measurement techniques, the study offered good conditions for testing the proposed CRP measurements benefits.

The site is typically exposed for about 5 months to winter conditions (from mid-November to mid-April). The peak snowfall for the monitoring interval was about 13 cm/day. Snow fall data was obtained from Iowa Environmental Mesonet (http://mesonet.agron.iastate.edu) and NOAA (http://www.nohrsc.noaa.gov). The snowfall measurements, obtained using the routine snow board method, were in good agreements for both data sources. The dominant wind speed during the monitoring time was 55 km/h while its direction was about perpendicular to the fence line. Storm durations were typically short, as shown in Figure 11.1d.

The design and development of the CRP system described next was motivated by the need to dynamically monitor the accumulations of snow deposits at snow fences in order to assess their efficiency (Basnet, 2015). This motivation stems from the lack of alternative analytical tools to accurately estimate variables involved in characterization of the process and the difficulties to monitor in-situ the complexity of the snow drifting. Of particular concern for the present context are the variability of the wind characteristics during the day-long storm events. Due to wind variability, the use of only synoptic measurements acquired immediately after a major storm events does not suffice for assessing accurately the fence performance as the rates of accumulation are continuously changing during the storm. Consequently, the ideal experimental apparatus has to be able to continuously estimate the snow accumulation rates as the storm develops. Such a capability enables additional insights into the details and phases of the snow accumulation

process, which is very valuable information for the engineers in charge of designing the snow fence system at a given site.

For illustration purposes, sample of the wind characteristics at the study site are provided below. Given that there were no direct measurements at the monitoring site, the wind velocity from 6 meteorological stations surrounding the monitoring area were used to track the wind dynamics during the snow events as well as for estimating seasonal snowfall averages (see Figures 11.2 and 11.3). The such-obtained values were found in good agreement with the direct measurements at the closest local meteorological station (i.e., Iowa Falls airport). Direct visual field observations on the orientation of the streaks of snow drifting on the ground confirmed the direction of the dominant wind (Figure 11.3b). Based on this checks, only the information from the closest meteorological station was subsequently used for the analysis. The same methodology was used to calculate the dominant wind speed and direction for the all observations.

It is to be noted, however, that the design and monitoring of snow fences using average values for the wind parameters is somewhat misleading, as the wind direction and its intensity might experience sudden changes, as illustrated in Figure 11.3b. The direct field observations confirmed that snow drifting was redirected with respect to the fence orientation over large time durations. These observations require further scrutiny as snow fence behavior is dramatically influenced by the wind direction, hence, the estimation of their efficiency needs to be evaluated commensurate with the frequency and duration of these changes.

The presentation of the site, snow accumulations, and of the wind characteristics driving the snow deposit formation suggest that the appropriate experimental apparatus for

monitoring the snow accumulation rates should ideally fulfill the following set of requirements:

- capability to map relatively large areas in relatively short time intervals, i.e., acquisition of snow depth information with high spatial and temporal resolution
- real time continuous operation both for observing the site status at any time as well as for supporting decisions for additional measurement needs
- unassisted, and remote-controlled operation with minimum need for site visits to avoid personnel exposure to a harsh winter environment
- minimally intrusive to avoid hazards associated with the conduct of the measurements and the disturbance of the surfaces to be mapped
- capability to acquire frequent measurements that can be remotely adjusted commensurate with the evolution of the storm events
- minimal disturbance to the road traffic during the monitoring of the site
- affordable acquisition, operation and data processing costs

The critical evaluation of the potential techniques for fulfilling the above requirements led to the identification of the CRP as a potential suitable monitoring solution. The main CRP advantage consist in the use of images as raw data for conducting the snow volume mapping. However, the conventional CRP implementation is associated with ancillary field data and operational aspects that has to be customized for the application of interest. The phased process leading to the assemblage of the working CRP configuration, establishment of measurement protocols, the assessment of the sensitivity, limitations, and the benefits of the assembled CRP system as well as the lessons learned are subsequently described.

11.4 CRP Overview

Photogrammetry can be described as the art and science of measuring and interpreting imagery in order to reconstruct 3D objects (Kunapo, 2005; Lerma et al., 2010; Maas, 1997). The technique has emerged from radiolocation, multilateration and radiometry, while its 3-D positioning estimative component (based on modeling) employs methods related to triangulation, trilateration and multidimensional scaling (Yakar and Yilmaz, 2008). Scaling the 3-D location of each point in the images requires few reference points to be surveyed at the measurement site (a small fraction from those needed by the above-reviewed methods). However, photogrammetry can produce stand-alone measurements in situations where the terrain topology cannot be physically measured (Yakar, 2009). Photogrammetry is, on average, 22% faster, 13% more accurate, and 33% cheaper compared to classical methods (Yakar and Yilmaz, 2008). Photogrammetric acquisition and data image processing can be done by a single field operator.

Depending on the recording camera location, photogrammetry can be divided into two basic categories: traditional, or aerial, and nontraditional, or close-range. In aerial photogrammetry, the camera is typically mounted on an aircraft and pointed vertically towards the land (Collier, 2002; Matthews, 2008). Multiple overlapping images of the land are taken as the aircraft flies along a flight path. These images are processed in a stereo-plotter, an instrument that lets an operator see two images at once in a stereo view. Advances in digital imagery and photogrammetric software during the last two decades have enabled the use of photogrammetric methods for a wider range of applications (Mass, 1997). At the same time, reducing the equipment cost and decreasing the computing resulted in a much more cost-effective photogrammetry-based process (Lenzano et al., 2014). These advances have revolutionized both aerial, but especially, terrestrial

measurements by removing many of the rigors of traditional aerial photogrammetry, thus moving stereoscopic image collection from the hands of the photogrammetric expert to those of field personnel. When images are taken from close proximity, the technique is labeled as Close Range Photogrammetry (CRP). For CRP, the camera is close to the object (less than 300 m) and is typically hand-held or set on a tripod or a pole (Matthews, 2008; Lerma et al., 2010; Luhmann et al., 2006). Usually this type of photogrammetry is non-topographic - that is, the output is in the form of drawings, 3-D models, measurements and point clouds rather than a topographic product such as a terrain model or a topographic map. CRP is typically reconstructing the actual terrain topography using a pair of photos of the same area (or object) taken from slightly different locations. If multiple overlapping images are taken from different angles, an even better-resolved 3-D reconstruction of the object can be obtained (Kraus, 1992; Wolf and Dewitt, 2000; Cooper and Robson, 1996).

CRP images are increasingly applied to digitally measure, and subsequently model, volumes of buildings, engineering structures, forensic and accident scenes, mines, earth-works, stock-piles, archaeological artifacts, and natural disasters (see www.photogrammetry.com). Given that images can be acquired with conventional cameras, the advent of low-cost, high-resolution cameras commercialized in recent years has produced an increased in popularity of CRP for a variety of practical applications. Using CRP in conjunction with high resolution, time-lapse photography sheds new insights into the understanding of complex processes such as surface erosion and other geomorphic processes at spatial and temporal scales that are difficult to measure using classical methods. Consequently, this technology has broad applicability for tracking in space and time of ecosystem and physical processes occurring in the nature. Recent applications

include capturing the rock characteristics (e.g., Sturzenegger and Stead, 2009), finding the potential erosion gully (e.g., Marzolff and Poesen, 2009), observing the kinematics of a landslide (e.g., Baldi et al., 2008), and snow depth mapping (e.g., Bühler et al., 2015; Prokop et al., 2015).

For the subsequent portion of the chapter, it is assumed that the reader is familiar with the fundamentals of photogrammetric method (including close-range approach); therefore only the salient features of the process are reiterated in this chapter. More details about the technique's general principles and methodologies can be found in Luhman et al. (2006). Specifics of the CRP technique for aerial and terrestrial photogrammetry applications can be found in Matthews (2008) and Schenk (2005), respectively. The photogrammetric processing performed to obtain the results reported in this chapter was conducted with the Leica Photogrammetry Suite Project Manager (LPS Project Manager), which is a component of ERDAS EMAGINE software (LPS, 2009). The LPS Project Manager has the ability to extract 3-D terrain information from a pair of images.

The CRP process as implemented for remotely tracking the temporal evolution of snow is illustrated in Table 11.1. The cloud of points with coordinates provided by the CRP software following Phase 3 was transferred to a post processing software − Tecplot (Tecplot 360, 2011). First, a two-dimensional rectangular area with resolution of about 2.5cm x 2.5cm was created as x and y coordinates for those points, then z-coordinates for cloud of points were transferred to the rectangular zone applying inverse distance interpolation that results in z-values for each grid points in the selected area.

11.5 CRP Implementation

11.5.1 Components customization and experimental arrangement

Images for CRP processing were acquired with a commercially-available Moultrie i65 GAME Spy camera equipped with a cell-phone based transmission unit (www.moultriegamemanagement.com). This camera, characterized by a focal length of 8 mm, a 5 mp native resolution sensor, and a 2.2μm x 2.2μm pixel size, can continuously capture photo frames or video segments up to the point of filling the memory card (32 GB in our case) of the camera. The off-the-shelf camera was installed in a weatherized plastic case (see Figure 11.4a). Embedded in the case were also a Global Positioning System (GPS) sensor, a backup battery, and a solar panel connected to the battery. The customized system containing all of the above-described components resulted in a stand-alone, self-powered observational node with real-time data transmission capabilities. The raw images for CRP processing were provided by a pair of such web-cameras set to record images every hour simultaneously. Sample images acquired with the pair of cameras set on a pole are illustrated in Figure 11.4c. An ancillary Moultrie Game Management System supported by the web-camera producer allowed accessing the acquired images in close to real time (see Figure 11.4d). The camera web-platform also allowed to remotely control the camera operating parameters such as the sampling frequency for the recording. Images were often received with some delay depending on weather and communication conditions at the site. Besides acquiring images for the CRP analysis, which was the primary role of the system, the system was also useful in alerting the team on the proper time to get out to the site for simultaneous measurements using other instruments.

In addition to the continuous recordings with the dual-camera system, the snow deposits were mapped in situ using synoptic measurements over the CRP-imaged area

using alternative survey instruments. There were three alternative measurement approaches used for this purpose. First, a set of marker poles were installed at the observation site using the spatial arrangement sketched in Figure 11.5a. The points of contact between the marker poles and the bare ground were surveyed before the winter season to provide the reference (bottom) surface for volume calculations. During the synoptic measurements, the snow depth at each marker pole was determined by directly measuring the distance from the snow surface to the tip of the pole using a measuring tape. These marker poles also provided fixed GCPs for supporting the CRP process. The second, and most often method used as an alternative survey measurement approach, was a GPS based real-time kinematic (RTK) survey. The RTK synoptic surveys included all the marker poles, as well as additional points (see Figure 11.5b) in the imaged area. The third snow-volume survey method consisted of measurements performed using a total station (Topcon GTS 235 Total Station).

11.5.2 Experimental protocols

The experimental protocol was progressively developed through successive field campaigns (see Table 11.2). The site was visited before the winter season at the time when the experimental equipment for continuous monitoring was installed. During the initial site visit, a RTK bare-ground survey was conducted to determine the coordinates of the marker poles acting as GCPs. Camera position (horizontal and vertical) was established using RTK, measuring tapes, and direct readings of the camera's inclination angles using the Angle Meter iPhone application. These angles were used only for initial guess during the camera calibration process. The height of each marker pole with respect to its base was also physically measured using measuring tapes. After the equipment installation,

provisions were taken to secure the equipment and ancillary supports against wind-induced vibrations and other incidental effects. The initial visit concluded with the acquisition of a set of images with the web-cameras to make sure that the system was ready.

For present discussion, we distinguish two types of measurement protocols: a) synoptic measurements (Protocol 1), and b) continuous measurements (Protocol 2). Synoptic measurements were carried out only for significant snow storms. During these measurements, the snow accumulations at the baseline points and at the additional points associated with the marker poles (see Figure 11.5a) were thoroughly surveyed. To secure good sets of GCPs for CRP, additional points dispersed over the imaged area (Figure 11.5b) were surveyed with various techniques. During the synoptic measurements, still photos were captured with the dual-camera system to support the CRP sensitivity analysis and to estimate the measurement accuracy through comparisons with results of other measurement approaches. The site visits for synoptic measurements were also occasions to check the status of each camera assembly component and to download the recorded images for subsequent processing.

Given the adversity of the measurement environment, the continuous unassisted snow deposition measurements (Protocol 2) was one of the main targets of the study. For these measurements, the images continuously acquired by the web-cameras were subsequently processed with the ERDAS software to calculate the changes in volume of snow accumulated at the fence. As we needed a camera set up that could work continuously in the adverse weather conditions (e.g., most of the time below freezing temperature and windy), we compromised for the quality of camera (e.g., the focal length is 8mm only). Given that the camera characteristics were not provided by the manufacturer and that the

devices used for setting the geometrical characteristics of the optical arrangement were of limited accuracy, a one-time calibration using 19 GCPs distributed over the entire area of interest was conducted (as shown in Figure 11.5). 15 GCPs consisting of metallic steel poles (Figure 11.5a) and 4 additional GCPs made of wood were placed in the near field area (Figure 11.5b). Subsequently, during the production, CRP measurements acquired with Protocol 2 using only 5 GCPs' information remotely (represented by green circle in Figure 11.5a).

The CRP analysis was conducted on the images acquired in the field after retrieving them from the cameras. This was typically done once every three weeks. As expected and will be further illustrated, Protocol 1 is more accurate than Protocol 2 in providing the volume estimates. The increase in accuracy comes, however, at the expense of costs and efforts associated with the presence at the sites during the measurements. Figure 11.6a illustrates a sequence of continuous and synoptic measurements acquired during a storm at the experimental site. Figure 11.6b illustrates the sample comparison between the elevations of the snow accumulations at 4 GCPs, as obtained with the P1 and P2 measurement approaches. The agreement between the two results confirms the reliability of the image analysis to calculate snow depth such that one can determine z-coordinate at GCPs to be used for CRP monitoring. Only few successful storm events were documented with both the P1 and P2 protocols because the trips were costly and effort intensive.

11.6 CRP Sensitivity and Accuracy Analysis

Prior to deploy the CRP components at the study site, we conducted several end-to-end tests at sites that were practically similar to those reported in the literature (e.g., Lerma et al., 2010; Matthews, 2008; Sturzenegger and Stead, 2009; Yakar, 2010). The site

tested for the end-to-end tests were rich in texture at the surface of the surveyed volumes compared to the snow surface that lacks prominent color gradients or visible geometrical texture. The results obtained for those preliminary studies are reported in Constantinescu et al. (2015) and were in good agreement with the alternative survey methods. Anticipating that these differences would pose upfront challenges for CRP processing when applied to snow surface images, we further explored the sensitivity and accuracy of the CRP to various parameters involved in snow surface mapping through another series conducted before to initiate the production CRP surveys at the field site. The critical review of these measurements are provided below as they provided useful practical hints for the technique's implementation in this new area of CRP application.

11.6.1 Effect of the density and distribution of the ground control points

For these sensitivity tests, 12 GCPs were initially used for our application to train the CRP software in the processing stage. Eight of these initial GCPs were distributed along a line crossing the snow deposits created by the snow fence, as illustrated in Figure 11.5a. This GCP arrangement was suggested by the close to two-dimensional shape of the snow deposit at the monitored fence. The GCP axis that is perpendicular to the fence direction is labeled as the baseline GCP. Processing successively the same image pairs by removing gradually GCPs from 12 to 8 and eventually to 4 led, as expected, to a loss in the accuracy of the snow surface reconstruction. The results of these tests are illustrated in Figure 11.7.

The comparison of results for 3 different cases of GCPs distribution/density was conducted based on the ground surface observed in the CRP results represented by dark red color (z=0m). There is negligible ground surface in the case of 12 GCPs distribution and this is comparable with what was observed in the field. But as the number of GCPS

311

was reduced from 12 to 8 by eliminating 4 of them in the processing stage, about 40% of the mapped area was vastly different from the visual observations in the field. When the number of GCPs was reduced to only 4, about 75% of the mapped area was poorly reconstructed. The snow surface contour was better resolved along the GCP line deteriorates rapidly over the area without GCPs. The total range of the resolved free-surface elevation (absolute values) is also changing with the number and distribution pattern of GCPs used in the processing.

11.6.2 Surface texture

The surface of the fresh snow deposit is practically without apparent texture in the recorded images. Moreover, the smoothness of the deposit shape and the bright white color do not create many distinguishable features in the images. These image features are in stark contrast with surfaces used for other CRP applications reported in previous studies. Figure 11.8a clearly illustrates the connection between the lack of texture and the number of tie points identified by the photogrammetry software. Specifically, it can be observed that in the far field where the texture is poor, there are few points. The presence of the footprints created by the crew working at the site in the near field produced a multitude of recognizable features in both images (see the bottom of Figure 11.8a). For older snow coverage, the quality of the surface reconstruction is somewhat improved as shown in Figure 11.8b. Snow melting and the transitions between bare and snow-covered areas illustrated in Figure 11.8b provide more distinguishable features on the surface to be mapped. In turn, this facilitates the creation of tie points by the CRP software.

The above-provided examples illustrate typical challenges encountered in dealing with the snow volume surfaces in various stages of their accumulations. These challenges

lead to a situation whereby even if the site, instrumentation, imaging conditions, and image acquisition protocols are identical, the technique displays widely different efficiencies in reconstructing the volume surface topography depending on the age of the snow deposit. The worst measurement conditions occur right after the falling of fresh snow over the bare ground or previous snow ground cover when mapping of the surface is impossible due to the absence of recognizable texture at their surface.

The above-mentioned limitation led the authors to the idea of creating artificial image texture atop of the snow fall volumes by spreading light materials over the fresh snow fall as described next. For this purpose, dried leaves and light wood chips were dispersed over the mapped area using mechanical spreaders as illustrated in Figures 11.9a and 11.9b. This material was distributed over the snow surface to be mapped using specially-designed particle-blowing cannons that spread the material efficiently and fast. These cannons are commonly used for shooting confetti in show business. The cannons are built in various sizes, configurations and operating modes. They can be deployed at any site using power produced by portable generators. Figure 11.9c shows an example of snow surface map created using CRP applied to "seeded" snow surface. A snow profile extracted across the section D-D (see Figure 11.9c) as an example is presented in Figure 11.9d.

11.6.3 CRP mapping accuracy

Although the CRP technology is a mature, widely applied technique, documentation of its accuracy with alternative instrumentation is rarely reported (i.e., Lerma et al., 2010; Matthews, 2008; Sturzenegger and Stead, 2009; Yakar, 2010). The accuracy of the CRP 3-D reconstruction depends on all components and steps involved in the measurement process: camera resolution and its positioning (e.g., the distance from the

camera to object, angle between the camera providing images), equipment characteristics (e.g. optical parameters for the imaging camera), and methods used in image-processing (e.g., pattern recognition, spatial interpolation). The assessment of the sources of errors for all the technique's components is a complex task and it is beyond the scope of the present study. An end-to-end comparison of the CRP results with measurements acquired with alternative instruments are reported here as a surrogate for a full-fledged uncertainty analysis.

The evaluation of the CRP accuracy was made over a 40 m long, 21 m wide area that displays a total elevation difference of 2 m (matching closely the 2 m fence height). The quantitative accuracy evaluation was made at 5 points where RTK measurement were available. The same GCPs were used for conducting survey Protocol 2 (see Table 11.2). The GCPs, distributed as illustrated in Figure 11.10a, were deployed at the beginning of the monitoring and secured for stability for the entire monitoring duration. The software also calculates the (x, y, z) coordinates for GCPs that eliminates the requirement of identifying GCPs in the 3d model manually. The visualization of the difference between the GCP (x, y, z) coordinates calculated by the photogrammetry software (CRP processing outcome) and those obtained from the RTK survey are plotted in Figure 11.10b. The uncertainty in the RTK measurements used for reference is about ±2.5 cm (Trimble Correction services). The percentage differences between the CRP coordinate estimation (x, y, z) and RTK measurements at the five points are provided in Table 11.3. The largest difference among the compared points in the z direction is 15.5% (at the GCP #2) that is equivalent to 31 cm absolute value. The differences in the x and y coordinates are, expected, considerable smaller as the 5 points are used as input for the CRP software. The major

sources for the differences in the z coordinate are attributed to the poor resolution of the camera and the difficulties to optimally recognize texture on fresh snow in the recorded images.

11.7 Tracking Snow Deposition during a Strom Event

Dynamic tracking of the snow accumulations during storm events has been the main target of this continuously evolving technologic development. The development was an extensive (three winter seasons) trial-and-error process during all its phases: preliminary design and testing of the assembled components, correction applications, formulation of field deployment logistics, development of operation protocols, and conduct of alternative measurements for CRP implementation and evaluation of its efficiency. Unfortunately, during the monitoring with the final configuration of the CRP system deployed at the site (last monitored winter), there were few storm events that occurred during daylight (see Figure 11.1d). The only relevant example for illustrating the benefits of the dynamic snow deposit mapping is the largest storm of the 2013-2014 CRP deployment. The storm was characterized by a 12.75 cm snowfall with wind gusts up 55 km/h (see Figure 11.12). Notable is the large variability of the wind direction during the intense snow fall. The results reported below are obtained using only Protocol 2 measurements, i.e., unassisted image recording using only 5 GCPs deployed at the site as illustrated in Figure 11.10a. Images acquired during the event and CRP processing results are shown in Figure 11.11. The snow volume budget is presented in Figure 11.12. The initial volume of snow deposited downwind the fence before the storm was 362 m^3. The accumulation of the drifted fresh snow fall resulted in an increase of the volume 443 m^3 (see Figure 11.12). The figure also provides the wind velocity record obtained as specified in Section 11.3. The

wind velocity record provided in the figure confirms the high variability of the wind direction and intensity during the storm passage. An integral part of the changes in the volume of the snow deposit is the ambient temperature variation. Similarly to the wind velocity estimation, the temperature at the experimental site was obtained using measurements at six stations surrounding the experimental site. Given that the temperature was roughly constant during the monitored snow storm it can be inferred that the mapped volumes are mostly related to snow drifting. Moreover, given the short duration of the storm the effect of the snow compaction can be considered negligible. This availability of this type of information is critical for providing new insights in the investigation of the snow drifting and deposition processes.

The proof-of-concept dynamic monitoring of snow deposition described above illustrates that overall, the CRP configuration and measurement protocols are satisfactory for accomplishing the task. The two main limitations of the newly developed technique are: a) coping with the fresh snow visualization, and, b) acquiring images during night time. The artificial "seeding" approach that we tested showed that this might overcome the night-time illumination issues, at the expense of having personnel present in the field. If a method to apply the seeding without physical presence can be provided by, for example, having in the field an automated network of seed feeders that can be triggered remotely based on the monitoring of the real time snow fall, then, in principle, the developed CRP measurement method attains its goals. The night-time operation issue cannot be solved using the current web-cameras. This limitation can be overcome if an alternative image recording configuration is assembled to incorporate illumination devices triggered automatically

during the night time. The solution might be feasible for small storms but it would be not applicable for large storms when the visibility is drastically reduced.

11.8 Conclusions

This chapter presents results of a phased development leading to a practical monitoring arrangement and ancillary measurement protocols for dynamically tracking the formation of snow deposits at snow fences protecting the roads from drifting snow. The assembled technique is generic and can be extended in any situation where the mapping of the volume of deposited snow is of interest. The CRP configuration reported herein was obtained using off-the-shelf components assembled through a phased process, whereby complexities associated with this unique CRP applications were addressed with engineering judgement and engagement of complementary measures inspired from other field experimental methods. Two protocols for conducting the measurements were established as part of this study. The first one requires assistance from alternative surveying measurements. The other one is accomplished using only remote measurements (see Table 11.2). The comparison of simultaneous measurements obtained with the two protocols confirmed their agreement, hence the possibility of using a measurement procedure that does not require deployment of personnel in the field while performing measurements with an accuracy comparable with that of alternative conventional monitoring techniques.

The results of this technological development are not exhaustive and can be further enhanced by more exploration and integration of newly developed relevant technologies. Special attention should be devoted to coping with the lack of surface texture and color gradients on the surface of the fresh snow fall accumulations and operating the system during night time. For situation where the measurement environment was satisfactory, the

317

assembled CRP configuration and measurement protocols could be employed continuously in adverse weather conditions even if the optical devices for recording the images were at the low end of the available technology. Lower quality imaging can be, up to a certain degree, overcome using an increased number of ground control points in the field, especially in the calibration stage of the CRP process. The CRP implementation protocols, optimized as described in this study, led to differences of not more than 16% compared to the conventional intrusive measurement approaches.

The main contribution of the study is the extension of conventional CRP range of applications by enabling dynamic mapping of the snow deposits formation using a real-time, automated and unassisted monitoring approach. A secondary contribution is the testing and validation of a 'seeding of the free surface' approach that overcomes some of the difficulties in finding visible patterns used for three-dimensional volume reconstruction. We expect that the fast advancement of the recording and communication technology will gradually overcome this limitation. The study's contributions demonstrate the benefits of using such a non-intrusive monitoring method at a cost that is not prohibitive. To the knowledge of the present authors, such a method was not previously tested and assessed in the photogrammetry literature.

The results obtained in the present study lead to the conclusion that the CRP technique has unique capabilities to map snow elevations over large areas using only a pair of cameras that are automatically operated. The method can be continuously operated, thus allowing to remotely track the temporal evolution of the snow volume, which is difficult, or even impossible, to perform with conventional mapping means. The imaged-based technology offers the unique ability to simultaneously collect snow landscape panoramas

and details with time steps commensurate with the in-situ development of the snow transport and deposition processes. The technique is especially suitable in assisting the optimization of snow fence design, especially at sites where standard solutions based on semi-empirical design formulas were shown not to work as expected.

a)   b)   c)

d)
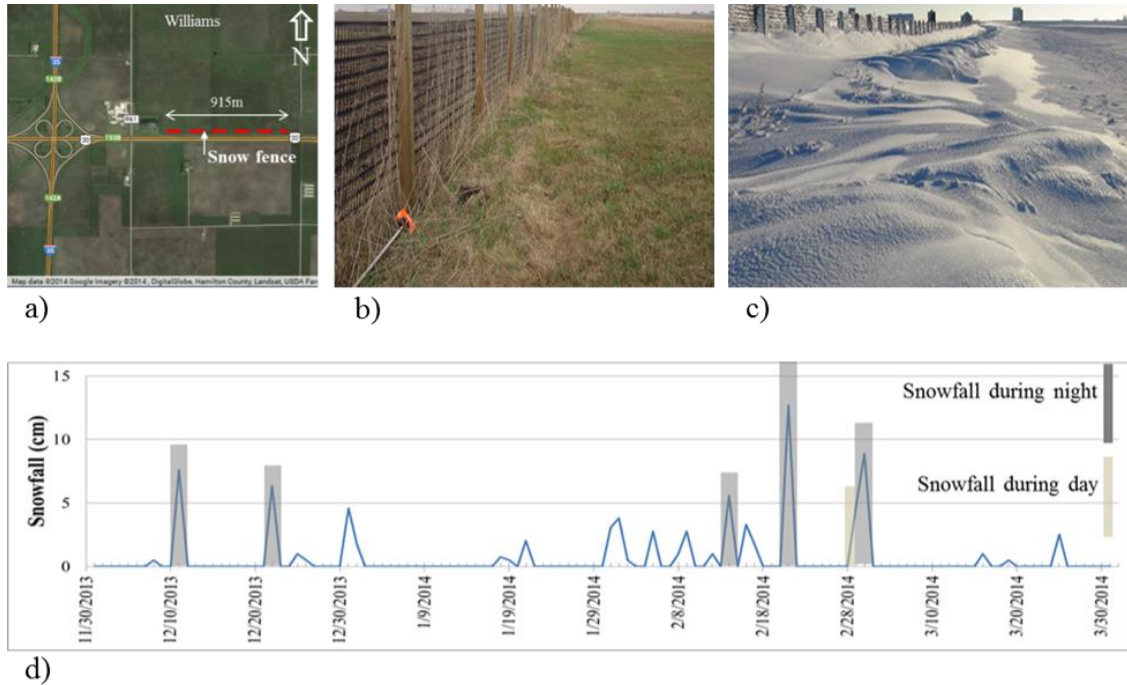
Figure 11.1 CRP survey site located on Highway 20, Williams (Iowa, U.S.A.): a) location on Google map; b) photo of the bare-ground site (November 2013); c) snow retained by the snow fence (February, 2014); d) snow-storm timing and duration at the study site (winter season 2013-2014). Data source: Iowa Environmental Mesonet (www.mesonet.agron.iastate.edu).

a)   b)
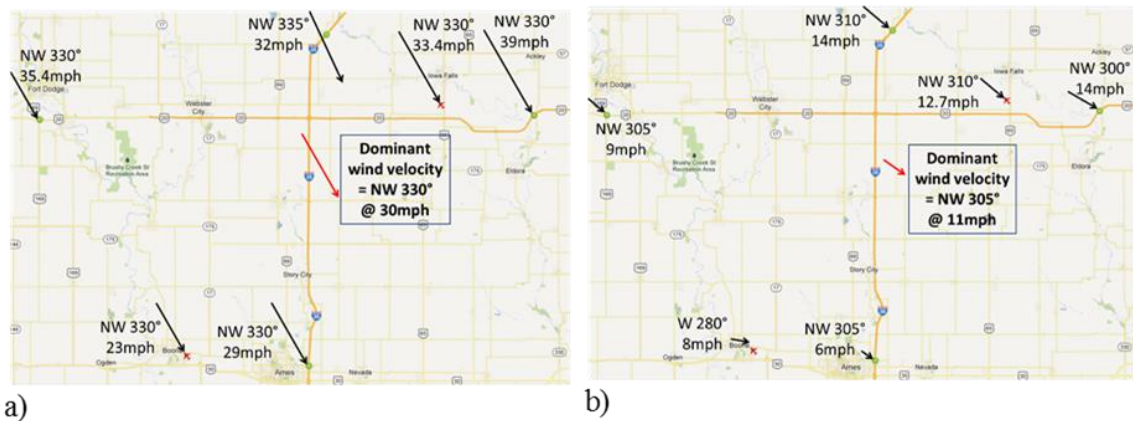
Figure 11.2 Spatial wind distribution at the study site: a) December 20, 2012, 9:45 am; b) December 21, 2012, 9:45 am.

320
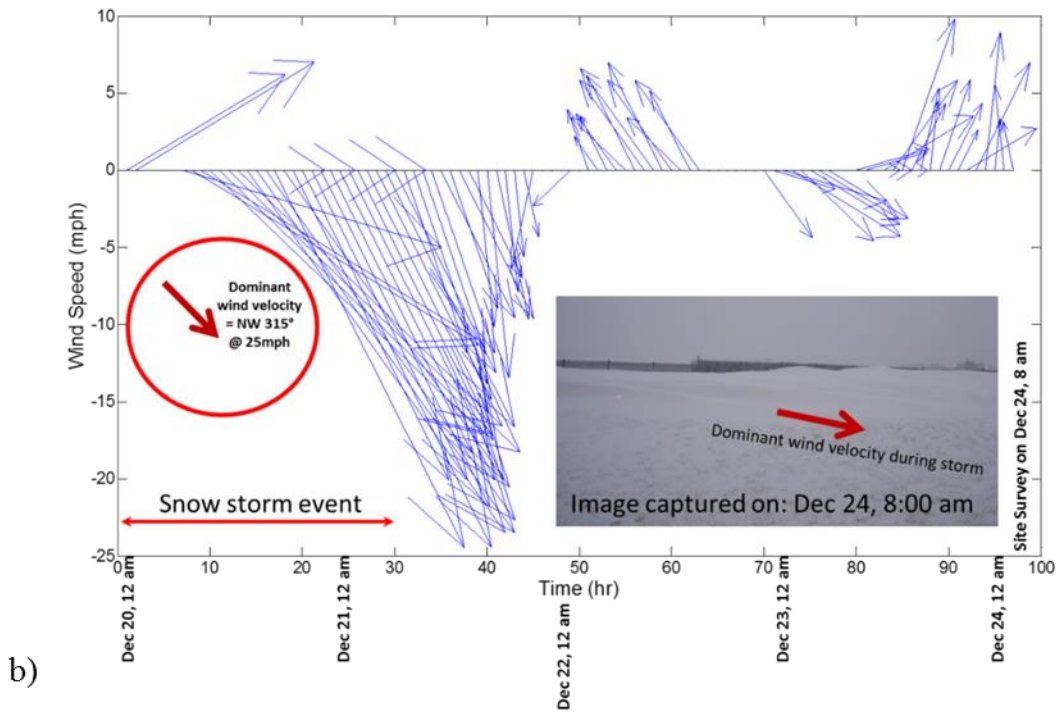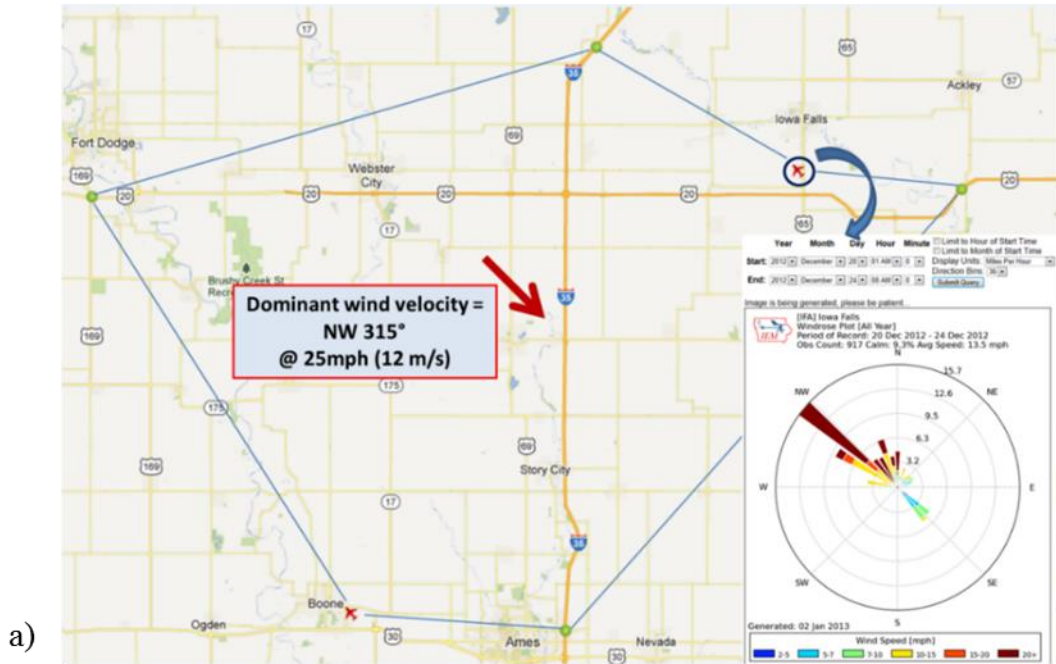
Figure 11.3 Wind characteristics for the observation site during the December 20-24, 2012 snowstorm: a) comparison of areal wind velocity with local data; b) wind variation at one of the stations for the duration of the storm.
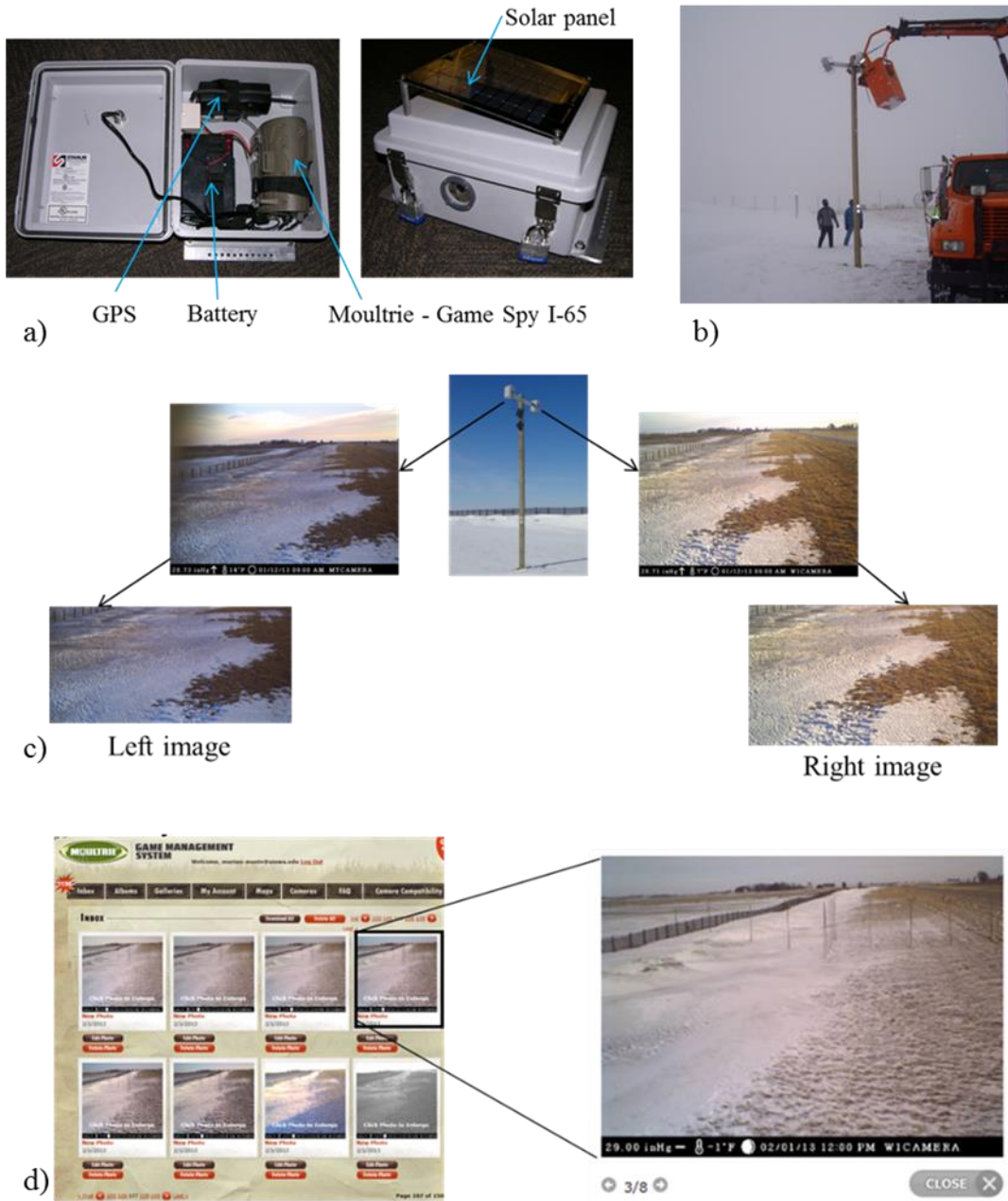
Figure 11.4 The image-based system used for site monitoring: a) the camera assembly; b) camera installation in the pole; c) raw images acquired for CRP processing; d) the real-time, web-based image-management platform.
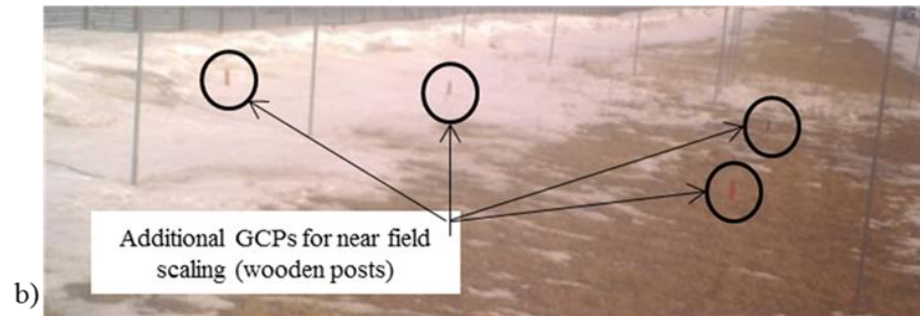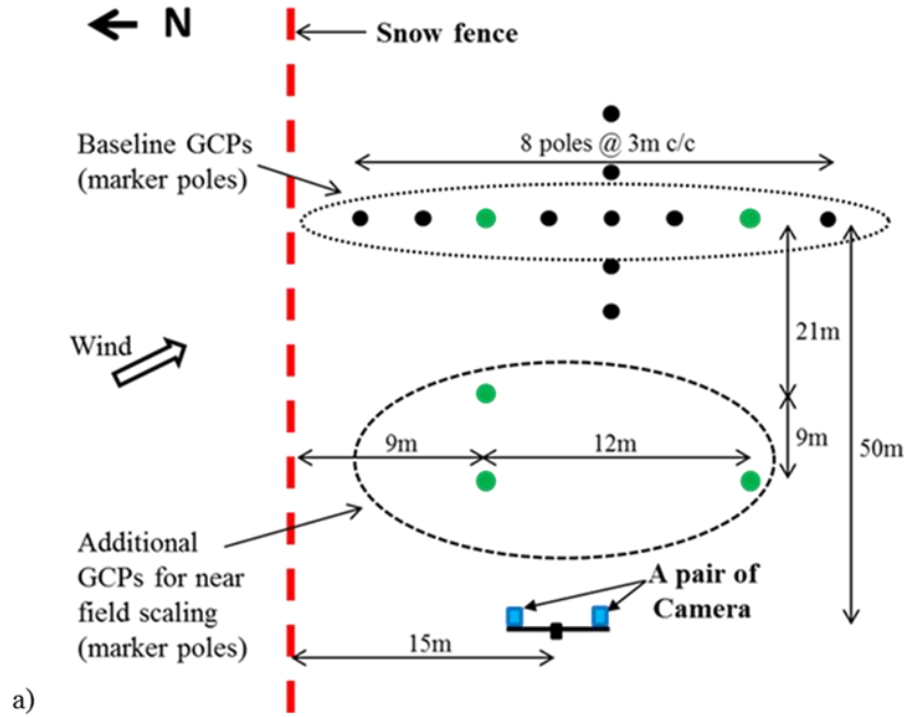
Figure 11.5 Experimental arrangement of the site and RTK field survey: a) schematic diagram with 15 in-situ markers poles as GCPs (not at scale); b) a photograph displaying 4 additional GCPs (small wood posts).
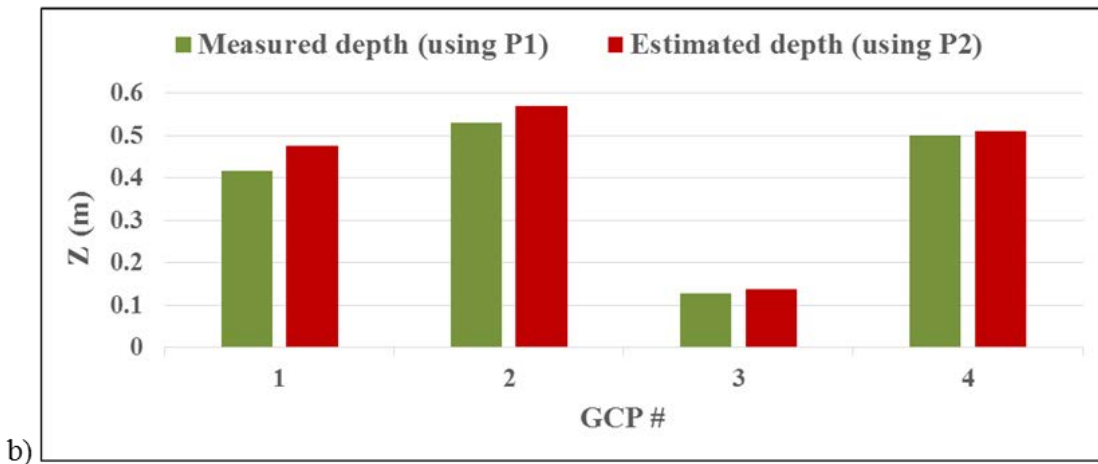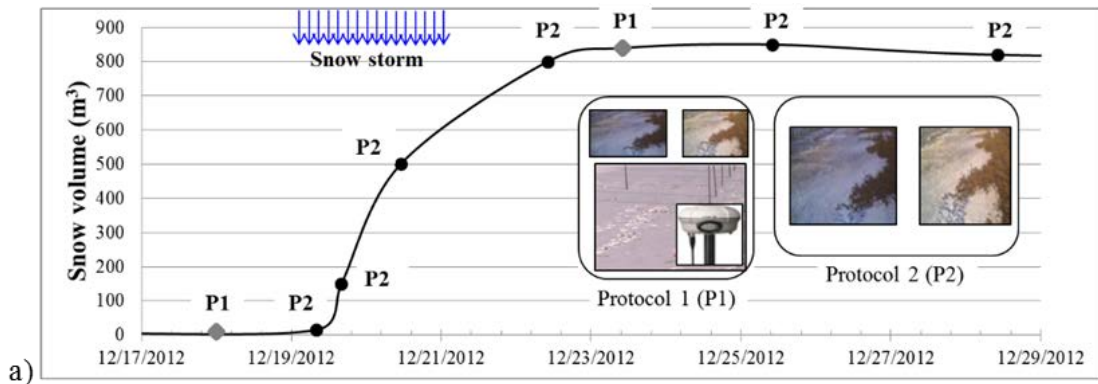
Figure 11.6 Tracking snow storm events: a) combination of continuous and synoptic measurements during the duration of a storm; b) comparison of snow depth calculated using images only (P2) with the snow depth measured at the field with RTK (P1).
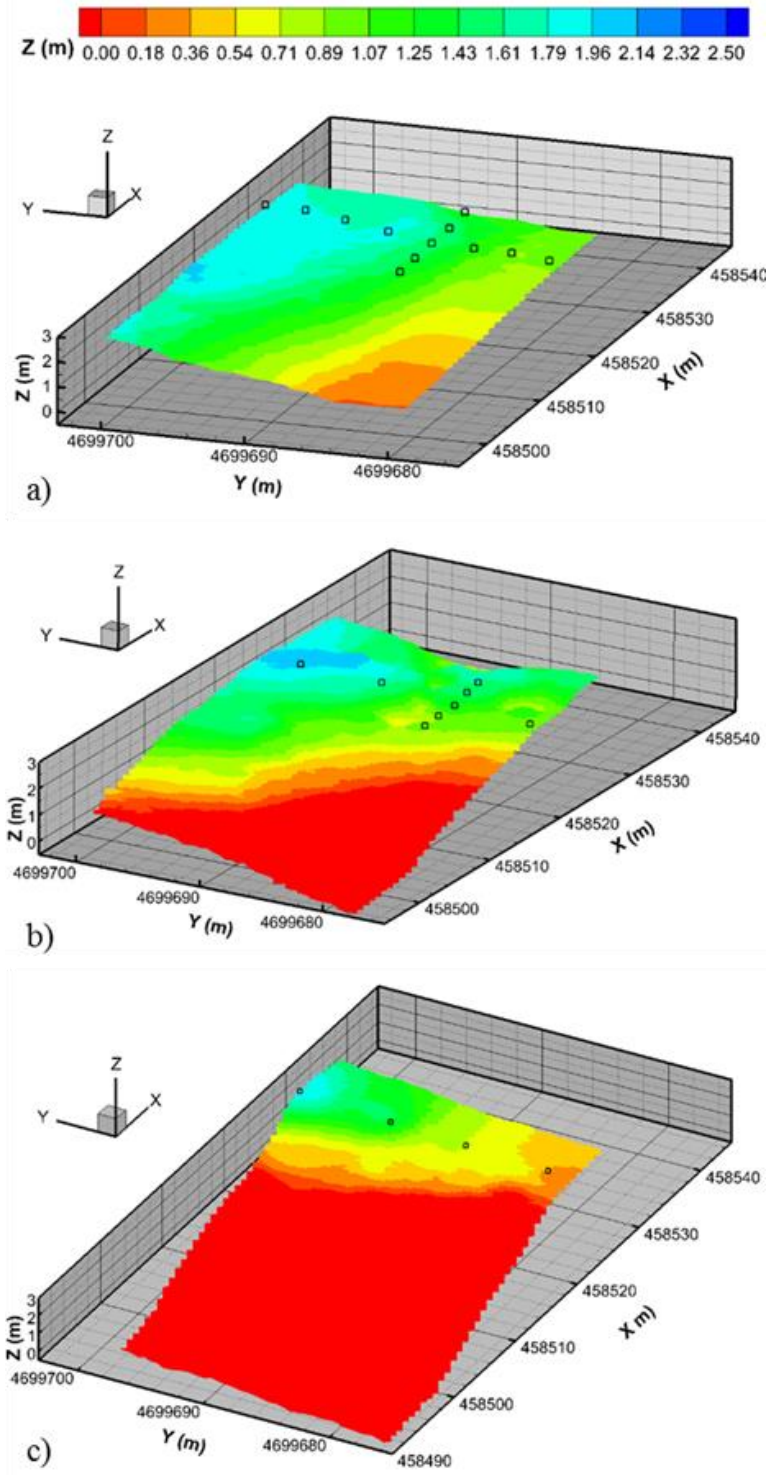
Figure 11.7 Sensitivity analysis: importance of the distribution pattern of the control points: a) using 12 GCPs; b) using 8 GCPs; c) using 4 GCPs. The CRP results are obtained using the same image pair dataset.
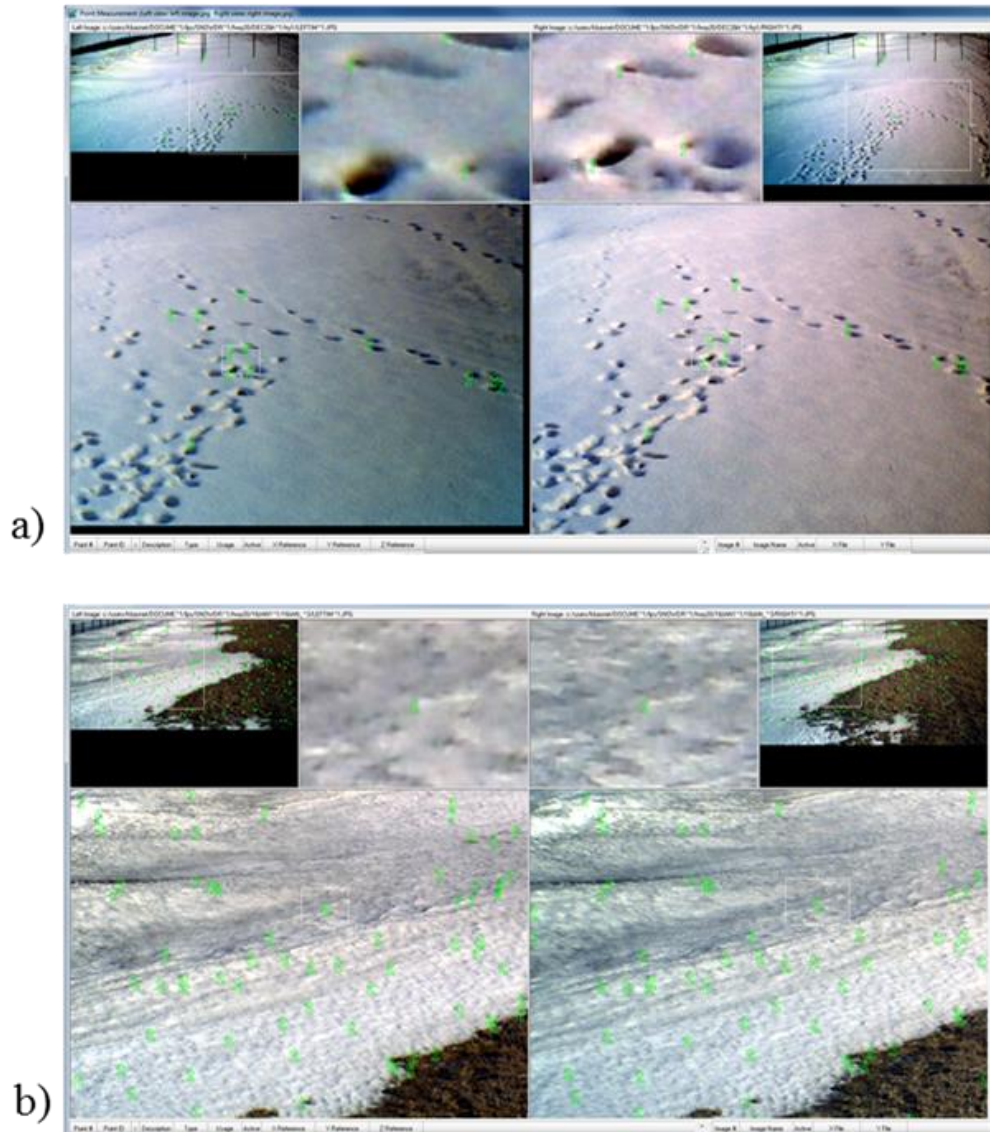
Figure 11.8 Texture effect on the identification of tie points (ERDAS software screen shots): a) a limited number of tie points are generated on the fresh snow deposit; It can be observed that the smooth undisturbed snow surface area in the lower-right corner of the images does not produce any tie points. The tie points are generated where dents in the surface are visible; b) the texture created due to snow melting lead to the creation of a sufficient number of tie points for practically same lighting conditions.
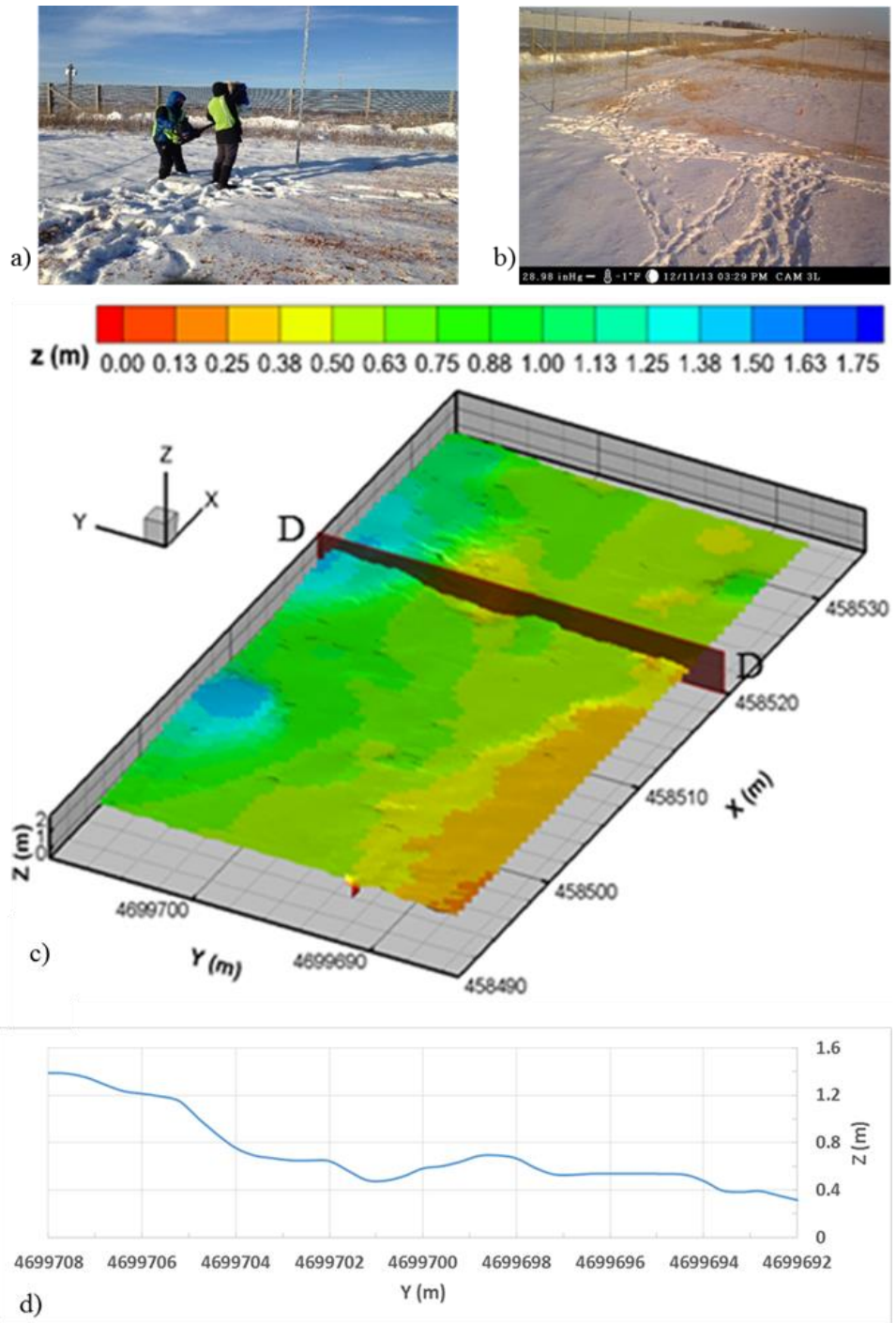
Figure 11.9 Improvement of the surface texture by spreading light materials over the snow volume surface: a) use of the cannon at the experimental site; b) fresh snow seeded with leaves and wood chips; c) results of the CRP processing using the seeded surfaces; d) sample snow profile extracted along the D-D section.
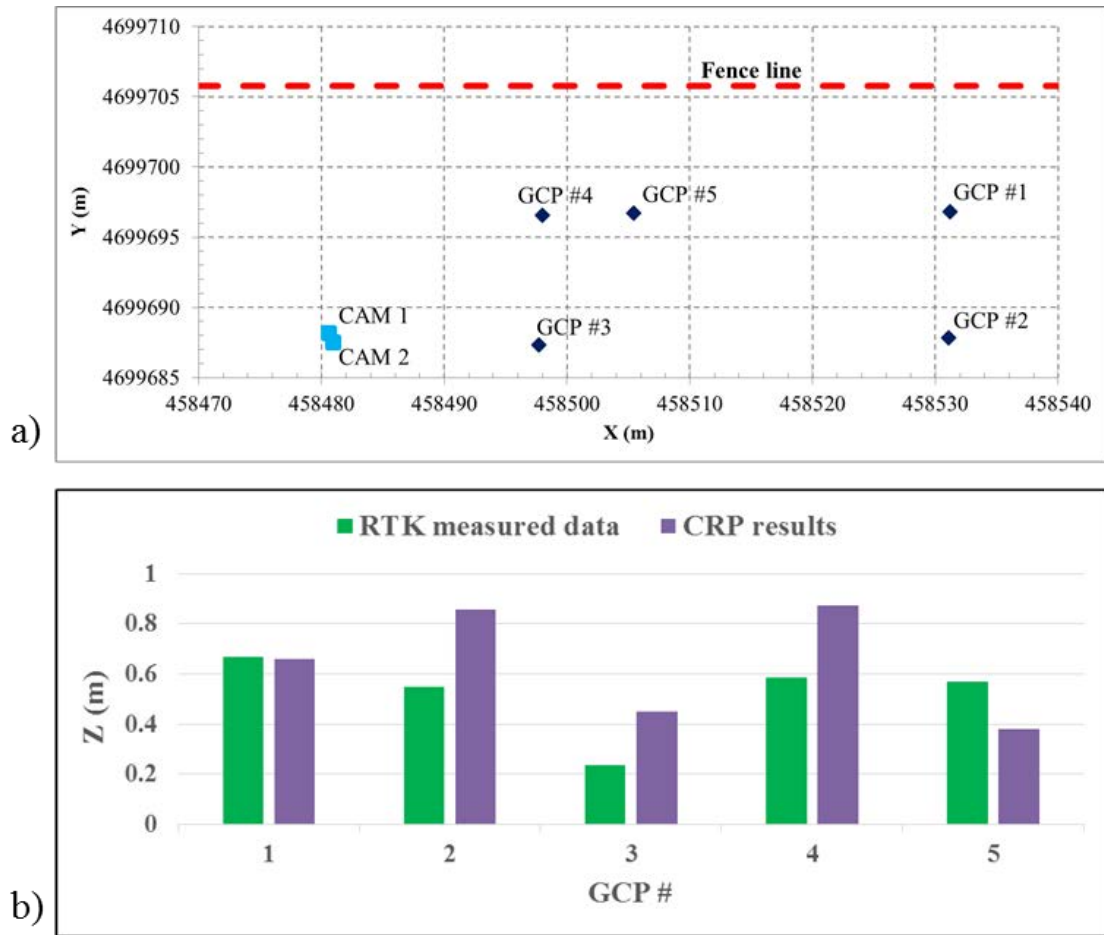
Figure 11.10 Comparison between CRP point elevation estimates and RTK measurements: a) location of the GCPs used for comparison; b) differences in snow depth at the comparison points.
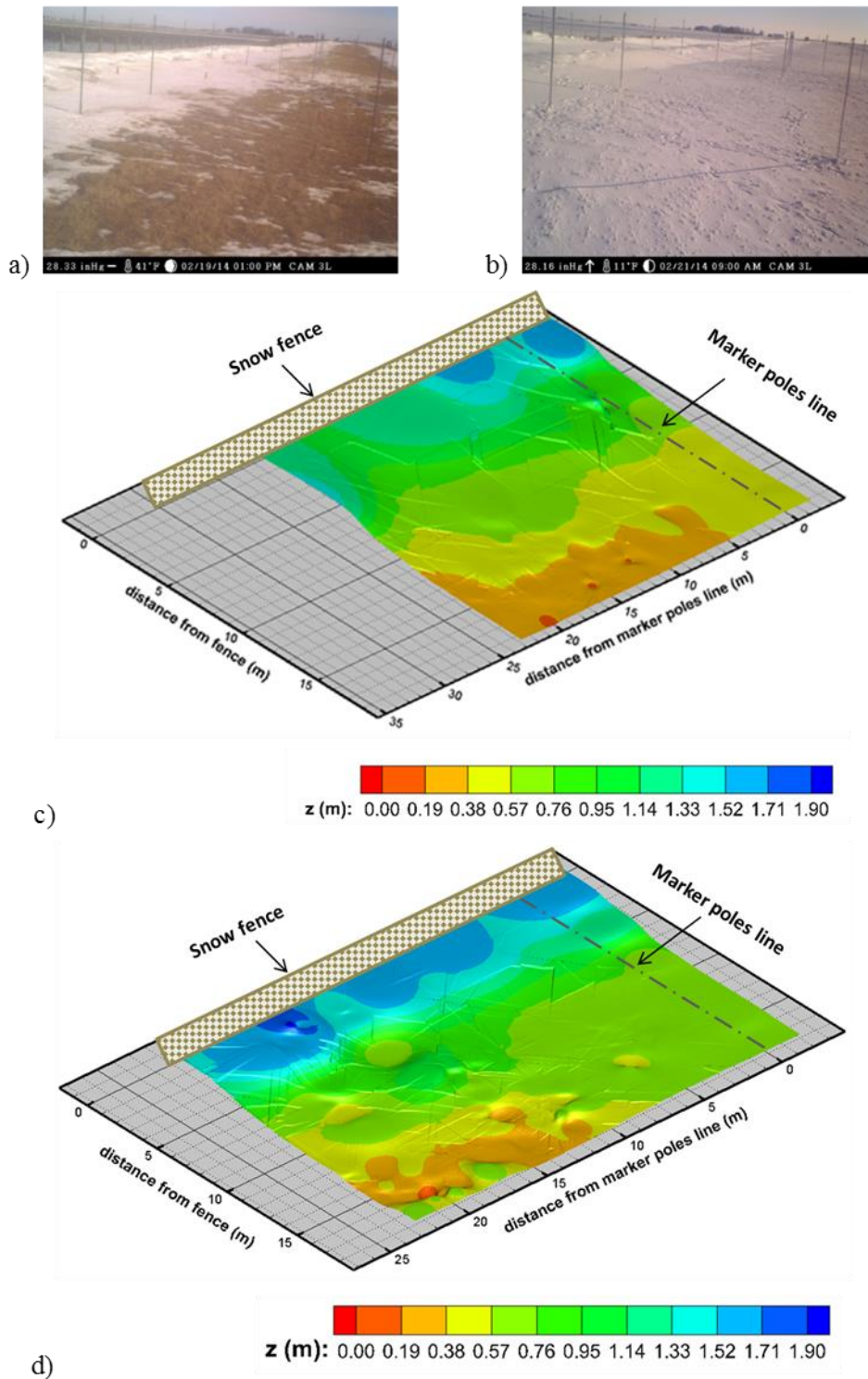
Figure 11.11 Snow tracking event using the customized CRP; a) image of the site before the storm; b) image of the site after the storm; c) snow mapping before the storm; d) snow mapping after the storm.
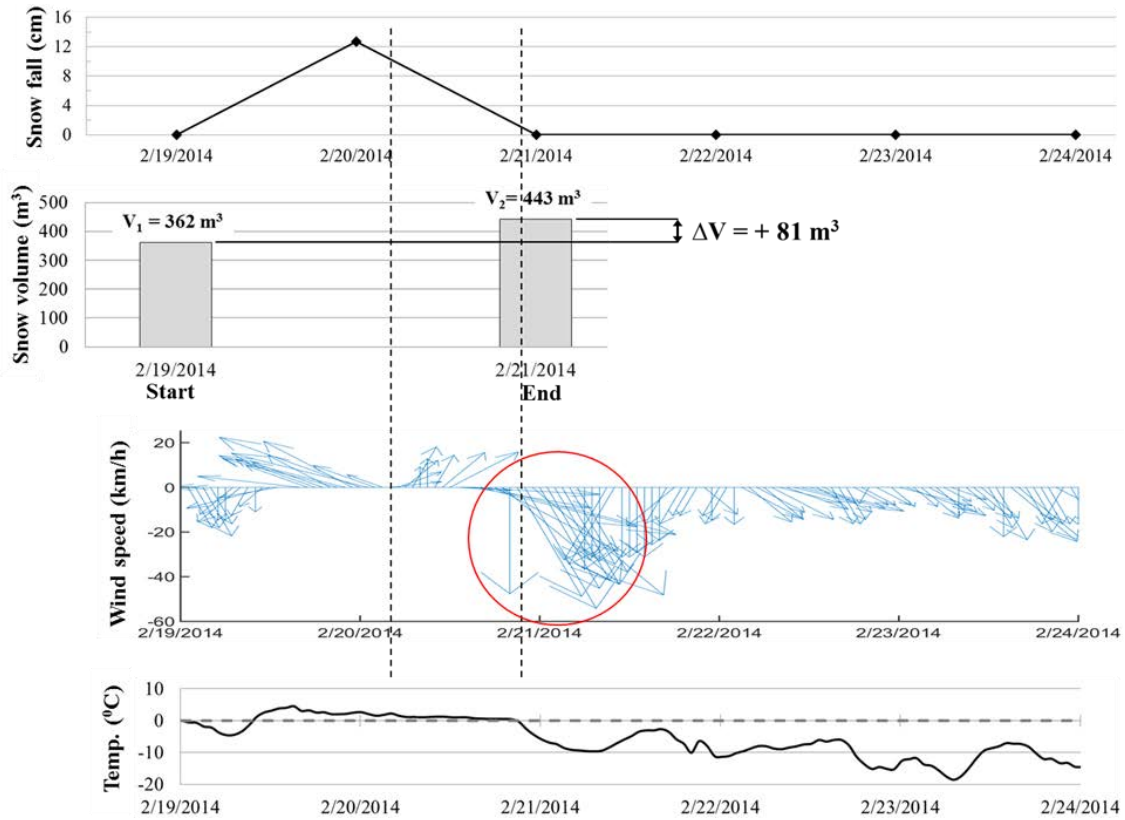
Figure 11.12 Illustration of the snow accumulation budget during a snow storm in conjunction with the time series of wind and temperature variation during the same event. The significant snowfall period during the storm is marked by the dashed vertical lines. The red circle indicates the peak wind velocity recorded during the storm. The wind direction for this time interval coincides with the seasonal dominant wind direction and it is about perpendicular to the fence orientation. Data source for snow fall, wind and temperature: Iowa Environmental Mesonet (www.mesonet.agron.iastate.edu).

Table 11.1 Phases in CRP implementation process.

	CRP Phase	Hard/Soft Components	Outcomes
1	Camera calibration (using 19 Ground-control Points - GCPs)	A pair of images, coordinates of camera positions and GCPs, focal length and pixel size of each camera	Camera inclination angles, calibrated focal length
2	Validation of continuous CRP monitoring for 5 GCPs (Field survey required)	A pair of images, coordinates of 5 GCPs	
3	Continuous CRP monitoring using 5 GCPs (generation of tie points, triangulation and automatic terrain extraction using CRP software)	A pair of images, estimated z-coordinate at 5 GCPs using images	Coordinates for cloud of points over the targeted area
4	Post processing using Tecplot		Contours of snow elevations and change in snow volume

Table 11.2 Experimental protocols.

I. Pre-winter (bare-ground) survey	II. Synoptic measurements (P1)	III. Continuous monitoring (P2)
1. RTK survey a.marker poles b.additional GCPs 2. Tape measurements of marker poles' height	1. RTK survey 2. Total station 3. Tape measurements of snow depth at the marker poles 4. Video and still photos of various site components	1. Images acquired continuously 2. CRP analysis using image-based estimates of z-coordinates at 5 GCPs
Measurement outcomes		
Baseline for snow volume estimation	Calibration/validation of mapping tools for volume estimation	Continuous CRP for tracking change in snow volume

Table 11.3 Accuracy of CRP results.

GCP #	|% error|		
	X	Y	Z
1	0.14	0.03	0.4
2	2.12	0.78	15.5
3	0.9	0.23	10.6
4	0.76	0.75	14.2
5	0.57	0.1	9.3

CHAPTER 12 CONCLUSIONS AND FUTURE WORK

The present thesis investigated flow and turbulence structure past porous plates/barriers and their implications for mitigating snow drifting problems when such barriers (snow fences) are installed in the vicinity of roadways. The study employed a range of numerical and experimental techniques to achieve this goal that include 3D LES and 2D RANS numerical simulations, RTK, LSPIV and 3D photogrammetry techniques to measure ground elevations and snow deposits in the field. Besides collecting field data needed to optimize the design of snow fences, the study also developed, tested and implemented novel protocols and methodologies to perform these measurements in the field and to propose improved designs.

Following validation of the numerical model, the first part of the study used high-resolution fully three-dimensional LES to perform a detailed parametric study needed to understand how the wake structure and its spectral content, the unsteady and mean loads on the porous/solid plate and the bed friction velocity distributions change as a function of the plate porosity, relative bottom gap, relative hole size and bed roughness. Besides its relevance for applications related to the design of snow fences, the results of these simulations contributed to enhancing the general understanding of flow past thin porous plates situated in the vicinity of a solid no-slip boundary, a configuration that is important in many engineering applications (e.g., wind barriers offering protection against hurricanes, barriers controlling Aeolian sand transport in arid and coastal regions). Such information is critical to develop strategies to control the flow structure downwind of the plate. In particular, the LES flow fields allowed clarifying how the interactions between the bottom and the top separated shear layers change with increasing bottom gap and what is the effect of the bleeding flow on the interactions between the separated shear layers that determine the coherence of the large-scale eddies at large distances from the wake. Analysis of the LES results also allowed to determine what are the threshold values of G/H

for solid and porous plates when the wake structure changes from a wake containing mainly co-rotating vortices originating in the top separated shear layer to a wake containing counter-rotating billow vortices generated by the interaction of the top and bottom separated shear layers, as observed in the wake of bluff bodies situated at large distances from the channel bed. The analysis also provided quantitative data on how the wake structure gradually approaches the canonical case of flow past a solid plate with a very large bottom gap, where the effect of the bottom boundary on the wake flow is negligible.

One big limitation of the present study is that the present numerical model does not allow to model the transport of particles (e.g., sand particles, snow-flakes) and does not include a deformable boundary model to account for the change of the ground geometry as a result of particle deposition. These two features are essential for the model to be used as a direct tool to improve the design of snow/sand fences. If such a model would be available, direct estimation of the temporal evolution of the particle deposits (e.g., amount of snow accumulated downstream of the barrier) and of the deposition length away from the barrier would be possible. These limitations also apply for the RANS simulations performed in the second part of the study. Still, a detailed understanding of the flow aerodynamics and wake structure is an essential first step toward the development of such multi-physics models that can be used as design tools in practical applications involving solid/porous barriers and particle transport/deposition induced by these barriers.

In the second part of the study, the focus was on the design of lightweight plastic snow fences that are commonly used to protect roads in the US Midwest against the snow drifting and that, if properly designed, can work well along road regions with narrow right of ways. As part of the present thesis, a general novel methodology was developed, tested and validated to improve the design of snow fences. The novel methodology is based on monitoring of sites containing snow fences, measurements of the snow deposit profiles using various techniques and 2-D RANS simulations used to identify candidates for improved fence designs to be tested in the field. Using this novel methodology, an

334

improved design of lightweight snow fences was proposed that was shown to retain more snow over smaller distances from the fence compared to the standard design presently used for this type of snow fences.

Part of the monitoring program of the snow fence sites, several methods to determine the volume of snow retained by the fence after major snow storm events were tested and their advantages and disadvantages were assessed. This is important because the assessment of the performance of a fence design is based on the capacity of the fence to retain snow during major snow events. Measurement protocols were developed for the most successful techniques. Another major contribution of the present thesis was the development of a novel non-intrusive image-based technique that can be used to quantitatively estimate the temporal evolution of the volume of snow trapped by a fence over long periods of time. This technique is based on 3-D close range photogrammetry. Results showed that this technique can produce estimations of the snow deposits of comparable accuracy to that given by commonly used methods. This is the first application of this type of techniques to measurements of the snow deposits.

Several directions for future work are identified next. One such direction is to use similar LES calculations to understand the fundamental physics of flow through and downstream of porous obstacles of more complex shapes that are important for many engineering applications. Two particularly important geometries are arrays of porous plates (negligible-width) and isolated and arrays of rectangular porous obstacle of non-negligible width, which correspond to porous canopies of finite length with respect to the incoming flow direction. Another research direction is to perform two-phase flow simulations in which a Lagrangian Particle Transport module is used to determine the trajectories of the snow flakes, while accounting for drag and gravitational forces acting on the particles. This can be done using both LES and RANS calculations. In terms of practical applications related to the design of snow fences, the long term goal is to develop a capability to perform

time-accurate RANS simulations with a movable bed, whose surface evolves in time as a result of snow particles deposition.

The general methodology developed as part of the present thesis to monitor and improve the design of snow fences should be applied for other types of common structural snow fences and also for living snow fences. The 3D photogrammetry technique for applications related to measurements of snow deposits during winter time should be further improved in terms of its accuracy and robustness. Another direction for future research will be the use of LSPIV techniques to directly measure the flux of snow over the fence and the relative amount of snow relocated by the snow fence, which is one of the main input variables used by standard software used for the design of snow fences.

REFERENCES

Abdalla, I.E., Yang, Z. and Cook, M. (2009). "Computational analysis and flow structure of a transitional separated-reattached flow over a surface mounted obstacle and a forward-facing step." *International Journal of Computational Fluid Dynamics,* 23, 25-27.

Acharya, S., Dutta S., Myrum T.A., and Baker R.S. (1994). "Turbulent flow past a surface-mounted two-dimensional rib." *Journal of Fluids Engineering,* 116, 238-246.

Alhajraf, S. (2004). "Computational fluid dynamic modeling of drifting particles at porous fences." *Environmental Modeling & Software*, 19, 163-170.

Anno, Y. (1986). "Snow deflector built at the edge of a road cut." *Cold Regions Science and Technology,* 12, 121-129.

Arie, M. and Rouse, H. (1956). "Experiments on two-dimensional flow over a normal wall." *Journal of Fluid Mechanics,* 1 (2), 129-141.

Baetke, F. and Werner, H. (1990). "Numerical simulation of turbulent flow over surface-mounted obstacles with sharp edges and corners." *Journal of Wind Engineering and Industrial Aerodynamics,* 35, 129-147.

Baines, W.D. and Peterson, E.G. (1951). "An investigation of flow through screens." *Trans. ASME,* 72, 467-480.

Baldi, P., Genni, N., Fabris, M., and Zanuta, A. (2008). "Kinematics of a landslide derived from archival photogrammetry and GPS data." *Geomorphology*, 102, 435-444.

Baltaxe, R. (1967). "Airflow patterns in the lee of model windbreaks." *Archiv Meteorologie, Geophysik, und Bioklimatologie, Series B: Au¨gemeine und biologische Klimatologie,* Band 15, Hefi 3, 26 pp (in German, with English summary).

Basnet, K. and Ettema, R. (2011). "A large-scale particle image velocimetry for resolving unsteady flow features at cylinders." *Proceedings of the 34th World Congress of the International Association for Hydro-Environment Research and Engineering: 33rd Hydrology and Water Resources Symposium and 10th Conference on Hydraulics in Water Engineering."* Engineers Australia, Barton ACT, Australia, pp. 3378-3387.

Basnet, K., Constantinescu, G., Muste, M., and Ho, H. (2014). "Method to assess efficiency and improve design of snow fences." *Journal of Engineering Mechanics,* 04014136, doi: 10.1061/(ASCE)EM.1943-7889.0000871.

Bearman, P. and Obasaju, E. (1982). "An experimental study of pressure fluctuations on fixed and oscillating square section cylinders." *Journal of Fluid Mechanics,* 119, 297-321.

Bitog, J.P., Lee, I.B., Shin, M.H., Hong, S.W., Hwang, H.S., Seo, I.H., Yoo, J.I., Kwon, K.S., Kim, Y.H. and Han, J.W. (2009). "Numerical simulation of an array of fences in Saemangeum reclaimed land." *Atmospheric Environment,* 43, 4612-4621.

Borges, A.R. and Viegas, D.X. (1988). "Shelter effects on a row of coal piles to prevent wind erosion." *Journal of Wind Engineering and Industrial Aerodynamics,* 29, 145-154.

Bosh, G., Kappler, M. and Rodi, W. (1996). "Experiments on the flow past a square cylinder placed near a wall." *Journal of Experimental Thermal and Fluid Science,* 13, 292-305.

Bradley, E.F. and Mulhearn, P.J. (1983). "Development of velocity and shear stress distributions in the wake of a porous shelter fence." *Journal of Wind Engineering and Industrial Aerodynamics,* 15, 145-156.

Bühler, Y., Marty, M., Egli, L., Veitinger, J., Jonas, T., Thee, P., and Ginzler, C. (2015). "Snow depth mapping in high-alpine catchments using digital photogrammetry." *The Cryosphere,* 9 (1), 229-243.

Cabron, J.M. (1957). *"Shelterbelts and microclimate."*

Castro, I.P. (1971). "Wake characteristics of two-dimensional perforated plates normal to an air-stream." *Journal of Fluid Mechanics,* 46, 599-609.

Castro, I.P. and Haque, A. (1987). The structure of turbulent shear layer bounding a separation region. *Journal of Fluid Mechanics,* 179, 439-468.

Chang, K., Constantinescu, G. and Park, S.O. (2006), "Analysis of the flow and mass transfer process for the incompressible flow past an open cavity with a laminar and a fully turbulent incoming boundary layer." *Journal of Fluid Mechanics,* 561, 113-145.

Chang, K., Constantinescu, G. and Park, S.O. (2007). "The purging of a neutrally buoyant or a dense miscible contaminant from a rectangular cavity. Part II: The case of an incoming fully turbulent overflow." *ASCE Journal of Hydraulic Engineering,* 133 (4), 373-385.

Chang, K.S. and Constantinescu, G. (2013), "Coherent structures in developing flow over 2D dunes." *Water Resources Research,* 49, 2466-2460, doi: 10.1002/wrcr.20239

Chen, Z. and Jiang, X. (2009). "Large eddy simulation of a 3D channel flow with wall-mounted rectangular cylinders." *Modern Physics Letters B,* 23 (9), 301-304.

Cho, H. M. (1996). "Wind-tunnel and numerical simulation of flow over porous fences and particle saltation in atmospheric boundary layer." *Ph.D. dissertation,* Department of Mechanical and Aeronautical Engineering, University of California at Davis, Davis, CA, U.S.A.

Collier, P. (2002). "The impact on topographic mapping of developments in land and air survey: 1900-1939." *Cartography and Geographic Information Science,* 29 (3), 155-174.

Cong, X.C., Cao, S.Q., Chen, Z.L., Peng, S.T. and Yang, S.L. (2011). "Impact of the installation scenario of porous fences on wind-blown particle emission in open coal yards." *Journal of Atmospheric Environment,* 45, 5247-5253.

Constantinescu, S.G., A. Bhatti and T. Tokyay (2008). "A numerical study of wind loads on large highway sign structures." *SEI 2008 Structures Congress,* Vancouver, Canada, April 2008.

Constantinescu G., Koken, M. and Zeng, J. (2011). "The structure of turbulent flow in an open channel bend of strong curvature with deformed bed: insight provided by an eddy resolving numerical simulation." *Water Resources Research,* 47, W05515, doi:10.1029/2010WR010114.

Constantinescu, G., Muste, M., and Basnet, K. (2015). "Optimization of Snow Drifting Mitigation and Control Methods for Iowa Conditions." *Technical Report*, TR-626. http://publications.iowa.gov/id/eprint/19046.

Cooper, M.A.R. and Robson, S. (1996). Theory of Close Range Photogrammetry, Close Range Photogrammetry and Machine Vision, pp. 9-51.

Corneils, W.M. and Gabriels, D. (2005). "Optimal windbreak design for wind-erosion control." *Journal of Arid Environments,* 61, 315-332.

de Bray, B.G. (1957). "Low speed wind tunnel tests on perforated square flat plates normal to the air stream: drag and velocity fluctuation measurements." *Aeronautics Research Council Technical Report,* Current Paper No. 323.

Deems, J.S., Painter, T.H., and Finnegan, D.C. (2013). "Lidar measurement of snow depth: a review." *Journal of Glaciology,* 59 (215), 467-479.

Dong, Z., Luo, W., Qian, G., and Wang, H. (2007). "A wind tunnel simulation of the mean velocity fields behind upright porous fences." *Agricultural and Forest Meteorology,* 146, 82-93.

Dong, Z., Qian, G., Luo, W. and Wang, H. (2006). "Threshold velocity for wind erosion: the effects of porous fences." *Environmental Geology,* 51, 471-475.

Dong, Z., Luo, W., Qian, G., Lu, P., and Wang, H. (2010). "A wind tunnel simulation of the turbulence fields behind upright porous wind fences." *Journal of Arid Environments,* 74, 193-207.

Duan, Z., Yang, W. and Jia, X. (2011a). "Wind tunnel study on the flow characteristics of wake behind planar and non-planar porous fences." *Remote Sensing, Environment and Transportation Engineering,* doi: 10.1109/RSETE.2011.5964434.

Duan, Z., Yang, W., Pengfei, L. and Zhu, Y. (2011b). "Effect of porosity on the flow characteristics behind planar and non-planar porous fences." *Journal of Communication in Information Science and Management Engineering,* 1 (10), 15-21.

Durão, D.F.G., Gouveia, P.S.T., and Pereira, J.C.F. (1991). "Velocity characteristics of the flow around a square cross section cylinder placed near a channel wall." *Experiments in Fluids,* 11, 341-350.

Fang, F.M. and Wang, D.Y. (1997). "On the flow around a vertical porous fence." *Journal of Wind Engineering and Industrial Aerodynamics,* 67/67, 415-424.

Fenced in: Keeping snow off the road (2008). *Technology News,* September-October 2008. http://www.intrans.iastate.edu/ltap/tech_news/2008/sept-oct/fenced_in.pdf.

Finnigan, J. J. and Bradley, E. F. (1983). "The turbulent kinetic energy budget behind a porous barrier: an analysis in streamline coordinates." *Journal of Wind Engineering and Industrial Aerodynamics,* 15, 157-168.

Fujita, I. and Kunita, Y. (2011). "Application of aerial LSPIV to the 2002 flood of the Yodo River using a helicopter mounted high density video camera." *Journal of Hydro-environment Research,* 5 (4), 323-331.

Gannett, H. (1906). "Manual of Topographic Methods." USGS Bulletinn No. 307, Series F, Geography, Government Printing office, Washington, DC.

García Nieto, P.J., del Coz Díaz, J.J., Castro-Fresno, D., and Ballester, Muñoz, F. (2010). "Numerical simulation of the performance of a snow fence with airfoil snow plates by FVM." *Journal of Computational and Applied Mathematics,* 234, 1200-1210.

Gatziolis, D., Popescu, S., Sheridan, R. and Ku, N.-W. (2010). "Evaluation of terrestrial LiDAR technology for the development of local tree volume equations." *Proc., Silvilaser 2010, The 10th International conference on LiDAR applications for assessing forest ecosystems,* Freiburg, Germany, 197-205.

Gonzales-Juez, E., Meiburg, E., T. Tokyay and Constantinescu, G. (2010). "Gravity current flow past a circular cylinder: forces, wall shear stresses and implications or scour." *Journal of Fluid Mechanics,* 649, 69-102. doi: 0.1017/S002211200999334X.

Guan, D., Zhang, Y. and Zhu, T. (2003). "A wind-tunnel study of windbreak drag." *Agricultural and forest meteorology,* Vol. 118, Issues 1-2, pp. 75-84.

Fujita, I. and Kunita, Y. (2011), "Application of aerial LSPIV to the 2002 flood of the Yodo River using a helicopter mounted high density video camera." *Journal of Hydro-environment Research,* 5, 323-331.

Hagen, L.J. and Skidmore, E.L. (1971). "Windbreak drag as influenced by porosity." *Trans. ASAE,* 14, 464-465.

Haniu, H., Sakamoto, H., and Takai, K. (2009). "Improvement of blower type snow fences by control of the shear layer." *Journal of Natural Disaster Science,* 17, 53-64.

Hauet, A., Muste, M., and Ho, H-C. (2008). "Digital mapping of waterway hydrodynamics, banks and floodplain using imagery." *CD-ROM Proceedings of ASCE World Environmental and Water Resources Congress.*

Hauet, A., Muste, M., and Ho, H-C. (2009). "Digital mapping of riverine waterway hydrodynamic and geomorphic features." *Earth Surface Processes and Landforms,* 34, 242-252.

Heisler, G. M. and Dewalle, D. R. (1988). "Effects of windbreak structure on wind flow." *Agriculture, Ecosystems and Environment,* 22/23, 41-69.

Hoerner, S.F. (1965). "Fluid dynamics drag: practical information on aerodynamic drag and hydrodynamic resistance." *ISBN-13: 978-9991194448.*

Hood, J.L. and Hayashi, M. (2010). "Assessing the application of a laser rangefinder for determining snow depth in inaccessible alpine terrain." *Hydrol. Earth Syst. Sci.,* 14, 901-910.

Huang, L.M., Chan H.C. and Lee J.T. (2012). "A numerical study on flow around nonuniform porous fences." *Journal of Applied Mathematics,* 2012, doi:10.1155/2012/268371.

Hwang Robert, R., Chow Y.C., and Peng Y.F. (1999). "Numerical study of turbulent flow over two-dimensional surface-mounted ribs in a channel." *International Journal for Numerical Methods in Fluids*, 31, 767-785.

Ikeda, T. and Durbin, P. (2007). "Direct simulations of a rough-wall channel flow." *Journal of Fluid Mechanics,* 571, 235-263.

Iowa DOT: Iowa's Cooperative Snow Fence Program (2005). http://www.iowadot.gov/maintenance/pdf/ snowfencebooklet.pdf.

Iowa Environmental Mesonet, http://www.mesonet.agron.iastate.edu/.

Jiang, R., Jáuregui, D.V., White, and K.R. 2008. Close-range photogrammetry applications in bridge measurement: Literature review. *Measurement* 41, 823-834.

Kim, H.B. and Lee, S.J. (2001). "Hole diameter effect on flow characteristics of wake behind porous fences having the same porosity." *Fluid Dynamics Research,* 28, 449-464.

Kim, H.B. and Lee, S.J. (2002). "The structure of turbulent shear flow around a two-dimensional porous fence having a bottom gap." *Journal of Fluids and Structures,* 16 (3), 317-329.

Kirkil, G. and Constantinescu, G. (2009). "Nature of flow and turbulence structure around an in-stream vertical plate in a shallow channel and the implications for sediment erosion," *Water Resources Research*, Vol. 45, W06412, doi:10.1029/2008WR007363.

Kizil, U. and Tisor, L. (2011). "Evaluation of RTK-GPS and total station for applications in land surveying." *Journal of Earth Syst. Sci.,* 120 (2), 215-221.

Krajnovic, S. and Davidson, L. (2002). "Large eddy simulation of the flow about a bluff body," *AIAA Journal,* 40, 927-936.

Kramer, T. and Joska, J (2008). "A quadtree mesh readaptation for the simulation of unsteady flow and transport," Proceedings of the *International Conference on Fluvial Hydraulics*, Izmir, Turkey, 2008, 783-790.

Kraus, K. (1992). *Photogrammetry, fundamentals and standard processes,* Vol. I, Fourth Revised and Enlarged Ed., Dümmler, Bonn.

Kunapo, J. (2005). "Spatial data integration for classification of 3D point clouds from digital photogrammetry." *Applied GIS,* Vol. 1, No. 3, pp. 26.1-26.15.

Lee, S. and Bienkiewicz, B. (1997). "Large-eddy simulation of wind effects on bluff bodies using the finite element method." *Journal of Wind Engineering and Industrial Aerodynamics,* 67-68, 601-609.

Lee, S.J. and Kim, H.B. (1998). "Velocity field measurements of flow around a triangular prism behind a porous fence." *Journal of Wind Engineering and Industrial Aerodynamics,* 77/78, 521-530.

Lee, S.J. and Kim, H.B. (1999). "Laboratory measurements of velocity and turbulence field behind porous fences." *Journal of Wind Engineering and Industrial Aerodynamics,* 80, 311-326.

Lee, S.J. and Lim, H.C. (2001). "A numerical study on flow around a triangular prism located behind a porous fence." *Fluid Dynamics Research,* 28 (3), 209-221.

Lee, S.J. and Park, C.W. (1999). "Surface pressure characteristics on a triangular prism located behind a porous fence." *Journal of Wind Engineering and Industrial Aerodynamics,* 80, 69-83.

Lee, S.J., Park, K.C. and Park, C.W. (2002). "Wind tunnel observations about the shelter effect of porous fences on the sand particle movements." *Atmospheric Environment,* 36, 1453-1463.

Lenzano, M.G., Lannutti, E., Toth, C., Lenzano, L. and Lovecchio, A. (2014). "Assessment of ice-dam collapse by time-lapse photos at the Perito Moreno Glacier, Argentina." The International Achieves of the Photogrammetry, Remote Sensing and Spatial Information Sciences, Volume XL-1, 2014: ISPRS Technical Commission I Symosium, Denver, Colorado, USA, 211-217.

Lerma, J.L., Navarro, S., Cabrelles, M. and Villaverde, V. (2010). "Terrestrial laser scanning and close range photogrammetry for 3D archaeological documentation: the Upper Palaeolithic of Parpallo´ as a case study." *Journal of Archaeological Science,* 37, 499-507.

Li, W., Wang, F. and Bell, S. (2007). "Simulating the sheltering effects of windbreaks in urban outdoor open space." *Journal of Wind Engineering and Industrial Aerodynamics,* 95, 533-549.

Lohász, M.M., Rambaud, P. and Benocci, C. (2006). "Flow features in a fully developed ribbed duct flow as a result of MILES." *Flow, Turbulence and Combustion,* 77:1-4, 59-76.

Lindsey, W. F. (1938). "Drag of cylinders of simple shapes." *NACA, TR.* 619, 169-176.

Lin, Y., Jin, J., Zou, B., Cong, Z., Wen, X., Tu, X. and Ye, J. (1984). "Effect of fence techniques in leveling sand accumulation around sand-breaks." *Journal of Desert Research,* 4 (3), 16–25.

LPS Project Manager (2009). "User's guide, November 2009." ERDAS, Inc. 5051 Peachtree Corners Circle, Suite 100, Norcross, GA 30092, USA.

Luhman, T., Robson, S., Kyle, S., and Harley, I. (2011). "Close range photogrammetry: principles, techniques and applications." ISBN-13: 978-1849950572.

Lyn, D.A., Einav, S., Rodi, W. and Park, J.H. (1995). "A laser-Doppler velocimetry study of ensemble-averaged characteristics of the turbulent near wake of a square cylinder." *Journal of Fluid Mechanics,* 304, 285-319.

Mahesh, K., Constantinescu, S.G. and Moin, P. (2004). "A numerical method for large eddy simulation in complex geometries." *Journal of Computational Physics,* 197, 215-240.

Marshall, J.K. (1967). "The effect of shelter on the productivity of grass lands and field crops." *Field Crop Abstracts,* 20, 1-14.

Martinuzzi, R.J., Bailey, S.C.C. and Kopp, G.A. (2003). "Influence of wall proximity on vortex shedding from a square cylinder." *Experiments in Fluids,* 34, 585-596.

Marzolff, I. and Poesen, J. (2009). "The potential of 3D gully monitoring with GIS using high-resolution aerial photography and a digital photogrammetry system." *Geomorphology*, 111, 48-60.

Mass, H.-G. (1997). "Concepts of real-time photogrammetry." *Human Movement Science,* 16, 189-199.

Matthews, N.A. (2008). "Aerial and close-range photogrammetric technology: providing resource documentation, interpretation, and preservation." *Technical Note 428*. U.S.

Department of the Interior, Bureau of Land Management, National Operations Center, Denver, Colorado.

Matthews, N.A. (2008). "Aerial and close-range photogrammetric technology: providing resource documentation, interpretation, and preservation." *Technical Note 428*. U.S. Department of the Interior, Bureau of Land Management, National Operations Center, Denver, Colorado. pp 42.

Moskal, L.M. and Zheng, G. (2012). "Retrieving forest inventory variables with terrestrial laser scanning (TLS) in urban heterogeneous forest." *Remote Sensing,* 4, 1-20.

Muste, M., Hauet, A., Ho, H-C., and Nakato, T. (2009). "Quantitative mapping of waterways characteristics at bridge sites." *IIHR Technical Report No. 470,* IIHR Hydroscience & Engineering, The University of Iowa, Iowa City, IA.

Muste, M., Ho, H-C., and Kim, D. (2011). "Considerations on direct stream flow measurements using video imagery: Outlook and research needs." *Journal of Hydro-environment Research,* 5, 289-300.

Moultrie Game Management System. www.moultriegamemanagement.com.

Najjar, F.M. and Vanka, S.P. (1993). "Numerical study of a separated-reattaching flow." *Theoretical and Computational Fluid Dynamics,* 5, 291-308.

Nixon, W.A., Davison, M., and Kochumman, G. (2006). "Living snow fences, Iowa Highway Research Board Project TR 460 Final Report." *IIHR Technical Report 460,* IIHR-Hydroscience and Engineering, College of Engineering, The University of Iowa.

Norberg, C. (1993). "Flow around rectangular cylinders: Pressure forces and wake frequencies." *Journal of Wind Engineering and Industrial Aerodynamics,* 49, 187–196.

Ooi, S.K., Constantinescu, G. and Weber, L. (2009). "Numerical simulations of lock-exchange compositional gravity current." *Journal of Fluid Mechanics,* 635, 361-388.

Orellano, A. and Wengle, H. (2000). "Numerical simulation (DNS and LES) of manipulated turbulent boundary layer flow over a surface-mounted fence." *Eur. Journal Mech. B – Fluids,* 19, 765-788.

Panigrahi, P.K. (2009). "PIV investigation of flow behind surface mounted detached square cylinder." *Journal of Fluids Engineering,* 131, 011202-1, doi: 10.1115/1.3026721.

Patton, E.G., Shaw, R.H., Judd, M.J. and Raupach, M.R. (1998). "Large-eddy simulation of windbreak flow." *Boundary-Layer Meteorology,* 87, 275-306.

Perera, M.D. (1981). "Shelter behind two-dimensional solid and porous fences." *Journal of Wind Engineering and Industrial Aerodynamics,* 8, 93-104.

Photogrammetry. http://www.photogrammetry.com/.

Photomodeler. http://www.photomodeler.com/products/how-it-works.html.

Pierce, C.D. and Moin, P. (2001). "Progress-variable approach for large-eddy simulation of turbulent combustion." *Mech. Eng. Dept. Rep.,* TF-80, Standford University.

Plate, E.J. (1964). "The drag on a smooth flat plate with a fence immersed in its turbulent boundary layer." *ASME Paper No. 64-FE-17,* 12pp.

Plate, E.J. (1971). "The aerodynamics of shelterbelts." *Agricultural Meteorology,* 8, 203-222.

Prokop, A. (2008). "Assessing the applicability of terrestrial laser scanning for spatial snow depth measurements." *Cold Regions Science and Technology,* 54(3), 155-163.

Prokop, A. and Delaney, C.M. (2012). "Positioning of avalanche protection measures using snow depth mapping via terrestrial laser scanning." *Proceedings, 2012 International Snow Science Workshop,* Anchorage, Alaska.

Prokop, A., Schon, P., Singer, F., Pulfer, G., Naaim, M., Thibert E., and Soruco, A. (2015). "Merging terrestrial laser scanning technology with photogrammetric and total station data for the determination of avalanche modeling parameters." *Cold Regions Science and Technology,* 110, 223-230.

Prokop, A., Schirmer, M., Rub, M., Lehning, M. and Stocker, M. (2008). "A comparison of measurement methods: terrestrial laser scanning, tachymetry and snow probing for the determination of the spatial snow-depth distribution on slopes. *Annals of Glaciology,* 49, 210-216.

Raine, J.K. and Stevenson, D.C. (1977). "Wind protection by model fences in a simulated atmospheric boundary layer." *Journal of Industrial Aerodynamics,* 2, 159-180.

Ranga raju, K.G., Garde, R.J., Singh, S.K., Singh, N. (1988). "Experimental study on characteristics of flow past porous fences." *Journal of Wind Engineering and Industrial Aerodynamics,* 29, 155-163.

Rodi, W. (1997). "Comparison of LES and RANS calculations of the flow around bluff bodies." *Journal of Wind Engineering and Industrial Aerodynamics*, 1997, 69, 55-75.

Rodi, W., Constantinescu, G. and Stoesser, T. (2013). *"Large-eddy simulation in hydraulics." IAHR Monograph, CRC Press,* Taylor & Francis Group (ISBN-10: 1138000247)

Rodi, W., Ferziger, J.H., Breuer, M. and Pourquie, M. (1997). "Status of large eddy simulation: results of a workshop." *T. ASME Journal of Fluids Engineering,* 119, 248-262.

Saif, A.M., Mohamed, A.M.I., and Alam Eldein, A.M. (2010). "Variable porosity wind fences to control Aeolian sand transport." CD-ROM *Proceedings of Tenth International Congress of Fluid Dynamics*.

Santiago, J.L., Martin, F., Cuerva, A., Bezdenejnykh, N. and Sanz-Andres, A. (2007). "Experimental and numerical study of wind flow behind windbreaks." *Atmospheric Environment,* 41, 6406-6420.

Sañudo-Fontaned, L.A., Castro-Fresno, D., del Coz-Díaz, J.J., and Rodriguez-Hernandez, J. (2011). "Classification and comparison of snow fences for the protection of transport infrastructures." *Journal of Cold Regions Engineering,* 25, 162-181.

Schenk, T. (2005). "Introduction to photogrammetry." *GS 400.02, Autumn Quarter 2005*. Department of Civil and Environmental Engineering and Geodetic Science. The Ohio State University, 2070 Neil Ave., Columbus, OH 43210, USA.

Seginer, I. (1972). "Windbreak drag calculated from the horizontal velocity field." *Boundary-Layer Meteorology,* 3, 87-97.

Shah, K.B. and Ferziger, J.H. (1998). "Large eddy simulations of flow past a cubic obstacle." *PhD thesis,* Stanford University.

Shiau, B.S. (1992). "The turbulence structure behind the multiple windbreaks across-wind." *Journal of Wind Engineering and Industrial Aerodynamics*, 41-44, 461-468.

Shiau, B.S. (1995). "Measurement of the Reynolds stress behind multiple windbreaks across-wind." *Journal of Wind Engineering and Industrial Aerodynamics,* 54/55, 561-571.

Siller, H.A. and Fernholz, H.H. (1997). "Control of the separated flow downstream of a two-dimensional fence by low-frequency forcing." *Appl. Sci. Res.,* 57, 309-318.

Sinha, S., Liu, X. and Garcia, M. (2012). "Three-dimensional hydrodynamic modeling of the Chicago River," *Environmental Fluid Mechanics,* 12(5), 471-494.

Soole, P. and Poropat, G. (2000). "Highwall mapping using terrestrial photogrammetry." *Bowen Basin Symposium 2000 Proceedings, Rockhampton, 22-24 October, (2000)*, Ed. J.W. Beeston, pp. 343-346.

Srinivas, Y., Biswas, G., Parihar, A.S. and Ranjan, R. (2006). "Large-eddy simulation of high Reynolds number turbulent flow past a square cylinder." *Journal of Engineering Mechanics,* 132 (3), 327-335.

Sturzenegger, M. and Stead, D. (2009). "Close-range terrestrial digital photogrammetry and terrestrial laser scanning for discontinuity characterization on rock cuts." *Engineering Geology*, 106,163-182.

Tabler, R.D. (1991). "Snow fence guide." *Strategic Highway Research Program,* Washington, D.C., pp. 61.

Tabler, R.D. (2003). "Controlling drifting and blowing snow with snow fences and road design." *Final Report, NCHRP Project 20-7 (147),* Transportation Research Board of the National Academies, Washington, D.C.

Tani, N. (1952). "On the wind tunnel test of the model shelter-hedge." *Bull. Nat. Inst. Agri. Sci. Japan, Ser. A.,* 6, 75-80.

Tecplot 360 (2011). "User's manual, 2011." Tecplot, Inc. PO Box 52708, Bellevue, WA 98015, USA.

Tokyay, T., Constantinescu, G. and Meiburg, E. (2011). "Lock exchange gravity currents with a high volume of release propagating over an array of obstacles." *Journal of Fluid Mechanics,* 672, 570-605.

Tokyay, T., Constantinescu, G. and Meiburg, E. (2012). "Tail structure and bed friction velocity distribution of gravity currents propagating over an array of obstacles." *Journal of Fluid Mechanics,* 694, 252-291.

Topcon GTS 235 Total Station. http://geog.sfsu.edu/geog/field-equipment/topcon-gts-235-total-station.

Trimble Correction Services. http://www.trimble.com/agriculture/CorrectionServices/CenterPointRTK.aspx.

Tsubaki, R. and Fujita, I. (2010). "Unstructured grid generation using LiDAR data for urban flood inundation modelling," *Hydrological processes*, 24(11), 1404-1420.

Wang, G. and Vanka, S.P. (1996). "Large-eddy simulations of high Reynolds number turbulent flow over a square cylinder." Dept. of Mechanical and Industrial Engineering Rep. No. *CFD 96-02,* Univ. of Illinois at Urbana-Champaign, Ill.

Wang, H. and Takle, E.S. (1995). "A numerical simulation of boundary-layer flows near shelterbelts." *Boundary-Layer Meteorology,* 75, 141-173.

Wilson, J.D. (1985). "Numerical studies of flow through a windbreak." *Journal of Wind Engineering and Industrial Aerodynamics,* 21, 119-154.

Wilson, J.D. (1997). "A field study of the mean pressure about a windbreak." *Boundary-Layer Meteorology,* 85, 327-358.

Wilson, J.D. (2004). "Oblique, stratified winds about a shelter fence. Part II: comparison of measurements with numerical models." *Journal of Applied Meteorology,* 43, 1392-1409.

Wilson, J.D. and Mooney, C.J. (1997). "A numerical simulation of boundary-layer flows near shelterbelts-comments." *Boundary-Layer Meteorology,* 85, 137-149.

Wilson, J.D. and Yee, E. (2003). "Calculation of wind disturbed by an array of fences." *Agricultural and Forest Meteorology,* 115, 31-50.

Wilson, J.D. (1985). "Numerical studies of flow through a windbreak." *Journal of Wind Engineering and Industrial Aerodynamics,* 21, 119-154.

Wolf, P.R. and Dewitt, B.A. (2000). *Elements of photogrammetry with GIS applications,* The Mc Graw-Hill Companies, 3rd Edition, USA.

Wyoming Department of Transportation HEEP report (2007). "Controlling blowing snow – Snow drift profiler." http://www.heepweb.org/ProgramsReports/Reports/HEEPAgencyReports/tabid/96/EntryID/46/Default.aspx.

Yakar, M. (2009). "Usıng close range photogrammetry to measure the posıtıon of inaccessıble geologıcal features." *Experımental Technıques,* doi: 10.1111/j.1747-1567.2009.00583.

Yakar, M. and Yilmaz, H.M. (2008). "Using in volume computing of digital close range photogrammetry." *The International Archives of the Photogrammetry, Remote Sensing and Spatial Information Sciences. Vol. XXXVII. Part B3b. Beijing 2008.*

Yakar, M., Yilmaz, H.M., and Mutluoglu, O. (2010). "Close range photogrammetry and robotic total station in volume calculation." *International Journal of the Physical Sciences,* 5(2), 86-96.

Yang, K.S. and Ferziger, J.H. (1993). "Large-eddy simulation of turbulent obstacle flow using a dynamic subgrid-scale model." *AIAA Journal,* 31 (8), 1406-1413.

Yaragal, S.C., Govinda Ram H.S. and Keshava Murthy K. (1997). "An experimental investigation of flow fields downstream of solid and porous fences." *Journal of Wind Engineering,* 66, 127-140.

Yaragal, S.C., Govinda Ram H.S. and Keshava Murthy K. (2002). "Two-dimensional flow field behind perforated plates on a flat surface." *Journal of Wind Engineering,* 90, 75-90.